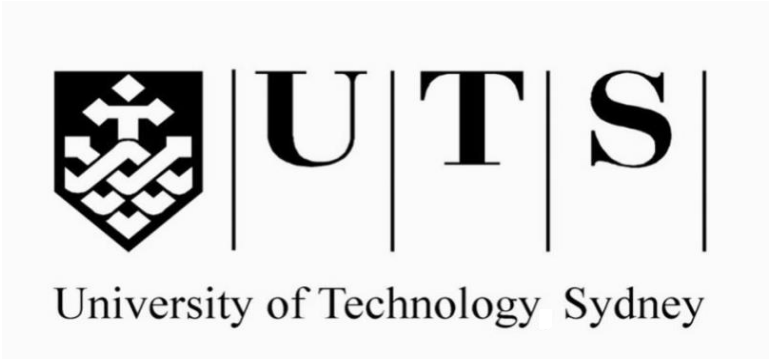

Faculty of Engineering and Information Technology

Robust topology optimization with hybrid uncertainties using level set methods

A thesis submitted for the degree of

Doctor of Philosophy

JING ZHENG

(2019)

Title of the thesis:

Robust topology optimization with hybrid uncertainties using level set methods

Ph.D. student:

Jing Zheng

E-mail: Jing.Zheng-3@student.uts.edu.au

Supervisor:

A/Prof Zhen Luo

E-mail: zhen.luo@uts.edu.au

Co-Supervisor and joint-supervisor:

Prof Nong Zhang

E-mail: nong.zhang@uts.edu.au

Prof Chao Jiang

E-mail: jiangc@hnu.edu.cn

Address:

School of Mechanical and Mechatronic Engineering

The University of Technology Sydney, Sydney, NSW 2007, Australia

Certificate of Original Authorship

I certify that the work in this thesis has not previously been submitted for a degree nor has it been submitted as part of requirements for a degree except as fully acknowledged within the text.

This thesis is the result of a research candidature conducted jointly with another University as part of a collaborative degree. This research is supported by the Australian Government Research Training Program.

I also certify that the thesis has been written by me. Any help that I have received in my research work and the preparation of the thesis itself has been acknowledged. In addition, I certify that all information sources and literature used are indicated in the thesis.

Signature of Student:

Production Note:
Signature removed prior to publication.

JING ZHENG

Date: 17/10/2018

Acknowledgments

I would like to take this opportunity to express my deep gratitude to all those who helped me throughout my candidature.

First and foremost, I would like to extend my sincere gratitude to my principal supervisor, A/Prof. Z Luo. During the studying of the course and the writing of the thesis, he had contributed greatly by giving useful suggestions and constructive criticism. He devoted a considerable portion of his time to reading my manuscripts and making suggestions for further revisions. Moreover, he gave me many encouragements and other help in my study and life. Also, I would like to express my heartfelt gratitude to my joint supervisor Prof. C Jiang and co-supervisor Prof. N Zhang for their support and guidance. Their outstanding knowledge, intelligence and wisdom have a profound influence on me.

I also wish to express my gratitude to Dr. Hao Li, Dr. Jinglai Wu, and Dr. Zhiliang Huang. They offered me great help and gave me many valuable suggestions. My sincere thanks should also go to my colleagues Bingyu Ni, Xiangyun Long, Zhe Zhang, Zhicheng Liu, Zhonghua Wang, Bochuan Li, Jie Gao, Huipeng Xue, Xinpeng Wei, Jiachang Tang, Haibo Liu, Teng Fang, Xinyu Jia, for their support.

My last and special thanks would go to my beloved family for their loving considerations and great confidence in me all through these years.

Jing Zheng

Sydney, 2018

Publications and Conference Contributions

International scientific journal publications

[1] **J Zheng**, Z Luo, C Jiang, BY Ni, JL Wu. Non-probabilistic reliability-based topology optimization with multidimensional parallelepiped convex model. Structural and Multidisciplinary Optimization, 2018, 57(6): 2205-2221.

[2] **J Zheng**, Z Luo, H Li, C Jiang. Robust topology optimization for cellular composites with hybrid uncertainties. International Journal for Numerical Methods in Engineering, 2018, 115(6): 695-713.

[3] **J Zheng**, Z Luo, C Jiang, JL Wu. Level-set topology optimization for robust design of structures under hybrid uncertainties. International Journal for Numerical Methods in Engineering, 2019, 117(5):523-542.

[4] **J Zheng**, Z Luo, C Jiang, J Gao. Robust topology optimization for concurrent design of dynamic structures under hybrid uncertainties. Mechanical Systems and Signal Processing, 2019, 120: 540-559.

[5] C Jiang, **J Zheng**, X Han. Probability-interval hybrid uncertainty analysis for structures with both aleatory and epistemic uncertainties: a review. Structural and Multidisciplinary Optimization, 2018, 57(6): 2485–2502.

[6] C Jiang, **J Zheng**, BY Ni, X Han. A probabilistic and interval hybrid reliability analysis method for structures with correlated uncertain parameters. International

Journal of Computational Methods, 2015, 12(04): 1540006.

[7] JL Wu, Z Luo, **J Zheng**, C Jiang. Incremental modeling of a new high-order polynomial surrogate model. Applied Mathematical Modelling, 2016, 40(7-8): 4681-4699.

[8] ZL Huang, C Jiang, YS Zhou, **J Zheng**, XY Long. Reliability-based design optimization for problems with interval distribution parameters. Structural and Multidisciplinary Optimization, 2017, 55(2), 513-528.

[9] ZL Huang, YS Zhou, C Jiang, **J Zheng**, X Han. Reliability-based multidisciplinary design optimization using incremental shifting vector strategy and its application in electronic product design. Acta Mechanica Sinica, 2018, 34(2): 285-302.

International conference publications

[10] **J Zheng**, Z Luo. Reliability-Based Topology Optimization for Continuum Structures with Non-probabilistic Uncertainty. The 12th World Congress of Structural and Multidisciplinary Optimization (WCSMO12). Springer, Germany, 2017: 390-395.

[11] **J Zheng**, C Jiang, Z Luo. A probability and interval reliability analysis method for structures considering correlation. The 12th World Congress on Computational Mechanics (WCCM XII), 24-29 July, 2016, Seoul, Korea. Paper NO. 151724.

List of Figures

Figure 3-1 A 2D boundary embedded as the zeros level set of a 3D level set function..... 40
Figure 3-2 Shape of CSRBFs..... 45
Figure 3-3 Design domain and boundary condition for the cantilever beam..... 58
Figure 3-4 The evolution process of the cantilever beam..... 60
Figure 3-5 Objective function iteration history of the cantilever beam..... 61
Figure 3-6 Volume constraint iteration history of the cantilever beam..... 61
Figure 3-7 Design domain and boundary condition for the MBB beam..... 61
Figure 3-8 The evolution process of the MBB beam..... 62
Figure 3-9 Objective function iteration history of the MBB beam..... 63
Figure 3-10 Volume constraint iteration history of the MBB beam..... 63
Figure 3-11 Design domain and boundary condition for the Michell-type structure..... 64
Figure 3-12 The evolution process of the Michell-type structure..... 65
Figure 3-13 Objective function iteration history of the Michell-type structure..... 66
Figure 3-14 Volume constraint iteration history of the Michell-type structure..... 66

Figure 4-1 Multi-index set χ_1 in a two dimensional space..... 72
Figure 4-2 Construction of the sparse grid..... 77

Figure 5-1 Design domain and boundary condition for example 1..... 104
Figure 5-2 Optimized results for deterministic and robust designs for example 1..... 105
Figure 5-3 Design domain and boundary condition for example 2..... 107
Figure 5-4 Optimized results for deterministic and robust designs for example 2..... 108
Figure 5-5 Design domain and boundary condition for example 3..... 110
Figure 5-6 Optimized results for deterministic and robust designs for example 3..... 111
Figure 5-7 Design domain and boundary condition for example 1..... 127
Figure 5-8 Optimized results for deterministic and robust designs for example 1..... 128
Figure 5-9 Convergent histories of example 1..... 129
Figure 5-10 Design domain and boundary condition for example 2..... 130
Figure 5-11 Optimized results for deterministic and robust designs for example 2..... 131
Figure 5-12 Convergent histories of example 2..... 131
Figure 5-13 Design domain and boundary condition for example 3..... 133
Figure 5-14 Optimized results for deterministic and robust designs for example 3..... 134
Figure 5-15 Convergent histories of example 3..... 134

Figure 6-1 The schematic diagram of the homogenization method..... 138
Figure 6-2 The schematic diagram of the multiscale system..... 144
Figure 6-3 The flowchart of the proposed method..... 156
Figure 6-4 Design domain and boundary condition for example 1 158
Figure 6-5 Optimized results in macro and micro scales for example 1..... 159
Figure 6-6 Convergent histories for example 1..... 161
Figure 6-7 Design domain and boundary condition for example 2 162
Figure 6-8 Optimized results in macro and micro scales for example 2..... 164
Figure 6-9 Convergent histories for example 2..... 165
Figure 6-10 Design domain and boundary condition for example 3 166
Figure 6-11 Optimized results in macro and micro scales for example 3..... 168
Figure 6-12 Convergent histories for example 3..... 169
Figure 6-13 The flowchart of the proposed method..... 182
Figure 6-14 Design domain and boundary condition for example 1 183
Figure 6-15 Optimized results in macro and micro scales for example 1..... 185
Figure 6-16 Convergent histories for example 1..... 186
Figure 6-17 Design domain and boundary condition for example 2 188
Figure 6-18 Optimized results in macro and micro scales for example 2..... 190
Figure 6-19 Convergent histories for example 2..... 190
Figure 6-20 Design domain and boundary condition for example 3 192
Figure 6-21 Optimized results in macro and micro scales for example 3..... 194
Figure 6-22 Convergent histories for example 3..... 194

List of Tables

Table 4-1 Nodes and weights of the Gauss-Hermite integration of one dimensional..... 76
Table 4-2 Multidimensional integration points 76
Table 4-3 Distribution types and parameter of variables 84
Table 4-4 Results of the performance function with hybrid uncertainties 86
Table 4-5 Distribution types and parameter of variables 94
Table 4-6 Results of the performance function with hybrid uncertainties 95

Table 5-1 Robust objective function of optimized designs for example 1..... 107
Table 5-2 Robust objective function of optimized designs for example 2..... 109
Table 5-3 Robust objective function of optimized designs for example 3.....112
Table 5-4 Robust objective function of optimized designs for example 1..... 130
Table 5-5 Robust objective function of optimized designs for example 2..... 132
Table 5-6 Robust objective function of optimized designs for example 3..... 135

Table 6-1 Robust objective function of optimized designs for example 1..... 162
Table 6-2 Robust objective function of optimized designs for example 2..... 166
Table 6-3 Robust objective function of optimized designs for example 3..... 169
Table 6-4 Robust objective function of optimized designs for example 1..... 188
Table 6-5 Robust objective function of optimized designs for example 2..... 191
Table 6-6 Robust objective function of optimized designs for example 3..... 195

Abbreviations

SIMP	Solid Isotropic Material with Penalization
ESO	Evolutionary Structural Optimization
BESO	Bi-directional Evolutionary Structural Optimization
LSM	Level Set Method
LSF	Level Set Function
PLSM	Parameterized Level Set Method
RBF	Radial Basis Function
GSRBF	Globally Supported Radial Basis Function
CSRBF	Compactly Supported Radial Basis Function
HJ-PDE	Hamilton-Jacobian Partial Derivative Equation
ODE	Ordinary Differential Equation
RBDO	Reliability-based Design and Optimization
RBTO	Reliability-based Topology Optimization
RTO	Robust Topology Optimization
KL	Karhunen-Loeve expansion
PCCI	Polynomial Chaos-Chebyshev Interval
SGNI	Sparse Grid Numerical Integration
HUDR	Hybrid Univariate Dimension Reduction
HDR	Hybrid Dimension Reduction
MCS	Monte Carlo Simulation
MR	Model Reduction
QSRV	Quasi-Static Ritz Vector
OC	Optimality Criteria
MMA	Method of Moving Asymptotes

Abstract

Topology optimization has been experiencing great popularity in a diversity of engineering areas. Parameters involved in most topology optimization problems are under deterministic assumptions. However, in practical applications, uncertainties are inevitably existing due to various reasons, such as manufacturing tolerances, loads, material properties, geometric dimensions and boundary conditions, as well as aging within the whole life circle of structural service. In particular, in the conceptual design by the topology optimization, more reliable results can be expected if uncertainties are taken into account, as the performance of a topological design varies with the uncertainties. In this setting, the deterministic assumption may result in a design that is unfeasible. Hence, it is of great importance to incorporate uncertainties into the topology optimization to account for unavoidable variations.

Probability models have been widely used to describe the uncertainties of parameters in structures, which in general require a sufficient number of samples to completely construct the distributions. However, in engineering, it is very difficult to gain complete information to accurately describe the probability distributions, while it is relatively easy to get their interval bounds for limited information. In practice, it is recognized that a structure often involves uncertainties of multiple sources, in which some uncertain parameters can be regarded as random variables and the others can be modelled as interval variables. Hence, a design problem under random-interval hybrid uncertainties consists of both the aleatory and epistemic uncertainties at the same time. In this thesis, the hybrid uncertainties will be

considered in topology optimization problems to achieve robust designs. The detailed contents are outlined as follows:

Chapter 1 provides a brief introduction for this research. Chapter 2 gives the background and a literature review. Chapter 3 describes the details of a parametric level set method (PLSM) based on compactly supported radial basis functions (CSRBFs). Some efficient random-interval hybrid uncertain analysis methods are developed in Chapter 4. In the following Chapters, the uncertainty analysis methods are then employed to formulate robust topology optimizations for structures with hybrid uncertainties, as follows:

In Chapter 5, robust topology optimization methods based on orthogonal polynomials are developed for both static and dynamic continuum structures with hybrid uncertainties. In Chapter 6, robust topology optimization methods based on dimension reduction methods are developed for the multi-scale design of static and dynamic structures with hybrid uncertainties.

Finally, conclusions and prospects are given in Chapter 7.

Key words: Topology optimization; level set method; hybrid uncertainty; orthogonal polynomial; dimension reduction method.

Contents

Certificate of Original Authorship I

Acknowledgments II

Publications and Conference Contributions III

List of Figures VI

List of Tables VIII

Abbreviations IX

Abstract X

Chapter 1 Introduction 4

1.1 Overview of the project 4

1.2 Research contribution 7

1.3 Outline of the thesis 8

Chapter 2 Background and literature review 10

2.1 Literature review of topology optimization 10

2.1.1 Topology optimization methods 10

2.1.2 Topological optimization of microstructural metamaterials 14

2.1.3 Multi-scale design of cellular composites 17

2.2 Literature review of uncertain analysis 19

2.2.1 Random uncertain analysis 19

2.2.2 Interval uncertain analysis 22

2.2.3 Random and interval hybrid uncertain analysis 26

2.3 Literature review of uncertain topology optimization 33

Chapter 3 A level set method for topology optimization 39

3.1 The level set method 39

3.1.1 Representation of the boundary via LSM 39

3.1.2 Hamilton-Jacobi Equation 40

3.2 The parametric level set method 42
3.2.1 Compactly Supported Radial Basis Functions 42
3.2.2 Parameterization of the level set function 46
3.3 Topology optimization based on the PLSM 48
3.3.1 Topology optimization formulation 48
3.3.2 Sensitivity analysis 50
3.4 Optimization method 53
3.4.1 Optimality Criteria Method 53
3.4.2 The Method of Moving Asymptotes 56
3.5 Numerical examples 58
Chapter 4 Random-interval hybrid uncertainty analysis 68
4.1 Hybrid uncertainty analysis method based on orthogonal polynomials 69
4.1.1 A hyperbolic Polynomial Chaos-Chebyshev Interval method (hPCCI) 69
4.1.2 An improved Polynomial Chaos-Chebyshev Interval method (iPCCI) 75
4.1.3 Numerical example 84
4.2 Hybrid uncertainty analysis method based on dimension reduction method 86
4.2.1 A Hybrid univariate dimension reduction method (HUDR) 87
4.2.2 A Hybrid dimension reduction method (HDR) 90
4.2.3 Numerical example 94
Chapter 5 Robust topology optimization for structures based on orthogonal polynomials 96
5.1 Robust topology optimization for static structures with hybrid uncertainties 96
5.1.1 Random field approximation by KL expansion 97
5.1.2 Robust topology optimization 100
5.1.3 Numerical examples 104
5.2 Robust topology optimization for dynamic structures with hybrid uncertainties 112
5.2.1 Dynamic topology optimization 113
5.2.2 Robust dynamic topology optimization 124
5.2.3 Numerical examples 127

5.3 Summary 135

Chapter 6 Robust topology optimization for cellular composites based on dimension reduction methods 137

6.1 Homogenization method 137

6.2 Parametric level sets for the multi-scale system 143

6.3 Robust topology optimization for multi-scale design of static structures with hybrid uncertainties 147

6.3.1 Deterministic multi-scale topology optimization 147

6.3.2 Robust topology optimization 152

6.3.3 Numerical examples 157

6.4 Robust topology optimization for multi-scale design of dynamic structures with hybrid uncertainties 170

6.4.1 Deterministic multi-scale dynamic topology optimization 170

6.4.2 Robust dynamic topology optimization 177

6.4.3 Numerical examples 183

6.5 Summary 196

Chapter 7 Summary and prospect 197

7.1 Summary 197

7.2 Perspective for future work 198

References 201

Chapter 1 Introduction

1.1 Overview of the project

Structural engineers always endeavor to search for more efficient use of material for structures to reduce weights but maintain high performances. Structural optimization has been developed as a computational design tool to find optimized structures via numerical procedures. Topology optimization has become a powerful tool for the design and development of new products. As a conceptual and preliminary design stage in the structural design, topology optimization is of vital importance and has witnessed a growing interest in engineering areas including architecture, mechanical, aerospace and marine engineering.

Topology optimization provides a numerical iterative process to redistribute the distribution of materials within a reference design domain under appropriate boundary conditions, so as to optimize the concerned structural performance. Traditionally, parameters for structures in topology optimization problems are generally assumed as deterministic ones. However, uncertainties such as manufacturing tolerances, load variations, materials are generally unavoidable in practice. Topology optimization with uncertainties has then become a more and more popular research area and result in fruitful outcomes during recent decades.

Uncertainty can be classified into two different types, namely aleatory and epistemic uncertainty. Aleatory uncertainty, also termed as objective or stochastic uncertainty, describes the inherent variability associated with a physical system or environment. Epistemic uncertainty or subjective uncertainty derives from some level of ignorance or incomplete information about

a physical system or environment. The probability model is a traditional uncertain model to describe the aleatory uncertainty which needs a large number of experimental samples to establish the probability distribution. Sometimes, due to testing difficulties or cost constraints, it is often difficult to establish accurate probability distributions for some parameters. As a complementary tool for probabilistic methods, interval model has drawn much attention in the areas of uncertain analysis and design. In many practical engineering problems, some uncertain parameters can be described by probability distributions, while some uncertain parameters can only be given by intervals for lack of sufficient samples. For these cases, random-interval hybrid models are more suitable and reasonable.

Uncertainties can be incorporated into topological optimization to formulate the reliability-based topology optimization (RBTO) or robust topology optimization (RTO). In RBTO problems, the optimization model is generally formulated with reliability constraints to account for uncertainties. For RTO problems, the optimization model usually aims to minimize both the mean and variance of the uncertain objective function. Uncertainties have caused many challenges including the modeling, sensitivity analysis, computational cost for topology optimization problems, so it is essential to develop practical and efficient methods to deal with this kind of problems. In this work, we will mainly focus on the development for robust topology optimization methods considering random and interval hybrid uncertainties. The main challenges in these problems are as follows: how to build the optimization model considering uncertainties; how to evaluate the robust objective function values efficiently and accurately; how to obtain the sensitivities with respect to design variables; how to stably solve the optimization model and at the same time save the computer cost as much as possible.

LSM has been developed a lot these years due to some unique features, for example, the smooth and clear boundary, topological flexibility by the merging and breaking of the boundaries, as well as the integrated process of topological shape optimization. The PLSM based on CSRBF can avoid some numerical issues in traditional LSMs from the velocity extension, re-initialization and Courant-Friedrichs-Lewy Condition. In this thesis, the topology optimization problems are all built and solved by this PLSM. Static and dynamic topology optimization for continuum structures with hybrid uncertainties are considered in Chapter 5. The orthogonal polynomials are used to build the hybrid uncertainty model and efficiently calculate the robust objective function. Apart from most conventional topology optimization problems which are focused on the use of solid materials, concurrent topology optimization for both composite macrostructure and material microstructure has become an attractive topic for researchers since material design for the microstructure may provide more flexibility in the design optimization. In Chapter 6, multi-scale topology optimization methods for static and dynamic structures with periodic microstructures are presented by using the PLSM in both scales. Dimension reduction schemes are employed to build hybrid uncertainty analysis methods, and corresponding RTO strategies are developed for the uncertain topology optimization problems.

The proposed RTO methods can be introduced to some other prospective areas for topology optimization, for example, mechanical metamaterial designs, heat conduction topology optimizations, thermal-elastic problems and so on. Moreover, the uncertainty analysis methods can also be extended in a different series of engineering problems, including structural reliability analysis, vehicle design, and civil engineering problems. The proposed

uncertain models and corresponding algorithms can be used to improve the robustness and reliability of product and system.

1.2 Research contribution

The specific objectives and contributions are given as follows:

(1) Polynomial Chaos-Chebyshev Interval (PCCI) method is a very efficient random-interval hybrid uncertainty analysis method. However, as the increasing of the number of the uncertain parameters, the calculation burden will become quite heavy. For problems with a relatively large number of uncertain variables, we proposed the so-called hyperbolic PCCI method by only retaining some important terms according to the sparsity-of-effects principle and the improved PCCI method based on the Sparse Grid Numerical Integration (SGNI). The proposed methods can keep the benefits of the PCCI method, and at the same time avoid the exponential increasing computational calculations.

(2) In traditional probability analysis, the dimension-reduction integrations have been proven very effective for uncertainty analysis. A uncertain propagation approach, termed as a hybrid univariate dimension reduction (HUDR) method is developed to efficiently evaluate the uncertain properties. For problems with large random variation or high non-linearity, a general Hybrid Dimension Reduction (HDR) method based on the bivariate dimensional reduction method is further proposed for the uncertainty analysis.

(3) With the proposed uncertainty analysis methods based on orthogonal polynomials, robust topology optimization methods are developed for the static and dynamic continuum structures with random-interval hybrid uncertainties.

(4) Based on dimension reduction schemes, robust topology optimization methods are developed for the multi-scale design of cellular composites with an array of identical microstructures subject to random-interval hybrid uncertainties.

1.3 Outline of the thesis

The thesis consists of 7 chapters, shown as follows:

Chapter 1: The background and the overview of this thesis are introduced.

Chapter 2: A literature review of the hybrid uncertainties, topology optimization and uncertain topology optimization will be given in this chapter.

Chapter 3: The PLSM is introduced in this chapter. PLSM is used as an alternative by incorporating the CSRBF to perform the structural topology optimization, and the original topology optimization problem can be turned into a parametric problem.

Chapter 4: In this chapter, several random-interval hybrid uncertainty analysis methods are proposed. One category is based on the orthogonal polynomials, and the other category is based on dimension reduction schemes. The proposed methods provide new paths for hybrid uncertainty analysis and offer tools for robust topology optimization for structures with uncertainties.

Chapter 5: This chapter consists of two main parts: robust topology optimization for static and dynamic structures with hybrid uncertainties. The polynomial based hybrid uncertainty analysis methods are used to evaluate the robust objective function values. Sensitivities with respect to the design variables are obtained after the uncertainty analysis.

Chapter 6: Multi-scale topology optimizations based on the PLSM for both static and dynamic composite structures are presented in this chapter. The dimension reduction method based hybrid uncertainty analysis methods are used to efficiently estimate the interval mean and variance for the objective function with random-interval hybrid uncertainties. The sensitivity information in both scales will be provided after the uncertainty analysis.

Chapter 7: Conclusions of this work are given and further recommendations are summarized.

Chapter 2 Background and literature review

2.1 Literature review of topology optimization

Structural optimization can be classified into size, shape and topology optimization, and has been developed as a computational design tool to optimize structures. Among these different optimizations, topology optimization has been recognized as the most promising but the most challenging approach in the conceptual design stage. According to different research objectives, structure optimization can be divided into discrete structural topology optimization [1 and continuum structural topology optimization [2 . The former aims at optimizing the discrete structures to obtain the optimal permutations and combinations of trusses. The latter is to obtain the optimal layout with holes for continuum structures to gain high performance and save material usage by using proper optimization solvers.

2.1.1 Topology optimization methods

Bendsøe and Kikuchi [2 developed the homogenization theory-based topology optimization method, and then topology optimization has experienced considerable development over the past two decades [3,4,5 . A series of typical methods have been developed in this field, such as solid isotropic material with penalization (SIMP) [6 , 7 , evolutionary structural optimization (ESO) [8 and its advanced version the bi-directional ESO (BESO) method [9 , level set method (LSM) [10,11,12 etc.

Topology optimization of continuum structures essentially belongs to a set of integer programming problems with a large number of discrete design variables 0 and 1. Zeros

represent holes in the structure; while ones represent solid materials in the structure. Because of the discontinuity of the objective function and the constraint, the efficient gradient-based optimization algorithms cannot be directly applied to these problems. Some combinatorial optimization methods, for example, evolutionary structural method, genetic method, have good global optimization ability, but still have some difficulties in solving the topology optimization problem with a large number of design variables. In order to overcome the drawbacks, the problems with discrete design variables can be changed to a relaxed optimization problem with range-bounded continuous design variables by allowing the design variables taking intermediate densities from 0 and 1. The homogenization method and SIMP method have been developed and widely employed for these problems.

Cheng and Olhoff [13] pointed out that a global optimal solution generally does not exist within the class of smooth functions, or within the class of smooth functions with a finite number of discontinuities, so composite materials should be introduced to expand the design space and obtain the global optimal results. This work led to a series of achievements in recent decades on topological design problems. Homogenization method was used to optimize the structural topology by Bendsøe and Kikuchi [2]. The main idea of the homogenization method based topology optimization is to introduce the concept of microstructures (unit cells) to obtain the best material layout in the design space. The macrostructure is assumed to be composed of porous material and each unit cell has some chosen design variables. The topology optimization methods based on the homogenization method can be divided into two types, the forward homogenization method [14,15 which is used to solve the macro topology optimization problem and the backward homogenization method [16,17,18,19 which is used

to design the material microstructures. A review of the homogenization method can be referred to [20,21 . The homogenization method has strict mathematical theory, and the existence and the uniqueness were both demonstrated [22 . However, there still exist some problems when using the homogenization method. For example, a large number of design variables (size and angle of the microstructure) may lead to very large compuptational cost and the sensitvities are complicated to obtain.

As an extension of the homogenization method, the SIMP method [6,7 has experienced great popularity in topology optimizations, owing to its conceptual simplicity and implementation easiness. The SIMP model is described as a nonlinear interpolation and used to indicate the dependence of practical material properties such as Young's modulus upon the relative material density of the element. The elasticity modulus of each element is modelled as the relative material density raised to some power times the actual elasticity modulus of solid material. In this method, there is no need to introduce microstructures, and the design variables are element densities, so the computational efficientcy has been greatly improved. During the implemention of the SIMP method, the local minimal phenomenon, numerical instabilities such as the checkerboards and mesh-dependence need to be depressed by using the perimeter control and mesh-independent filtering methods [23 . Many other topology optimization methods have also been proposed, for example, ESO method [8 , the BESO method [9 , point-wise design method [24,25,26], independent continuous mapping method [27,28] etc.

The level set method was originally developed by Osher and Sethian [29] for tracking and simulating the evolution of moving boundaries. The key point is to introduce the higher

dimensional level set function (LSF), and the moving boundary is implicit identified by the zero level set. Modelling the moving boundary by the level set method has many advantages, for example, the shape and topology can be described flexibly by the level sets, the boundaries are smooth and clear, the normal vector and the curvature can be easily obtained, the unique solution can be ensured by the viscous solution theory of the Hamilton-Jacobian partial derivative equation (H-J PDE). Due to these unique features, many topology optimization methods based on level sets [11,12,30,31 have been developed. However, the conventional level-set shape and topology optimization also has some numerical difficulties, as follows: (1) the design result is highly dependent on the initial design; (2) the time step constrained by the Courant–Friedrichs–Lewy condition must be sufficiently small to ensure numerical stability; (3) the LSF need to be periodically reinitialized as a signed distance function to maintain the numerical accuracy; (4) the normal velocities must be extended to the neighbourhood of the design boundary or to the whole domain. To make the optimization less sensitive to the initial guess and modify the original H-J PDE to deal with the numerical difficulties, many improved level set methods have been proposed [32,33,34,35,36,37]. Parametric LSM is considered as an effective alternative method for topology optimization. The LSF can be transformed into a parametric RBF form, either using globally supported basis functions [38,39], or compactly supported ones [40,41]. By using the parametric scheme, the H-J PDE can be transformed into ordinary differential equation (ODE), and many well-established gradient-based optimization algorithms can be directly applied.

A structure may have time-variant loadings, and thus the displacement, stress, and strain of the structure also change with time. Dynamic topology optimization is of great importance in

mechanical engineering and has been widely studied to solve many kinds of problems for structures. Eigenfrequency optimization problem which can keep the structural eigenfrequencies away from the driving frequency for avoidance of resonance is regarded as an important category of topology optimization for dynamic structures. Díaz and Kikuchi [42] first studied the shape and topology optimization of structures to maximize a natural frequency using homogenization method. Then a wide range of dynamic design problems such as the fundamental eigenfrequency maximizing problem [43,44], the distance of adjacent eigenfrequency maximizing problem [45], and the specified eigenfrequencies and eigenmode shapes problem [46,47] have been studied. Another important research topic is the frequency response optimization which reduces the local or global dynamic performance of a structure under dynamic loadings. Ma et al. [48,49] applied the homogenization method for the frequency analysis problems. Jog [50] minimized the vibrations of structures subjected to periodic loading with the definition of the dynamic compliance. In order to reduce the degrees of freedom of the FE procedure, Yoon [51] used model reduction (MR) schemes to reduce the computational cost of the finite element procedure. Liu et al. [52] developed a topology optimization algorithm of dynamic structures under single or multiple excitation frequencies. More recently, Shu et al. [53], Rong et al. [54] and Liu et al. [55] also investigated the structural frequency response optimization problems with a wide excitation frequency domain.

2.1.2 Topological optimization of microstructural metamaterials

Most conventional topology optimization methods are focused on the use of full solid materials with certain properties, which limit the capacity of topology optimization for more advanced designs and applications in order to search for lightweight but high performance

structures. Periodic cellular composites are modular materials assembled by incorporating heterogeneous elements with functions determined by their relatively smaller placements like microstructures or unit cells. For example, the typical cellular honeycomb composites composed of an array of periodic unit cells have been employed in automobile and aerospace industries [56 .

Material design aims at achieving some advanced and new-style materials such as ultra-light materials and auxetic materials to satisfy some high requirements for structures in practice. Micro-structured materials consist of a number of periodically arranged microstructures and possess some superior performance. Each microstructure consists of an optimized layout of material, allowing arbitrary topological changes of the microstructure. The assembled cellular composites introduce a new degree of design freedom to obtain light-weight and high-performance materials and the global multifunctional properties can be determined from the local configurations of heterogeneous cells. Hence, the importance of cellular composites has grown rapidly in engineering [57 . Cellular composites provide flexibility in implementing effective properties by only modifying microscopic cells rather than their constituents.

The homogenization method was used to determine the effective elastic constants of general composite materials based on the topologies of periodical material microstructures by Guedes and Kikuchi [58]. Then the homogenization theory was combined with topology optimization to formulate an inverse design procedure of periodic unit cells for gaining some specific effective properties [16]. Gibiansky and Sigmund [59] developed an inverse homogenization method to design the two-dimensional composites with a maximal effective bulk modulus. To maximize bulk modulus or shear modulus, Radman et al. [60] designed isotropic periodic

microstructures of cellular materials using BESO method. Guest JK and Prévost [61] built a multiphysics problem which is depended on the weight assigned to the stiffness and transport terms in the objective function to design periodic multifunctional materials for maximum effective elastic stiffness and fluid permeability. By considering both stiffness and permeability, a multi-objective optimization problem was proposed, and the Pareto fronts were used to estimate the upper bounds of the bulk modulus and fluid permeability cross-property space for periodic porous materials [62].

Micro-structured materials design has become one of the most promising applications of topology optimization [63]. For example, the expansion and contraction of materials are important to be considered when the environmental temperature changed. The thermal expansion can be used to measure the degree of temperature in changing the dimension of materials. Negative thermal expansion or zero thermal expansion material has the counterintuitive property when the temperature increased. Poisson's ratio is usually defined as the ratio of transverse contraction strain to longitudinal extension strain under uniaxial tension. Due to these specific properties and the potential for a range of applications, many researchers have devoted considerable efforts to optimize material effective properties to achieved micro-structured materials with various novel effective properties mentioned above, such as the exotic thermomechanical properties [64], extreme thermal properties [65], and Negative Poisson's Ratios [66,67].

2.1.3 Multi-scale design of cellular composites

In industrial applications, the materials and structures are required to satisfy multifunctional requirements with lightweights. For example, the thermal insulation material, the sound insulation material in the airplane, and the impact resistance material in vehicles. Topology optimization has the ability to deal with both macrostructures and metamaterials, so the structures can be optimized concurrently in both in the macro scale and the micro material scale to obtain an outstanding performance. The microstructure reflects the micro (local) material properties, and the macrostructure shows the macro (global) distributions which is affected by the applied boundary conditions. It has become a trend to study the integrated topology optimization where the material and structural are optimized concurrently.

There have been some topology optimization methods for the concurrent design of the host macrostructure and its microstructures. The multi-scale topology optimization aims at designing the structures composed of cellular composites on the micro scale and the macro scale simultaneously according to the given boundary conditions. The layouts of materials can then be optimized to a large extend and the structure performance can be expected to be the best. The multi-scale lightweight cellular composites provide new opportunities in many advanced engineering applications (e.g. bioengineering materials) [68 and may enhance the structural performances (e.g. thermal and thermo-elastic effects) [69,70 .

Rodrigues et al. [71 developed a hierarchical computational procedure for optimizing the macrostructure material distribution as well as designing the point-wise material microstructures, in which allows unique microstructure in each macro finite elements. Xia

and Breitkopf [72] proposed a concurrent design of material and structure using the FE2 framework to address the nonlinearity of the macroscopic equilibrium. These methods can achieve an optimized structural performance at both macro and micro scales, but the computational cost and the manufacturing difficulties are greatly increased due to the point to point design pattern. Some layer-wise and subdomain design methods are proposed for the integrated topology optimization problems to reduce the cost. Based on the SIMP method, Zhang and Sun [73] proposed an integrated optimization approach for the compliance minimization designs of layered structures considering scale-related effects. Coelho and Rodrigues [74] dealt with a compliance optimization of sandwich structures with a porous cellular core. Li et al. [75] proposed a multi-scale topology optimization method for the design of integrated materials and structures by taking advantage of both cellular composites and functionally graded materials. The SIMP was applied to generate an overall multilayered layout, and the microstructure for each layer was designed by integrating the numerical homogenization into a level set approach. Later, they [76] developed a novel concurrent design for cellular structures consisting of multiple patches of material microstructures using a level set-based method.

Microstructural variations in the micro scale may cost large calculations and result in manufacturing difficulties. In this case, periodic assumption is often made in order to meet the computational design and manufacturing requirements in practice. Based on this periodic assumption, the macroscopic composite structure is often assumed to have an array of identical microstructures that are periodically configured with the same shape and topology. Liu et al. [77] proposed a so-called PAMP (Porous Anisotropic Material with Penalization)

model to optimize the macroscopic and microscopic material distributions simultaneously. In [78 , composite material involving two or three different material phases was designed by using the homogenization method to minimize the mean compliance of the macrostructure.

In order to improve structural dynamic characteristics, concurrent topology optimization for both composite macrostructure and material microstructure has also become an attractive topic for researchers. For maximizing the fundamental frequency of a structure, Niu et al. [79 , Liu et al. [80 and Zuo et al. [81 performed the topology optimization for composite structure and material design. Vicente et al. [82 proposed a concurrent topology optimization methodology to minimize the frequency response based on BESO method. In order to minimize the dynamic compliance, Xu et al. [83 built a concurrent topology optimization model of composite macrostructure and multi-phase periodic microstructure by the BESO method. The above literature for structures, microstructures and concurrent designs are mainly based on deterministic assumptions. In the following sections, reviews about uncertainty analysis and topology optimizations considering uncertainties will be introduced.

2.2 Literature review of uncertain analysis

2.2.1 Random uncertain analysis

Probabilistic method has a profound mathematical theory basis and has been widely studied with the development of a series of techniques in the field of uncertain research. From a statistic view, Monte Carlo method is basically a most widely used method for uncertainty analysis. It selects a large number of samples based on the distributions of inputs, and then run the model to get the statistic characteristics of outputs. The results from Monte Carlo

method is often used as the reference of other probability methods. Monte Carlo method is considered as an accurate tool but with the cost of high computational. Taken advantage of probabilistic theory based on probability distributions, many non-statistic methods, for example, Polynomial Chaos (PC) expansion [84,85 , and dimension reduction method [86,87 are presented and proved to have a very good approximation performance.

The PC method has become a very popular uncertainty analysis method due to its good efficiency and accuracy to evaluate the output performances functions with stochastic uncertainties and has been applied in a series of engineering applications [88 . By the PC expansions, the random outputs are represented by a series of multivariate PC bases built from univariate orthogonal basis with respect to the distributions of the random variables. A primary task in the PC method is to evaluate the PC coefficients, and a series of intrusive and non-intrusive methods have been developed [89,90 . In the intrusive method, the coefficients of the PC expansion are obtained using a Galerkin scheme [89,91 that leads to a system of coupled deterministic equations, hence modifications to the existing deterministic solvers are required. As an alternative, non-intrusive computational schemes which can treat the original deterministic solvers as blackbox are proposed. The two principal strategies to calculate the PC coefficients non-intrusively are the projection approach and the regression approach [92 . In the projection method, PC coefficients are recast as multidimensional integrals [93,94 , while in the regression approach, the PC coefficients are estimated by setting up a least-square minimization problem based on sampling strategies [95,96,97,98 . The PC expansion methods are proved to be very efficient, however, the computational burden will increase dramatically as the increasing of the dimensions.

The calculation of the origin moment of an uncertain function is a multidimensional integration, which generally requires very large computations. Dimension reduction method [86,87 is a technique to efficiently estimate the origin moments. The main idea of the method is to approximate the *n*-dimensional intergration function by the summation of a series of D-dimensional functions (D<*n*). The univariate dimension-reduction method was proposed by Rahman [86 to solve the multi-dimensional integration for calculating the response of mechanical systems. The method approximates the response moments by moments of single random variables, and can efficiently provide the estimations of the statistic moments. In order to improve the accuracy for problems with large random variation and/or non-linearity, the bivariate and other multivariate dimension reduction approximations [87 were then developed to caculate the response moments, according to the properties of different problems. The dimension reduction methods have also been widely applied in uncecrtainty analysis, reliability analysis and design optimizations [99,100,101,102,103 due to its good features.

Traditional reliability analysis and design methods adopt the probability model to deal with the uncertain variables. Hasofer and Lind [104 developed a first-order reliability method in which the reliability index is defined as a minimum distance from the original point to the limit state surface. Hasofer-Lind reliability index has clear physical meaning and can well describe the reliability of structure. However, the probability variables are required to obey normal distributions. Rackwitz&Fiessler [105 then proposed the HL-RF method, in which the non-normal variables are turned into normal variables by an equivalent transformation. Considering the parametric correlation, Rosenblatt [106 equivalently transformed the original distributions into independent ones with the given union cumulative distribution

function. Nataf [107 gave an approximate transformation, in which the correlations change during the transformation process is considered.

Reliability-based design and optimization (RBDO) [108,109 aims at obtaining the optimal structures under reliability constraints considering the uncertainties during the optimization process. Nowadays, RBDO has become a research focus in uncertainty analysis and has witnessed the development of a series of methods [110, 111, 112 and applications [113,114,115. RBDO is generally a double loop process, the outer loop is an optimization of the design variable and the inner loop is reliability analysis. Finite element models which may be time consuming are common in practical engineering problems, so the double loop process involving these models may need a large amount of calculation, which is one of the major difficulties for RBDO problems. Response surface approximation [116,117,118 is used in RBDO to replace the original simulation model to decrease computational cost. However, obtain the response surface still need to call the time consuming simulation model, so that there may still exit efficiency problems. Single-loop method [119,120,121 is a decoupled method to deal with the double loop RBDO, which can avoid the nest optimization process. RBDO methods also have been applied in many engineering problems, for example, the multi-objective problem [122, the multidisciplinary problem [123, and the time variant problem [124.

2.2.2 Interval uncertain analysis

The prerequisite for using the probability model is that we need to acquire large numbers of experimental samples to establish accurate probability distributions of the uncertain

parameters. Nevertheless, in actual engineering problems, due to testing difficulties or cost constraints, it is often difficult to acquire sufficient experimental samples to establish accurate probability distributions for some parameters. As a result, probability distribution assumptions often have to be made for parameters when using probability methods to analyze the structural uncertainty. However, there have been researches indicating that even a small deviation of the distribution parameters from the real values is likely to bring about a very large error of the uncertainty analysis [125 .

On the other hand, through extensive engineering practice, it is found that though it is very difficult to obtain accurate probability distributions of the uncertain parameters when the sample information is insufficient, it is generally not difficult to obtain the variation intervals of the parameters based on the limited data and engineering experience. For example, in sheet metal forming analysis, it is difficult to obtain the probability distribution of the friction coefficient between the mold and the sheet due to the complexity of the lubricating environment; however, based on the existing experience, we know that such a friction coefficient lies within the interval [0.1,0.2 [126 . Another example it that in actual product processing we generally know the tolerance of a dimension parameter based on the precision of the processing equipment. Therefore, it is very easy to determine an interval for the actual dimension after processing based on the nominal design value and the tolerance. For this kind of problem, the interval method shows a good advantage. The systematic proposal and application of interval method can be traced to the 1970s [127 or even earlier, when it was mainly used for the error analysis of numerical calculations.

Interval method belongs to one of the typical non-probabilistic methods. Interval model makes it possible to measure bounds of the outputs for systems with bounded parameters without knowing the complete information. Recently, the interval method has drawn much attention and is experiencing popularity in the areas of uncertain analysis and design. Based on the interval arithmetic, the upper and lower bounds of the solution will be obtained. Interval arithmetic is popular for its simplicity and practicability, but there are still some shortcomings. On the one hand, for complex systems with implicit functions or finite element models, interval arithmetic is difficult to solve the corresponding problems. On the other hand, relatively large overestimation may be caused during the calculation process.

In the early 1990s, Ben-Haim and Elishakoff [125,128,129 firstly introduced the interval method into structural analysis and later aroused extensive attention in structural uncertainty analysis and design optimization. Qiu et al. [130,131,132 developed a series of the non-probabilistic interval analysis method to conduct uncertainty propagation analysis for structural static mechanics, eigenvalues, and dynamical problems. An interval analysis method for the static or dynamic response of the structures with interval parameters was presented by improving the conventional first order Taylor expansion [133 . Zhang et al. [134 discussed the dynamic response of vibration control problem of structures with interval parameters by combing the interval finite element method and precise time integration method. A general uncertain optimization model was investigated in which the objective function and constraints were both nonlinear and uncertain, and an efficient sequential nonlinear interval number programming method was constructed to deal with the interval optimization problems [135 .

Most of the aforementioned methods are based on Taylor series methods, neglecting the remainder interval terms. The low-order Taylor series are generally adopted to approximate the system responses, but they are limited to deal with problems with lower-level of uncertainties. High-order Taylor series expansion has higher approximation precision at the cost of large computational calculation, and could also lead to large overestimation. To obtain the dynamic response ranges of nonlinear systems with large uncertainty, Wu et al. [136,137 employed the Chebyshev series to approximate the true solution, through which higher numerical accuracy of the approximation can be achieved. The Chebyshev inclusion function was proposed to calculate the bounds of interval functions, due to its capability to effectively control the overestimation compared to the Taylor inclusion function. The Mehler integral method has been applied to find coefficients of the Chebyshev inclusion function. Chebyshev method is proved to have relatively higher precision than Taylor series and it's easy to adjust the series order to meet different requirements.

Interval variables are generally assumed to be independent of each other. When uncertain parameters are independent of each other, the uncertainty domain composed by the interval parameters is a "multidimensional box". However, in many actual engineering problems, there exist correlations among parameters, and these correlations may have a significant impact on the uncertainty analysis results. Convex model approaches constitute a type of effective method for dealing with the correlations of interval variables. By using a convex model, the uncertainty domain of the parameters is quantitatively described using a convex set, and any point in the set represents a possible realization of the uncertain parameters. The conventional interval model is actually a special form of the convex model under the condition

that the interval parameters are independent of each other. Various kinds of convex models have been developed in structural uncertainty analysis to address the parametric correlation problem, for example, ellipsoidal model [125,138 , super ellipsoid model [139 and multi-ellipsoid model [140,141 . Presently, interval model and ellipsoid model are two mostly widely used models to deal with independent and dependent variable problems, respectively. In order to better deal with parametric multi-source uncertainties, Jiang et al. [142 firstly proposed a multidimensional parallelepiped model which can simultaneously consider dependency and independency in one convex model. Later, they further proposed an improved multidimensional parallelepiped model which is more reasonable and more convenient for uncertainty analysis [143 .

2.2.3 Random and interval hybrid uncertain analysis

In recent years, with the continuous increase in the complexity of practical engineering structures and our high requirements for structural safety, engineers have started encountering a type of more complex and also very important uncertainty problem. For example, a practical structure often involves multidimensional uncertain parameters related to the material properties, loads, dimensions, etc. For some of these uncertain parameters, experimental testing is relatively convenient, or there are already large amounts of accumulated data available. However, for some other uncertain parameters, we cannot obtain a sufficient number of high-quality samples to create their precise probability distributions while their variation intervals can be only identified. This is the so-called random and interval hybrid uncertain problem.

When various types of uncertainties exist simultaneously, the calculation cost is relatively high and may even increase exponentially [144 . As noted by Oberkampf et al. [145 , establishing an effective hybrid mathematical model that contains various types of uncertainties is a very important and challenging problem. In addition, Berleant et al. [146 summarized the theoretical foundations and algorithms for hybrid uncertain problems as well as the related problems that need to be solved urgently. According to the different treatments to the uncertainty, the existing probability-interval hybrid uncertain models can be mainly classified into the following two types, Type I model and Type II model [147 . In Type I model, all the uncertain parameters in the structure are described using probability distribution functions. However, for some variables, the precise values of some important distribution parameters cannot be determined, and instead their interval estimations can be obtained. In Type II model, all the uncertain parameters in the structure are classified into two types. The precise probability distribution functions can be established for parameters with a sufficient number of samples. And for the parameters with an insufficient number of samples, only their intervals are identified. In the following, we will review the hybrid uncertainty analysis for these two types from three main aspects: the hybrid uncertainty propagation analysis, the hybrid structural reliability analysis and reliability-based design optimization.

2.2.3.1 Hybrid uncertainty propagation analysis

Uncertainty propagation analysis, i.e., quantifying the uncertainty of the performance function or response function based on the original parametric uncertainty, is generally of great importance for reliability analysis and design of a structure. For a random-interval hybrid uncertainty problem, the inputs have not only random variables but also interval

variables, and the performance function is no longer a simple probability variable or an interval variable but instead has both probabilistic and interval characteristics.

Elishakoff and Colombi [148 introduced the type I probability-interval hybrid model into the structural mechanics problem. Zhu and Elishakoff [149 treated the acoustic pressure of a periodic finite-span beam as a random variable containing bounded interval parameters, and solved the cross-spectral density function of both the transverse displacement and the bending moment responses of a periodic structure. Xia et al. [150 further applied the type I hybrid model in acoustic field prediction, and established a hybrid uncertain acoustic dynamic equilibrium equation and a corresponding analysis method. In addition, by using the first-order Taylor expansion and the random interval moment method proposed in Gao et al.[151 , they also obtained the upper and lower bounds of the expectation and variance of the sound pressure response vector. Li and Lu [152 applied the probability-interval hybrid uncertainty model in importance analysis of structures.

The research on Type II uncertainty propagation analysis, in recent years, has received more and more attention. Du et al. [153 assessed the robustness of a system with both probabilistic uncertainty and interval uncertainty. Based on the existing interval arithmetic operations, Gao et al. [151 developed the random interval arithmetic operations, and furthermore expanded the random variable functional moment method to probability-interval hybrid uncertain problems to create a random interval moment method. By combining the random interval moment method with perturbation theory, they proposed an efficient random interval perturbation method for determining the upper and lower bounds of the mean value and variance of structural response. After that, Gao et al. [154 further proposed a mixed-

perturbation Monte Carlo method for determining the means and variances of the static displacement and stress responses of a truss structure with hybrid parameters. By using the random interval perturbation method, Xia et al. [155 and Xia and Yu [156 applied the type II hybrid model in uncertainty propagation analysis of structural acoustic problems. Wu et al. [157 studied a vehicle dynamics problem containing probability and interval uncertain parameters, in which a polynomial-chaos-Chebyshev-interval method (PCCI) was proposed to determine the intervals of mean value and variance of the system response. Zi and Zhou [158 proposed a modified hybrid uncertain analysis method to predict the dynamic response field of the luffing system of an automobile crane with random and interval parameters. A unified interval and random Gegenbauer series expansion method was proposed [159 to evaluate the uncertain response of acoustic fields with both random and interval parameters. Recently, considering the spatial uncertainties, random and interval fields have also been studied in uncertainty analysis for structures [160,161,162 .

2.2.3.2 Hybrid structural reliability analysis

Reliability analysis refers to the quantitative evaluation of the reliability probability for a structure under given conditions, which constitutes a foundation for the safety design of structures. Over the past decade, reliability analysis has become an important research direction in random and interval hybrid uncertainty analysis, and a series of effective models and algorithms have been developed.

Several early studies on hybrid reliability analysis of type I model mainly focused on the linear performance functions. Qiu et al. [163 treated the mean values and variances of the strength and stress as interval parameters and derived the analytical formulation for

computing the upper and lower bounds of reliability index. They [164 further introduced the interval analysis method to system reliability problem and calculated the failure probability intervals and the reliability index intervals for series and parallel systems. Performance functions of actual engineering structures are mostly implicit nonlinear functions and often based on time-consuming simulation models such as the finite element models. Some progress have been made to ensure the analysis efficiency and accuracy for dealing with the hybrid uncertain problems. Jiang et al. [165 studied the type I hybrid reliability problem and performed the reliability analysis for two different forms of limit-state strips. Besides this, Jiang et al. [166 established two efficient single-loop algorithms based on the two classical FORMs, i.e., the reliability index approach and the performance measurement approach. Also, based on the Monte Carlo Simulations (MCS) and the weighted regression method, Xiao et al. [167 constructed a linearized tangent function to replace the original performance function, through which the reliability index interval was efficiently calculated. In addition to the aforementioned studies, the reliability analysis of type I hybrid model has also been expanded in some related fields, such as the time-variant reliability analysis [168 and the reliability sensitivity analysis [163,167 .

The study and application of structural reliability analysis for type II hybrid model can be traced to 2000s and even earlier. A random-interval hybrid reliability analysis generally involves a two-layer nested optimization. Focusing on the efficiency issue, three main types of methods have been developed which will be introduced below. The first type is the single-loop decoupling approach. Du [169 decoupled the nested optimization in hybrid reliability analysis into a series of iterations that are composed of the probabilistic reliability analysis

and the interval analysis. Based on this single-loop decoupling approach, Luo et al. [140 also dealt with a probability and convex-set hybrid reliability problem, in which the correlations among interval parameters could be taken into account. The second type is the response surface approach. Jiang et al. [170 developed an efficient response surface approach for probability-interval hybrid reliability analysis and used it in crack analysis of structures. Yang et al. [171,172 established a response surface for the performance function using an active learning Kriging model, and efficiently solved the created approximate hybrid reliability problem using MCS. The third type is the equivalent approach. This type of method aims to convert a probability-interval hybrid reliability problem to an equivalent probability reliability problem that can be well solved through the conventional methods. By treating interval parameters as uniformly distributed random variables, a type II hybrid reliability problem was converted to a conventional probability reliability problem [173 . Liu and Zhang [174 further expanded the equivalent method to deal with the probability and convex model hybrid reliability problem. In addition, Hu [175 compared several methods in type II hybrid reliability analysis in terms of efficiency and accuracy.

The parametric correlation problem is another focus in type II hybrid reliability analysis. Some studies have been carried out on this issue in recent years. Luo et al. [140 used a multi-ellipsoid convex model to address the multi-source uncertainty among interval variables, and proposed a probability and multi-ellipsoid hybrid reliability model with also an efficient decoupling algorithm. Wang et al. [176 used an ellipsoid model to describe the correlation among interval parameters, and constructed a probability and ellipsoid hybrid reliability model. Considering the correlation among different types of uncertain parameters. Jiang et al.

[177 introduced a sample correlation coefficient to measure the dependence between different types of uncertain variables including probability variables, probability and interval variables, and interval variables, and constructed a unified probability-interval hybrid reliability analysis method.

2.2.3.3 Reliability-based design optimization with hybrid uncertainty

The reliability-based design optimization (RBDO) has always been an important research direction in structural reliability field and could enable engineers to obtain an optimal structural design meeting the reliability constraints. After introducing the hybrid uncertainty, the RBDO problem will become much more complicated and difficult to solve, since the reliability of each constraint will be an interval rather than a specific value at the given design variables. Because of the optimization in the outer loop and the double-loop nested optimization of hybrid reliability analysis in the inner loop, the RBDO with hybrid uncertainties generally involves an extremely complicated "triple-loop" nested optimization, presenting huge challenges to its numerical solution in terms of calculation efficiency and convergence.

There are many developments on RBDO for the type II random-interval hybrid model. Du et al. [178 converted the hybrid reliability problem into a single-loop optimization problem based on the maximum failure probability, thereby converting the triple-loop optimization to a double-loop optimization, which was then solved by using the sequential optimization and reliability assessment method. After that, Du [179 further expanded the above method to the hybrid RBDO problem with dependent interval variables. Kang and Luo [141 and Luo et al. [180 created a performance-measurement-approach-based hybrid RBDO model, and then

developed an efficient single-loop decoupling approach based on the linearization of performance functions and the optimality conditions. Xia et al. [181 and Zhou et al. [182 considered not only the reliability of constraints but also the uncertainty in the objective function, and established new RBDO methods. Wang et al. [183 considered the correlation among the interval parameters and constructed an RBDO method under a mixture of random, interval and convex uncertainties. Recently, there are also some progresses emerging for RBDO of type I hybrid model [175,184,185 . Additionally, the hybrid RBDO currently has been applied to some practical engineering problems such as the robust design of mechanisms [153 , optimization of a box girder structure of the single-hull ship [186 , vehicle crashworthiness design of foam filled thin-walled structures [187 .

2.3 Literature review of uncertain topology optimization

It can be found that the majority of the topology optimization methods are based on the deterministic assumption. In engineering, however, various uncertainties are intrinsically existing with respect to material properties, boundary conditions, loads, geometric dimensions, manufacturing and so on. In particular, in the initial stage of conceptual design with topology optimization, more reliable results can be expected if the uncertainties are taken into consideration, as the performance of a topological design varies along with the impact of uncertainties. In this case, the deterministic assumption may result in a design that cannot meet the performance target and even an unfeasible design. Hence, to enhance the performance of the structural design, there is a strong demand to incorporate uncertainties into the topology optimization of structures to account for unavoidable variations for structural performances.

The RBTO and the RTO are two major paradigms for topology optimization problems under uncertainties [188 . RBTO is generally formulated with reliability constraints to account for uncertainties to optimize structures. In another word, RBTO is to address the reliability of a topologically optimized design by ensuring the satisfaction of constraints at some desired levels. RTO problems aim to optimize the expectation of the objective function and simultaneously make the objective function insensitive to the variations. The robust objective function is usually defined as a linear combination of lower order statistical properties (e.g. mean and variance) or under the worst-case condition (e.g. interval uncertainties), so as to minimize the influence of uncertainties.

Considering the uncertainties related to material properties [189,190,191 , applied loads [189,190,192,193,194,195 and geometries [191 , reliability constraints are introduced into topology optimizations to form the so-called RBTO problems. The inherent double loop process is a challenge in RBTO problems because the most probable point (MPP) has to be calculated by the reliability analysis at each iteration of the topology optimization. Many works have been focused on how to avoid the double loop optimization process that is often computationally prohibitive [196 . Kharmanda et al [192 introduced reliability constraints into topology optimization and developed a decoupling strategy in which they first search for the MPP, and then perform the deterministic design to minimize the compliance. Based on this efficient decoupling strategy, Liu et al. [197 investigated an RBTO approach for continuum structures based on topological description functions, and Du and Sun [198 developed a reliability-based vibro-acoustic microstructural topology optimization by taking the uncertainty of the load direction and excitation frequency into account. Based on a single

loop procedure proposed by Liang et al. [120 , Silva et al. [193 presented an RBTO method for both the structural component and system under loading uncertainty. Then Nguyen et al. [194 developed a single-loop RBTO approach using the matrix-based system reliability method, considering the statistical dependence between multiple limit-states.

For physical quantities (e.g. material field and distributed load) varying across the spatial domain, they should be more realistically modeled as random fields. RBTO for structures with random fields has been regarded as a challenging problem. Patel and Choi [199 applied probability neural network in truss structures with random field uncertainties and proposed a classification-based RBTO framework for structures with discontinuous, disjoint or nonlinear limit state functions. Jalalpour and Tootkaboni [200 proposed an efficient RBTO approach based on the stochastic perturbation method for structures involving random field material uncertainties. Keshavarzzadeh et al. [201 provided a systematic and efficient computational framework for RBTO using the non-intrusive polynomial chaos expansion where the loading and geometry uncertainties modelled by random fields.

The so-called Non-probability RBTO (NRBTO) problems are formulated for structures with interval uncertainties. The NRBTO can be regarded as an alternative but useful supplement to assist topological optimization with uncertainties, and the NRBTO problems are relatively seldom studied. For instance, Luo et al. [202 proposed a non-probabilistic reliability-based topology optimization method for the design of structures, based on the definition of a non-probabilistic reliability index. Xu et al. [203 developed a method for the NRBTO of dynamic structures with uncertain-but-bounded parameters using a BESO method. By introducing the

multidimensional parallelepiped convex model, interval uncertainties have been accounted for structures to minimize material volume under displacement constraints [204 .

These years, there have emerged a number of RTO methods for topology optimization for structures with random uncertainties. For RTO problems, the optimization model usually aims to minimize the mean and variance of the uncertain objective function. Guest and Igusa [205 presented an RTO method under loading and structural nodes location uncertainties. Guo et al. [206 developed an RTO method considering the uncertainty of boundary variations based on a level set framework. Zhao and Wang [207 proposed an approach for RTO with loading uncertainties based on linear elastic theory and orthogonal diagonalization of symmetric matrices. Zhang et al. [208 investigated dynamic topology optimization problems of large-scale structures under stationary random excitation. Csébfalvi [209 proposed an RTO method for the volume-constrained problem for continuum structures with probabilistic loading directions. Zhu et al. [210 explored methods in the time domain, the frequency domain, and the state space to evaluate the dynamic response for the stochastic dynamic topology optimization. A minimax-compliance approach [211 was presented for RTO with loading direction uncertainties. Long et al. [212 introduced a new formulation of RTO for structures considering the local failure and load uncertainty. Wang et al. [213 developed an RTO for compliant mechanisms with material and loading uncertainties.

RTO problem considering random fields have also been regarded as an important research area. The random field can normally be expressed using a finite number of random variables by the Series expansion methods, such as the Karhunen-Loeve (KL) expansion, the Orthogonal Series Expansion (OSE), and the Expansion Optimal Linear Estimation (EOLE)

[89,91 . Chen et al. [103 employed the KL expansion and the dimension reduction method to implement the RTO with random material properties and loading uncertainties. Tootkaboni et al. [214 combined the KL expansion with PC expansion for robust topology optimization design with random field material properties uncertainties. Also by using the KL expansion, Zhao and Wang [215 proposed an RTO considering random field loading uncertainty. By making some improvements of the uncertainty propagation and quantification method [215 , a concurrent RTO approach is developed for multiscale structures composed of multiple porous materials with random field loading uncertainties [216 . By modeling the geometry variations as stochastic fields, a robust design model was proposed based on the stochastic perturbation in [217 . Besides the KL expansion, Jansen et al. [218,219 used the EOLE method to discretize the random field, taking into account the geometric imperfections. A RTO approach was developed for continuum structures with failure constraints in [220 , in which the midpoint discretization technique is used to represent the random field for the material properties.

Interval uncertainties have also been considered in robust topology optimization problems, such as the ellipsoid-based models. For example, Guo et al [221 investigated the robust concurrent topology optimization with load uncertainties by the ellipsoid model. Zhang et al. [222 formulate a robust topology optimization problem based on the ellipsoid convex model for structures under dynamic excitations. Wu et al. [223 proposed a non-probabilistic robust topology optimization approach for structures under interval uncertainty by using the Chebyshev interval method [136 . To improve the robustness of the dynamic characteristics,

a multi-objective topology optimization model [224 of trusses with interval uncertainties is constructed based on the concept of interval possibility degree.

Since present, the majority of the current RBTO and RTO methods are focused either on the probabilistic or non-probabilistic uncertainties. Only a few works for topology optimization considering hybrid uncertainties have appeared. For instance, Wu et al [225 introduced random-interval uncertainties into the robust topological design of microstructures for mechanical metamaterials by using the PCCI method [157 . In [226 , the hybrid stochastic interval perturbation method is used to develop a robust topology optimization method for structures. He et al. [227 optimized the dynamic properties including dynamic-compliance and eigenvalue of the continuum structure with interval random parameters. An efficient hybrid univariate dimension reduction method [228 was proposed for the concurrent topology optimization of cellular composites. In this thesis, random-interval hybrid uncertainties will be considered in topology optimization problems including continuum topology optimization for static and dynamic structures, concurrent topology optimization for static and dynamic structures. Several new hybrid uncertainty analysis methods and the corresponding RTO methods will be built for these problems.

Chapter 3 A level set method for topology optimization

The efficient LSM was introduced in topology optimization design, and then became an attractive approach for topology optimization problems. The PLSM [37,40,41 which can avoid some undesirable features of most standard LSMs has been developed by incorporating the CSRBF, and has shown its advantages and widely applied in different topology optimization problems [75,76,229 . In PLSM, the time-space coupled problem is converted to a parametric problem by CSRBF, and then the H-JPDE is converted to an ODE which can be easily solved. The expansion coefficients (design variables) are temporal and the shape functions are spatial. The gradient-based optimization algorithms can be applied to update the design variables in the topology optimization problem. In this Chapter, we will give an introduction to the PLSM which will be employed as a topology optimization method in this work.

3.1 The level set method

3.1.1 Representation of the boundary via LSM

Structural design boundary is described implicitly by the zero level set of a higher-dimensional LSF by using a level set method. A two dimensional representation scheme is illustrated in Figure 3-1. $D \subset \mathbf{R}^d \left(d = 2,3\right)$ is a fixed reference space, Ω is a set of all the possible shapes, and Γ represents the structural boundary and corresponds to the zero level set. An LSF $\Phi\left(\mathbf{x}\right)$ which is Lipschits continuous is defined over the reference domain. The

design domain D can be divided into three parts, the solid region, design boundary, and void region:

$$\begin{cases} \Phi(\mathbf{x}) > 0 & \forall \mathbf{x} \in \Omega \setminus \Gamma \quad \text{(solid region)} \\ \Phi(\mathbf{x}) = 0 & \forall \mathbf{x} \in \Gamma \bigcap D \quad \text{(boundary)} \\ \Phi(\mathbf{x}) < 0 & \forall \mathbf{x} \in D \setminus \Omega \quad \text{(void region)} \end{cases} \tag{3-1}$$

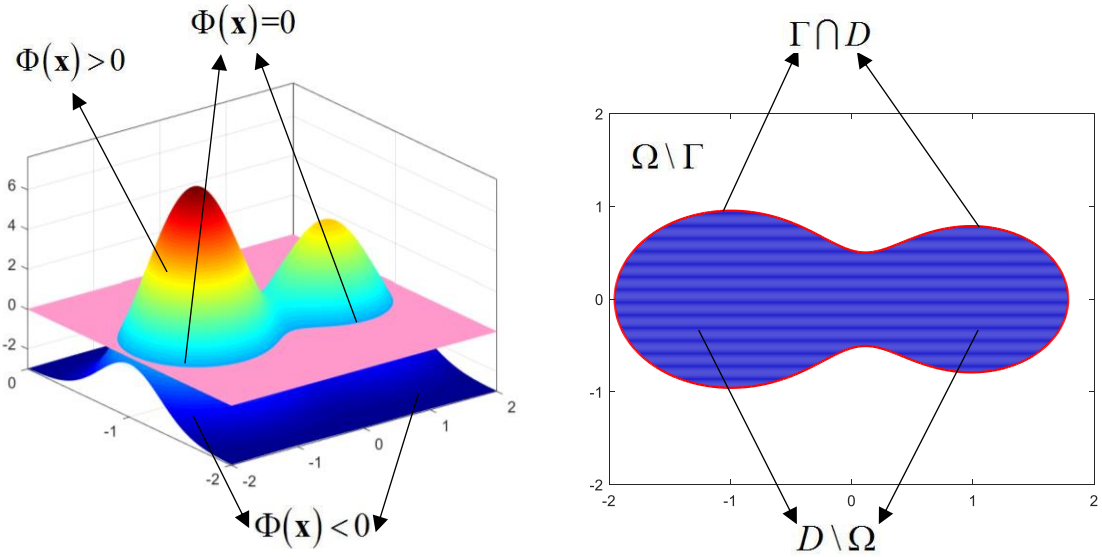

(a) 3D level set function (b) corresponding 2D geometry

Figure 3-1 A 2D boundary embedded as the zeros level set of a 3D level set function

3.1.2 Hamilton-Jacobi Equation

As presented in section 3.1.1, the boundary is represented as the zero level set of an LSF. The level set surface would move up and down on a fixed Euler grid during the optimization process, which leads to changes in the shape or topology of the boundary. In the conventional LSM, the LSF is evolved by Hamilton-Jacobi equation which can be numerically solved by the finite difference method [10,29 . The pseudo-time t is introduced for the dynamic process

of shape deformations to represent the motion of the design boundary, then the following Hamilton-Jacobian partial derivative equation (H-J PDE) can be obtained:

$$\frac{\partial \Phi(\mathbf{x},t)}{\partial t} + \mathbf{v} \cdot \nabla \Phi(\mathbf{x},t) = 0 \tag{3-2}$$

in which $\mathbf{v} = d\mathbf{x} / dt$ denotes the velocity field at the design boundary. The velocity field is consisting of the normal velocity field and tangent velocity field. Since only the normal velocity field contributes to the shape change of the design boundary, the equation (3-2) can be rewritten as:

$$\frac{\partial \Phi(\mathbf{x},t)}{\partial t} - v_n \cdot \nabla \Phi(\mathbf{x},t) = 0 \tag{3-3}$$

where the normal velocity is

$$v_n = \mathbf{v} \cdot \mathbf{n} = \frac{d\mathbf{x}}{dt} \cdot \left(-\frac{\nabla \Phi}{|\nabla \Phi|} \right) \tag{3-4}$$

where **n** is the unit normal vector pointing outward to the moving boundary, owing to the sign convention of the LSF. Hence, moving the boundary along the normal direction is equivalent to updating the LSF by finding solutions of the H-J PDE.

Traditionally, finite difference schemes [10 are usually applied to numerically implement the conventional level set structural optimization since it is generally quite difficult to calculate the velocity field through the H-J PDE. There are several numerical problems for an explicit difference scheme [40 . For example, the time-step size constrained by the Courant-Friedrichs-Lewy condition must be carefully set to ensure numerical stability. Re-

initializations are also needed to prevent nucleation of new holes. As another problem, the normal velocities must be extended to the neighborhood of the design boundary or to the whole domain to make the numerical solution feasible. These difficulties may impose restrictions on the applications of the conventional level set method.

3.2 The parametric level set method

As introduced above, the conventional level set methods have some numerical difficulties. In order to overcome these difficulties and improve computational efficiency, PLSMs are developed as alternatives to perform structural topology optimizations. The LSF can be discretized explicit by several methods such as radial basis function, polynomial functions, and spectral methods [38,41,230,231 . The parameters of the discretized LSF can be regarded as the variables of the topology optimization problem. In this case, the sensitivity-based optimization methods can be directly applied.

3.2.1 Compactly Supported Radial Basis Functions

A radial basis function (RBF) is a real-valued function whose value depends on the distance from the origin, or on the distance from a center point. RBFs can be used to efficiently approximate multivariate scattered data. Interpolation based on RBFs is generally efficient, and the data can be stored conveniently. There are several types of radial basis functions such as Gaussian, multiquadric, inverse quadratic and so on, and each basis function has a different shape and may result in a different interpolation surface. Radial basis functions can be used to approximate function $f(x)$ by the following form:

$$f(x)=\sum_{e=1}^{N}\alpha(x_e)\phi(\|x-x_e\|) \tag{3-5}$$

where $f(x)$is represented by a sum of N radial basis functions ϕ, each associated with a center x_e, and weighted by an appropriate coefficient $\alpha(x_e)$. The norm $\|\cdot\|$ is the Euclidean distance.

RBFs can be categories into globally supported RBFs (GSRBFs) or compactly supported RBFs (CSRBFs) by the sparsity of the interpolation matrix. GSRBFs have been used to interpolate the LSF to avoid the H-J PDE for structural topology optimization by Wang and Wang [38 . Though GSRBFs are smooth and efficient, the interpolation precision highly depends on the free shape parameter, and the fully dense matrix will cause difficulties in calculation especially when approximating systems with a large number of candidate points. By comparison, CSRBFs could be an attractive alternative for structural topology optimization due to its strictly positive definite property and matrix sparseness. Though the precision of CSRBF is a little lower than the GSRBF, the precisions for both can meet the requirements of the level set method.

Based on the CSRBF, a PLSM is proposed to turn the original LSF into a parametric form and improve the optimization efficiency [40 . The CSRBF based PLSM is used in this work to deal with the topology optimization problems. The LSF is approximated by positioning the CSRBFs at the pre-specified knots over the whole design domain:

$$\Phi(\mathbf{x},t)=\boldsymbol{\phi}(\mathbf{x})^{\mathrm{T}}\boldsymbol{\alpha}(t)=\sum_{e=1}^{N}\phi_e(\mathbf{x})\alpha_e(t) \tag{3-6}$$

where N is the number of knots, $\boldsymbol{\alpha}=[\alpha_1,\alpha_2,\cdots,\alpha_N]$ denotes the vector of expansion coefficients, $\boldsymbol{\phi}=[\phi_1,\phi_2,\cdots,\phi_N]$ is the CSRBF at the knots. CSRBFs with C2, C4 and C6 continuity are usually adopted to interpolate the LSF, expressed by the follows [232]:

$$\phi_e(\mathbf{x})=\max\{0,1-r_e(\mathbf{x})\}^4\left(4r_e(\mathbf{x})+1\right)\quad\text{(C2)} \tag{3-7}$$

$$\phi_e(\mathbf{x})=\max\{0,1-r_e(\mathbf{x})\}^6\left(35r_e^2(\mathbf{x})+18r_e(\mathbf{x})+3\right)\quad\text{(C4)} \tag{3-8}$$

$$\phi_e(\mathbf{x})=\max\{0,1-r_e(\mathbf{x})\}^8\left(32r_e^3(\mathbf{x})+25r_e^2(\mathbf{x})+8r_e(\mathbf{x})+1\right)\quad\text{(C6)} \tag{3-9}$$

in which

$$r_e(\mathbf{x})=\|\mathbf{x}-\mathbf{x}_e\|/R \tag{3-10}$$

where $\mathbf{x}_e$ is the coordinate of the eth knot, and R is the radius of a circular supported domain of this knot. R reflects the influence range of the control point and it should not be set too large or too small. Large radius value will increase the computation calculation, and small radius value may cause singularities. In our work, radius $R=R_C d$, R_C is set to be within [2.0, 4.0 , and d is determined by the neighborhood range of the current interpolation control point [233 .

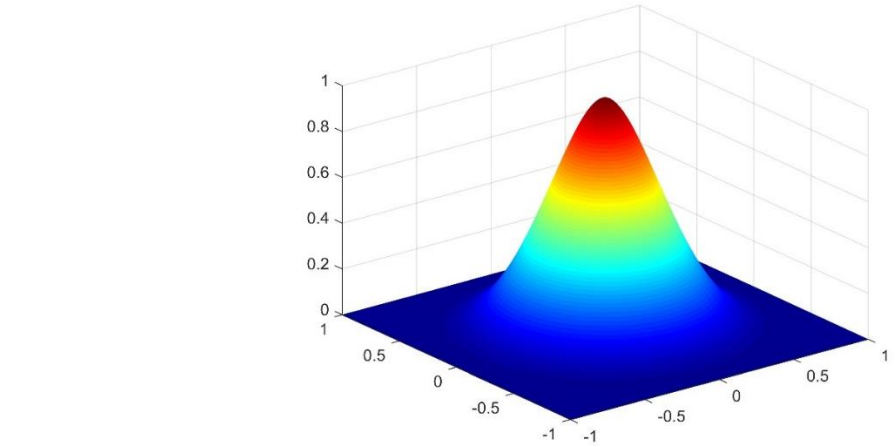

(1) Shapes of CSRBF-C2

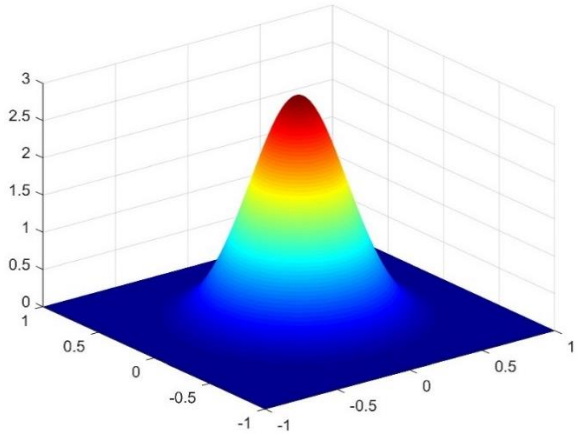

(2) Shape of CSRBF-C4

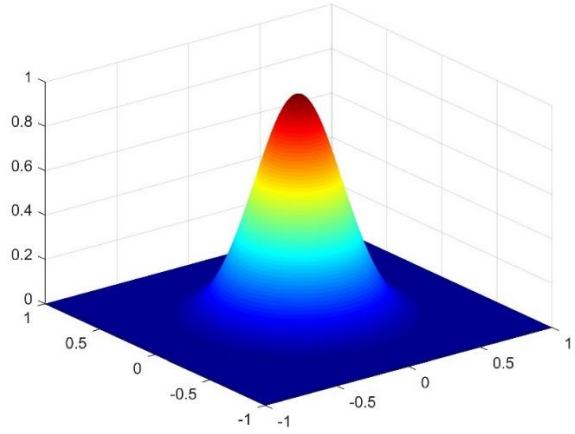

(3) Shape of CSRBF-C6

Figure 3-2 Shape of CSRBFs

Figure 3-2 shows the shapes of CSRBFs-C2, C4, and C6. It can be seen that these CSRBFs all have good differentiability and smoothness and it has been proved that the CSRBFs can approximate functions with desirable completeness once the interpolating points are properly arranged in the domain. From the above figures we can see that the CSRBFs-C6 has the highest differentiability relevant to the steepest caps of shape and derivatives. Hence, it might be more sensitive to the variations of the radius for the support domain. In general, these

CSRBFs can all be used in PLSM with a satisfactory precision. In this work, the CSRBFs-C2 is used to approximate the LSF.

3.2.2 Parameterization of the level set function

CSRBFs-C2 in Eq. (3-7) positioned in the prescribed nodes are used to approximate the LSF, then Eq. (3-6) can be rewritten as:

$$\mathbf{\Phi} = \mathbf{A}\boldsymbol{\alpha} \tag{3-11}$$

in which $\mathbf{\Phi}=\left[\Phi_1,\Phi_2,\cdots,\Phi_N\right]^{\mathrm{T}}$ are the values of the LSF at the interpolation points $x_1,x_2,\cdots,x_N$. **A** is a theoretically invertible collection matrix:

$$\mathbf{A}=\begin{bmatrix} \phi_1(x_1) & \phi_2(x_1) & \cdots & \phi_N(x_1) \\ \phi_1(x_2) & \phi_2(x_2) & \cdots & \phi_N(x_2) \\ \vdots & \vdots & \vdots & \vdots \\ \phi_1(x_N) & \phi_2(x_N) & \cdots & \phi_N(x_N) \end{bmatrix} \tag{3-12}$$

Eq. (3-11) shows that the time-space coupled LSF can be decoupled and expressed by shape functions and the expansion coefficients. The shape functions are only spatial function and the expansion coefficients are only time dependent. The collection matrix A can be determined when the CSRBFs and the interpolation points are fixed. That is to say, A is a constant matrix during the optimization process. The LSF can then be turned into a parametric form. It also indicates that the original design variables of the LSF Φ in the topology optimization have been transformed to a set of the expansion coefficients of the CSRBF interpolation. A sign distance function is used as an initial LSF, and the initial design variables are calculated from Eq.(3-11).

With the parameterized scheme, the Eq. (3-3) can be transformed into a new ODE as follows:

$$\boldsymbol{\phi}(\mathbf{x})^{\mathrm{T}}\,\dot{\boldsymbol{\alpha}}(t)-\mathbf{v}_n\cdot\left|\nabla\boldsymbol{\phi}(\mathbf{x})^{\mathrm{T}}\,\boldsymbol{\alpha}(t)\right|=0 \tag{3-13}$$

in which the normal velocity can be expressed by

$$\mathbf{v}_n=\frac{\boldsymbol{\phi}(\mathbf{x})^{\mathrm{T}}\,\dot{\boldsymbol{\alpha}}(t)}{\left|\nabla\boldsymbol{\phi}(\mathbf{x})^{\mathrm{T}}\,\boldsymbol{\alpha}(t)\right|},\ \dot{\boldsymbol{\alpha}}(t)=\frac{d\boldsymbol{\alpha}(t)}{dt} \tag{3-14}$$

Based on the above, the shape and topology change problem can be turned into a parametric problem. The H-J PDE driven topology optimization problem has been changed to an ODE driven one, and the normal velocity has been naturally extended to whole design domain, so it does not need to use any additional scheme to the velocity field to the design domain. The original topological optimization is transformed into a size optimization in which the expansion coefficients $\boldsymbol{\alpha}(t)$ are regarded as design variables, and the design variables will be updated during the optimization process based on the sensitivity information. Hence, the evolvement of the LSF and the propagation of the boundary are indicated by the update of the design variables based on a gradient-based optimization. Many sensitivity based optimization algorithms, including the optimality criteria (OC) [234, 235] and method of moving asymptotes (MMA) [236] can be directly applied.

3.3 Topology optimization based on the PLSM

3.3.1 Topology optimization formulation

A typical topology optimization for structures is to minimize the structural compliance with a volume constraint. A smaller structural compliance represents a higher stiffness. By PLSM, the topology optimization problem can be formulated as follows:

$$\begin{aligned} \min_{\boldsymbol{\alpha}} \ & C(\mathbf{u},\Phi)=\int_{\Omega} f(\mathbf{u})H(\Phi)d\Omega \\ \text{s.t.} \ & G(\Phi)=\int_{\Omega} H(\Phi)d\Omega - fV_0 \le 0 \\ & a(\mathbf{u},\mathbf{v},\Phi)=l(\mathbf{v},\Phi) \ \forall \mathbf{v}\in\tilde{\mathbf{U}} \\ & \alpha_{\min}\le\alpha_e\le\alpha_{\max}, e=1,2,\cdots,N \end{aligned} \tag{3-15}$$

where the objective function is:

$$f(\mathbf{u})=\varepsilon_{ij}^{\mathrm{T}}(\mathbf{u})E_{ijkl}\varepsilon_{kl}(\mathbf{u}) \tag{3-16}$$

$a(\mathbf{u},\mathbf{v},\Phi)=l(\mathbf{u},\mathbf{v})$ is the state equation for the elastic continuum in the weak form. The bilinear energy form $a(\mathbf{u},\mathbf{v},\Phi)$ is described as:

$$a(\mathbf{u},\mathbf{v},\Phi)=\int_{\Omega}\varepsilon_{ij}^{\mathrm{T}}(\mathbf{u})E_{ijkl}\varepsilon_{kl}(\mathbf{v})H(\Phi)d\Omega \tag{3-17}$$

The linear load form is given as:

$$l(\mathbf{v},\Phi)=\int_{\Omega}\mathbf{p}\mathbf{v}H(\Phi)d\Omega+\int_{\Omega}\boldsymbol{\tau}\mathbf{v}\delta(\Phi)|\nabla\Phi|d\Omega \tag{3-18}$$

where $\alpha_e(e=1,2,\cdots,N)$ are the design variables, which are actually N expansion coefficients in the CSRBF interpolation. $\alpha_{\min}$ and $\alpha_{\max}$ are recognized as the upper and lower

bounds of the design variables to stabilize the iteration. G is the volume constraint, f is the volume fraction and V_0 is the maximum allowable volume. $\mathbf{u}$ is the actual displacement field and v is the virtual displacement field which is belonging to the kinematically admissible set of displacements $\tilde{\mathbf{U}}$. ε represents the strain field, and E represents the elastic matrix. $\mathbf{p}$ denotes the body force, and $\boldsymbol{\tau}$ denotes the boundary force. $H(\Phi)$ denotes the sufficiently smooth Heaviside function [11 :

$$H(\Phi)=\begin{cases}\zeta, & \Phi<-\Delta \\ \dfrac{3(1-\zeta)}{4}\left(\dfrac{\Phi}{\Delta}-\dfrac{\Phi^3}{3\Delta^3}\right)+\dfrac{1+\zeta}{2}, & -\Delta\le\Phi\le\Delta \\ 1. & \Phi\ge\Delta\end{cases} \tag{3-19}$$

where ζ is a small positive number to avoid singularity, and Δ describes the width for the numerical approximation of $H(\Phi)$. $\delta(\Phi)$ denotes the Dirac function, which is the derivative of $H(\Phi)$:

$$\delta(\Phi)=\begin{cases}\dfrac{3(1-\zeta)}{4\Delta}\left(1-\dfrac{\Phi^2}{\Delta^2}\right), & |\Phi|\le\Delta \\ 0. & |\Phi|>\Delta\end{cases} \tag{3-20}$$

Finite element method is used to solve the elastic equation, and the LSF is approximated by CSRBFs on the given interpolation points. That is to say, there are two grids in this problem, one is the grid for Finite Element Analysis (FEA), and the other is the grid for the LSF. For convenience, we assume these two grids are the same in this work. In this case, N represents the control points for the LSF and also denotes the nodes number of the finite elements.

The finite elements will be cut when the structural boundary moves with the evolution of LSF and this will lead to the boundary discontinuity. This problem is relatively difficult to solve using the standard FEA method since time-consuming re-mesh is needed. Ersatz material model [41] is used to avoid the re-mesh and solve the boundary discontinuity in this problem. By the ersatz material model, the incomplete element caused by the structure boundary will be considered as a full element with an artificial density. The stiffness matrix for the element then can be calculated based on the artificial density.

3.3.2 Sensitivity analysis

The theory of shape derivative and the adjoint method are used to deduce the sensitivities [11, 237 . The shape derivative means the first derivative of the function with respect to time, then the derivatives for the objective function, the bilinear energy form, the linear load form with respect to time can be expressed as the follows respectively:

$$\frac{\partial C(\mathbf{u},\Phi)}{\partial t}=\int_{\Omega}2\varepsilon_{ij}^{\mathrm{T}}(\dot{\mathbf{u}})E_{ijkl}\varepsilon_{kl}(\mathbf{u})H(\Phi)d\Omega+\int_{\Omega}\varepsilon_{ij}^{\mathrm{T}}(\mathbf{u})E_{ijkl}\varepsilon_{kl}(\mathbf{u})\delta(\Phi)\frac{\partial\Phi}{\partial t}d\Omega \tag{3-21}$$

$$\begin{aligned}\frac{\partial a(\mathbf{u},\mathbf{v},\Phi)}{\partial t}=&\int_{\Omega}\varepsilon_{ij}^{\mathrm{T}}(\dot{\mathbf{u}})E_{ijkl}\varepsilon_{kl}(\mathbf{v})H(\Phi)d\Omega+\int_{\Omega}\varepsilon_{ij}^{\mathrm{T}}(\mathbf{u})E_{ijkl}\varepsilon_{kl}(\dot{\mathbf{v}})H(\Phi)d\Omega\\&+\int_{\Omega}\varepsilon_{ij}^{\mathrm{T}}(\mathbf{u})E_{ijkl}\varepsilon_{kl}(\mathbf{v})\delta(\Phi)\frac{\partial\Phi}{\partial t}d\Omega\end{aligned} \tag{3-22}$$

$$\frac{\partial l(\mathbf{v},\Phi)}{\partial t}=\int_{\Omega}\left(p\dot{\mathbf{v}}+div\left(p\dot{\mathbf{v}}\mathbf{n}\right)\right)H(\Phi)d\Omega+\int_{\Omega}\left(\mathbf{p}\mathbf{v}+div\left(\boldsymbol{\tau}\mathbf{v}\mathbf{n}\right)\right)\delta(\Phi)\frac{\partial\Phi}{\partial t}d\Omega \tag{3-23}$$

Since $\dot{\mathbf{v}}\in\mathbf{U}$, we can get the conjugate equation:

$$a(\mathbf{u},\dot{\mathbf{v}},\Phi)=l(\dot{\mathbf{v}},\Phi) \tag{3-24}$$

Then

$$\int_\Omega \varepsilon_{ij}^{\mathrm{T}}(\mathbf{u}) E_{ijkl} \varepsilon_{kl}(\dot{\mathbf{v}}) H(\Phi) d\Omega = \int_\Omega \left(\mathbf{p}\dot{\mathbf{v}} + div(\boldsymbol{\tau}\dot{\mathbf{v}}\mathbf{n})\right) H(\Phi) d\Omega \tag{3-25}$$

Differentiating the elastic equilibrium condition with respect to time, we can obtain:

$$\frac{\partial a(\mathbf{u},\mathbf{v},\Phi)}{\partial t} = \frac{\partial l(\mathbf{u},\mathbf{v})}{\partial t} \tag{3-26}$$

That is:

$$\begin{aligned} &\int_\Omega \varepsilon_{ij}^{\mathrm{T}}(\dot{\mathbf{u}}) E_{ijkl} \varepsilon_{kl}(\mathbf{v}) H(\Phi) d\Omega + \int_\Omega \varepsilon_{ij}^{\mathrm{T}}(\mathbf{u}) E_{ijkl} \varepsilon_{kl}(\dot{\mathbf{v}}) H(\Phi) d\Omega + \int_\Omega \varepsilon_{ij}^{\mathrm{T}}(\mathbf{u}) E_{ijkl} \varepsilon_{kl}(\mathbf{v}) \delta(\Phi) \frac{\partial \Phi}{\partial t} d\Omega \\ &= \int_\Omega \left(\mathbf{p}\dot{\mathbf{v}} + div(\mathbf{p}\dot{\mathbf{v}}\mathbf{n})\right) H(\Phi) d\Omega + \int_\Omega \left(\mathbf{p}\mathbf{v} + div(\boldsymbol{\tau}\mathbf{v}\mathbf{n})\right) \delta(\Phi) \frac{\partial \Phi}{\partial t} d\Omega \end{aligned} \tag{3-27}$$

From Eq. (3-25), Eq. (3-27) can be rewritten as:

$$\begin{aligned} &\int_\Omega \varepsilon_{ij}^{\mathrm{T}}(\dot{\mathbf{u}}) E_{ijkl} \varepsilon_{kl}(\mathbf{v}) H(\Phi) d\Omega \\ &= \int_\Omega \left(\mathbf{p}\mathbf{v} + div(\boldsymbol{\tau}\mathbf{v}\mathbf{n})\right) \delta(\Phi) \frac{\partial \Phi}{\partial t} d\Omega - \int_\Omega \varepsilon_{ij}^{\mathrm{T}}(\mathbf{u}) E_{ijkl} \varepsilon_{kl}(\mathbf{v}) \delta(\Phi) \frac{\partial \Phi}{\partial t} d\Omega \end{aligned} \tag{3-28}$$

Since the structural compliance optimization is a self-adjoint problem, then:

$$\begin{aligned} &\int_\Omega \varepsilon_{ij}^{\mathrm{T}}(\dot{\mathbf{u}}) E_{ijkl} \varepsilon_{kl}(\mathbf{u}) H(\Phi) d\Omega \\ &= \int_\Omega \left(\mathbf{p}\mathbf{u} + div(\boldsymbol{\tau}\mathbf{u}\mathbf{n})\right) \delta(\Phi) \frac{\partial \Phi}{\partial t} d\Omega - \int_\Omega \varepsilon_{ij}^{\mathrm{T}}(\mathbf{u}) E_{ijkl} \varepsilon_{kl}(\mathbf{u}) \delta(\Phi) \frac{\partial \Phi}{\partial t} d\Omega \\ &= \int_\Omega \left(\mathbf{p}\mathbf{u} + div(\boldsymbol{\tau}\mathbf{u}\mathbf{n})\right) \delta(\Phi) |\nabla \Phi| \mathbf{v}_n d\Omega - \int_\Omega \varepsilon_{ij}^{\mathrm{T}}(\mathbf{u}) E_{ijkl} \varepsilon_{kl}(\mathbf{u}) \delta(\Phi) |\nabla \Phi| \mathbf{v}_n d\Omega \end{aligned} \tag{3-29}$$

Substituting Eq. (3-29) into Eq. (3-21):

$$\frac{\partial C(\mathbf{u},\Phi)}{\partial t} = \int_\Omega 2 \left[\left(\mathbf{p}\mathbf{u} + div(\boldsymbol{\tau}\mathbf{u}\mathbf{n})\right) - \frac{1}{2} \varepsilon_{ij}^{\mathrm{T}}(\mathbf{u}) E_{ijkl} \varepsilon_{kl}(\mathbf{u}) \right] \delta(\Phi) |\nabla \Phi| \mathbf{v}_n d\Omega \tag{3-30}$$

in which

$$div(\boldsymbol{\tau}\mathbf{un}) = \nabla(\boldsymbol{\tau}\mathbf{u})\cdot\frac{\nabla\Phi}{|\nabla\Phi|} + \left(\nabla\cdot\frac{\nabla\Phi}{|\nabla\Phi|}\right)\boldsymbol{\tau}\mathbf{u} \tag{3-31}$$

By Eq. (3-14), Eq. (3-30) can be re-expressed as:

$$\frac{\partial C(\mathbf{u},\Phi)}{\partial t} = \sum_{i=1}^{N}\int_{\Omega}\beta(\mathbf{u},\Phi)\varphi_i(\mathbf{x})\delta(\Phi)\frac{d\alpha_i(t)}{dt}d\Omega \tag{3-32}$$

$$\beta(\mathbf{u},\Phi) = 2\left(\mathbf{pu} - \frac{1}{2}\varepsilon_{ij}^{\mathrm{T}}(\mathbf{u})E_{ijkl}\varepsilon_{kl}(\mathbf{u}) + \nabla(\boldsymbol{\tau}\mathbf{u})\cdot\frac{\nabla\Phi}{|\nabla\Phi|} + \left(\nabla\cdot\frac{\nabla\Phi}{|\nabla\Phi|}\right)\boldsymbol{\tau}\mathbf{u}\right) \tag{3-33}$$

According to the chain rule, we can get:

$$\frac{\partial C(\mathbf{u},\Phi)}{\partial t} = \sum_{e=1}^{N}\frac{\partial C(\mathbf{u},\Phi)}{\partial\alpha_e(t)}\cdot\frac{d\alpha_e(t)}{dt} \tag{3-34}$$

Comparing Eqs. (3-32) and (3-34):

$$\frac{\partial C(\mathbf{u},\Phi)}{\partial\alpha_e(t)} = \int_{\Omega}\beta(\mathbf{u},\Phi)\varphi_e(\mathbf{x})\delta(\Phi)d\Omega \tag{3-35}$$

Similarly, the derivatives of the volume constraint with respect to the design variable can be computed as:

$$\frac{\partial G(\Phi)}{\partial\alpha_e} = \int_{\Omega}\varphi_e(\mathbf{x})\delta(\Phi)d\Omega \tag{3-36}$$

Therefore, the general shape and topology optimization problem has been transformed into a general size optimization problem, which enables the direct application of the gradient-based optimization algorithms.

3.4 Optimization method

There generally exist a large number of design variables in topology optimization problems, so it is relatively difficult to solve these high-dimensional optimization problems. Among the optimization methods, the gradient-based optimization algorithms have some advantages for solving the topology optimization problems. The OC method [234,235 and the MMA method [236 are both popular optimization schemes to be employed in topology optimization. The OC method is very efficient for optimization problems with a large number of design variables with single constraint, which is a typical case in the continuous shape and topology optimization with a material usage constraint. MMA is a powerful and theoretically well-established scheme which can solve optimization problems with multiple constraints.

3.4.1 Optimality Criteria Method

OC method aims at building an iteration format based on the design criterial to update the design variables until convergent. OC method can convergent quickly and generally only needs a small number of iterations in spite of the number of design variables or the complexity of the problems. The main idea of the OC method is to build the iteration equation. However, the iteration criteria should be different for different kinds of optimization problems. The development of the OC criteria experienced developments from the intuition criteria such as the strength criterion, synchronization failure criterion, full stress criterion and the rational criteria such as the Kuhn-Tucker conditions. By the Kuhn-Tucker condition, OC method can get the local optimal solution or even the global optimal solution of the optimization problem.

In the PLSM, OC method is used to update the expansion coefficients $\boldsymbol{\alpha}$ of the CSRBF interpolation. The optimization problem of the structural stiffness design is described by Eq. (3-15), this can be regarded as a non-linear programing problem with inequalities. Introducing Lagrange multipliers Λ, λ, $\lambda_e^1, \lambda_e^2 \left(e = 1, 2, \cdots, N\right)$, the original optimization problem will be turned into a problem without constraints as follows:

$$L = C\left(\mathbf{u}, \Phi\right) + \Lambda G\left(\Phi\right) + \lambda\left(a\left(\mathbf{u}, \mathbf{v}, \Phi\right) - l\left(\mathbf{u}, \mathbf{v}\right)\right) + \lambda_e^1\left(\alpha_{\min} - \alpha_e\right) + \lambda_e^2\left(\alpha_e - \alpha_{\max}\right) \quad (3\text{-}37)$$

where λ is the Lagrange multiplier related to the equilibrium condition, and can be neglect in the allowable linear elastic space. Then the Kuhn-Tucker conditions can be obtained by:

$$\begin{cases} \dfrac{\partial L}{\partial \alpha_e} = \dfrac{\partial C\left(\mathbf{u}, \Phi\right)}{\partial \alpha_e} + \Lambda \dfrac{\partial G\left(\Phi\right)}{\partial \alpha_e} - \lambda_e^1 + \lambda_e^2 = \begin{cases} =0, \ \alpha_{\min} \le \alpha_e \le \alpha_{\max} \\ \ge 0, \alpha_e \le \alpha_{\min} \\ \le 0, \alpha_e \ge \alpha_{\max} \end{cases} \\ \begin{cases} \int_\Omega H\left(\Phi\right) d\Omega - fV_0 \le 0 \\ \Lambda\left(\int_\Omega H\left(\Phi\right) d\Omega - fV_0\right) = 0, \Lambda \ge 0 \end{cases} \\ \begin{cases} \alpha_{\min} - \alpha_e \le 0 \\ \alpha_e - \alpha_{\max} \le 0 \\ \lambda_e^1\left(\alpha_{\min} - \alpha_e\right) = 0, \lambda_e^1 \ge 0 \\ \lambda_e^2\left(\alpha_e - \alpha_{\max}\right) = 0, \lambda_e^2 \ge 0 \end{cases} \end{cases} \quad (3\text{-}38)$$

From the above we can see that, if the expansion coefficients are within the constraints $\alpha_{\min} \le \alpha_e \le \alpha_{\max}$, then the design variables are active and it can be changed during the optimization process. Otherwise, the design variables are passive variables which cannot be changed and are only determined by the lower or upper bounds. If $\alpha_e \le \alpha_{\min}$, we can get $\lambda_e^1 \ge 0$

and $\lambda_e^2=0$, that is to say, the lower bounds are active. If $\alpha_e \geq \alpha_{\max}$, we can get $\lambda_e^2 \geq 0$ and $\lambda_e^1=0$, that is to say, the upper bounds are active. The Kuhn-Tucker conditions consist of a large number of non-linear algebraic equations, so it is difficult to be solved especially when there are many design elements. In this case, heuristic iteration schemes based on the Kuhn-Tucker conditions have been developed as alternatives to efficiently update the design variables.

Assuming that the design variables are active, the stationary condition can be rewritten as:

$$\frac{\partial L}{\partial \alpha_e} = \frac{\partial C(\mathbf{u},\Phi)}{\partial \alpha_e} + \Lambda \frac{\partial G(\Phi)}{\partial \alpha_e} = 0 \tag{3-39}$$

Based on the above equation, an updating format can be designed as follows:

$$\alpha_e^{(k+1)} = \left(\frac{\partial C(\mathbf{u},\Phi)}{\partial \alpha_e^{(k)}} / \Lambda \frac{\partial G(\Phi)}{\partial \alpha_e^{(k)}} \right) \alpha_e^{(k)} \tag{3-40}$$

in which *k* denotes the current iteration step. It is defined that:

$$B_e^{(k)} = \frac{\partial C(\mathbf{u},\Phi)}{\partial \alpha_e^{(k)}} \Bigg/ \left(\max\left(\mu, \Lambda^{(k)} \frac{\partial G(\Phi)}{\partial \alpha_e^{(k)}} \right) \right) \tag{3-41}$$

where μ is a very small positive constant used to remove the zero terms. Then, the iteration pattern for the design variables can be described as:

$$\alpha_e^{(k+1)} = \begin{cases} \min\left[(m+1)\alpha_e^{(k)}, \alpha_{\max} \right], if\ \min\left[(m+1)\alpha_e^{(k)}, \alpha_{\max} \right] \leq \left[B_e^{(k)} \right]^{\varsigma} \alpha_e^{(k)} \\ \left[B_e^{(k)} \right]^{\varsigma} \alpha_e^{(k)}, if \begin{cases} \max\left[(1-m)\alpha_e^{(k)}, \alpha_{\min} \right] < \left[B_e^{(k)} \right]^{\varsigma} \alpha_e^{(k)} \\ \left[B_e^{(k)} \right]^{\varsigma} \alpha_e^{(k)} < \min\left[(m+1)\alpha_e^{(k)}, \alpha_{\max} \right] \end{cases} \\ \max\left[(1-m)\alpha_e^{(k)}, \alpha_{\min} \right], if \left[B_e^{(k)} \right]^{\varsigma} \alpha_e^{(k)} \leq \max\left[(1-m)\alpha_e^{(k)}, \alpha_{\min} \right] \end{cases} \tag{3-42}$$

where $m(0<m<1)$ is a positive move-limit, $\varsigma(0<\varsigma<1)$ is a numerical damping coefficient where Λ is a Lagrangian multiplier that can be found by a bi-sectioning algorithm.

3.4.2 The Method of Moving Asymptotes

The OC method is efficient for problems with a large number of design variables and with a single constraint. However, it is difficult to deal with problems with multiple constraints. A method, which is called the "Method of Moving Asymptotes" (MMA), has been proposed based on a special type of convex approximation to deal with optimization problems with multiple constraints. In MMA, the original optimization problem is transformed into a set of linearized, convex sub-problems based on the first or second derivatives at the current and previous points. MMA is a kind of sequential convex programming method and has become a popular optimization scheme for topology optimization problems.

By introducing artificial parameters, the original optimization formulation in Eq. (3-15) can be re-expressed as:

$$\begin{aligned}
\min_{\boldsymbol{\alpha}} \quad & f_0(\boldsymbol{\alpha}) + a_0 z + \sum_{j=1}^{m}\left(b_j y_j + \frac{1}{2} d_j y_j^2\right) \\
\text{s.t.} \quad & f_j(\boldsymbol{\alpha}) - a_j z - y_j \le 0, j = 1,2,\cdots,m \\
& z \ge 0, y_j \ge 0, j = 1,2,\cdots,m \\
& \alpha_{\min} \le \alpha_e \le \alpha_{\max}, e = 1,2,\cdots,N
\end{aligned} \tag{3-43}$$

where $f_0(\boldsymbol{\alpha})$ is the objective function, $f_j(\boldsymbol{\alpha}),(j=1,2,\cdots,m)$ are the constraints and $\alpha_e,(e=1,2,\cdots,N)$ are the design variables. a_0, a_j, b_j and d_j are given real numbers which satisfy $a_0 > 0$, $a_j \ge 0, b_j \ge 0, d_j \ge 0$, and $b_j + d_j > 0$. $y = (y_1, y_2, \cdots, y_m)^{\mathrm{T}} \in \mathbb{R}^m$, and $z \in \mathbb{R}$.

m is the number of constraints and N is the number of design variables. $\alpha_1, \alpha_2, \cdots, \alpha_N$ are the natural optimization variables, while $y_1, y_2, \cdots, y_m$ and z are the artificial optimization variables.

The optimization problem will be solved by an iteration process. At the current kth step, the design variables are $\boldsymbol{\alpha}^{(k)}$, and the objective function and the constraints are replaced by certain convex functions $f_0^{(k)}(\boldsymbol{\alpha})$ and $f_j^{(k)}(\boldsymbol{\alpha})$. Then a new sub-problem is generated as follows:

$$\begin{aligned} \min_{\boldsymbol{\alpha}} \ & f_0^{(k)}(\boldsymbol{\alpha}) + a_0 z + \sum_{j=1}^{m}\left(b_j y_j + \frac{1}{2} d_j y_j^2\right) \\ \text{s.t.} \ & f_j^{(k)}(\boldsymbol{\alpha}) - a_j z - y_j \le 0, j = 1,2,\cdots,m \\ & z \ge 0, y_j \ge 0, j = 1,2,\cdots,m \\ & \alpha_{\min} \le \alpha_e^{(k)} \le \alpha_{\max}, e = 1,2,\cdots,N \end{aligned} \tag{3-44}$$

where $0.9l_e^{(k)} + 0.1\alpha_e^{(k)} \le \alpha_e^{(k)} \le 0.9u_e^{(k)} + 0.1\alpha_e^{(k)}, e = 1,2,\cdots N$. The approximating functions are obtained as:

$$f_j^{(k)}(\boldsymbol{\alpha}) = \sum_{e=1}^{N}\left(\frac{p_{je}^{(k)}}{u_e^{(k)} - \alpha_e^{(k)}} + \frac{q_{je}^{(k)}}{\alpha_e^{(k)} - l_e^{(k)}}\right) + r_j^{(k)} \tag{3-45}$$

where

$$p_{je}^{(k)} = \left(u_e^{(k)} - \alpha_e^{(k)}\right)^2 \left(1.001\max\left(0, \frac{\partial f_j}{\partial \alpha_e}\left(\boldsymbol{\alpha}^{(k)}\right)\right) + 0.001\max\left(0, -\frac{\partial f_j}{\partial \alpha_e}\left(\boldsymbol{\alpha}^{(k)}\right)\right) + \frac{\rho_j}{\alpha_e^{\max} - \alpha_e^{\min}}\right) \tag{3-46}$$

$$q_{je}^{(k)} = \left(\alpha_e^{(k)} - l_e^{(k)}\right)^2 \left(0.001\max\left(0, \frac{\partial f_j}{\partial \alpha_e}\left(\boldsymbol{\alpha}^{(k)}\right)\right) + 1.001\max\left(0, -\frac{\partial f_j}{\partial \alpha_e}\left(\boldsymbol{\alpha}^{(k)}\right)\right) + \frac{\rho_j}{\alpha_e^{\max} - \alpha_e^{\min}}\right) \tag{3-47}$$

$$r_j^{(k)} = f_j\left(\boldsymbol{\alpha}^{(k)}\right) - \sum_{e=1}^{N}\left(\frac{p_{je}^{(k)}}{u_e^{(k)} - \alpha_e^{(k)}} + \frac{q_{je}^{(k)}}{\alpha_e^{(k)} - l_e^{(k)}}\right) \tag{3-48}$$

in which ρ_j is the default parameter which is set to be $\rho_j = 10^{-5}$, $l_e^{(k)}$ and $u_e^{(k)}$ are the moving asymptotes which are updated in each iteration based on information from previous iteration points. The approximating functions are strictly convex, so there is always a unique optimal solution of the MMA sub-problem. It is noted that although all sub-problems are strictly convex, a globally convergent solution can still not be guaranteed if the original problem itself is not convex.

3.5 Numerical examples

Figure 3-3 Design domain and boundary condition for the cantilever beam

Consider a 2:1 (length=1.6m and width=0.8m) cantilever beam, the boundary conditions are given in Figure 3-3. A vertical load F_1=$5\times10^5 N$ is applied on the middle point of the right bound of the beam. The objective function is to minimize the structural compliance under the

volume fraction of 0.5. The structure is discretized by 80×40 four-node quadrilateral (Q4) elements.

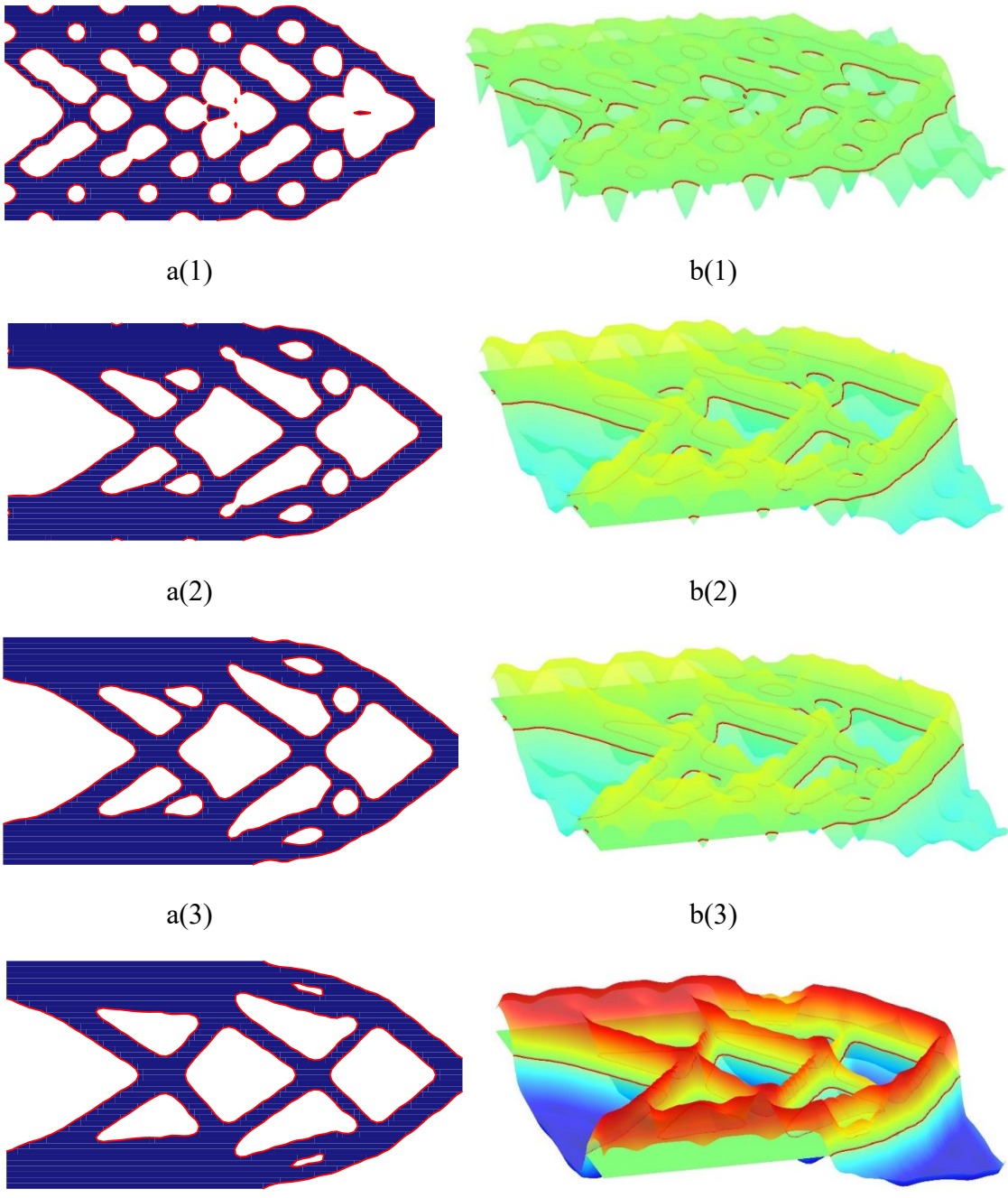

a(1) b(1)

a(2) b(2)

a(3) b(3)

a(4) b(4)

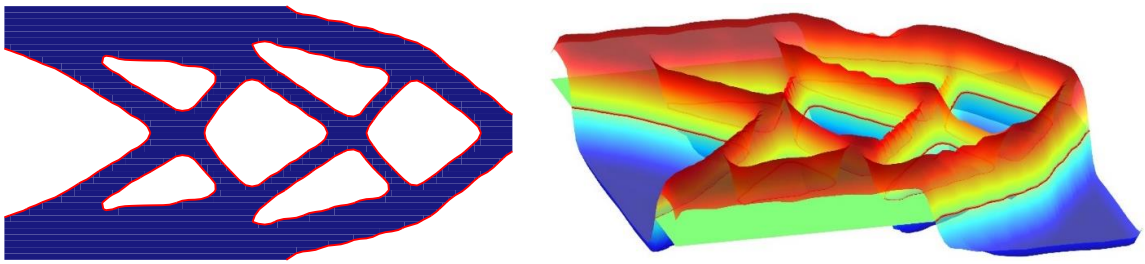

a(5) b(5)

Figure 3-4 The evolution process of the cantilever beam

The histories of the design boundary changes are given in Figure 3-4. Figure 3-4 a(1)-a(5) show the optimal configurations during the optimization process, and b(1)-b(5) show the related level set surfaces during the optimization process. In Figure 3-4, a(1)-a(4) and b(1)-b(4) are the contours and LSFs at iteration steps 5, 15, 20, and 50, a(5) and b(5) are the optimal design and related LSF.

It can be seen that the optimal result is characterized by a smooth boundary, which shows that the PLSM method is able to handle the shape and topology optimization by using the CSRBFs to represent the LSFs. The iteration histories of the objective function and the volume constraint are shown in Figure 3-5 and Figure 3-6. It shows that the PLSM method has good computational stability. The structural compliance rapidly decreases from over 500 to nearly 200 within 20 iterations. The evolvement of the structural topology is relatively remarkable at the earlier optimization steps, and after that comes the local and detailed evolvement. Finally, the structure compliance is reduced to 215.36 and the material usage is retained at 50%.

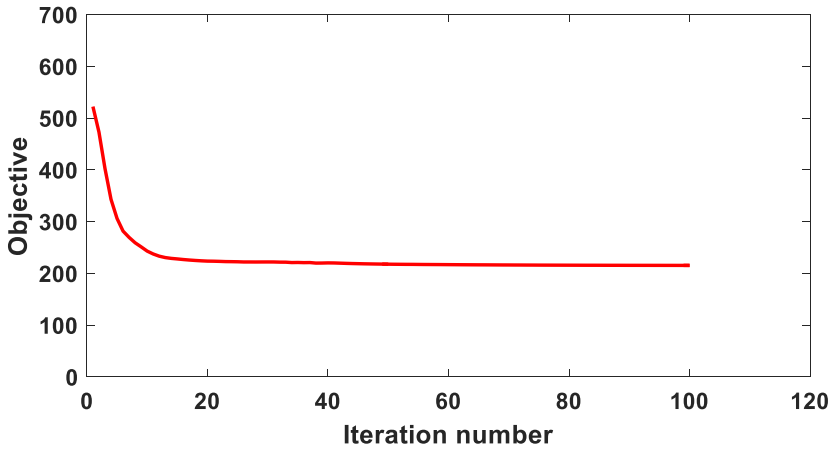

Figure 3-5 Objective function iteration history of the cantilever beam

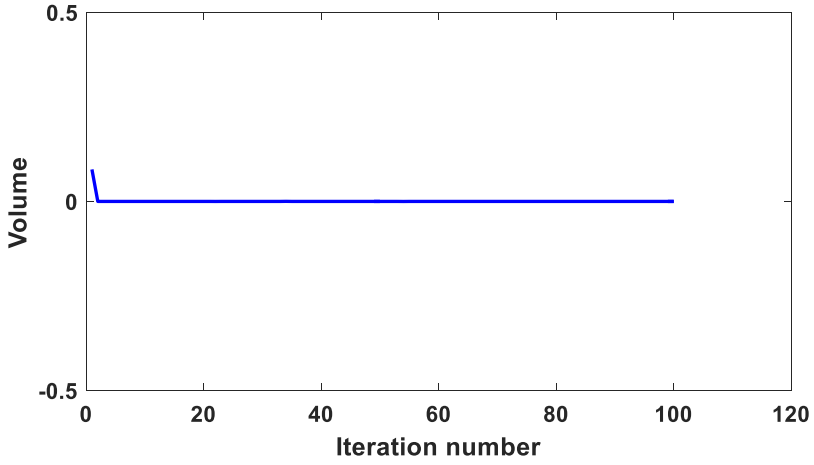

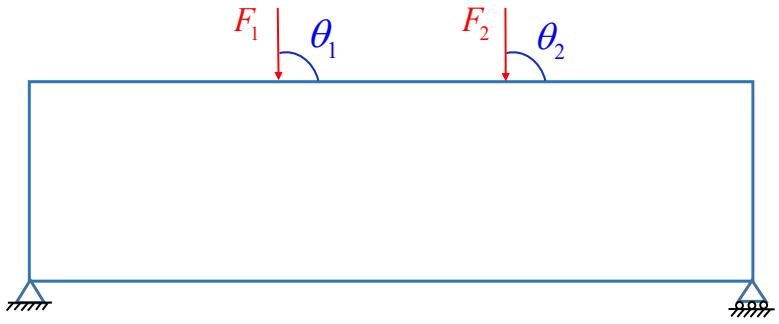

Figure 3-7 Design domain and boundary condition for the MBB beam

Consider a 4:1 (length=1.2m and width=0.3m) MBB beam, the boundary conditions are given in Figure 3-7. The lower left corner of the beam is clamped and lower right corner of the beam is simply supported. Two vertical loads $F_1=5\times10^5 N$ and $F_2=5\times10^5 N$ are applied on the upper bound of the beam. The objective function is to minimize the structural strain energy and the volume fraction is set as 50%. The structure is discretized by 120×30 Q4 elements.

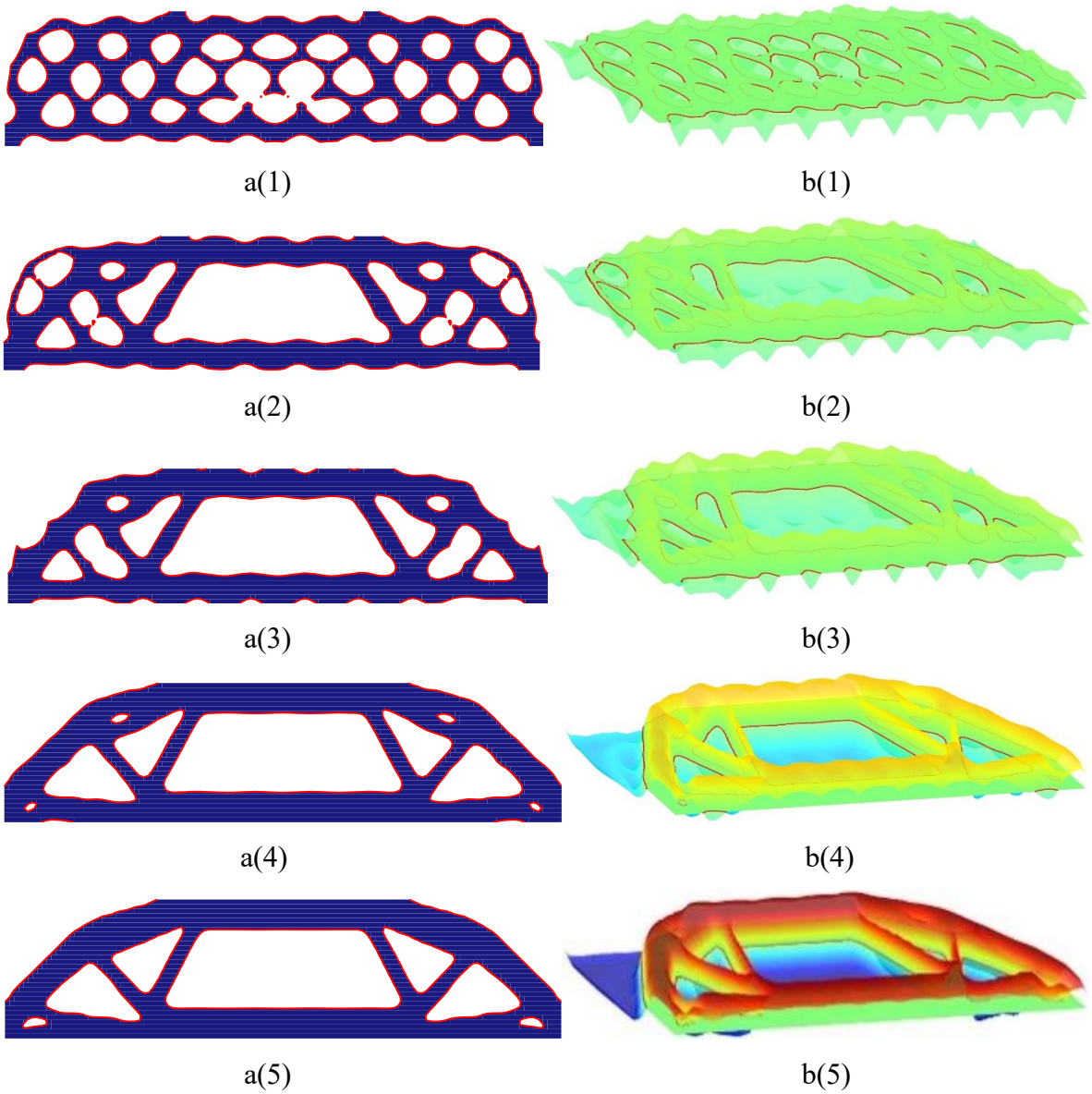

Figure 3-8 The evolution process of the MBB beam

Figure 3-8 shows the evolution process of the topology optimization for the MBB beam. Figure 3-8 a(1)-a(5) are the structure configurations during the evolution process, and b(1)-b(5) are the corresponding LSFs during the evolution process. In Figure 3-8, a(1)-a(4) and b(1)-b(4) are the contours and LSFs at iteration steps 5, 15, 20, and 50, a(5) and b(5) are the optimal design and related LSF.

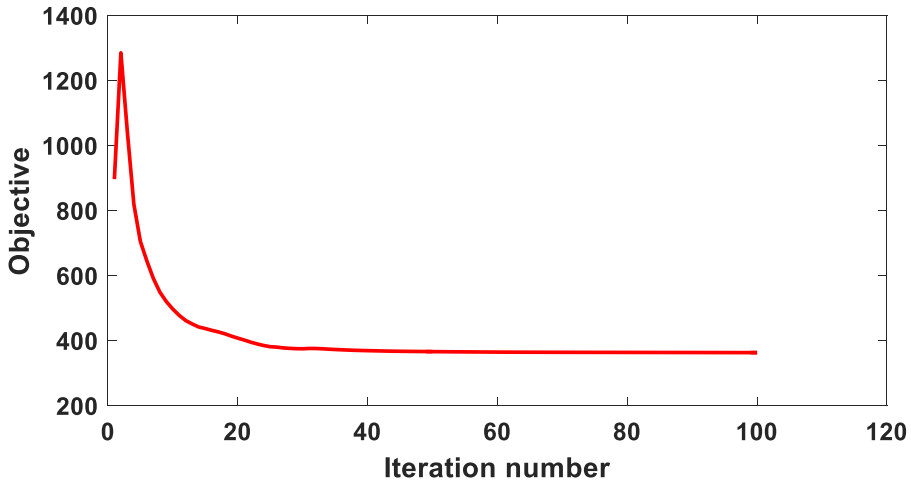

Figure 3-9 Objective function iteration history of the MBB beam

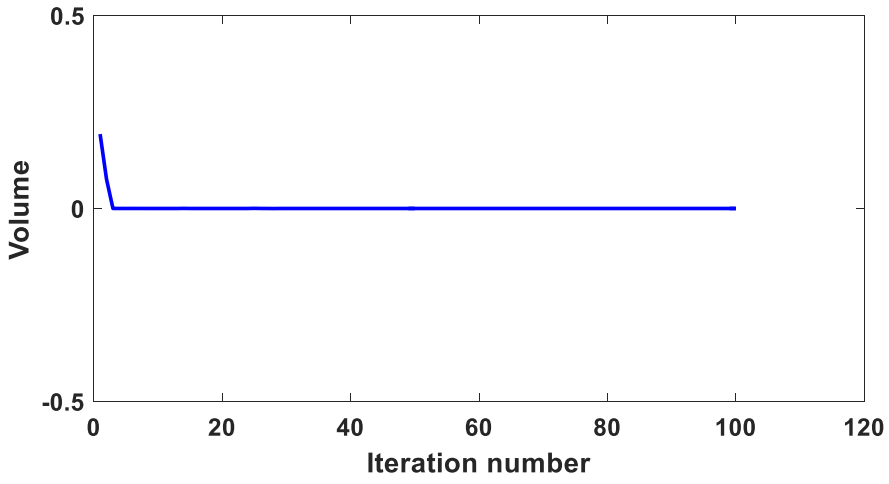

Figure 3-10 Volume constraint iteration history of the MBB beam

The convergent histories of the objective value (structural compliance) and the volume constraint are present in Figure 3-9 and Figure 3-10. The structural compliance rapidly decreases within 40 iterations and then the iteration process comes to a stable variation

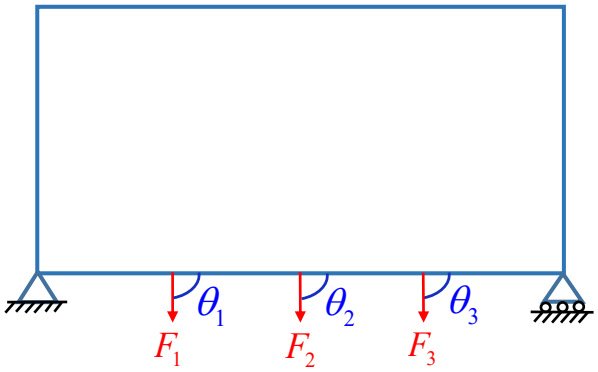

Figure 3-11 Design domain and boundary condition for the Michell-type structure

Consider a 2:1 (length=1.6m and width=0.8m) the Michell-type structure, the boundary conditions are given in Figure 3-11. The lower left corner of the beam is clamped and lower right corner of the beam is simply supported. Three vertical loads $F_1=5\times10^5 N$, $F_2=5\times10^5 N$ and $F_3=5\times10^5 N$ are applied on the lower bound of the beam. The structure is discretized by 80×40 Q4 elements.

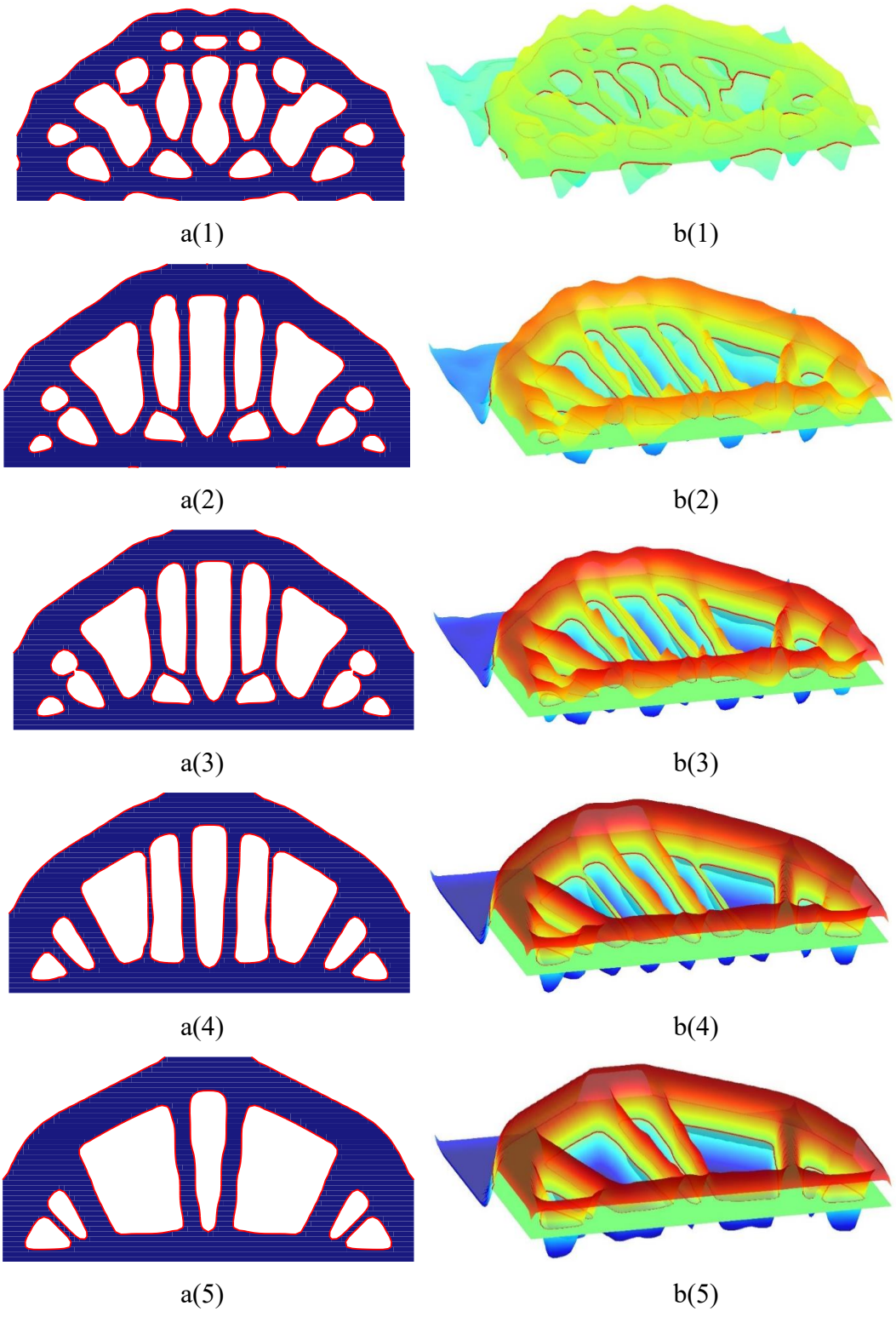

Figure 3-12 The evolution process of the Michell-type structure

This numerical example is a typical structural topology design problems to find a structure with minimum compliance under a prescribed volume fraction which is given as 50% in this example. The optimization results are given in Figure 3-12. The contours in Figure 3-12 a(1)-a(5) denote the material distributions of the design results during the optimization process, while the surfaces in Figure 3-12 b(1)-b(5) represent the corresponding LSFs during the evolution.

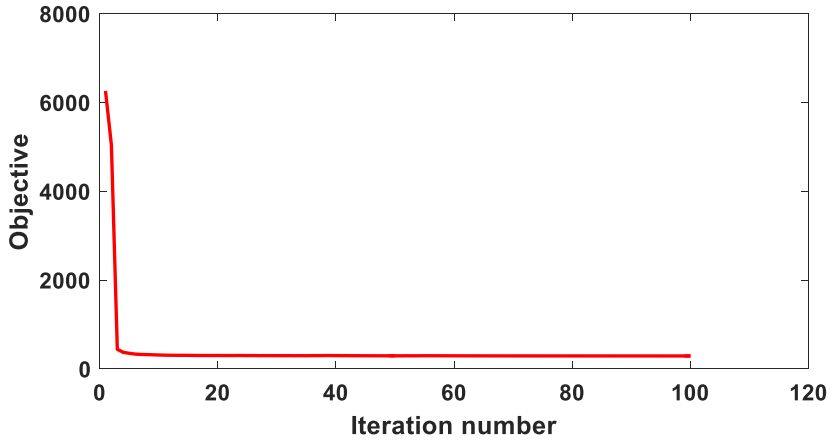

Figure 3-13 Objective function iteration history of the Michell-type structure

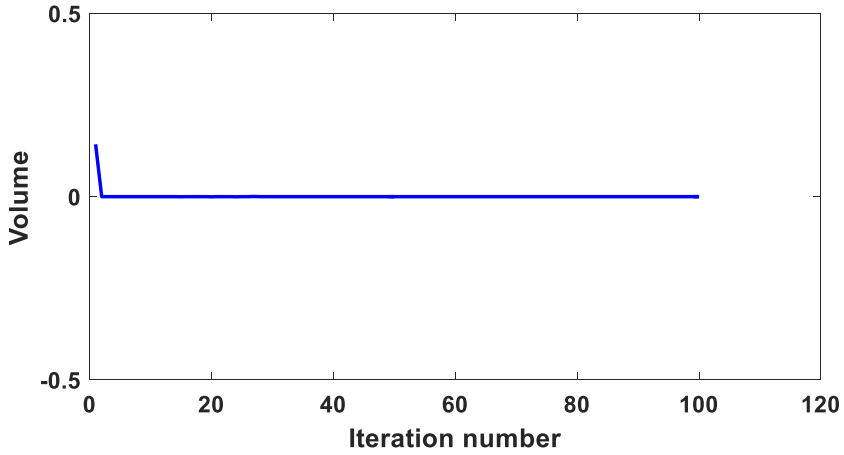

Figure 3-14 Volume constraint iteration history of the Michell-type structure

The PLSM method has been proved to have good computational stability from the iteration histories of the objective function and the volume constraint in Figure 3-13 and Figure 3-14. The structural compliance rapidly decreases from over 6000 to under 300 within 25 iterations. Later, the structural compliance reduced slightly while the shape and topology of the structure evolve changed. At last, the structure compliance is reduced to 291.09 and the material usage is retained at 50%.

Chapter 4 Random-interval hybrid uncertainty analysis

For a random-interval hybrid uncertain problem, the distribution of the objective function will consist of an upper bound and a lower bound. However, due to the difficulty in obtaining the precise solution, almost all the current studies in hybrid uncertainty analysis are developed to obtain the intervals of the lower moments (mean and standard variance) of the objective function. For improving the computational efficiency, the existing hybrid uncertainty analysis method mostly employed the first-order Taylor expansion or the second-order Taylor expansion to approximate the function. However, the first-order Taylor expansion generally cannot ensure a satisfactory accuracy, and the second-order Taylor expansion involves the second-order derivatives which may have difficulties in calculation. Therefore, how to develop new and more efficient random-interval hybrid uncertainty propagation analysis methods is of great significance in engineering. In traditional probability analysis, the polynomial chaos expansions [84,85 and the dimension-reduction integration [86,87 have been proven very effective for uncertainty propagation analysis. Combing the dimension-reduction integration or the polynomial chaos expansions with the random-interval hybrid models may provide new and efficient ways for hybrid uncertainty propagation analysis. In this Chapter, some hybrid uncertainty analysis methods based on polynomial chaos and dimension reduction schemes are developed to evaluate the mean and standard variance of performance functions. The uncertainty analysis methods will then be employed and applied in topology optimization problems in the following Chapters.

4.1 Hybrid uncertainty analysis method based on orthogonal polynomials

Recently, a Polynomial Chaos-Chebyshev Interval (PCCI) method [157 was proposed to estimate the mean and variation bounds of the response. This method is proved to be effective and has been applied in many design optimization problems [184,225 . However, the computational cost will increase exponentially with the increasing number of the uncertain variables. In this section, we will improve the original PCCI method from two aspects: the terms of the polynomials and the samples of the variables. The improved methods will reduce the calculation and alleviate the "high dimensional curse", while keeping good numerical precision. A mathematical example will be provided to show the effectiveness of the proposed methods in this section. The polynomial based uncertainty analysis methods will be applied in the RTOs for continuum structures in Chapter 5, the numerical examples in Chapter 5 also demonstrate the efficiency and accuracy of the proposed method.

4.1.1 A hyperbolic Polynomial Chaos-Chebyshev Interval method (hPCCI)

Consider a performance function C with random uncertain variables $\mathbf{X}$ and interval uncertain variables $\mathbf{Y}$. If the random variables are not standard random variables, we should firstly transform them into standard normal variables ξ through a probability transformation [238 . For interval variables, they can also be transformed into standard interval random variables, and $\mathbf{Y}$ can be transformed into standard interval variables $\boldsymbol{\eta}$ through a linear transformation. For convenience, we suppose the uncertain variables to be standard normal variable

$\boldsymbol{\xi} \sim N(0,1)$ and standard interval variable $\boldsymbol{\eta} \in [-1,1]$. In this section, we will propose a hyperbolic PCCI method for random-interval hybrid uncertainty analysis.

By only considering the random uncertainties, the performance function *C* can be expanded as follows based on PC expansion:

$$C(\boldsymbol{\xi}, \boldsymbol{\eta}) = \sum_{\boldsymbol{\chi}_1 \in \mathbb{N}^n} h_{\boldsymbol{\chi}_1}(\boldsymbol{\eta}) H_{\boldsymbol{\chi}_1}(\boldsymbol{\xi}) \tag{4-1}$$

in which $\boldsymbol{\chi}_1$ is a multi-index that identifies the components of the multivariate polynomials. $h_{\boldsymbol{\chi}_1}(\boldsymbol{\eta})$ is the corresponding coefficient, and $H_{\boldsymbol{\chi}_1}(\boldsymbol{\xi})$ is the multivariate Hermite polynomial built from a set of univariate orthonormal polynomials $\mathcal{H}_{\chi_1^i}(\xi_i)$ that satisfy:

$$\left\langle \mathcal{H}_{\chi_1^{i_1}}(\xi_i), \mathcal{H}_{\chi_1^{i_2}}(\xi_i) \right\rangle = \int \mathcal{H}_{\chi_1^{i_1}}(\xi_i) \mathcal{H}_{\chi_1^{i_2}}(\xi_i) f(\xi_i) d\xi_i = \delta_{\chi_1^{i_1} \chi_1^{i_2}} \tag{4-2}$$

where $\delta_{i_1 i_2}$ is the Kronecker delta, i_1 and i_2 identify the input random variables. $f(\xi_i)$ is the marginal distribution of the standard Gaussian distribution. The multivariate polynomials $H_{\boldsymbol{\chi}_1}(\boldsymbol{\xi})$ are then assembled as the tensor product of their univariate counterparts:

$$H_{\boldsymbol{\chi}_1}(\boldsymbol{\xi}) = \prod_{i=1}^{n} \mathcal{H}_{\chi_1^i}(\xi_i), \text{ where } \chi_1^i = 0,1,\cdots,p \tag{4-3}$$

where *p* is the polynomial degree to retain only the multivariate polynomials of degree at most *p*. PC expansion in Eq. (4-1) can explicitly approximate the random response of a system with input random variables.

For an n dimensional Hermite polynomial with order p, $\boldsymbol{\chi}_1$ will include $(p+1)^n$ terms. The PC terms will be extremely large when n and p become larger. During the calculation of the corresponding PC coefficients, it is noted that the number of model evaluations (e.g. FEA calls) increases dramatically with the PC size, while the PC size increases exponentially with the number of input uncertain variables. In practice, the lower order PC expansions are more important for structural performances than the higher order ones according to the sparsity-of-effect principle [239 . Hence, we can keep the lower order terms by using the standard truncation scheme [184 to make the computation more efficient under a reasonable numerical accuracy. Also, the number of terms for the standard truncated PC is $\binom{n+p}{p}$, which still grows factorially with the dimension of uncertain variables. The rapid growth of the computation cost restrains the applicability of the PC expansion only to relatively lower dimensions problems.

To reduce the computational cost for both the full PC and the standard truncated PC, hyperbolic index sets [92,240 are used to slow down the growth of the PC expansion terms associated with the dimensionality. The hyperbolic truncation scheme which is defined as a parametric q-quasi-norm is employed here to truncate the polynomial chaos expansion:

$$\mathcal{A}_q^{n,p} = \left\{ \boldsymbol{\chi}_1 \in \mathbb{N}^n : \left\| \boldsymbol{\chi}_1 \right\|_q \le p \right\} \tag{4-4}$$

where

$$\left\| \boldsymbol{\chi}_1 \right\|_q = \left(\sum_{i=1}^{n} \left(\chi_1^i \right)^q \right)^{1/q}, 0 < q < 1 \tag{4-5}$$

For polynomial chaos with n=2 and p=4, Figure 4-1 (a)-(c) show the multi-index sets for full PC, truncated PC with q=1 and hyperbolic PC with q=0.75, respectively. As illustrated in Figure 4-1, hyperbolic truncation keeps the important lower order interaction terms and exclude the higher order interaction terms. In this chapter, q=0.75 will be used in the hyperbolic truncation scheme.

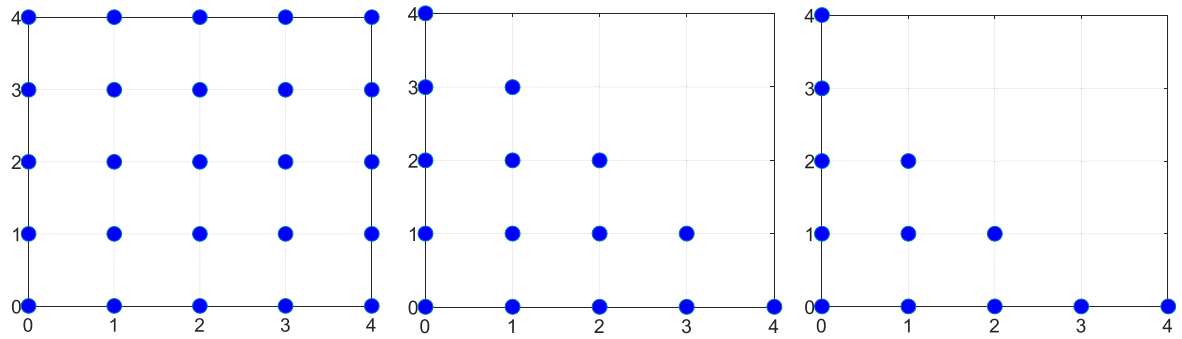

Figure 4-1 Multi-index set $\boldsymbol{\chi}_1$ in a two dimensional space

In order to calculate the coefficient $\mathbf{h}_{\boldsymbol{\chi}_1}$, the following minimization problem can be formulated:

$$\hat{\mathbf{h}}(\boldsymbol{\eta}) = \arg\min \mathrm{E}\left[C(\boldsymbol{\xi}, \boldsymbol{\eta}) - \mathbf{h}^{\mathrm{T}}(\boldsymbol{\eta}) \mathbf{H}(\boldsymbol{\xi}) \right] \tag{4-6}$$

where $\mathbf{h}(\boldsymbol{\eta})$ and $\mathbf{H}(\boldsymbol{\xi})$ are vectors including all the coefficients and the PC terms, respectively, and $\mathrm{E}[\cdot]$ is the expectation of a function. The collocation method is used to evaluate the coefficients, using the model output at a given experimental design $\boldsymbol{\alpha} = \left[\boldsymbol{\xi}^{(1)}, \boldsymbol{\xi}^{(2)}, \cdots, \boldsymbol{\xi}^{(l)} \right]$, then the ordinary least square solution of Eq. (4-6) can be obtained by:

$$\hat{\mathbf{h}}(\boldsymbol{\eta}) = \left(\mathbf{A}^{\mathrm{T}} \mathbf{A} \right)^{-1} \mathbf{A}^{\mathrm{T}} \mathbf{C}(\boldsymbol{\xi}, \boldsymbol{\eta}) \tag{4-7}$$

where $\mathbf{A}$ represents the sample matrix in which $A_{rs} = H_{\boldsymbol{\chi}_1^{(s)}}\left(\boldsymbol{\xi}^{(r)}\right)$, $\boldsymbol{\xi}^{(r)}$ is the collocation point of random variables selected from the zeros of the Hermite polynomials, and $\mathbf{C}(\boldsymbol{\xi},\boldsymbol{\eta})$ is the model output (structure compliance) vector at the collocation points. In order to ensure the numerical stability, the number of the sampling points must be higher than the number of coefficients and the design size is recommended to set to be twice the number of the coefficient for obtaining robust estimates [241 .

Taken the interval uncertainties into consideration, the left side of the Eq. (4-1) contains both the interval and the random uncertainties, while multivariate polynomials at the right side are only functions of the random variables, and the coefficients are functions with interval uncertainties. Taking the coefficient as an interval function and expanding it by using the Chebyshev inclusion function [136,137 , we can obtain:

$$h_{\boldsymbol{\chi}_1}(\boldsymbol{\eta}) = \sum_{\boldsymbol{\chi}_2 \in \mathbb{N}^m} c_{\boldsymbol{\chi}_1,\boldsymbol{\chi}_2} \Psi_{\boldsymbol{\chi}_2}(\boldsymbol{\eta}) \tag{4-8}$$

where $c_{\boldsymbol{\chi}_1,\boldsymbol{\chi}_2}$ is the Chebyshev coefficient and $\Psi_{\boldsymbol{\chi}_2}(\boldsymbol{\eta}) = \prod_{j=1}^{m} \varphi_{\chi_2^j}(\eta_j) = \prod_{j=1}^{m} \cos(\chi_2^j[\theta_j])$ is the multivariate Chebyshev polynomial built from the univariate Chebyshev polynomial $\varphi_{\chi_2^j}(\eta_j)$. $\left[\theta_j\right] = \arccos(\eta_j) = [0,\pi]$, $j = 1,2,\cdots,m$, and $\chi_2^j, j = 1,2,\cdots,m$ constitutes an index vector in the index set $\boldsymbol{\chi}_2$. From Eqs. (4-1) and (4-8), the performance function with hybrid uncertainties can be approximate by:

$$C(\boldsymbol{\xi},\boldsymbol{\eta}) = \sum_{\boldsymbol{\chi}_1 \in \mathbb{N}^n} \sum_{\boldsymbol{\chi}_2 \in \mathbb{N}^m} c_{\boldsymbol{\chi}_1,\boldsymbol{\chi}_2} \Psi_{\boldsymbol{\chi}_2}(\boldsymbol{\eta}) H_{\boldsymbol{\chi}_1}(\boldsymbol{\xi}) \tag{4-9}$$

The coefficient matrix $\mathbf{c}_{\chi_1,\chi_2}$ can be obtained by using the least squares method twice [157 :

$$\mathbf{c}_{\chi_1,\chi_2} = \left(\mathbf{B}^{\mathrm{T}}\mathbf{B}\right)^{-1}\mathbf{B}\mathbf{C}^{\mathrm{T}}\left(\boldsymbol{\xi},\boldsymbol{\eta}\right)\mathbf{A}\left(\mathbf{A}\mathbf{A}^{\mathrm{T}}\right)^{-1} \tag{4-10}$$

where $\mathbf{B}$ represents the sample matrix in which $B_{rs} = \varphi_{\chi_2^{(s)}}\left(\boldsymbol{\eta}^{(r)}\right)$, and $\boldsymbol{\eta}^{(r)}$ is the rth collocation point of interval variables selected from the zeros of the Chebyshev polynomials. The interval mean and interval variance of the performance function can be calculated by:

$$\mu\left(C\left(\boldsymbol{\xi},\boldsymbol{\eta}\right)\right) = h_{\mathbf{0}}\left(\boldsymbol{\eta}\right) = \sum_{\chi_2\in\mathbb{N}^m} c_{\mathbf{0},\chi_2}\Psi_{\chi_2}\left(\boldsymbol{\eta}\right) \tag{4-11}$$

$$\sigma^2\left(C\left(\boldsymbol{\xi},\boldsymbol{\eta}\right)\right) = \sum_{\chi_1\in\mathbb{N}^n,\chi_1\neq\mathbf{0}}\left(h_{\chi_1}\left(\boldsymbol{\eta}\right)\right)^2 = \sum_{\chi_1\in\mathbb{N}^n,\chi_1\neq\mathbf{0}}\left(\sum_{\chi_2\in\mathbb{N}^m} c_{\chi_1,\chi_2}\Psi_{\chi_2}\left(\boldsymbol{\eta}\right)\right)^2 \tag{4-12}$$

From the above, we can see that the mean and variance are functions with interval uncertainties. Based on the characteristics of the trigonometric functions, we know that $\Psi_{\mathbf{0}}\left(\boldsymbol{\eta}\right) = 0$ and $\Psi_{\chi_2}\left(\boldsymbol{\eta}\right) = \left[-1,1\right]$, so the bounds of the mean and standard variance can be easily approximated, as follows:

$$\begin{aligned}\mu\left(C\left(\boldsymbol{\xi},\boldsymbol{\eta}\right)\right) &= \left[\max\sum_{\chi_2\in\mathbb{N}^m} c_{\mathbf{0},\chi_2}\Psi_{\chi_2}\left(\boldsymbol{\eta}\right), \max\sum_{\chi_2\in\mathbb{N}^m} c_{\mathbf{0},\chi_2}\Psi_{\chi_2}\left(\boldsymbol{\eta}\right)\right] \\ &= \left[c_{\mathbf{0},\mathbf{0}} - \left(\sum_{\chi_2\in\mathbb{N}^m,\chi_2\neq\mathbf{0}}\left|c_{\mathbf{0},\chi_2}\right|\right),\ c_{\mathbf{0},\mathbf{0}} + \left(\sum_{\chi_2\in\mathbb{N}^m,\chi_2\neq\mathbf{0}}\left|c_{\mathbf{0},\chi_2}\right|\right)\right]\end{aligned} \tag{4-13}$$

$$\sigma\left(C(\boldsymbol{\xi},\boldsymbol{\eta})\right)=\left[\sqrt{\min\sum_{\boldsymbol{\chi}_1\in\mathbb{N}^n,\boldsymbol{\chi}_1\neq\mathbf{0}}\left(\sum_{\boldsymbol{\chi}_2\in\mathbb{N}^m}c_{\boldsymbol{\chi}_1,\boldsymbol{\chi}_2}\Psi_{\boldsymbol{\chi}_2}(\boldsymbol{\eta})\right)^2},\sqrt{\max\sum_{\boldsymbol{\chi}_1\in\mathbb{N}^n,\boldsymbol{\chi}_1\neq\mathbf{0}}\left(\sum_{\boldsymbol{\chi}_2\in\mathbb{N}^m}c_{\boldsymbol{\chi}_1,\boldsymbol{\chi}_2}\Psi_{\boldsymbol{\chi}_2}(\boldsymbol{\eta})\right)^2}\right]$$
$$=\left[\sqrt{\sum_{\boldsymbol{\chi}_1\in\mathbb{N}^n,\boldsymbol{\chi}_1\neq\mathbf{0}}\sum_{\boldsymbol{\chi}_2\in\mathbb{N}^m}c_{\boldsymbol{\chi}_1,\boldsymbol{\chi}_2}^2-2\left|\sum_{\boldsymbol{\chi}_1\in\mathbb{N}^n,\boldsymbol{\chi}_1\neq\mathbf{0}}\sum_{\boldsymbol{\chi}_2\in\mathbb{N}^m}c_{\boldsymbol{\chi}_1,\boldsymbol{\chi}_2^{(k_1)}}c_{\boldsymbol{\chi}_1,\boldsymbol{\chi}_2^{(k_2)}}\right|},\sqrt{\sum_{\boldsymbol{\chi}_1\in\mathbb{N}^n,\boldsymbol{\chi}_1\neq\mathbf{0}}\sum_{\boldsymbol{\chi}_2\in\mathbb{N}^m}c_{\boldsymbol{\chi}_1,\boldsymbol{\chi}_2}^2+2\left|\sum_{\boldsymbol{\chi}_1\in\mathbb{N}^n,\boldsymbol{\chi}_1\neq\mathbf{0}}\sum_{\boldsymbol{\chi}_2\in\mathbb{N}^m}c_{\boldsymbol{\chi}_1,\boldsymbol{\chi}_2^{(k_1)}}c_{\boldsymbol{\chi}_1,\boldsymbol{\chi}_2^{(k_2)}}\right|}\right] \tag{4-14}$$

where $\boldsymbol{\chi}_2^{(k_1)}$ and $\boldsymbol{\chi}_2^{(k_1)}$ are two realizations of the index $\boldsymbol{\chi}_2$.

4.1.2 An improved Polynomial Chaos-Chebyshev Interval method (iPCCI)

4.1.2.1 Sparse Grid Numerical Integration

The sparse grid method is firstly proposed by Smolyak [242 and has been applied in numerical integration, uncertainty analysis, reliability analysis, and design optimization problems [243,244,245 . The sparse grid method is to build the multidimensional integration points from the one dimensional integration points of one variable of a given order, and the choice of the integration points is based on the distribution of the variable. For random variables, Hermite integration points are used to be the one dimensional integration points, as shown in Table 4-1. D_1^r and Q_1^r are set to be the node and the weight of the *r*th order, and $\zeta_{1,d}^r$ is defined as the *d*th element in D_1^k.

Suppose the precision level of the integration is *k*, for an *n* dimensional problem, the multidimensional nodes $D_n^{(k)}$ from the sparse grid method is as follows:

$$D_n^{(k)}=\bigcup_{k+1\le|r|\le k+n}D_1^{r_1}\otimes D_1^{r_2}\cdots\otimes D_1^{r_n} \tag{4-15}$$

where $|r| = r_1 + r_2 + ... + r_n$, $r_j (j = 1, 2, \cdots, n)$ is the order of the one dimensional Gauss-Hermite integration, and $r_j \geq 1$. $\otimes$ represents the tensor product. In order to show the multidimensional integration points in detail, we take the case of *k*=2, and *n*=2 as an example, as shown in Table 4-2. For better illustration, Figure 4-2 also gives the construction of sparse grid based on Gaussian quadrature nodes.

Table 4-1 Nodes and weights of the Gauss-Hermite integration of one dimensional

Order	Nodes	Weights
1	$D_1^1 = 0$	$Q_1^1 = 1$
2	$D_1^2 = \{-1, 1\}$	$Q_1^2 = \{0.5, 0.5\}$
3	$D_1^3 = \{-1.7321, 0, 1.7321\}$	$Q_1^3 = \{0.1667, 0.6667, 0.1667\}$
4	$D_1^4 = \{-2.3344, -0.7420,$ $0.7420, 2.3344\}$	$Q_1^4 = \{-0.0459, 0.4541,$ $0.4541, 0.0459\}$

Table 4-2 Multidimensional integration points

$\|r\|$	r_1	r_2	$D_1^{r_1} \otimes D_1^{r_2}$	D_2^2
3	1	2	$\{(0,-1),(0,1)\}$	$\{(0,-1),(0,1),(-1,0),(1,0),$ $(0,-1.7321),(0,0),(0,1.7321),$ $(-1,-1),(-1,1),(1,-1),(1,1),$ $(-1.7321,0),(1.7321,0)\}$
	2	1	$\{(-1,0),(1,0)\}$	
4	1	3	$\{(0,-1.7321),(0,0),(0,1.7321)\}$	
	2	2	$\{(-1,-1),(-1,1),(1,-1),(1,1)\}$	
	3	1	$\{(-1.7321,0),(0,0),(1.7321,0)\}$	

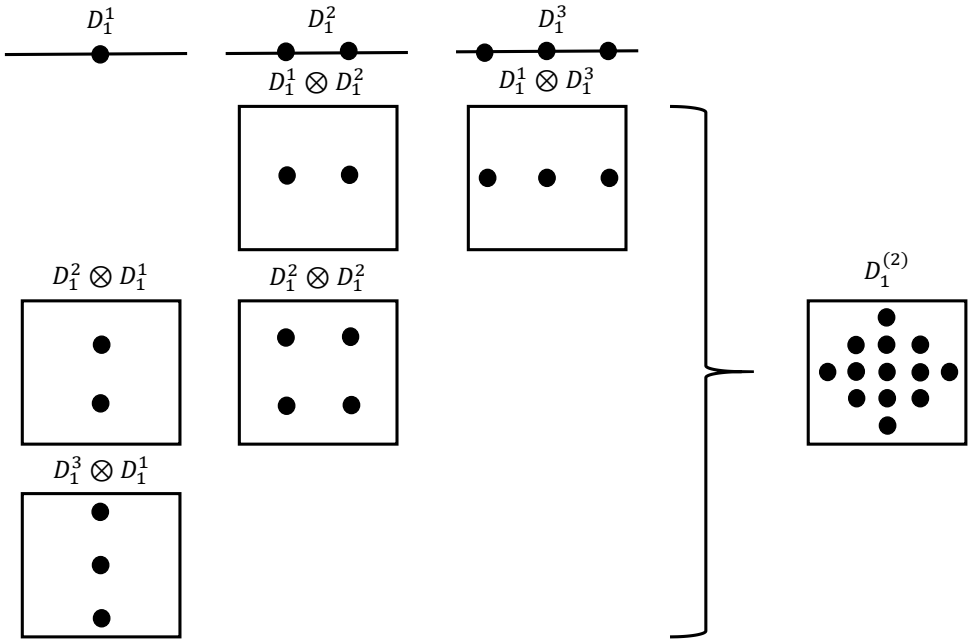

Figure 4-2 Construction of the sparse grid

Similar to the process as shown in Table 4-2, for an n dimensional with the kth precision, the integration points can be built. For an integration point, the weight q_l corresponding to the lth collocation point $\zeta_l = \left[\zeta_{1,d_1}^{r_1}, \cdots, \zeta_{1,d_n}^{r_n}\right]^{\mathrm{T}} \in D_n^k$ is given as [246 :

$$q_l = (-1)^{k+n-|r|}\binom{n-1}{k+n-|r|}\left(q_{1,d_1}^{r_1} q_{1,d_2}^{r_2} \cdots q_{1,d_n}^{r_n}\right) \tag{4-16}$$

where $q_{1,d_n}^{r_n}$ is the weight for the one dimensional point $\zeta_{1,d_n}^{r_n}\left(\zeta_{1,d_n}^{r_n} \in D_1^{r_n}\right)$. An integration problem with a variable ζ can be calculated by the Gauss interpolation:

$$\int g(\zeta) f(\zeta) d\zeta = \sum_{l=1}^{NI} q_l g(\zeta_l) \tag{4-17}$$

in which NI is the number of the integration points. For an n dimensional problem, when k=1,2, the interpolation points of the spares grid is [244 :

$$\begin{aligned} NI &= 2n+1, && k=1 \\ NI &= 2n^2+3n+1, && k=2 \end{aligned} \tag{4-18}$$

From Eq. (4-18) we know that, in a low-dimension problem, with the same level *k*, the sparse grid approach may need more collocation points than the full grid approach [243 because sparse grids are better suited for high-dimensional problems. However, when *d* increases, the number of collocation points of the sparse grid method is much smaller than that of the full grid. For example, if $n=6, k=2$, the number of the interpolation points is 85, but the number will be 729 for the full tensor product even if we only choose three integration nodes for one variable. SGNI will be introduced into the procedure in PCCI method to improve the efficiently in calculating the polynomial coefficients.

4.1.2.2 Hybrid uncertainty analysis by the iPCCI method

Polynomial Chaos expansion for random variables

For convenience of description, $\xi_i (i=1,2,\cdots,n)$ is considered to be standard normal variable belong to *N*(0,1). The fundamental idea of PC expansion is to approximate functions with random uncertainties by sums of orthogonal polynomials of random independent variables, then a function $F(\boldsymbol{\xi})$ which is viewed as a function of the random uncertainties can be expanded by the orthogonal polynomial chaos expansion with order *p*, as follows:

$$F(\boldsymbol{\xi}) = \sum_{\boldsymbol{\chi}_1 \in \mathbb{N}^n} h_{\boldsymbol{\chi}_1} H_{\boldsymbol{\chi}_1}(\boldsymbol{\xi}) \tag{4-19}$$

in which $\boldsymbol{\chi}_1$ is a multi-index that identifies the components of the multivariate polynomials, and $\boldsymbol{\chi}_1$ is obtained by the basic truncation scheme:

$$\mathcal{A}^{n,p}=\left\{\boldsymbol{\chi}_1\in\mathbb{N}^n:\sum_{k=1}^{n}\chi_1^k\le p\right\} \tag{4-20}$$

$h_{\boldsymbol{\chi}_1}$ is the corresponding coefficient and $H_{\boldsymbol{\chi}_1}(\boldsymbol{\xi})=\prod_{k=1}^{n}\mathcal{H}_{\chi_1^k}(\xi_k)$, $\chi_1^k=0,1,\cdots,p$ is the multivariate Hermite polynomial. $\mathcal{H}_{\chi_1^k}(\xi_k)$ is the univariate orthonormal polynomial, defined as:

$$\left\langle\mathcal{H}_{\chi_1^{k1}}(\xi_k),\mathcal{H}_{\chi_1^{k2}}(\xi_k)\right\rangle=\int\mathcal{H}_{\chi_1^{k1}}(\xi_k)\mathcal{H}_{\chi_1^{k2}}(\xi_k)f(\xi)d\xi=\delta_{\chi_1^{k1}\chi_1^{k2}} \tag{4-21}$$

where δ_{ij} is the Kronecker delta. $f(\xi)$ is the probability distribution function of the standard normal random variable. With the orthogonality, the polynomial coefficients in Eq. (4-19) can be obtained via the following equation:

$$h_{\boldsymbol{\chi}_1}=\int F(\boldsymbol{\xi})H_{\boldsymbol{\chi}_1}(\boldsymbol{\xi})f(\boldsymbol{\xi})d\boldsymbol{\xi} \tag{4-22}$$

This multidimensional integration problem can be solved by Gaussian-Hermite quadrature. Standard multivariate Gaussian quadrature is generally achieved by a tensor-product of roots of the corresponding polynomial basis functions. For a polynomial with degree *p*, (*p*+1) integration points are needed in each dimension. Therefore, the number of integration nodes increases rapidly with the number of input variables. Smolyak sparse quadrature is an alternative approach to obtain the original tensor-product multi-dimensional quadrature [243 , similar to Eq. (4-17), the integration problem in Eq. (4-22) can be calculated as follows:

$$\int F(\boldsymbol{\xi})H_{\boldsymbol{\chi}_1}(\boldsymbol{\xi})f(\boldsymbol{\xi})d\boldsymbol{\xi}=\sum_{l=1}^{NI}q_lF(\boldsymbol{\xi}_l)H_{\boldsymbol{\chi}_1}(\boldsymbol{\xi}_l) \tag{4-23}$$

where q_l is the weight corresponding to the *l*th collocation point $\boldsymbol{\xi}_l$ of the uncertain variables. The weights are derived from a combination of lower order standard quadrature terms as in Eq (4-16). After getting the coefficients h_{χ_1}, the statistic characteristics of *F* can be obtained by using the orthogonality of Hermite polynomials. The mean of *F* is given by the first coefficient, and the variance of *F* can be expressed by the sum of the square of other coefficients, as follows:

$$\mu\left(F\left(\boldsymbol{\xi}\right)\right)=h_{\mathbf{0}},\ \sigma^2\left(F\left(\boldsymbol{\xi}\right)\right)=\sum_{\boldsymbol{\chi}_1\in\mathbb{N}^n,\boldsymbol{\chi}_1\neq\mathbf{0}}h_{\boldsymbol{\chi}_1}^2 \tag{4-24}$$

Chebyshev inclusion function for interval variables

A function G is considered as an interval function with standard interval variables $\boldsymbol{\eta}$. Since the interval variables have lower bounds and upper bounds, the interval function $G\left(\boldsymbol{\eta}\right)$ also belongs to a bounded interval. Then can be approximated by the following *q*th order truncated Chebyshev series:

$$G\left(\boldsymbol{\eta}\right)=\sum_{\boldsymbol{\chi}_2\in\mathbb{N}^m}\left(1/2\right)^l\hat{c}_{\boldsymbol{\chi}_2}\Psi_{\boldsymbol{\chi}_2}\left(\boldsymbol{\eta}\right)=\sum_{\boldsymbol{\chi}_2\in\mathbb{N}^m}c_{\boldsymbol{\chi}_2}\Psi_{\boldsymbol{\chi}_2}\left(\boldsymbol{\eta}\right) \tag{4-25}$$

where $\hat{c}_{\boldsymbol{\chi}_2}$ is the corresponding coefficient while *l* denotes the total number of the zero(s) to be occurred in the subscripts set, and $\Psi_{\boldsymbol{\chi}_2}\left(\boldsymbol{\eta}\right)=\prod_{k=1}^{m}\cos(\chi_2^k[\theta_k])$ is the multivariate Chebyshev polynomial which is built from the univariate Chebyshev polynomial. $\left[\theta_k\right]=\arccos\left(\eta_k\right)=\left[0,\pi\right],k=1,2,\cdots,m$, and $\chi_2^k=0,1,\cdots,q$ constitutes an index vector in the index set $\boldsymbol{\chi}_2$. For convenience, we denote $\left(1/2\right)^l\hat{c}_{\boldsymbol{\chi}_2}$ to be $c_{\boldsymbol{\chi}_2}$ since $\left(1/2\right)^l$ is a constant

value. The coefficients $\hat{c}_{\chi_2}$ and can be calculated by the Gaussian-Chebyshev numerical quadrature as follows:

$$\begin{aligned}\hat{c}_{\chi_2} &= \left(2/\pi\right)^m \int_0^{\pi} G\left(\cos\boldsymbol{\theta}\right)\prod_{k=1}^{m}\cos(\chi_2^k[\theta_k])d\boldsymbol{\theta} \\ &\approx \left(2/\left(q+1\right)\right)^m \sum_{l=1}^{NI}\left(G\left(\cos\boldsymbol{\theta}_l\right)\prod_{k=1}^{m}\cos(\chi_2^k[\theta_{l_k}])\right)\end{aligned} \tag{4-26}$$

The interpolation points $\boldsymbol{\theta}_l$ are the Smolyak tensor product of each dimensional interpolation points, and the interpolation points of each dimension are defined as the zeros of Chebyshev polynomial with order $q+1$:

$$\theta_{l_k} = \frac{2l_k-1}{q+1}\cdot\frac{\pi}{2}, l_k = 1,2,\cdots,q+1 \tag{4-27}$$

Using Eq. (4-26), we will obtain the coefficients in Eq. (4-25). For a function $G\left(\boldsymbol{\eta}\right)$ which is a very complicated model or even black-box model without explicit expressions, we can evaluate the bounds of this function by using the function values at some interpolation points. Based on the characteristics of the trigonometric functions, we can find that $\prod_{k=1}^{m}\cos(\chi_2^k[\theta_k]) = \left[-1,1\right]$, so the bounds of the interval function $G\left(\boldsymbol{\eta}\right)$ can be calculated as:

$$G\left(\boldsymbol{\eta}\right) = c_{\mathbf{0}} + \left(\sum_{\chi_2\in\mathbb{N}^m,\chi_2\neq\mathbf{0}}\left|c_{\chi_2}\right|\right)\left[-1,1\right] = \left[c_{\mathbf{0}} - \sum_{\chi_2\in\mathbb{N}^m,\chi_2\neq\mathbf{0}}\left|c_{\chi_2}\right|, c_{\mathbf{0}} + \sum_{\chi_2\in\mathbb{N}^m,\chi_2\neq\mathbf{0}}\left|c_{\chi_2}\right|\right] \tag{4-28}$$

iPCCI for hybrid variables

With random uncertain variables $\boldsymbol{\xi}$ and interval uncertain variables $\boldsymbol{\eta}$, the performance function $C(\boldsymbol{\xi},\boldsymbol{\eta})$ will have both random and interval properties. If the uncertain variables are not standard variables in a problem, we should firstly transform them into standard normal variables and standard interval variables. For convenience of description, $\xi_i(i=1,2,\cdots,n)$ is considered to be standard normal variable belong to $N(0,1)$ and $\eta_j(j=1,2,\cdots,m)$ is considered to be standard interval variable belong to [-1,1 .

Firstly, expanding $C(\boldsymbol{\xi},\boldsymbol{\eta})$ with respect to random variable $\boldsymbol{\xi}$ by using the PC expansion, we can obtain:

$$C(\boldsymbol{\xi},\boldsymbol{\eta})=\sum_{\boldsymbol{\chi}_1\in\mathbb{N}^n} h_{\boldsymbol{\chi}_1}(\boldsymbol{\eta})H_{\boldsymbol{\chi}_1}(\boldsymbol{\xi}) \tag{4-29}$$

where the $h_{\boldsymbol{\chi}_1}$ denotes the coefficients of Hermit polynomials. The left side of Eq. (4-29) contains both the interval variable and the random variable, while $H_{\boldsymbol{\chi}_1}(\boldsymbol{\xi})$ at the right side is only the function of the random variable $\boldsymbol{\xi}$, and the coefficients $h_{\boldsymbol{\chi}_1}$ is a function with interval uncertainties. Regard the coefficients as an interval function, expanding it using the Chebyshev inclusion function, we can obtain:

$$h_{\boldsymbol{\chi}_1}(\boldsymbol{\eta})=\sum_{\boldsymbol{\chi}_2\in\mathbb{N}^m} c_{\boldsymbol{\chi}_1,\boldsymbol{\chi}_2}\Psi_{\boldsymbol{\chi}_2}(\boldsymbol{\eta}) \tag{4-30}$$

From Eqs. (4-29) and (4-30), the original function with hybrid uncertainties can be approximate by:

$$C(\boldsymbol{\xi},\boldsymbol{\eta}) = \sum_{\boldsymbol{\chi}_1 \in \mathbb{N}^n} \sum_{\boldsymbol{\chi}_2 \in \mathbb{N}^m} c_{\boldsymbol{\chi}_1,\boldsymbol{\chi}_2} \Psi_{\boldsymbol{\chi}_2}(\boldsymbol{\eta}) H_{\boldsymbol{\chi}_1}(\boldsymbol{\xi}) \tag{4-31}$$

The coefficients can be obtained by using the integrals in Eqs. (4-17) and (4-26). The interval mean and interval variance can then be calculated by:

$$\mu\left(C(\boldsymbol{\xi},\boldsymbol{\eta})\right) = h_{\mathbf{0}}(\boldsymbol{\eta}) = \sum_{\boldsymbol{\chi}_2 \in \mathbb{N}^m} c_{\mathbf{0},\boldsymbol{\chi}_2} \Psi_{\boldsymbol{\chi}_2}(\boldsymbol{\eta}) \tag{4-32}$$

$$\sigma^2\left(C(\boldsymbol{\xi},\boldsymbol{\eta})\right) = \sum_{\boldsymbol{\chi}_1 \in \mathbb{N}^n, \boldsymbol{\chi}_1 \neq \mathbf{0}} \left(h_{\boldsymbol{\chi}_1}(\boldsymbol{\eta})\right)^2 = \sum_{\boldsymbol{\chi}_1 \in \mathbb{N}^n, \boldsymbol{\chi}_1 \neq \mathbf{0}} \left(\sum_{\boldsymbol{\chi}_2 \in \mathbb{N}^m} c_{\boldsymbol{\chi}_1,\boldsymbol{\chi}_2} \Psi_{\boldsymbol{\chi}_2}(\boldsymbol{\eta}) \right)^2 \tag{4-33}$$

From the above we can see that the mean and variance are functions with interval uncertainties. Using the interval arithmetic and considering the condition $\Psi_{\mathbf{0}}(\boldsymbol{\eta}) = 0$ and $\Psi_{\boldsymbol{\chi}_2}(\boldsymbol{\eta}) = [-1,1]$, the bounds of the interval functions can be estimated by:

$$\begin{aligned} \mu\left(C(\boldsymbol{\xi},\boldsymbol{\eta})\right) &= \left[\min \sum_{\boldsymbol{\chi}_2 \in \mathbb{N}^m} c_{\mathbf{0},\boldsymbol{\chi}_2} \Psi_{\boldsymbol{\chi}_2}(\boldsymbol{\eta}), \max \sum_{\boldsymbol{\chi}_2 \in \mathbb{N}^m} c_{\mathbf{0},\boldsymbol{\chi}_2} \Psi_{\boldsymbol{\chi}_2}(\boldsymbol{\eta}) \right] \\ &= \left[c_{\mathbf{0},\mathbf{0}} + \left(\sum_{\boldsymbol{\chi}_2 \in \mathbb{N}^m, \boldsymbol{\chi}_2 \neq \mathbf{0}} \left| c_{\mathbf{0},\boldsymbol{\chi}_2} \right| \right), c_{\mathbf{0},\mathbf{0}} + \left(\sum_{\boldsymbol{\chi}_2 \in \mathbb{N}^m, \boldsymbol{\chi}_2 \neq \mathbf{0}} \left| c_{\mathbf{0},\boldsymbol{\chi}_2} \right| \right) \right] \end{aligned} \tag{4-34}$$

$$\begin{aligned} \sigma\left(C(\boldsymbol{\xi},\boldsymbol{\eta})\right) &= \left[\sqrt{\min \sum_{\boldsymbol{\chi}_1 \in \mathbb{N}^n, \boldsymbol{\chi}_1 \neq \mathbf{0}} \left(\sum_{\boldsymbol{\chi}_2 \in \mathbb{N}^m} c_{\boldsymbol{\chi}_1,\boldsymbol{\chi}_2} \Psi_{\boldsymbol{\chi}_2}(\boldsymbol{\eta}) \right)^2}, \sqrt{\max \sum_{\boldsymbol{\chi}_1 \in \mathbb{N}^n, \boldsymbol{\chi}_1 \neq \mathbf{0}} \left(\sum_{\boldsymbol{\chi}_2 \in \mathbb{N}^m} c_{\boldsymbol{\chi}_1,\boldsymbol{\chi}_2} \Psi_{\boldsymbol{\chi}_2}(\boldsymbol{\eta}) \right)^2} \right] \\ &= \left[\sqrt{\sum_{\boldsymbol{\chi}_1 \in \mathbb{N}^n, \boldsymbol{\chi}_1 \neq \mathbf{0}} \sum_{\boldsymbol{\chi}_2 \in \mathbb{N}^m} c_{\boldsymbol{\chi}_1,\boldsymbol{\chi}_2}^2 - 2 \left| \sum_{\boldsymbol{\chi}_1 \in \mathbb{N}^n, \boldsymbol{\chi}_1 \neq \mathbf{0}} \sum_{\boldsymbol{\chi}_2 \in \mathbb{N}^m} c_{\boldsymbol{\chi}_1,\boldsymbol{\chi}_2^{(k_1)}} c_{\boldsymbol{\chi}_1,\boldsymbol{\chi}_2^{(k_2)}} \right|}, \sqrt{\sum_{\boldsymbol{\chi}_1 \in \mathbb{N}^n, \boldsymbol{\chi}_1 \neq \mathbf{0}} \sum_{\boldsymbol{\chi}_2 \in \mathbb{N}^m} c_{\boldsymbol{\chi}_1,\boldsymbol{\chi}_2}^2 + 2 \left| \sum_{\boldsymbol{\chi}_1 \in \mathbb{N}^n, \boldsymbol{\chi}_1 \neq \mathbf{0}} \sum_{\boldsymbol{\chi}_2 \in \mathbb{N}^m} c_{\boldsymbol{\chi}_1,\boldsymbol{\chi}_2^{(k_1)}} c_{\boldsymbol{\chi}_1,\boldsymbol{\chi}_2^{(k_2)}} \right|} \right] \end{aligned} \tag{4-35}$$

where $\boldsymbol{\chi}_2^i$ and $\boldsymbol{\chi}_2^j$ are two realizations of the index $\boldsymbol{\chi}_2$.

4.1.3 Numerical example

A Numerical example is considered in this section to show the efficiency of the proposed methods. A performance function C(**X**,**Y**) with random variables **X** and interval variables **Y** is given as follows:

$$\begin{aligned} C(\mathbf{X},\mathbf{Y}) &= X_1+X_2+X_3+X_4+X_1^2Y_1^2+X_2^2Y_2^2+X_3^2Y_3^2+X_4^2Y_4^2 \\ &+\left(\sin(X_1)\right)^2\left(\cos(X_2)\right)^2+\left(\sin(X_2)\right)^2\left(\cos(X_3)\right)^2+\left(\sin(X_3)\right)^2\left(\cos(X_4)\right)^2 \end{aligned} \tag{4-36}$$

There are four random variables X_1, X_2, X_3, X_4 and four interval variables Y_1, Y_2, Y_3, Y_4 in the concerned uncertain performance function. The distribution types and parameters of the variables are provided in Table 4-3. For random variables, parameter 1 and 2 represent the mean and standard variance respectively, and for interval variables, parameter 1 and 2 denote the lower and upper bounds respectively.

Table 4-3 Distribution types and parameter of variables

Uncertain variables	Parameter1	Paramete2	Distribution type
X_1	1	0.15	Normal
X_2	1	0.15	Normal
X_3	1	0.15	Normal
X_4	1	0.15	Normal
Y_1	-1	1	Interval
Y_2	-1	1	Interval
Y_3	-1	1	Interval
Y_4	-1	1	Interval

With random and interval uncertain variables, the performance function has both random and interval properties. With the distributions of the uncertain variables, we can obtain the bounds of the mean and standard variance of the performance function. The detailed results are given in Table 4-4, including the interval means, interval standard variances, and the function calls. The results from the original PCCI, the proposed hPCCI and iPCCI are given for comparison. For verification purpose, the results from 10^{10} MCS are used as the reference results.

Overall, the results from the methods based on the orthogonal polynomials are close to those from the MCS. That is to say, the proposed methods have good numerical accuracy. The number of function calls is the function evaluation for the calculation of the polynomial coefficients. The collocation points or the integration points of uncertain variables are selected from the zeros of the higher dimensional orthogonal polynomials. In the original PCCI, full tensor points are used to evaluate the coefficients. For the second order polynomials, the full tensor points number is 3^4=81 for four uncertain variables, so the total function calls number for PCCI is 81^2. The function calls in hPCCI and iPCCI are both smaller than the original PCCI, while still keep a required precision.

In hPCCI, the important lower PC terms are kept while the higher order PC terms are ignored to eliminate the rapid increasing of the expansion terms. This will reduce the computational calculation but on the other hand bring about some errors, especially for problems with relatively important higher order products. For example, the lower bounds of the standard variance from hPCCI and iPCCI are 0.2341 and 0.2411, respectively. The iPCCI result is close to the MCS reference result 0.2441. In iPCCI, the SNGI is employed to obtain the polynomial coefficients. For high-dimensional problems, the sparse grid points will be much

less than the full tensor points. This method may be suitable for more different problems but the computational cost is higher than the hPCCI.

Table 4-4 Results of the performance function with hybrid uncertainties

Method	Mean	Standard variance	Function calls
PCCI	[4.6315,8.7215	[0.2472,0.8349	81^2
hPCCI	[4.6469,8.7369	[0.2341,0.8215	18^2
iPCCI	[4.6316,8.7216	[0.2411,0.8273	45^2
MCS	[4.6337,8.5115	[0.2441,0.7997	10^{10}

4.2 Hybrid uncertainty analysis method based on dimension reduction method

In this section, two hybrid uncertainty analysis methods namely the hybrid univariate dimension reduction method (HUDR) and hybrid dimension reduction method (HDR) are proposed based on the dimension reduction methods. A mathematical example will be provided to validate the proposed methods in this section. The dimension reduction based uncertainty analysis methods will be applied in the RTO for cellular composites in Chapter 6, the numerical examples in Chapter 6 also demonstrate the efficiency and accuracy of the proposed method.

4.2.1 A Hybrid univariate dimension reduction method (HUDR)

A HUDR method is proposed for efficient structural analysis of hybrid uncertainties. For a performance function $C = C(\mathbf{X},\mathbf{Y})$. with *n* probabilistic variables and *m* interval variables, the *k*th origin moment $E(C^k)$ can be expressed as:

$$\begin{aligned} E(C^k) &= E\left(\left[C\left(\mathbf{X},\mathbf{Y}\right)\right]^k\right) = \int_{-\infty}^{\infty}\int_{-\infty}^{\infty}...\int_{-\infty}^{\infty} C^k\left(\mathbf{X},\mathbf{Y}\right) f\left(X_1,X_2,...,X_n\right) dX_1 dX_2 ... dX_n \\ &= \int_{-\infty}^{\infty}\int_{-\infty}^{\infty}...\int_{-\infty}^{\infty} C^k\left(\mathbf{X},\mathbf{Y}\right) f\left(X_1\right) f\left(X_2\right) ... f\left(X_n\right) dX_1 dX_2 ... dX_n \end{aligned} \tag{4-37}$$

where $f\left(X_1,X_2,...,X_n\right)$ is the joint probability distribution function of the random uncertain variables.

Firstly, we assume that interval variables are fixed, so the above equation becomes a multidimensional integral problem with probabilistic uncertainties. By the univariate dimension reduction method [86 , the multidimensional problem will be transformed into a series of one-dimensional problems. As a result, the multidimensional Gauss integral is changed to a one-dimensional Gauss integral. By introducing the univariate dimension reduction technique, the performance function can be approximated as follows:

$$C\left(\mathbf{X},\mathbf{Y}\right) \cong \sum_{j=1}^{n} \hat{C}_j\left(\mathbf{X},\mathbf{Y}\right) - \left(n-1\right) C\left(u_1,u_2,\cdots,u_n\right) \tag{4-38}$$

where $\hat{C}_j\left(\mathbf{X},\mathbf{Y}\right) = C\left(u_1,\cdots,u_{j-1},X_j,u_{j+1},\cdots,u_n\right)$, u_j is the mean value of X_j. Then the kth origin moment of the output performance is given by:

$$E(C^k) = E\left(\left[\sum_{j=1}^{n} \hat{C}_j\left(\mathbf{X},\mathbf{Y}\right) - \left(n-1\right) C\left(u_1,u_2,\cdots,u_n\right)\right]^k\right) \tag{4-39}$$

Based on the binomial theorem, we can obtain:

$$E(C^k)=\sum_{i=0}^{k}\binom{k}{i}E\left(\sum_{i=1}^{n}\hat{C}_j(\mathbf{X},\mathbf{Y})\right)^i\left[-(n-1)C(u_1,u_2,\cdots,u_n)\right]^{k-i} \tag{4-40}$$

in which $\binom{k}{i}=\dfrac{k!}{i!(k-i)!}$ is the binomial expansion coefficient. Define:

$$S_j^i=E\left[\left\{\sum_{i=1}^{j}\hat{C}_j(\mathbf{X},\mathbf{Y})\right\}^i\right] \tag{4-41}$$

in which $j=1,\cdots,n$, $i=1,\cdots,k$. S_j^i can be calculated by the following recursion formula:

$$\begin{aligned}
&S_1^i=E\left[\left(\hat{C}_1(\mathbf{X},\mathbf{Y})\right)^i\right]; && i=1,\cdots,k\\
&S_2^i=\sum_{l=0}^{i}\binom{i}{l}S_1^lE\left[\left(\hat{C}_2(\mathbf{X},\mathbf{Y})\right)^{i-l}\right]; && i=1,\cdots,k\\
&\vdots\\
&S_j^i=\sum_{l=0}^{i}\binom{i}{l}S_{j-1}^lE\left[\left(\hat{C}_j(\mathbf{X},\mathbf{Y})\right)^{i-l}\right]; && i=1,\cdots,k\\
&\vdots\\
&S_n^i=\sum_{l=0}^{i}\binom{i}{l}S_{n-1}^lE\left[\left(\hat{C}_n(\mathbf{X},\mathbf{Y})\right)^{i-l}\right]; && i=1,\cdots,k
\end{aligned} \tag{4-42}$$

Then

$$E(C^k(\mathbf{Y}))=\sum_{i=0}^{k}\binom{k}{i}S_n^i\left[-(n-1)C(u_1,u_2,\cdots,u_n)\right]^{k-i} \tag{4-43}$$

From the above, we can see that the origin moments of the system can be calculated from the origin moments of subsystems with a single variable. For random variables with normal distributions, the first and second moments of the univariate function $\hat{C}_j(\mathbf{X},\mathbf{Y})$ are obtained

by using Gauss-Hermite numerical integral. For random variables with other distributions, we can firstly transform the variables into normal distributions through a probability transformation [238 and then calculate the first and second moments by using Gauss-Hermite numerical integral. For simplicity but without losing any generality, we assume the random variables under normal distributions.

After obtaining the origin moments in (4-43), the mean and the standard deviation of the performance function *C* can be given as:

$$\begin{cases} \mu(C) = E(C(\mathbf{Y})) \\ \sigma(C) = \left(E(C^2(\mathbf{Y})) - E^2(C(\mathbf{Y}))\right)^{1/2} \end{cases} \tag{4-44}$$

If we take interval variables into consideration, the $\mu(C)$ and $\sigma(C)$ are intervals rather than single values:

$$\begin{cases} \mu(C) = \left[\min\limits_{\mathbf{Y}} \mu(C(\mathbf{Y})), \max\limits_{\mathbf{Y}} \mu(C(\mathbf{Y})) \right] \\ \sigma(C) = \left[\min\limits_{\mathbf{Y}} \sigma(C(\mathbf{Y})), \max\limits_{\mathbf{Y}} \sigma(C(\mathbf{Y})) \right] \end{cases} \tag{4-45}$$

Similarly, by the dimension reduction scheme [247 , the interval functions $\mu(C)$ and $\sigma(C)$ can be approximated as follows:

$$\begin{aligned} \mu(C(Y_1, Y_2, \cdots, Y_m)) \cong\ & \mu(C(Y_1, Y_2^C, \cdots, Y_m^C)) + \mu(C(Y_1^C, Y_2, \cdots, Y_m^C)) + \cdots \\ & + \mu(C(Y_1^C, Y_2^C, \cdots, Y_m)) - (m-1) \cdot \mu(C(Y_1^C, Y_2^C, \cdots, Y_m^C)) \end{aligned} \tag{4-46}$$

$$\begin{aligned} \sigma(C(Y_1, Y_2, \cdots, Y_m)) \cong\ & \sigma(C(Y_1, Y_2^C, \cdots, Y_m^C)) + \sigma(C(Y_1^C, Y_2, \cdots, Y_m^C)) + \cdots \\ & + \sigma(C(Y_1^C, Y_2^C, \cdots, Y_m)) - (m-1) \cdot \sigma(C(Y_1^C, Y_2^C, \cdots, Y_m^C)) \end{aligned} \tag{4-47}$$

From Eqs. (4-46) and (4-47) we can see that the interval functions are approximated by a series of subfunctions with one interval variable Y_i. Assume that $d_i(Y_i)$ is a function with an interval variable Y_i, using the first order Taylor series:

$$d_i(Y_i) \cong d_i(Y_i^C) + \nabla d_i \cdot (Y_i - Y_i^C) \tag{4-48}$$

where ∇d_i represents the sensitivity of d_i with respect to interval variable Y_i. In order to obtain the maximum value of d_i, we can get the corresponding interval value from the sign of the sensitivity of d_i: if $\nabla d_i > 0$, $Y_i = Y_i^R$; if $\nabla d_i < 0$,$Y_i = Y_i^L$. At last, the bounds of $\mu(C)$ and $\sigma(C)$ can be obtained.

If we assume there are *n* random variables and *m* interval variables, by using the hybrid univariate dimension reduction method, only (3*n*+1)×(2*m*+1) function calls are needed in the approximation of the performance function. Hence, the proposed uncertainty analysis method (HUDR) shows very good computational efficiency in the hybrid uncertainty analysis.

4.2.2 A Hybrid dimension reduction method (HDR)

As expressed in Eq. (4-37), the calculation of the origin moment of an performance function $C = C(\mathbf{X}, \mathbf{Y})$ with *n* probabilistic variables and *m* interval variables generally requires very large computations. Dimension reduction method is a technique to efficiently estimate the origin moments [86,87 . The main idea of the method is to approximate the *n*-dimensional intergration function by the summation of a series of D-dimensional functions (D<*n*).

Firstly, we assume that interval variables are fixed, so Eq. (4-37) is a multidimensional integral problem with probabilistic uncertainties. In section 4.2.1, the univariate dimension reduction method (D=1) is employed to evaluate the performance function with hybrid uncertainties. In the univariate dimension reduction method, the multidimensional problem will be transformed into a series of one-dimensional problems. The univariate dimension reduction method is proved to have good computational efficiency and accuracy. However, it may not be adequate for problems with large random variation and/or high non-linearity. The bivariate dimension reduction is employed here to more accurately evaluate the origin moments.

$E(C^k(\mathbf{X},\mathbf{Y})), k=1,2$ denote the first and second origin moments of the output performance. Let $Z(\mathbf{X},\mathbf{Y})=C^k(\mathbf{X},\mathbf{Y})$, by introducing the bivariate dimension reduction technique, $Z(\mathbf{X},\mathbf{Y})$ can be approximated as follows:

$$Z(\mathbf{X},\mathbf{Y}) \cong \sum_{i=0}^{2}(-1)^i \binom{n+i-3}{i} Z_{2-i} \tag{4-49}$$

where

$$Z_0 = Z(u_1,u_2,\cdots,u_n) \tag{4-50}$$

$$Z_1 = \sum_{j=1}^{n} Z(u_1,\cdots,u_{j-1},X_j,u_{j+1},\cdots,u_n) \tag{4-51}$$

$$Z_2 = \sum_{j_1<j_2}^{n} Z(u_1,\cdots,u_{j_1-1},X_{j_1},u_{j_1+1},\cdots,u_{j_2-1},X_{j_2},u_{j_2+1},\cdots,u_n) \tag{4-52}$$

in which u_j is the mean value of the $X_j\left(j=1,2,\cdots,n\right)$. From the Eq. (4-49) we can see that the multidimensional problem will be turned into a summation of one-dimensional problems and two-dimensional problems. Substituting Eq. (4-49) into Eq. (4-37), it yields:

$$\begin{aligned}
&E\left(Z\left(\mathbf{X},\mathbf{Y}\right)\right)=\sum_{i=0}^{2}\left(-1\right)^{i}\binom{n+i-3}{i}\int_{-\infty}^{\infty}\cdots\int_{-\infty}^{\infty}Z_{2-i}f\left(X_1,X_2,...,X_n\right)dX_1dX_2...dX_n\\
&=\sum_{j_1<j_2}^{n}\int_{-\infty}^{\infty}\int_{-\infty}^{\infty}Z\left(u_1,\cdots,X_{j_1},\cdots,X_{j_2},\cdots,u_n\right)f\left(X_{j_1}\right)f\left(X_{j_2}\right)dX_{j_1}dX_{j_2}\\
&+\left(-1\right)\times\binom{n-2}{1}\sum_{j=1}^{n}\int_{-\infty}^{\infty}Z\left(u_1,\cdots,u_{j-1},X_j,u_{j+1},\cdots,u_n\right)f\left(X_j\right)dX_j\\
&+\binom{n-2}{1}Z\left(u_1,\cdots,u_{j-1},u_j,u_{j+1},\cdots,u_n\right)
\end{aligned}\tag{4-53}$$

For random variables with normal distributions, we firstly transform the random variable X_j into a normal variable $\tilde{X}_j$ that follows a distribution of $N(0,1/2)$, through a linear transformation [100 . For random variables with other distributions, we can also transform the variables into normal distributions through a probability transformation [238 , and then calculate the moment by using Gauss-Hermite numerical integral. For simplicity but without losing any generality, we assume the random variables under normal distributions. The one-dimensional integrals are calculated by:

$$\begin{aligned}
&\mathbf{I}_1=\int_{-\infty}^{\infty}Z\left(u_1,\cdots,u_{j-1},X_j,u_{j+1},\cdots,u_n\right)f\left(X_j\right)dX_j=\int_{-\infty}^{\infty}Z\left(0,\cdots,0,\tilde{X}_j,0,\cdots,0\right)f\left(\tilde{X}_j\right)d\tilde{X}_j\\
&=\frac{1}{\sqrt{\pi}}\sum_{I=1}^{r}q_IZ\left(0,\cdots,0,\tilde{X}_{q_I},0,\cdots,0\right)
\end{aligned}\tag{4-54}$$

where r is the quadrature order (the number of abscissas); and $\tilde{X}_{q_I}$ and q_I are abscissas (Gauss points) and weights (Gauss weights). Similarly, the two-dimensional integrals can be calculated as:

$$\begin{aligned}\mathbf{I}_2 &= \int_{-\infty}^{\infty}\int_{-\infty}^{\infty} Z\left(u_1,\cdots,X_{j_1},\cdots,X_{j_2},\cdots,u_n\right) f\left(X_{j_1}\right) f\left(X_{j_2}\right) dX_{j_1} dX_{j_2} \\ &= \int_{-\infty}^{\infty}\int_{-\infty}^{\infty} Z\left(0,\cdots,\tilde{X}_{j_1},\cdots,\tilde{X}_{j_2},\cdots,0\right) f\left(\tilde{X}_{j_1}\right) f\left(\tilde{X}_{j_2}\right) d\tilde{X}_{j_1} d\tilde{X}_{j_2} \\ &= \left(\frac{1}{\sqrt{\pi}}\right)^2 \sum_{I_1=1}^{r_1}\sum_{I_2=1}^{r_2} q_{I_1} q_{I_2} Z\left(0,\cdots,\tilde{X}_{q_{I_1}},\cdots,\tilde{X}_{q_{I_2}},\cdots,0\right)\end{aligned} \tag{4-55}$$

where r_1, r_2 denote the quadrature order (the number of abscissas) used in the $\tilde{X}_{j_1}$, $\tilde{X}_{j_2}$ directions, $\tilde{X}_{q_{I_1}}$, $\tilde{X}_{q_{I_2}}$ are Gauss points, and q_{I_1}, q_{I_2} are the corresponding weights. Here three Gauss points are employed for a random variable in the numerical integration. After obtaining the one-dimensional and two-dimensional integrals in Eq. (4-53), $E\left(C^k\left(\mathbf{X},\mathbf{Y}\right)\right)$ can be achieved. Then the mean value and the standard deviation of the performance function can be obtained by Eq. (4-44). In the second step, we will take the interval variables into consideration. Similarly, by the main idea of the dimension reduction, the bounds of the mean and variance can be calculated by Eqs. (4-46)-(4-48).

By the proposed method, the original problem will be reduced from a higher dimension to a lower dimension, and thus save computational cost in evaluating the random and interval quantities. For a problem with *n* random variables and *m* interval variables, by using the proposed hybrid dimension reduction method, the number of function calls is given as:

$$\left(\binom{n}{2}\cdot 3^2 + \binom{n}{1}\cdot 3 + 1\right)\cdot\left(2m+1\right) = \left(\frac{9n\left(n-1\right)}{2} + 3n + 1\right)\cdot\left(2m+1\right) \tag{4-56}$$

For example, for a performance function with six random variables and two interval variables, the total number of function evaluations in Eq. (4-53) is 154, which is much less than the evaluations (36=729) of the direct integral. The required function evaluations in Eq. (4-46) or

(4-47) is 5, which is much less than traditional scanning method for interval uncertainties. Furthermore, the computational cost will not increase exponentially with the increasing of the number of the uncertain parameters. Hence, the proposed method shows very good computational efficiency in the uncertainty analysis.

4.2.3 Numerical example

Consider a performance function $C(\mathbf{X},\mathbf{Y})$:

$$C(\mathbf{X},\mathbf{Y})=X_1^3Y_1+X_2^3Y_2+X_3^3Y_3+X_4^3Y_4+X_1^2X_2^2+X_2^2X_3^2+X_3^2X_4^2 \tag{4-57}$$

in which $\mathbf{X}$ denotes the random vector with four random variables X_1, X_2, X_3, X_4, and $\mathbf{Y}$ denotes the interval vector with four interval variables Y_1, Y_2, Y_3, Y_4. The distribution types and parameters of the variables are given in Table 4-5.

Table 4-5 Distribution types and parameter of variables

Uncertain variable	Parameter1	Paramete2	Distribution type
X_1	10	1	Normal
X_2	10	1	Normal
X_3	10	1	Normal
X_4	10	1	Normal
Y_1	9	11	Interval
Y_2	9	11	Interval
Y_3	9	11	Interval
Y_4	9	11	Interval

In Table 4-5, for random variables, parameter 1 and 2 represent the mean and standard variance respectively, and for interval variables, parameter 1 and 2 denote the lower and upper bounds respectively. The proposed HUDR and HDR are used to evaluate the interval mean and standard variance of the performance function. The results from 10^{10} MCS are also provided for reference. As shown in Table 4-6, in general, the results from the proposed methods are close to the reference results from MCS. However, the results of the HUDR are less accurate than those of the HDR. For example, the upper bounds of the standard variances from HUDR and HDR are 1.2895×10^4 and 1.2976×10^4 respectively. We can see that the HDR result is closer to that result from MCS than HUDR. The multidimensional integrals are approximated by a series of one dimensional integrals of a single uncertain variable in the HUDR, this will lose some information in the cross terms in the function. However, in the HDR, and the multidimensional integrals are approximated by a series of one dimensional integrals and two dimensional integrals, so the precision can be improved, especially for problems with more cross terms. However, on the other hand, the HDR will cost more calculation than the HUDR. We need to balance the computational burden and the numerical precision and make choice of an uncertainty analysis method for different problems.

Table 4-6 Results of the performance function with hybrid uncertainties

Method	Mean	Standard variance	Function calls
HUDR	$[6.7680\times10^4,7.5920\times10^4$	$[1.1689\times10^4,1.2895\times10^4$	117
HDR	$[6.7683\times10^4,7.5871\times10^4$	$[1.1772\times10^4,1.2976\times10^4$	603
MCS	$[6.7658\times10^4,7.5871\times10^4$	$[1.1791\times10^4,1.2988\times10^4$	10^{10}

Chapter 5 Robust topology optimization for structures based on orthogonal polynomials

Traditionally, the topology optimization problems are mainly focused on deterministic assumptions. Recent decades, uncertainties have aroused much attention and been introduced in topology optimizations to formulate RBTOs and RTOs. There are a number of achievements related to uncertain topology optimization for structures with random uncertainties or interval uncertainties. However, in practice, some uncertain variables may have adequate samples while the others only have a small number of samples. It is appropriate that those uncertain variables with adequate samples can be treated as random variables, while the other uncertain variables can only be described by intervals. In this Chapter, random-interval hybrid uncertainties related to loadings and material properties will be considered for static and dynamic structures to obtain robust designs. The orthogonal polynomial based hybrid uncertainty analysis methods proposed in section 4.1 will be applied to evaluate the robust objective functions.

5.1 Robust topology optimization for static structures with hybrid uncertainties

For physical quantities (e.g. material field and distributed load) varying across the spatial domain, it is more realistically to model them as random fields. The random field can normally be expressed using a finite number of random variables by the Series expansion methods, such as the KL expansion, the OSE, and the EOLE [89,91 . In this section, random

field uncertainties and interval uncertainties are considered for static structures. The random fields are discretized into several random variables, and then the hPCCI method is used to efficiently estimate the interval mean and variance of the compliance for structures with the hybrid uncertainties based on the parametric level-set method.

5.1.1 Random field approximation by KL expansion

For the consideration of the computational cost, the random field can normally be expressed using a finite number of random variables. The KL expansion is a popular method to discretize the random fields. KL expansion has certain interesting characteristics and properties and becomes one of the most popular series expansion methods. Generally speaking, only a small number of terms are needed for the approximation to reach a prescribed precision when using the KL expansion. Moreover, KL expansion gives the best accuracy when dealing with random fields with exponential covariance kernels comparing with the other expansion methods. Particularly, for Gaussian random fields, the random variables after discretization are a set of independent standard normal variables, which could provide much convenience for the uncertain analysis.

A random field $\mathbf{R}(\mathbf{z},\theta)$ is defined in a Hilbert space L^2. $\mathbf{z}\in D$, where D represents the system geometry. θ is an element of the sample space which is used to indicate the random uncertainties. The exponential kernel is considered for the Gaussian random fields:

$$\rho(\mathbf{z},\mathbf{z}') = \exp\left(-\frac{\|\mathbf{z}-\mathbf{z}'\|}{a}\right) \tag{5-1}$$

where a is the correlation length. Following Mercer's Theorem [248 , it has the following spectral or eigen-decomposition:

$$\rho(\mathbf{z},\mathbf{z}') = \sum_{i=1}^{\infty} \lambda_i \varphi_i(\mathbf{z}) \varphi_i(\mathbf{z}') \tag{5-2}$$

The eigenvalues λ_i and eigenfunctions φ_i are the solutions of the homogeneous Fredholm integral equation:

$$\int_D \rho(\mathbf{z},\mathbf{z}') \varphi_i(\mathbf{z}') dD_{\mathbf{z}'} = \lambda_i \varphi_i(\mathbf{z}) \tag{5-3}$$

By KL expansion, the random field can be approximated by:

$$\tilde{\mathbf{R}}(\mathbf{z},\theta) = \mu + \sum_{i=1}^{n} \sigma \sqrt{\lambda_i} \xi_i(\theta) \varphi_i(\mathbf{z}) \tag{5-4}$$

where μ and σ are the mean and standard variance of the random field. If $\Omega=[\mathbf{z}_{\min}, \mathbf{z}_{\max}$ is non-symmetrical, a shift parameter is computed:

$$T = \frac{\mathbf{z}_{\min} + \mathbf{z}_{\max}}{2} \tag{5-5}$$

Then the non-symmetrical domain can be transformed into a symmetrical domain:

$$D' = \left[\frac{\mathbf{z}_{\min} - \mathbf{z}_{\max}}{2}, \frac{\mathbf{z}_{\max} - \mathbf{z}_{\min}}{2} \right] \tag{5-6}$$

The random field represented by the KL expansion is then rewritten as:

$$\mathbf{R}(\mathbf{z},\theta) = \mu + \sum_{i=1}^{n} \sigma\sqrt{\lambda_i}\xi_i(\theta)\varphi_i(\mathbf{z}-T) \tag{5-7}$$

Due to the orthogonality of the eigenfunctions, the random variables ξ_i can be calculated by:

$$\xi_i(\theta) = \frac{1}{\sqrt{\lambda_i}} \int_{D'} \left(\mathbf{R}(\mathbf{z},\theta) - \mu\right)\varphi_i(\mathbf{z}-T)\, dD' \tag{5-8}$$

Particularly, for the Gaussian random field, the random variables ξ_i are independent standard normal variables with zero means and unit variances.

In this section, uncertain loads and material properties (e.g. Young's modulus) will be assumed as Gaussian random fields. In mathematics, it may be questionable to model the material properties as Gaussian random fields, because the realizations of Gaussian random variables can be negative in value but the material properties should be positive in nature. As noted in [249 , the Young's modulus can be regarded as the Gaussian distributions in engineering for most robust design problems, and the negative material properties can be avoided when appropriate conditions applied to ensure sample points to be bounded within an allowable range. Alternatively, we can employ models mathematically more rigorous as replacements for random material properties, such as the non-negative distributions (e.g. lognormal distributions) that can be transformed into Gaussian fields through a non-linear transformation [250 , and then the proposed method can be applied directly.

5.1.2 Robust topology optimization

5.1.2.1 Robust topology optimization formulation

The random uncertain variables **X** or random fields **R** will be firstly transformed into standard normal random variables $\boldsymbol{\xi}$, and interval uncertain variables **Y** will be transformed into standard interval variables $\boldsymbol{\eta}$. $\boldsymbol{\xi}=\left(\xi_1,\xi_2,\cdots,\xi_n\right)$ is the probability vector and $\boldsymbol{\eta}=\left(\eta_1,\eta_2,\cdots,\eta_m\right)$ is the interval vector in a structure. $\xi_i(i=1,2,\cdots,n)$ is the *i*th probability uncertain variable and $\eta_j(j=1,2,\cdots,m)$ is the *j*th interval variable. With both random and interval uncertainties, the structure compliance can then be expressed as $C\left(\boldsymbol{\xi},\boldsymbol{\eta}\right)$. The robust objective function is defined as a linear combination of the mean μ and standard deviation σ of structure compliance due to the random and interval variables:

$$g=\mu\left(C\left(\boldsymbol{\xi},\boldsymbol{\eta}\right)\right)+h\cdot\sigma\left(C\left(\boldsymbol{\xi},\boldsymbol{\eta}\right)\right) \tag{5-9}$$

where *h* is the weighting coefficients, which is set as 1 here. The mean and variance of the objective function will be intervals subject to the interval uncertainties. In this case, the new robust objective function is then defined under the worst case for the RTO problem:

$$g=\mu^R\left(C\left(\boldsymbol{\xi},\boldsymbol{\eta}\right)\right)+\sigma^R\left(C\left(\boldsymbol{\xi},\boldsymbol{\eta}\right)\right) \tag{5-10}$$

where μ^R and σ^R are the upper bounds of the interval mean and variance respectively. In this way, the robust optimization problem can be formulated as follows:

$$\begin{aligned} &\min_{\boldsymbol{\alpha}} \ \ g = \mu^R + \sigma^R \\ &s.t. \ \ V = \int_\Omega H\left(\Phi\left(\xi,\boldsymbol{\eta}\right)\right)d\Omega \le V_{max} \\ &\qquad \mathbf{K}\left(\xi,\boldsymbol{\eta}\right)\mathbf{U}\left(\xi,\boldsymbol{\eta}\right) = \mathbf{F}\left(\xi,\boldsymbol{\eta}\right) \\ &\qquad \alpha_{\min} \le \alpha_e \le \alpha_{\max}, e = 1,2,\cdots,N \end{aligned} \tag{5-11}$$

where $\alpha_e\left(e=1,2,\cdots,N\right)$ are the design variables, N is the number of design variables. $\alpha_{\min}$ and $\alpha_{\max}$ represent the upper and lower bounds of the design variables.

The robust objective function for the RTO problem in Eq. (5-11) is defined by the upper bounds of the mean and standard variance of the compliance and can be calculated using the hPCCI proposed in section 4.1.1. From Eqs. (4-13) and (4-14), we can obtain:

$$\begin{aligned} g &= \mu^R\left(C\left(\xi,\boldsymbol{\eta}\right)\right) + \sigma^R\left(C\left(\xi,\boldsymbol{\eta}\right)\right) \\ &= c_{\mathbf{0},\mathbf{0}} + \left(\sum_{\boldsymbol{\chi}_2\in\mathbb{N}^m,\boldsymbol{\chi}_2\neq\mathbf{0}}\left|c_{\mathbf{0},\boldsymbol{\chi}_2}\right|\right) + \sqrt{\sum_{\boldsymbol{\chi}_1\in\mathbb{N}^n,\boldsymbol{\chi}_1\neq\mathbf{0}}\sum_{\boldsymbol{\chi}_2\in\mathbb{N}^m} c_{\boldsymbol{\chi}_1,\boldsymbol{\chi}_2}^2 + 2\left|\sum_{\boldsymbol{\chi}_1\in\mathbb{N}^n,\boldsymbol{\chi}_1\neq\mathbf{0}}\sum_{\boldsymbol{\chi}_2\in\mathbb{N}^m} c_{\boldsymbol{\chi}_1,\boldsymbol{\chi}_2^{(k_1)}}c_{\boldsymbol{\chi}_1,\boldsymbol{\chi}_2^{(k_2)}}\right|} \\ &= c_{\mathbf{0},\mathbf{0}} + \left(\sum_{\boldsymbol{\chi}_2\in\mathbb{N}^m,\boldsymbol{\chi}_2\neq\mathbf{0}}\left|c_{\mathbf{0},\boldsymbol{\chi}_2}\right|\right) + \sqrt{\sum_{\boldsymbol{\chi}_1\in\mathbb{N}^n,\boldsymbol{\chi}_1\neq\mathbf{0}}\sum_{\boldsymbol{\chi}_2\in\mathbb{N}^m} c_{\boldsymbol{\chi}_1,\boldsymbol{\chi}_2}^2 + 2\left|\Upsilon\right|} \end{aligned} \tag{5-12}$$

in which $\Upsilon = \sum_{\boldsymbol{\chi}_1\in\mathbb{N}^n,\boldsymbol{\chi}_1\neq\mathbf{0}}\sum_{\boldsymbol{\chi}_2\in\mathbb{N}^m} c_{\boldsymbol{\chi}_1,\boldsymbol{\chi}_2^{(k_1)}}c_{\boldsymbol{\chi}_1,\boldsymbol{\chi}_2^{(k_2)}}$.

5.1.2.2 Sensitivity analysis

In this chapter, the MMA is used to update the design variables in the topology optimization. MMA is a gradient-based optimization method, so the sensitivities of the robust objective function with respect to the design variables need to be computed. Based on the chain rule, the derivative of the robust objective function with respect to the design variable α_e is:

$$\frac{\partial g}{\partial \alpha_e}=\frac{\partial c_{\mathbf{0},\mathbf{0}}}{\partial \alpha_e}+\left(\sum_{\chi_2\in\mathbb{N}^m,\chi_2\neq\mathbf{0}}\frac{\partial\left|c_{\mathbf{0},\chi_2}\right|}{\partial \alpha_e}\right)+\frac{1}{\sigma^R}\sum_{\chi_1\in\mathbb{N}^n,\chi_1\neq\mathbf{0}}\left(\sum_{\chi_2\in\mathbb{N}^m}c_{\chi_1,\chi_2}\frac{\partial c_{\chi_1,\chi_2}}{\partial \alpha_e}+\left|\Upsilon\right|/\partial \alpha_e\right) \tag{5-13}$$

Using the sign function:

$$\text{sign(x)}=\begin{cases}-1, & \text{x}<0\\ 0, & \text{x}=0\\ 1, & \text{x}>0\end{cases} \tag{5-14}$$

The sensitivities in Eq. (5-13) can be re-expressed as:

$$\begin{aligned}\frac{\partial g}{\partial \alpha_e}=&\frac{\partial c_{\mathbf{0},\mathbf{0}}}{\partial \alpha_e}+\left(\sum_{\chi_2\in\mathbb{N}^m,\chi_2\neq\mathbf{0}}\frac{\partial\left(c_{\mathbf{0},\chi_2}\text{sign}\left(c_{\mathbf{0},\chi_2}\right)\right)}{\partial \alpha_e}\right)\\&+\frac{1}{\sigma^R}\sum_{\chi_1\in\mathbb{N}^n,\chi_1\neq\mathbf{0}}\left(\sum_{\chi_2\in\mathbb{N}^m}c_{\chi_1,\chi_2}\frac{\partial c_{\chi_1,\chi_2}}{\partial \alpha_e}+\left(\Upsilon\,\text{sign}\left(\Upsilon\right)\right)/\partial \alpha_e\right)\end{aligned} \tag{5-15}$$

Since the sign function in the above equation is not differentiable at the point x=0, the Heaviside projection method is used to smooth the sign function using the tanh function as:

$$\text{sign(x)}=\tanh(\ell\,\text{x}) \tag{5-16}$$

where ℓ is a positive number, $\ell=100$ is used here. Then the Eq. (5-15) is transformed into:

$$\begin{aligned}\frac{\partial g}{\partial \alpha_e}=&\frac{\partial c_{\mathbf{0},\mathbf{0}}}{\partial \alpha_e}+\sum_{\chi_2\in\mathbb{N}^m,\chi_2\neq\mathbf{0}}\left(\tanh\left(\ell c_{\mathbf{0},\chi_2}\right)+\ell c_{\mathbf{0},\chi_2}\,\text{sech}^2\left(\ell c_{\mathbf{0},\chi_2}\right)\right)\frac{\partial c_{\mathbf{0},\chi_2}}{\partial \alpha_e}\\&+\frac{1}{\sigma^R}\sum_{\chi_1\in\mathbb{N}^n,\chi_1\neq\mathbf{0}}\left(\begin{array}{l}\displaystyle\sum_{\chi_2\in\mathbb{N}^m}c_{\chi_1,\chi_2}\frac{\partial c_{\chi_1,\chi_2}}{\partial \alpha_e}+\left(\tanh\left(\ell\Upsilon\right)+\ell\Upsilon\,\text{sech}^2\left(\ell\Upsilon\right)\right)\\ \times\left(\displaystyle\sum_{\chi_1\in\mathbb{N}^n,\chi_1\neq\mathbf{0}}\sum_{\chi_2\in\mathbb{N}^m}\left(c_{\chi_1,\chi_2^i}\frac{\partial c_{\chi_1,\chi_2^j}}{\partial \alpha_e}+\partial c_{\chi_1,\chi_2^j}\frac{\partial c_{\chi_1,\chi_2^i}}{\partial \alpha_e}\right)\right)\end{array}\right)\end{aligned} \tag{5-17}$$

In the above equation, $\partial c_{\chi_1,\chi_2} \big/ \partial \alpha_e$ is still the unknown part. The sensitivity in Eq. (3-35) can be regarded as a function, and can be expanded as follows:

$$\frac{\partial C(\boldsymbol{\alpha})}{\partial \alpha_e} = \sum_{\chi_1 \in \mathbb{N}^n} \sum_{\chi_2 \in \mathbb{N}^m} \gamma_{\chi_1,\chi_2} \Psi_{\chi_2}(\boldsymbol{\eta}) H_{\chi_1}(\boldsymbol{\xi}) \tag{5-18}$$

where γ_{χ_1,χ_2} are the coefficients in the expansion. On the other hand, by differentiating the Eq. (4-9) with respect to design variable on both sides, we can get the derivatives as:

$$\frac{\partial C(\boldsymbol{\alpha})}{\partial \alpha_e} = \sum_{\chi_1 \in \mathbb{N}^n} \sum_{\chi_2 \in \mathbb{N}^m} \frac{\partial c_{\chi_1,\chi_2}}{\partial \alpha_e} \Psi_{\chi_2}(\boldsymbol{\eta}) H_{\chi_1}(\boldsymbol{\xi}) \tag{5-19}$$

Comparing Eqs. (5-18) and (5-19), we can get:

$$\frac{\partial c_{\chi_1,\chi_2}}{\partial \alpha_e} = \gamma_{\chi_1,\chi_2} \tag{5-20}$$

Substituting Eq. (5-20) into Eq. (5-17), the final expression of the sensitivities of the robust objective function can be obtained:

$$\begin{aligned} \frac{\partial g}{\partial \alpha_e} = \frac{\partial c_{\mathbf{0},\mathbf{0}}}{\partial \alpha_e} + \sum_{\chi_2 \in \mathbb{N}^m, \chi_2 \neq \mathbf{0}} \left(\tanh\left(\ell c_{\mathbf{0},\chi_2}\right) + \ell c_{\mathbf{0},\chi_2} \operatorname{sech}^2\left(\ell c_{\mathbf{0},\chi_2}\right) \right) \gamma_{\mathbf{0},\chi_2} \\ + \frac{1}{\sigma^R} \sum_{\chi_1 \in \mathbb{N}^n, \chi_1 \neq \mathbf{0}} \left(\begin{array}{l} \displaystyle\sum_{\chi_2 \in \mathbb{N}^m} c_{\chi_1,\chi_2} \gamma_{\chi_1,\chi_2} + \left(\tanh(\ell \Upsilon) + \ell \Upsilon \operatorname{sech}^2(\ell \Upsilon) \right) \\ \times \left(\displaystyle\sum_{\chi_1 \in \mathbb{N}^n, \chi_1 \neq \mathbf{0}} \sum_{\chi_2 \in \mathbb{N}^m} \left(c_{\chi_1,\chi_2^i} \gamma_{\chi_1,\chi_2^j} + \partial c_{\chi_1,\chi_2^j} \gamma_{\chi_1,\chi_2^i} \right) \right) \end{array} \right) \end{aligned} \tag{5-21}$$

5.1.3 Numerical examples

In this section, the loadings and/or the material properties in the examples are considered as hybrid uncertain parameters. In order to illustrate the importance of uncertainties,

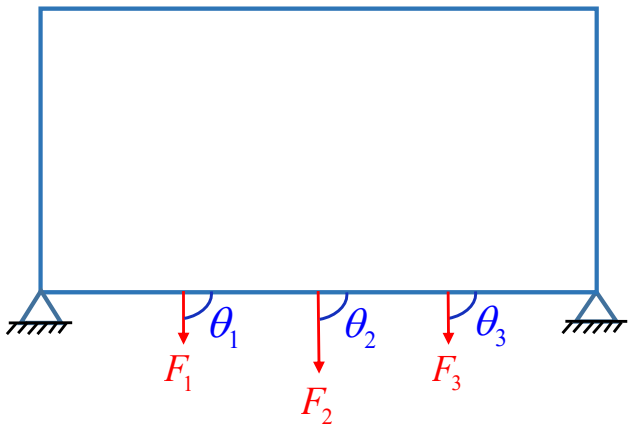

Figure 5-1 Design domain and boundary condition for example 1

A structure with 2:1 length-width ratio is investigated in this example. As shown in Figure 5-1, three external loads F_1, F_2 and F_3 are vertically applied on the lower side of the structure. The lower left and right corners of the beam are clamped. The elastic tensor for the artificial material model is E=1 and its Poisson's ratio is υ=0.3. The three loads F_1, F_2 and F_3 are assumed as random variables, and the load directions θ_1, θ_2, and θ_3 are considered as interval variables. The structure is discretized by 80×40 Q4 elements, and the volume fraction is 0.5.

This optimization problem is to minimize the compliance of the structure, so as to find the optimized topology for the structure under hybrid uncertainties.

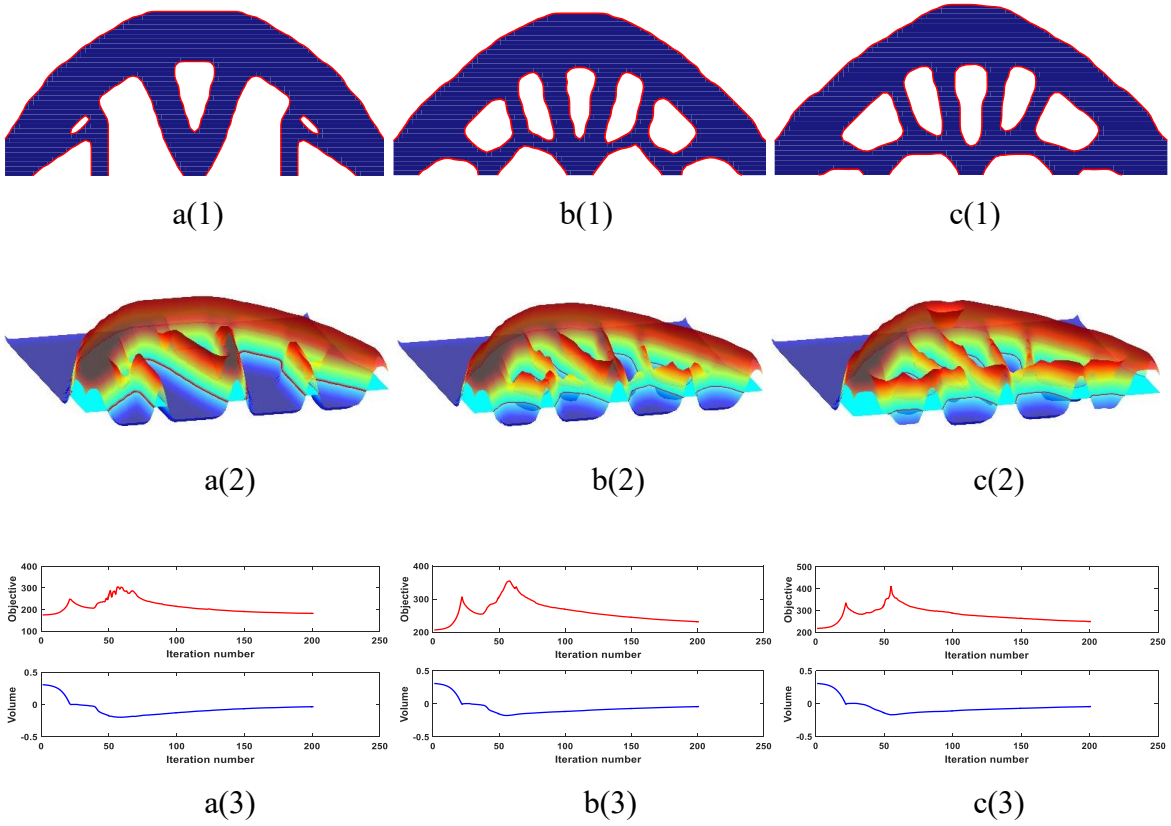

Figure 5-2 Optimized results for deterministic and robust designs for example 1

In this example, only random variables and interval variables are considered in order to verify the effectiveness of the proposed method. The three loads F_1, F_2 and F_3 are assumed as normal variables with mean values $[1,3,1]$ and standard variances $[0.1,0.3,0.1]$, and the load directions θ_1, θ_2, and θ_3 are considered as intervals $[80^\circ,100^\circ]$ in uncertain case 1 and the intervals are set to be $[70^\circ,110^\circ]$ in uncertain case 2. Figure 5-2 presents the design results for both deterministic and robust topology optimization. Figure 5-2 a(1)~a(3) are results of

the deterministic design, b(1)~b(3) are results of the robust design under uncertain case 1, and c(1)~c(3) are results of the robust design under uncertain case 2. In Figure 5-2, a(1), b(1) and c(1) are the optimized topologies, a(2), b(2) and c(2) are the one dimensional higher LSF, and a(3), b(3) and c(3) are the iteration histories. It can be seen that the final topologies for the structure with uncertainties are different from the deterministic design, so it is essential to incorporate uncertainties into topology optimization process. The iteration histories of both objective function and volume constraint show that the proposed method has good computational efficiency and stability.

In order to prove the effectiveness of the proposed method, some detailed results about the robust objective function values (e.g. mean and standard variance) of the robust and the deterministic designs under the uncertainties are given in Table 5-1. When applying the uncertain case 1 to both deterministic and uncertain designs, the robust objective function values are 241.74 and 228.27, and when applying the uncertain case 2 to both deterministic and uncertain designs, the robust objective function values are 316.66 and 241.43, which indicate that the robust design can result in better objective function values under uncertainties.

As a reference, the robust objective function values by MCS and the FEA calls are also given. Under uncertain case 1, the error of the deterministic result from hPCCI is 0.25% compared with MCS result, while the error of the robust result from hPCCI is 0.23% compared with MCS result. Under uncertain case 2, the error of the deterministic result from hPCCI is 0.33% compared with MCS result, while the error of the robust result from hPCCI is 0.84% compared with MCS result. For the structure with three random variables and three interval variables, by the second order orthogonal polynomials, only 196 (2*7*2*7) FEA calls are

needed to approximate the robust objective function by using the hPCCI. We can see that the hPCCI will achieve close results to MCS results, and at the same time save the computational cost.

Table 5-1 Robust objective function of optimized designs for example 1

Situations	Method	Mean	Standard variance	Robust objective function value	FEA calls
Deterministic design under uncertainties 1	hPCCI	210.87	30.87	241.74	196
	MCS	210.38	30.75	241.13	1×10^7
Deterministic design under uncertainties 2	hPCCI	274.85	41.81	316.66	196
	MCS	274.19	41.41	315.60	1×10^7
Robust design 1 under uncertainties 1	hPCCI	199.99	28.28	228.27	196
	MCS	198.90	28.84	227.74	1×10^7
Robust design 2	hPCCI	211.33	31.10	241.43	196

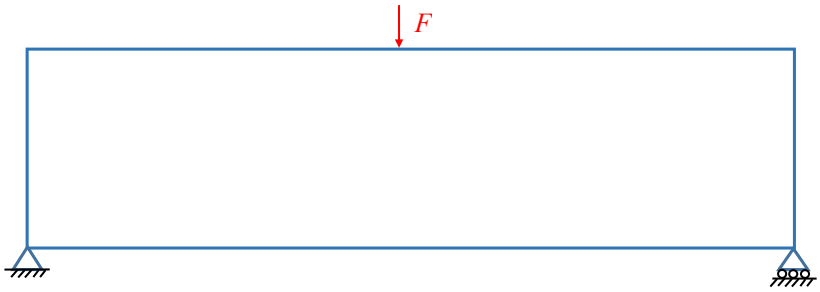

Figure 5-3 Design domain and boundary condition for example 2

A long MBB with 4:1 length-width ratio is considered in this example. As shown in Figure 5-3, an external load is vertically applied on the upper side of the structure. The lower left corner of the beam is clamped and the lower right corner is simply supported. The magnitude of the loading F is within the interval [0.9,1.1 . The Poisson's ratio is υ=0.3 , and the elastic tensor is assumed to be a Gauss random field with mean equals to 1 and standard deviation equals to 0.2. The correlation between any two points in the random field is described by an exponential kernel in which the correlation lengths are set to be 8 and 2 in X and Y directions respectively. In this example, six terms are used to approximate the random field using the KL expansion. The structure is discretized by 120×30 Q4 elements, and the volume fraction is 0.5.

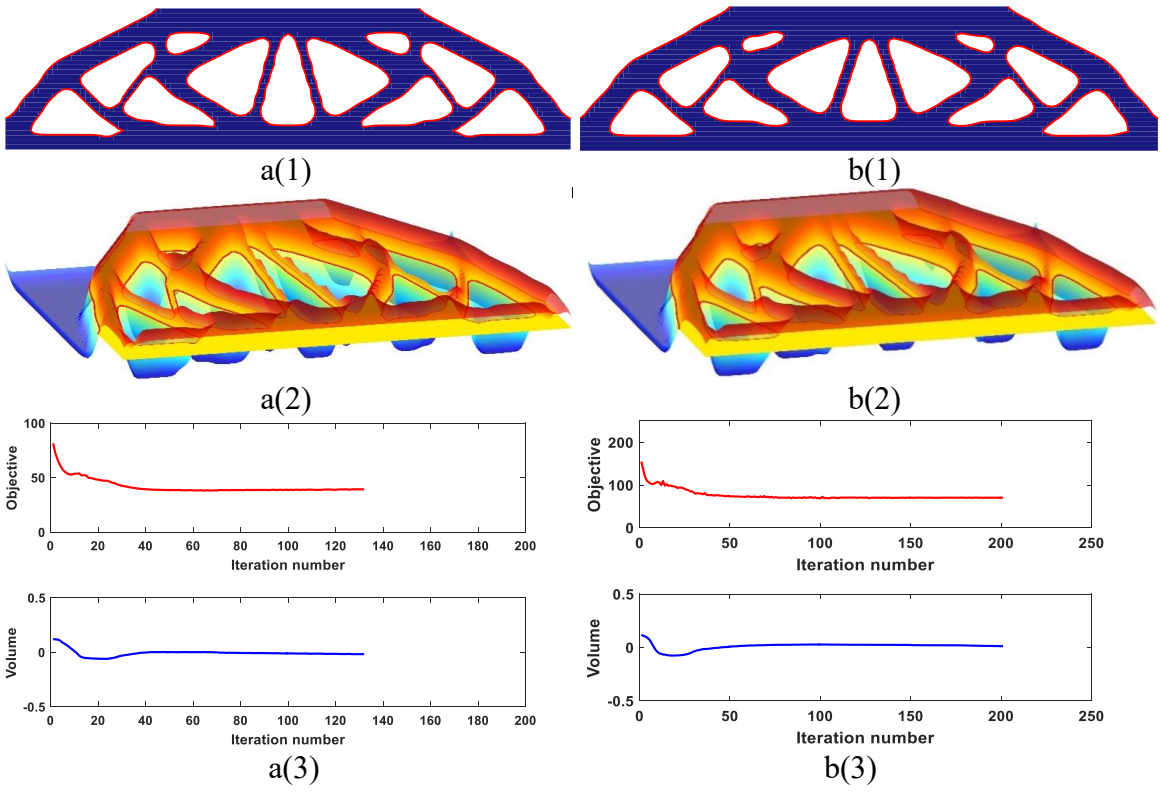

Figure 5-4 Optimized results for deterministic and robust designs for example 2

Figure 5-4 presents the design results for both deterministic and robust topology optimizations. The topologies of the deterministic and the robust results are similar in this example, but some local shape and size are different. Figure 5-4 a(1)~a(3) are results of the deterministic design, and b(1)~b(3) are results of the robust design under uncertainties. By giving the same uncertain boundary conditions, we evaluate the robust objective function values for both deterministic and robust design results. The robust objective function value of the deterministic design is 8.1% higher than the robust design, and the mean and the standard deviation of the robust design (50.28 and 21.27 respectively) are both smaller than those of the deterministic design (54.36 and 23.46 respectively). It shows that the robust topology optimization results in a more robust design than the deterministic optimization under uncertainties. The robust objective function values and the FEA calls by MCS are also provided in Table 5-2. From the results we can conclude that hPCCI will keep a good accuracy while saving a large amount of computational cost.

Table 5-2 Robust objective function of optimized designs for example 2

Situations	Method	Mean	Standard variance	Robust objective function value	FEA calls
Deterministic design under uncertainties	hPCCI	54.36	23.46	77.82	156
	MCS	53.99	23.38	77.37	1×10^6
Robust design under uncertainties	hPCCI	50.28	21.27	71.55	156
	MCS	49.65	21.46	71.11	1×10^6

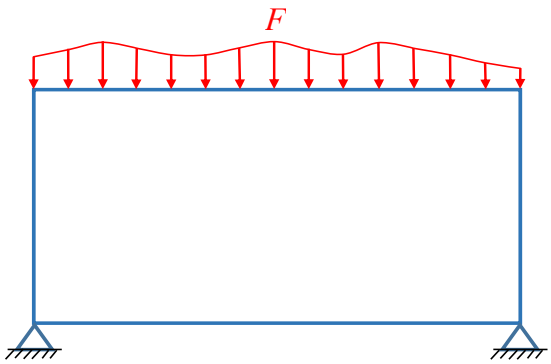

Figure 5-5 Design domain and boundary condition for example 3

A 2D bridge structure with 2:1 length-width ratio is investigated in this example. As shown in Figure 5-5, the lower left and right corners of the beam are clamped. The Poisson's ratio is υ=0.3 , and the elastic tensor E for the artificial material property is set to be within [0.9, 1.1 . A distributed load F is applied at the top. The load magnitude at each point is assumed to obey a normal distribution with mean equals to 10 and standard deviation equals to 3, and the correlation length of the random field is set to be 2. In this example, six terms are used to approximate the random field using the KL expansion. The structure is discretized by 80×40 Q4 elements, and the volume fraction is 0.5.

Figure 5-6 gives the design results for both deterministic and uncertain situations. In this example, the two design results have some obvious differences although they have similar topologies. Table 5-3 gives the objective function values (both the mean and variance) for both deterministic and robust designs under the same uncertainties. And from the robust objective function values, we can conclude that the robust design can achieve a more robust result under uncertainties. As a reference, the results by 10^6 MCS are also provided to show

the accuracy of the proposed method. Under uncertainties, the error of the deterministic result from hPCCI is 0.24% compared with MCS result, and the error of the robust result from hPCCI is 0.20% compared with MCS result. In conclusion, the proposed method only needs a small number of FEA calls, and at the same time, keeps a good numerical precision.

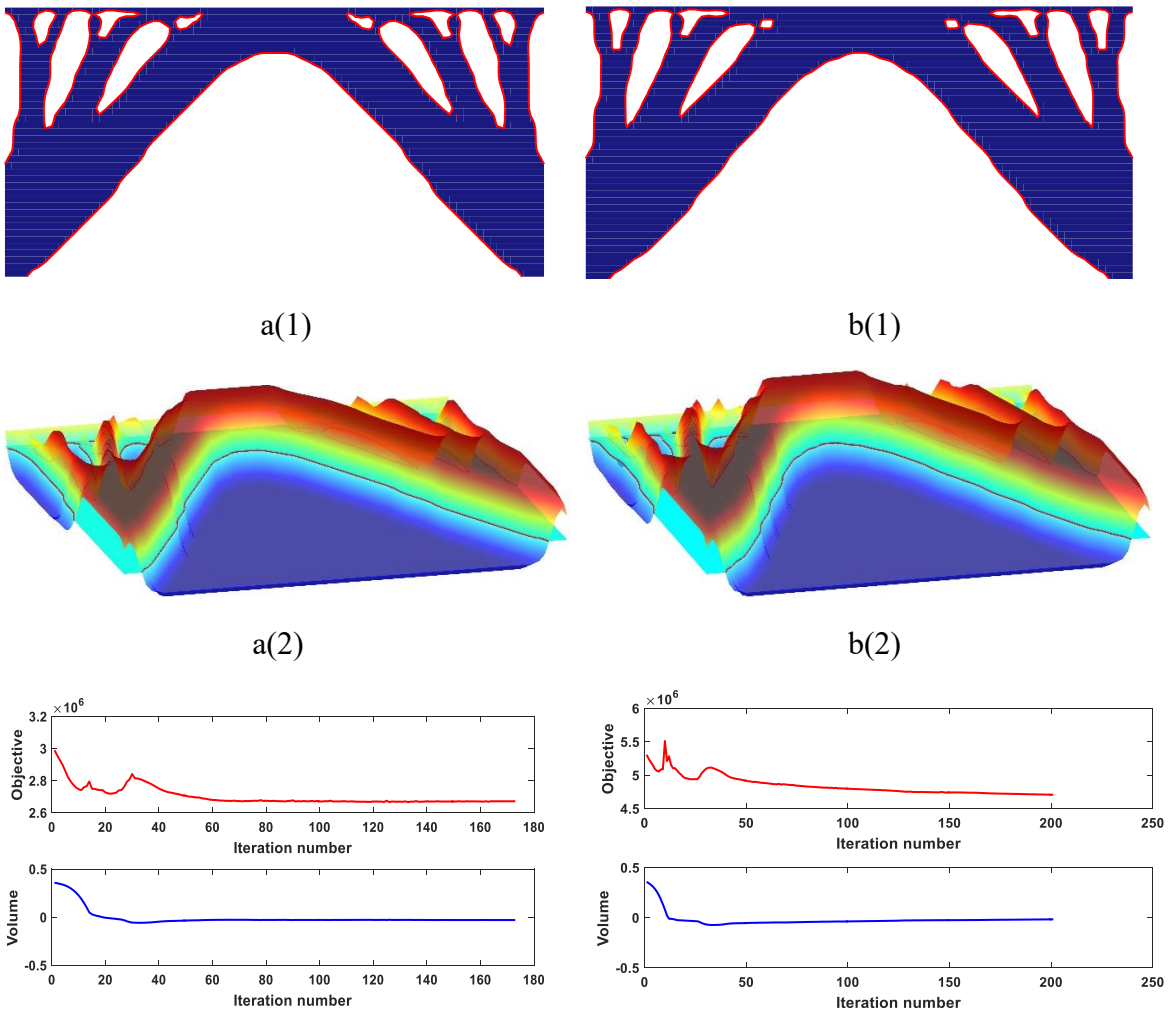

Figure 5-6 Optimized results for deterministic and robust designs for example 3

Table 5-3 Robust objective function of optimized designs for example 3

Situations	Method	Mean	Standard variance	Robust objective function value	FEA calls
Deterministic design under uncertainties	hPCCI	3.2527×10^6	1.5706×10^6	4.8233×10^6	156
	MCS	3.2419×10^6	1.5698×10^6	4.8117×10^6	1×10^6
Robust design under uncertainties	hPCCI	3.1715×10^6	1.5386×10^6	4.7101×10^6	156
	MCS	3.1668×10^6	1.5339×10^6	4.7007×10^6	1×10^6

5.2 Robust topology optimization for dynamic structures with hybrid uncertainties

In static problems, the loadings of a structure will not change with time. In practice, structures will be subject to time-variant loadings, and thus the displacement, stress, and strain of the structures also change with time. Topology optimization for dynamic structures is of great importance in engineering and has been widely applied to many kinds of problems for structures. Topology optimization for dynamic structures can be divided into two main categories: eigenfrequency optimization problems and frequency response optimization problems. The eigenfrequency optimization problem keeps the structural eigenfrequencies away from the driving frequency for the avoidance of resonance. As another important and complex research topic in structural dynamic optimization, frequency response optimization reduces the frequency response and suppresses the resonance of a structure under dynamic

loadings. In this section, we focus on the frequency response problems for structures with hybrid uncertainties.

5.2.1 Dynamic topology optimization

5.2.1.1 Dynamic finite element analysis

Different from static finite element equation, dynamic finite element equation has damping force and inertia force except for active force. That is to say, the loadings on an element include active force $\mathbf{F}$, damping force $\mathbf{F}_c$ and inertia force $\mathbf{F}_m$. The active force is as follows:

$$\mathbf{F} = \mathbf{F}_p + \mathbf{F}_s + \mathbf{F}_v \tag{5-22}$$

in which $\mathbf{F}_p$ is the concentrated force on points, $\mathbf{F}_s$ represents the force on the surface, and $\mathbf{F}_v$ represents the force on the body. The damping force $\mathbf{F}_c$ is related to the velocity, and has an opposite direction of the velocity:

$$\mathbf{F}_c = -\mathbf{C}_e\dot{\boldsymbol{\delta}} = -\mathbf{C}_e\mathbf{N}\dot{\boldsymbol{\delta}}_e \tag{5-23}$$

in which $\boldsymbol{\delta}$ is the displacement in the element, $\boldsymbol{\delta}^e$ is the nodal displacement, $\mathbf{N}$ is the shape function and $\mathbf{C}_e$ is the damping matrix. The inertia force $\mathbf{R}_m$ is related to the mass and the accelerated velocity, and also has an opposite direction:

$$\mathbf{F}_m = -\rho\ddot{\boldsymbol{\delta}} = -\rho\mathbf{N}\ddot{\boldsymbol{\delta}}_e \tag{5-24}$$

Based on the virtual work principle, the virtual work from the external forces δW is equivalent to the virtual work from the internal forces δU :

$$\delta W = \delta U \tag{5-25}$$

$$\begin{aligned}&[\boldsymbol{\delta}_e^*]^{\mathrm{T}}\mathbf{N}^{\mathrm{T}}\mathbf{R}_p + \int_S [\boldsymbol{\delta}_e^*]^{\mathrm{T}}\mathbf{N}^{\mathrm{T}}\mathbf{F}_s dS + \int_V [\boldsymbol{\delta}_e^*]^{\mathrm{T}}\mathbf{N}^{\mathrm{T}}\mathbf{F}_v dV + \int_V [\boldsymbol{\delta}_e^*]^{\mathrm{T}}\mathbf{N}^{\mathrm{T}}\mathbf{F}_c dV \\ &+\int_V [\boldsymbol{\delta}_e^*]^{\mathrm{T}}\mathbf{N}^{\mathrm{T}}\mathbf{R}_m dV = \int_V [\boldsymbol{\varepsilon}^*]^{\mathrm{T}}\boldsymbol{\delta}_e dV = \int_V [\boldsymbol{\delta}_e^*]^{\mathrm{T}}\mathbf{B}^{\mathrm{T}}\mathbf{E}\mathbf{B}\boldsymbol{\delta}_e dV\end{aligned} \tag{5-26}$$

where $\mathbf{B}$ is the strain-displacement matrix, and $\mathbf{E}$ is the elastic matrix, $\boldsymbol{\delta}_e^*$ is the virtual displacement of the element. Considering Eqs. (5-23) and (5-24), Eq. (5-26) can be rewritten as:

$$\begin{aligned}&\mathbf{N}^{\mathrm{T}}\mathbf{F}_p + \int_S \mathbf{N}^{\mathrm{T}}\mathbf{F}_s dS + \int_V \mathbf{N}^{\mathrm{T}}\mathbf{F}_v dV \\ &= \int_V \mathbf{B}^{\mathrm{T}}\mathbf{E}\mathbf{B}\boldsymbol{\delta}_e dV + \int_V \mathbf{C}_e\mathbf{N}^{\mathrm{T}}\mathbf{N}\dot{\boldsymbol{\delta}}_e dV + \int_V \rho\mathbf{N}^{\mathrm{T}}\mathbf{N}\ddot{\boldsymbol{\delta}}_e dV\end{aligned} \tag{5-27}$$

Then the dynamic finite element equation for an element is:

$$\mathbf{M}_e\ddot{\boldsymbol{\delta}}_e + \mathbf{C}_e\dot{\boldsymbol{\delta}}_e + \mathbf{K}_e\boldsymbol{\delta}_e = \mathbf{F}_e \tag{5-28}$$

in which

$$\begin{cases}\mathbf{F}_e = \mathbf{N}^{\mathrm{T}}\mathbf{F}_p + \int_S \mathbf{N}^{\mathrm{T}}\mathbf{F}_s dS + \int_V \mathbf{N}^{\mathrm{T}}\mathbf{F}_v dV \\ \mathbf{K}_e = \int_V \mathbf{B}^{\mathrm{T}}\mathbf{E}\mathbf{B}dV \\ \mathbf{C}_e = \int_V \mathbf{C}_e\mathbf{N}^{\mathrm{T}}\mathbf{N}dV \\ \mathbf{M}_e = \int_V \rho\mathbf{N}^{\mathrm{T}}\mathbf{N}dV\end{cases} \tag{5-29}$$

Then the structure finite element equation is

$$\mathbf{M}\ddot{\boldsymbol{\delta}} + \mathbf{C}\dot{\boldsymbol{\delta}} + \mathbf{K}\boldsymbol{\delta} = \mathbf{F} \tag{5-30}$$

where $\mathbf{M}$ is the global mass matrix, $\mathbf{C}$ is the global damping matrix, $\mathbf{K}$ is the global stiffness matrix, and $\mathbf{F}$ is the loading of the structure. In practical engineering, it is difficult to give the

precise damping matrix. Based on the Rayleigh damping model, with the parameters A and B, the global damping matrix can be expressed as the liner combination of the mass matrix and the stiffness matrix:

$$\mathbf{C} = A\mathbf{K} + B\mathbf{M} \tag{5-31}$$

For a harmonic excitation with frequency w, then the loading, displacement, velocity and accelerated velocity can be respectively expressed as the following:

$$\begin{aligned} \mathbf{F} &= \mathbf{P}e^{iwt} \\ \boldsymbol{\delta} &= \mathbf{U}e^{iwt} \\ \dot{\boldsymbol{\delta}} &= iw\mathbf{U}e^{iwt} \\ \ddot{\boldsymbol{\delta}} &= -w^2\mathbf{U}e^{iwt} \end{aligned} \tag{5-32}$$

where **P** is the magnitude of the dynamic load, **U** is the response displacement. Then the finite element equation (5-30) can be rewritten as:

$$\left(\mathbf{K} + iw\mathbf{C} - w^2\mathbf{M}\right)\mathbf{U} = \mathbf{P} \tag{5-33}$$

in which $\mathbf{S} = \mathbf{K} + iw\mathbf{C} - w^2\mathbf{M}$ is defined as the dynamic stiffness matrix.

5.2.1.2 Dynamic topology optimization formulation

Dynamic topology optimization can be conducted in the time domain or in the frequency domain. Dynamic topology optimization in the time domain is to maximize the stiffness of the structures within the specified time under dynamic loads [251,252,253 . According to different response ranges, the frequency response optimization problem can be categorized into two types: local frequency response optimization and global frequency response

optimization [52,53 . Frequency response optimization reduces the frequency response at a part or the whole structure, so as to improve the local or global dynamic performance of the structure under the excitation force. This chapter will investigate the global frequency response topology optimization for structures under harmonic loads with a certain excitation frequency. Based on the parametric LSM, topology optimization problem for a dynamic structure can be formulated as:

$$\begin{aligned} &\min_{\boldsymbol{\alpha}} : J = \left|J_c\left(\boldsymbol{\alpha}\right)\right| = \left|\int_\Omega \mathbf{P}^{\mathrm{T}}\mathbf{U}H\left(\Phi\right)d\Omega\right| \\ &\text{s.t.} \left(\mathbf{K} + iw\mathbf{C} - w^2\mathbf{M}\right)\mathbf{U} = \mathbf{P} \\ &\int_\Omega H\left(\Phi\right)d\Omega - fV_0 \le 0 \\ &\alpha_{\min} \le \alpha_e \le \alpha_{\max}, e = 1,2,\cdots,N \end{aligned} \tag{5-34}$$

in which the objective function J is the module of the structural dynamic compliance J_c, defined by $J = \sqrt{J_R{}^2 + J_I{}^2}$. J_R and J_I are the real and image parts of J_c. Φ represents the LSF, H represents the Heaviside function, V_0 is the total volume of the structure, f is the volume fraction, α_e is the design variable, $\alpha_{\min}$ and $\alpha_{\max}$ are the minimum and the maximum value of the design variables, N is the number of the design variables.

5.2.1.3 The model reduction scheme for topology optimization

Dynamic topology optimization generally requires a large amount of computational cost due to the dynamic FEA. In order to reduce the calculation time, a series of model reduction (MR) schemes such as the Guyan reduction method, the modal truncation method, the mode superposition method, the Ritz vector method (RV), and the Quasi-static Ritz vector method (QSRV) have been proposed to solve the problem [48,254,255,256,257 . Dynamic FEA is

time consuming especially for a large number of degrees of freedom. The MR scheme is an efficient way to transform a set of the system equation into a set of reduced equations with a smaller number of degrees of freedom. This does not mean we will use with a small number of elements for the structure but mean to reduce the number of degrees of freedom of the finite element model and change the global dynamic stiffness matrix to a reduced dynamic stiffness matrix by transforming the nodal coordinate system into a generalized modal coordinate system [258,259 .

There are many kinds of MR schemes, and these methods generally aim to reduce the number of degrees of freedom by finding efficient reduction bases for dynamic structures. Among those, the GR method reduces the mass matrix based on partitioning the stiffness matrix. The other methods have similar mechanisms in reducing the scale of the finite element system. They transform a large number of system equations into a small number of equations by changing the orthogonal bases in the original coordinates to the some chosen modal bases, thus approximating the displacement response by the approximated response.

The main process of the model reduction method is briefly introduced as follows. For a structure with N degrees of freedom, the approximated displacement response $\tilde{\mathbf{U}}$ can be expressed as:

$$\mathbf{U} \cong \tilde{\mathbf{U}}=\boldsymbol{\Psi}\mathbf{Q}, \boldsymbol{\Psi}=\left[\boldsymbol{\psi}_1, \boldsymbol{\psi}_2, \cdots, \boldsymbol{\psi}_{N_d}\right], \left(N_d \leq N\right) \tag{5-35}$$

where $\boldsymbol{\Psi}$ is the matrix of a series of the considered orthonormal basis $\boldsymbol{\psi}_i$, and $\mathbf{Q}$ is the frequency dependent vector of the order N_d. Based on the Eq. (5-35), pre-multiplying $\boldsymbol{\Psi}^{\mathrm{T}}$ into the Eq. (5-33):

$$\underbrace{\left[\boldsymbol{\Psi}^{\mathrm{T}}\left(\mathbf{K}+jw\mathbf{C}-w^{2}\mathbf{M}\right)\boldsymbol{\Psi}\right]}_{n_d\times n_d}\mathbf{Q}=\underbrace{\boldsymbol{\Psi}^{\mathrm{T}}\mathbf{P}}_{n_d\times 1} \tag{5-36}$$

By solving the above equation, $\mathbf{Q}$ can be calculated, and then the approximated displacement $\tilde{\mathbf{U}}$ can be obtained. The calculation efficiency and precision mainly depend on the matrix $\boldsymbol{\Psi}$, so it is of importance to properly choose the orthonormal basis $\boldsymbol{\psi}_i$ and n_d.

The Ritz vector method and the quasi-static Ritz vector method are model reduction approaches based on Ritz vector [51 . In the Ritz vector method, the reduction bases matrix $\boldsymbol{\Psi}$ is constructed by considering the mass matrix $\mathbf{M}$, stiffness matrix $\mathbf{K}$, and external force $\mathbf{P}$. The first basis is constructed by solving the static equation:

$$\boldsymbol{\Psi}_1^{*}=\mathbf{K}^{-1}\mathbf{P} \tag{5-37}$$

Then $\boldsymbol{\psi}_1$ is achieved by normalizing the static displacement to the mass matrix as follows:

$$\boldsymbol{\Psi}_1=\frac{1}{\boldsymbol{\Psi}_1^{*}\mathbf{M}\boldsymbol{\Psi}_1^{*}}\boldsymbol{\Psi}_1^{*} \tag{5-38}$$

The next basis can then be sequentially obtained by considering the previous bases, the mass and stiffness matrices:

$$\boldsymbol{\Psi}_i^{*}=\mathbf{K}^{-1}\left(\mathbf{M}\boldsymbol{\Psi}_{i-1}\right) \tag{5-39}$$

Then we should perform the orthogonalization and normalization:

$$\boldsymbol{\Psi}_i^{**}=\boldsymbol{\Psi}_i^{*}-\sum_{k=1}^{i-1}\left(\boldsymbol{\Psi}_k^{*\mathrm{T}}\mathbf{M}\boldsymbol{\Psi}_k^{*}\right)\boldsymbol{\Psi}_k,\boldsymbol{\Psi}_i=\frac{1}{\boldsymbol{\Psi}_i^{**\mathrm{T}}\mathbf{M}\boldsymbol{\Psi}_i^{**}}\boldsymbol{\Psi}_i^{**} \tag{5-40}$$

in which $\mathbf{\Psi}_i^*$ and $\mathbf{\Psi}_i^{**}$ are the intermediate variables. All the bases can be constructed by repeating the above equations. The matrix $\mathbf{\Psi}$ for the model reduction is built from all the bases vectors. The number of the chosen bases can be decided based on the accuracy we need in the dynamic FEA. After obtaining the bases and solving the equation (5-36), the displacement can then be approximated as follows:

$$\mathbf{U} = \mathbf{\Psi Q} \tag{5-41}$$

The QSRV method is an extended form of the RV method. The reduction bases are obtained from a quasi-static process, and the dynamic response of a structure can then be better approximated near at the center frequency. The first basis can be constructed:

$$\mathbf{\Psi}_1^* = \left(\mathbf{K} - w_c^2\mathbf{M}\right)^{-1}\mathbf{P}, \mathbf{\Psi}_1 = \frac{1}{\mathbf{\Psi}_1^*\mathbf{M}\mathbf{\Psi}_1^*}\mathbf{\Psi}_1^* \tag{5-42}$$

Then the other bases can then be sequentially obtained:

$$\mathbf{\Psi}_i^* = \left(\mathbf{K} - w_c^2\mathbf{M}\right)^{-1}\left(\mathbf{M}\mathbf{\Psi}_{i-1}\right) \tag{5-43}$$

$$\mathbf{\Psi}_i^{**} = \mathbf{\Psi}_i^* - \sum_{k=1}^{i-1}\left(\mathbf{\Psi}_k^{*\mathrm{T}}\mathbf{M}\mathbf{\Psi}_k^*\right)\mathbf{\Psi}_k, \mathbf{\Psi}_i = \frac{1}{\mathbf{\Psi}_i^{**\mathrm{T}}\mathbf{M}\mathbf{\Psi}_i^{**}}\mathbf{\Psi}_i^{**} \tag{5-44}$$

where w_c is the center frequency of interest. Similarly, the response of the structure can then be approximated by equation (5-41). From the above, we can see that if $w_c = 0$, the QSRV method will become the RV method. Here, QSRV will be applied to approximate the structure response in the dynamic FEA.

5.2.1.4 Sensitivity analysis

The global frequency optimization for structures is a self-adjoint problem. The theories of the shape derivative and material derivative, as well as the adjoint method [237 , are applied to deduce the sensitivities with respect to the design variables. Topology optimization problem for a dynamic structure can be re-expressed as:

$$\begin{aligned}
&\min_{\boldsymbol{\alpha}} J(\mathbf{u},\Phi) = \left|J_c(\mathbf{u},\Phi)\right| = \left|\int_\Omega \mathbf{P}^{\mathrm{T}}\mathbf{U}H(\Phi)d\Omega\right| \\
&\text{s.t.}\quad k(u,v,\Phi) + iwc(u,v,\Phi) - w^2 m(u,v,\Phi) = l(v,\Phi) \\
&\qquad G(u,\Phi) = \int_\Omega H(\Phi)d\Omega - V_{max} \le 0 \\
&\qquad \alpha_{e,\min} \le \alpha_e \le \alpha_{e,\max},\ \forall v \in \mathbf{U},\ \ \mathbf{u}|_{\Gamma_d} = \mathbf{u}_0
\end{aligned} \tag{5-45}$$

in which $k(\mathbf{u},\mathbf{v},\Phi)$ is the semi-bilinear form of the structural stiffness, $c(\mathbf{u},\mathbf{v},\Phi)$ is the semi-bilinear form of the structural damping, $m(\mathbf{u},\mathbf{v},\Phi)$ the semi-bilinear form of the structural mass, and $l(\mathbf{v})$ is the semi-bilinear form of the loading, as follows:

$$\begin{aligned}
k(\mathbf{u},\mathbf{v},\Phi) &= \int_\Omega E_{ijkl}\varepsilon_{ij}(\mathbf{u})\varepsilon_{kl}(\mathbf{v})H(\Phi)d\Omega \\
m(\mathbf{u},\mathbf{v},\Phi) &= \int_\Omega \rho\mathbf{u}\mathbf{v}H(\Phi)d\Omega \\
c(\mathbf{u},\mathbf{v},\Phi) &= A\int_\Omega E_{ijkl}\varepsilon_{ij}(\mathbf{u})\varepsilon_{kl}(\mathbf{v})H(\Phi)d\Omega + B\int_\Omega \rho\mathbf{u}\mathbf{v}H(\Phi)d\Omega \\
l(\mathbf{v},\Phi) &= \int_\Omega \mathbf{p}\mathbf{v}H(\Phi)d\Omega + \int_{\Gamma_n} \boldsymbol{\tau}\mathbf{v}d\Gamma_n
\end{aligned} \tag{5-46}$$

Then the dynamic compliance can be rewritten as:

$$\begin{aligned}
&J_c(\mathbf{u},\Phi) = \int_\Omega \mathbf{p}\mathbf{u}H(\Phi)d\Omega + \int_{\Gamma_n} \boldsymbol{\tau}\mathbf{u}d\Gamma_n \\
&= (1+i\omega A)k(\mathbf{u},\mathbf{u},\Phi) + (i\omega B - \omega^2)m(\mathbf{u},\mathbf{u},\Phi) \\
&= (1+i\omega A)\int_\Omega E_{ijkl}\varepsilon_{ij}(\mathbf{u})\varepsilon_{kl}(\mathbf{u})H(\Phi)d\Omega + (i\omega B - \omega^2)\int_\Omega \rho\mathbf{u}\mathbf{u}H(\Phi)d\Omega \\
&= \int_\Omega \left((1+i\omega A)E_{ijkl}\varepsilon_{ij}(\mathbf{u})\varepsilon_{kl}(\mathbf{u}) + (i\omega B - \omega^2)\rho\mathbf{u}\mathbf{u}\right)H(\Phi)d\Omega
\end{aligned} \tag{5-47}$$

The material derivative of the dynamic compliance is:

$$\begin{aligned}\dot{J}_c(\mathbf{u},\Phi) &= 2\int_\Omega \left((1+i\omega A)E_{ijkl}\varepsilon_{ij}(\dot{\mathbf{u}})\varepsilon_{kl}(\mathbf{u}) + \left(i\omega B-\omega^2\right)\rho\dot{\mathbf{u}}\mathbf{u}\right)H(\Phi)d\Omega \\ &+\int_{\partial\Omega}\left((1+i\omega A)E_{ijkl}\varepsilon_{ij}(\mathbf{u})\varepsilon_{kl}(\mathbf{u}) + \left(i\omega B-\omega^2\right)\rho\mathbf{u}\mathbf{u}\right)\mathbf{v}_n d\Gamma\end{aligned} \tag{5-48}$$

From Eqs. (5-45) and (5-46), the dynamic state equation is:

$$(1+i\omega A)k(\mathbf{u},\mathbf{v},\Phi) + \left(i\omega B-\omega^2\right)m(\mathbf{u},\mathbf{v},\Phi) = \int_\Omega \mathbf{p}\mathbf{v}H(\Phi)d\Omega + \int_{\Gamma_n}\boldsymbol{\tau}\mathbf{v}d\Gamma_n \tag{5-49}$$

By the material derivative, we can then obtain:

$$\begin{aligned}&(1+i\omega A)\left[k(\dot{\mathbf{u}},\mathbf{v},\Phi)+k(\mathbf{u},\dot{\mathbf{v}},\Phi)+\int_{\partial\Omega}\left(E_{ijkl}\varepsilon_{ij}(\mathbf{u})\varepsilon_{kl}(\mathbf{v})\right)\mathbf{v}_n d\Gamma\right] \\ &+\left(i\omega B-\omega^2\right)\left[m(\dot{\mathbf{u}},\mathbf{v},\Phi)+m(\mathbf{u},\dot{\mathbf{v}},\Phi)+\int_{\partial\Omega}(\rho\mathbf{u}\mathbf{v})\mathbf{v}_n d\Gamma\right] \\ &=\int_\Omega \mathbf{p}\dot{\mathbf{v}}H(\Phi)d\Omega+\int_{\partial\Omega}(\mathbf{p}\mathbf{v})\mathbf{v}_n d\Gamma+\int_{\Gamma_n}\boldsymbol{\tau}\dot{\mathbf{v}}d\Gamma_n+\int_{\partial\Omega}\left(\nabla(\boldsymbol{\tau}\mathbf{v})\cdot\mathbf{n}+\kappa(\boldsymbol{\tau}\mathbf{v})\right)\mathbf{v}_n d\Gamma\end{aligned} \tag{5-50}$$

Since $\dot{\mathbf{v}}\in\mathbf{U}$, the dynamic state equation (5-49) will be:

$$(1+i\omega A)k(\mathbf{u},\dot{\mathbf{v}},\Phi) + \left(i\omega B-\omega^2\right)m(\mathbf{u},\dot{\mathbf{v}},\Phi) = \int_\Omega \mathbf{p}\dot{\mathbf{v}}H(\Phi)d\Omega + \int_{\Gamma_n}\boldsymbol{\tau}\dot{\mathbf{v}}d\Gamma_n \tag{5-51}$$

Put equation (5-51) into (5-50), we can get:

$$\begin{aligned}&(1+i\omega A)k(\dot{\mathbf{u}},\mathbf{v},\Phi)+\left(i\omega B-\omega^2\right)m(\dot{\mathbf{u}},\mathbf{v},\Phi) \\ &=\int_{\partial\Omega}\left[\mathbf{p}\mathbf{v}-(1+i\omega A)E_{ijkl}\varepsilon_{ij}(\mathbf{u})\varepsilon_{kl}(\mathbf{v})-\left(i\omega B-\omega^2\right)\rho\mathbf{u}\mathbf{v}+\nabla(\boldsymbol{\tau}\mathbf{v})\cdot\mathbf{n}+\kappa(\boldsymbol{\tau}\mathbf{v})\right]\mathbf{v}_n d\Gamma\end{aligned} \tag{5-52}$$

The global frequency optimization is a self-adjoint problem, then we can define $\mathbf{v}=\mathbf{u}$. The above equation can then be rewritten as:

$$\begin{aligned}&(1+i\omega A)k(\dot{\mathbf{u}},\mathbf{u},\Phi)+\left(i\omega B-\omega^2\right)m(\dot{\mathbf{u}},\mathbf{u},\Phi) \\ &=\int_{\partial\Omega}\left[\mathbf{p}\mathbf{u}-(1+i\omega A)E_{ijkl}\varepsilon_{ij}(\mathbf{u})\varepsilon_{kl}(\mathbf{u})-\left(i\omega B-\omega^2\right)\rho\mathbf{u}\mathbf{u}+\nabla(\boldsymbol{\tau}\mathbf{u})\cdot\mathbf{n}+\kappa(\boldsymbol{\tau}\mathbf{u})\right]\mathbf{v}_n d\Gamma\end{aligned} \tag{5-53}$$

Then the material derivative of the dynamic compliance is:

$$\begin{aligned}\dot{J}_c(\mathbf{u},\Phi) &= \int_{\partial\Omega} 2\begin{pmatrix}\mathbf{pu}-(1+i\omega A)E_{ijkl}\varepsilon_{ij}(\mathbf{u})\varepsilon_{kl}(\mathbf{u})\\ -(i\omega B-\omega^2)\rho\mathbf{uu}+\nabla(\boldsymbol{\tau}\mathbf{u})\cdot\mathbf{n}+\kappa(\boldsymbol{\tau}\mathbf{u})\end{pmatrix}\mathbf{v}_n d\Gamma \\ &+\int_{\partial\Omega}\left((1+i\omega A)k(\mathbf{u},\mathbf{u},\Phi)+(i\omega B-\omega^2)m(\mathbf{u},\mathbf{u},\Phi)\right)\mathbf{v}_n d\Gamma \\ &=\int_{\partial\Omega}\gamma(\mathbf{u})\mathbf{v}_n d\Gamma\end{aligned} \tag{5-54}$$

in which:

$$\gamma(\mathbf{u}) = 2\mathbf{pu}-(1+i\omega A)E_{ijkl}\varepsilon_{ij}(\mathbf{u})\varepsilon_{kl}(\mathbf{u})-(i\omega B-\omega^2)\rho\mathbf{uu}+2\left(\nabla(\boldsymbol{\tau}\mathbf{u})\cdot\mathbf{n}+\kappa(\boldsymbol{\tau}\mathbf{u})\right) \tag{5-55}$$

Introducing Lagrange multipliers Λ and λ, the original optimization problem (5-45) will be turned into the following:

$$L = J_c(\mathbf{u},\Phi)+\lambda\left[k(\mathbf{u},\mathbf{v},\Phi)+iwc(\mathbf{u},\mathbf{v},\Phi)-w^2m(\mathbf{u},\mathbf{v},\Phi)-l(\mathbf{v},\Phi)\right]+\Lambda G(\mathbf{u},\Phi) \tag{5-56}$$

Take the derivative of the Lagrange function:

$$\frac{\partial L}{\partial t} = \frac{\partial J_c(\mathbf{u},\Phi)}{\partial t}+\Lambda\frac{\partial G(\mathbf{u},\Phi)}{\partial t} = \int_{\partial\Omega}\gamma(\mathbf{u})\mathbf{v}_n d\Gamma+\Lambda\int_{\partial\Omega}\mathbf{v}_n d\Gamma \tag{5-57}$$

The boundary derivative can be turned into volume derivative:

$$|\partial\Omega| = \int_\Gamma d\Gamma = \int_\Omega \delta(\Phi)|\nabla\Phi| d\Omega \tag{5-58}$$

Then equation (5-57) can be rewritten as:

$$\frac{\partial L}{\partial t} = \int_\Omega \gamma(\mathbf{u})\mathbf{v}_n\delta(\Phi)|\nabla\Phi| d\Omega+\Lambda\int_\Omega \mathbf{v}_n\delta(\Phi)|\nabla\Phi| d\Omega \tag{5-59}$$

Based on the velocity field from the CSRBF interpolation, we can obtain:

$$\begin{aligned}\frac{\partial L}{\partial t} &= \int_\Omega \gamma(\mathbf{u}) \frac{\boldsymbol{\phi}(\mathbf{x})^{\mathrm{T}} \dot{\boldsymbol{\alpha}}(t)}{\left|\nabla \boldsymbol{\phi}(\mathbf{x})^{\mathrm{T}} \boldsymbol{\alpha}(t)\right|} \delta(\Phi) |\nabla \Phi| d\Omega + \Lambda \int_\Omega \frac{\boldsymbol{\phi}(\mathbf{x})^{\mathrm{T}} \dot{\boldsymbol{\alpha}}(t)}{\left|\nabla \boldsymbol{\phi}(\mathbf{x})^{\mathrm{T}} \boldsymbol{\alpha}(t)\right|} \delta(\Phi) |\nabla \Phi| d\Omega \\ &= \left[\int_\Omega \gamma(\mathbf{u}) \frac{\boldsymbol{\phi}(\mathbf{x})^{\mathrm{T}}}{\left|\nabla \boldsymbol{\phi}(\mathbf{x})^{\mathrm{T}} \boldsymbol{\alpha}(t)\right|} \delta(\Phi) |\nabla \Phi| d\Omega \right] \dot{\boldsymbol{\alpha}}(t) + \Lambda \left[\int_\Omega \frac{\boldsymbol{\phi}(\mathbf{x})^{\mathrm{T}}}{\left|\nabla \boldsymbol{\phi}(\mathbf{x})^{\mathrm{T}} \boldsymbol{\alpha}(t)\right|} \delta(\Phi) |\nabla \Phi| d\Omega \right] \dot{\boldsymbol{\alpha}}(t) \\ &= \left[\sum_{e=1}^{N} \int_\Omega \gamma(\mathbf{u}) \frac{\varphi_e(\mathbf{x})^{\mathrm{T}}}{\left|\nabla \boldsymbol{\phi}(\mathbf{x})^{\mathrm{T}} \boldsymbol{\alpha}(t)\right|} \delta(\Phi) |\nabla \Phi| d\Omega \right] \dot{\boldsymbol{\alpha}}(t) + \Lambda \left[\sum_{e=1}^{N} \int_\Omega \frac{\varphi_e(\mathbf{x})^{\mathrm{T}}}{\left|\nabla \boldsymbol{\phi}(\mathbf{x})^{\mathrm{T}} \boldsymbol{\alpha}(t)\right|} \delta(\Phi) |\nabla \Phi| d\Omega \right] \dot{\boldsymbol{\alpha}}(t)\end{aligned} \tag{5-60}$$

where $i = 1, 2, \cdots, N$ represents the control point of the CSRBF. On the other hand, according to the chain rule:

$$\frac{\partial L}{\partial t} = \left[\sum_{e=1}^{N} \frac{\partial J_c(\mathbf{u}, \Phi)}{\partial \alpha_e(t)} \right] \dot{\boldsymbol{\alpha}}(t) + \Lambda \left[\sum_{e=1}^{N} \frac{\partial G(\mathbf{u}, \Phi)}{\partial \alpha_e(t)} \right] \dot{\boldsymbol{\alpha}}(t) \tag{5-61}$$

Comparing Eqs. (5-60) and (5-61), the sensitivities of the objective function with respect to the expansion coefficients are:

$$\frac{\partial J_c(\mathbf{u}, \Phi)}{\partial \alpha_e(t)} = \int_\Omega \gamma(\mathbf{u}) \frac{\varphi_e(x)}{\left|(\nabla \boldsymbol{\varphi})^T \boldsymbol{\alpha}(t)\right|} \delta(\Phi) |\nabla \Phi| d\Omega = \int_\Omega \gamma(\mathbf{u}) \varphi_e(x) \delta(\Phi) d\Omega \tag{5-62}$$

Based on the chain rule, the derivatives of the objective function with respect to the expansion coefficients can then be calculated by:

$$\frac{\partial J}{\partial \alpha_e} = \frac{1}{J} \left(J_R \frac{\partial J_R}{\partial \alpha_e} + J_I \frac{\partial J_I}{\partial \alpha_e} \right) \tag{5-63}$$

And the sensitivities of the volume constraint with respect to the expansion coefficients are:

$$\frac{\partial G(\mathbf{u}, \Phi)}{\partial \alpha_e(t)} = \int_\Omega \varphi_e(x) \delta(\Phi) d\Omega \tag{5-64}$$

5.2.2 Robust dynamic topology optimization

5.2.2.1 Robust dynamic topology optimization formulation

$\boldsymbol{\xi} = (\xi_1, \xi_2, \cdots, \xi_n)$ is regarded as the probability vector and $\boldsymbol{\eta} = (\eta_1, \eta_2, \cdots, \eta_m)$ is regarded as the interval vector in a structure. With hybrid uncertainties, the dynamic structure compliance can then be expressed as $J(\boldsymbol{\xi}, \boldsymbol{\eta})$. The robust objective function is defined as a linear combination of the mean μ and standard deviation σ of structure compliance:

$$g = \mu\left(J(\boldsymbol{\xi}, \boldsymbol{\eta})\right) + h \cdot \sigma\left(J(\boldsymbol{\xi}, \boldsymbol{\eta})\right) \tag{5-65}$$

where h is the weighting coefficients, which is set as 1 here. The above is belonging to an interval rather than a constant value according to the interval uncertainties, we define the new robust objective function under the worst case and the RTO problem is given as:

$$\begin{aligned} &\min_{\boldsymbol{\alpha}} \ \mathrm{g} = \max\left(\mu\left(J(\boldsymbol{\xi}, \boldsymbol{\eta})\right) + \sigma\left(J(\boldsymbol{\xi}, \boldsymbol{\eta})\right)\right) \\ &s.t. \ \ V = \int_{\Omega} H\left(\Phi(\boldsymbol{\xi}, \boldsymbol{\eta})\right) d\Omega \le V_{max} \\ &\quad \left(\mathbf{K} + jw\mathbf{C} - w^2\mathbf{M}\right)\mathbf{U} = \mathbf{P} \\ &\quad \alpha_{\min} \le \alpha_e \le \alpha_{\max}, e = 1, 2, \cdots, N \end{aligned} \tag{5-66}$$

where $\alpha_e^{\mathrm{MA}} (e = 1, 2, \cdots, N)$ is the design variable of the eth finite element, and N is the number of the design variables. $\mathbf{M}$ is the global mass matrix, $\mathbf{C}$ is the global damping matrix, $\mathbf{K}$ is the global stiffness matrix, and $\mathbf{P}$ is the magnitude of the dynamic load with frequency w.

Using the proposed iPCCI method in section 4.1.2, the robust objective function can be evaluated from Eqs. (4-34) and (4-35), as follows:

$$
\begin{aligned}
g &= \mu^R\left(J\left(\boldsymbol{\xi},\boldsymbol{\eta}\right)\right)+\sigma^R\left(J\left(\boldsymbol{\xi},\boldsymbol{\eta}\right)\right) \\
&= c_{\mathbf{0},\mathbf{0}}+\left(\sum_{\boldsymbol{\chi}_2\in\mathbb{N}^m,\boldsymbol{\chi}_2\neq\mathbf{0}}\left|c_{\mathbf{0},\boldsymbol{\chi}_2}\right|\right)+\sqrt{\sum_{\boldsymbol{\chi}_1\in\mathbb{N}^n,\boldsymbol{\chi}_1\neq\mathbf{0}}\sum_{\boldsymbol{\chi}_2\in\mathbb{N}^m}c_{\boldsymbol{\chi}_1,\boldsymbol{\chi}_2}^2+2\left|\sum_{\boldsymbol{\chi}_1\in\mathbb{N}^n,\boldsymbol{\chi}_1\neq\mathbf{0}}\sum_{\boldsymbol{\chi}_2\in\mathbb{N}^m}c_{\boldsymbol{\chi}_1,\boldsymbol{\chi}_2^i}c_{\boldsymbol{\chi}_1,\boldsymbol{\chi}_2^j}\right|} \\
&= c_{\mathbf{0},\mathbf{0}}+\left(\sum_{\boldsymbol{\chi}_2\in\mathbb{N}^m,\boldsymbol{\chi}_2\neq\mathbf{0}}\left|c_{\mathbf{0},\boldsymbol{\chi}_2}\right|\right)+\sqrt{\sum_{\boldsymbol{\chi}_1\in\mathbb{N}^n,\boldsymbol{\chi}_1\neq\mathbf{0}}\sum_{\boldsymbol{\chi}_2\in\mathbb{N}^m}c_{\boldsymbol{\chi}_1,\boldsymbol{\chi}_2}^2+2\left|\Upsilon\right|}
\end{aligned}
\tag{5-67}
$$

in which $\Upsilon=\sum_{\boldsymbol{\chi}_1\in\mathbb{N}^n,\boldsymbol{\chi}_1\neq\mathbf{0}}\sum_{\boldsymbol{\chi}_2\in\mathbb{N}^m}c_{\boldsymbol{\chi}_1,\boldsymbol{\chi}_2^i}c_{\boldsymbol{\chi}_1,\boldsymbol{\chi}_2^j}$.

5.2.2.2 Sensitivity analysis

In Eq. (5-67), g is a function of design variables **α**, and the coefficients $c_{\boldsymbol{\chi}_1,\boldsymbol{\chi}_2}$ also depend on the design variables. The sensitivities of the robust objective function with respect to the design variables are:

$$
\frac{\partial g}{\partial\alpha_e}=\frac{\partial c_{\mathbf{0},\mathbf{0}}}{\partial\alpha_e}+\left(\sum_{\boldsymbol{\chi}_2\in\mathbb{N}^m,\boldsymbol{\chi}_2\neq\mathbf{0}}\frac{\partial\left|c_{\mathbf{0},\boldsymbol{\chi}_2}\right|}{\partial\alpha_e}\right)+\frac{1}{\sigma^R}\sum_{\boldsymbol{\chi}_1\in\mathbb{N}^n,\boldsymbol{\chi}_1\neq\mathbf{0}}\left(\sum_{\boldsymbol{\chi}_2\in\mathbb{N}^m}c_{\boldsymbol{\chi}_1,\boldsymbol{\chi}_2}\frac{\partial c_{\boldsymbol{\chi}_1,\boldsymbol{\chi}_2}}{\partial\alpha_e}+\left|\Upsilon\right|/\partial\alpha_e\right)
\tag{5-68}
$$

Using the sign function in (5-14), the sensitivities in Eq. (5-68) can be re-expressed as:

$$
\frac{\partial g}{\partial\alpha_e}=\frac{\partial c_{\mathbf{0},\mathbf{0}}}{\partial\alpha_e}+\left(\sum_{\boldsymbol{\chi}_2\in\mathbb{N}^m,\boldsymbol{\chi}_2\neq\mathbf{0}}\frac{\partial\left(c_{\mathbf{0},\boldsymbol{\chi}_2}\operatorname{sign}\left(c_{\mathbf{0},\boldsymbol{\chi}_2}\right)\right)}{\partial\alpha_e}\right)+\frac{1}{\sigma^R}\sum_{\boldsymbol{\chi}_1\in\mathbb{N}^n,\boldsymbol{\chi}_1\neq\mathbf{0}}\left(\sum_{\boldsymbol{\chi}_2\in\mathbb{N}^m}c_{\boldsymbol{\chi}_1,\boldsymbol{\chi}_2}\frac{\partial c_{\boldsymbol{\chi}_1,\boldsymbol{\chi}_2}}{\partial\alpha_e}+\left(\Upsilon\operatorname{sign}\left(\Upsilon\right)\right)/\partial\alpha_e\right)
\tag{5-69}
$$

Since the sign function in the above equation is not differentiable at the point x=0, the Heaviside projection method is used to smooth the sign function using the tanh function in Eq. (5-16). Then the Eq. (5-69) is transformed into:

$$\frac{\partial g}{\partial \alpha_e}=\frac{\partial c_{\mathbf{0},\mathbf{0}}}{\partial \alpha_e}+\sum_{\chi_2\in\mathbb{N}^m,\chi_2\neq\mathbf{0}}\left(\tanh\left(\ell c_{\mathbf{0},\chi_2}\right)+\ell c_{\mathbf{0},\chi_2}\operatorname{sech}^2\left(\ell c_{\mathbf{0},\chi_2}\right)\right)\frac{\partial c_{\mathbf{0},\chi_2}}{\partial \alpha_e}$$
$$+\frac{1}{\sigma^R}\sum_{\chi_1\in\mathbb{N}^n,\chi_1\neq\mathbf{0}}\left(\begin{array}{l}\displaystyle\sum_{\chi_2\in\mathbb{N}^m}c_{\chi_1,\chi_2}\frac{\partial c_{\chi_1,\chi_2}}{\partial \alpha_e}+\left(\tanh\left(\ell\Upsilon\right)+\ell\Upsilon\operatorname{sech}^2\left(\ell\Upsilon\right)\right)\\ \times\left(\displaystyle\sum_{\chi_1\in\mathbb{N}^n,\chi_1\neq\mathbf{0}}\sum_{\chi_2\in\mathbb{N}^m}\left(c_{\chi_1,\chi_2^j}\frac{\partial c_{\chi_1,\chi_2^j}}{\partial \alpha_e}+\partial c_{\chi_1,\chi_2^j}\frac{\partial c_{\chi_1,\chi_2^j}}{\partial \alpha_e}\right)\right)\end{array}\right) \tag{5-70}$$

In the above equation, $\partial c_{\chi_1,\chi_2}/\partial \alpha_e$ is still the unknown part. The sensitivity in Eq. (5-62) can be as a function, and can be expanded by the PCCI as follows:

$$\frac{\partial J(\boldsymbol{\alpha})}{\partial \alpha_e}=\int_\Omega \gamma(u)\varphi_e(x)\delta(\Phi)d\Omega=\sum_{\chi_1\in\mathbb{N}^n}\sum_{\chi_2\in\mathbb{N}^m}\gamma_{\chi_1,\chi_2}\Psi_{\chi_2}(\boldsymbol{\eta})H_{\chi_1}(\boldsymbol{\xi}) \tag{5-71}$$

where γ_{χ_1,χ_2} are the coefficients in the PCCI expansion. On the other hand, by differentiating the Eq. (4-31) with respect to design variable on both sides, we can get the derivatives as:

$$\frac{\partial J(\boldsymbol{\alpha})}{\partial \alpha_e}=\sum_{\chi_1\in\mathbb{N}^n}\sum_{\chi_2\in\mathbb{N}^m}\frac{\partial c_{\chi_1,\chi_2}}{\partial \alpha_e}\Psi_{\chi_2}(\boldsymbol{\eta})H_{\chi_1}(\boldsymbol{\xi}) \tag{5-72}$$

Comparing Eqs. (5-71) and (5-72), we can get:

$$\frac{\partial c_{\chi_1,\chi_2}}{\partial \alpha_e}=\gamma_{\chi_1,\chi_2} \tag{5-73}$$

Substituting Eq. (5-73) into Eq. (5-70), the final expression of the sensitivities of the robust objective function can be obtained:

$$\frac{\partial g}{\partial \alpha_e}=\frac{\partial c_{\mathbf{0},\mathbf{0}}}{\partial \alpha_e}+\sum_{\chi_2\in\mathbb{N}^m,\chi_2\neq\mathbf{0}}\left(\tanh\left(\ell c_{\mathbf{0},\chi_2}\right)+\ell c_{\mathbf{0},\chi_2}\,\mathrm{sech}^2\left(\ell c_{\mathbf{0},\chi_2}\right)\right)\gamma_{\mathbf{0},\chi_2}$$
$$+\frac{1}{\sigma^R}\sum_{\chi_1\in\mathbb{N}^n,\chi_1\neq\mathbf{0}}\left(\begin{array}{l}c_{\chi_1,\chi_2}\gamma_{\chi_1,\chi_2}+\left(\tanh\left(\ell\Upsilon\right)+\ell\Upsilon\,\mathrm{sech}^2\left(\ell\Upsilon\right)\right)\\ \times\left(\sum_{\chi_1\in\mathbb{N}^n,\chi_1\neq\mathbf{0}}\sum_{\chi_2\in\mathbb{N}^m}\left(c_{\chi_1,\chi_2^i}\gamma_{\chi_1,\chi_2^j}+\partial c_{\chi_1,\chi_2^j}\gamma_{\chi_1,\chi_2^i}\right)\right)\end{array}\right) \tag{5-74}$$

5.2.3 Numerical examples

In this section, three examples are presented. In these examples, the mass density is $\rho=2700g/cm^3$, and the damping coefficients are $A=0.05, B=0.002$. In uncertain situations, the applied loadings and/or the material properties are considered as uncertain parameters. In the deterministic situations, the corresponding parameters are set as the mean values of the random variables and the midpoint values of the interval variables.

Example 1

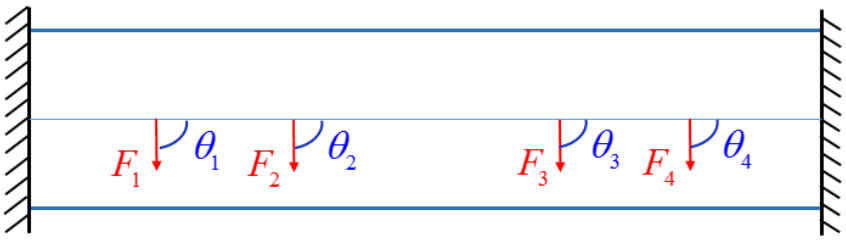

Figure 5-7 Design domain and boundary condition for example 1

As shown in Figure 5-7, four dynamic loads F_1, F_2, F_3 and F_4 with frequency $w=100Hz$ are applied on the structure. The length of the structure is $6m$ and the width is $1m$. The left and the right boundaries of the beam are clamped. The elastic tensor is given as $E=7\times10^{10}$ Pa and the Poisson's ratio is given as $\upsilon=0.3$. The load directions are considered

as normal random variables, while the load maganitudes are assumed to be interval variables. The mean value of the load directions are set to be $\pi/2$, the standard variances of the load directions are given as $\pi/18$. The lower bounds of the load maganitudes are $2.7\times10^5 N$ and the upper bounds of the load maganitudes are set to be $3.3\times10^5 N$. The structure is discretized by 120×20 Q4 elements, and the volume fraction is 0.5.

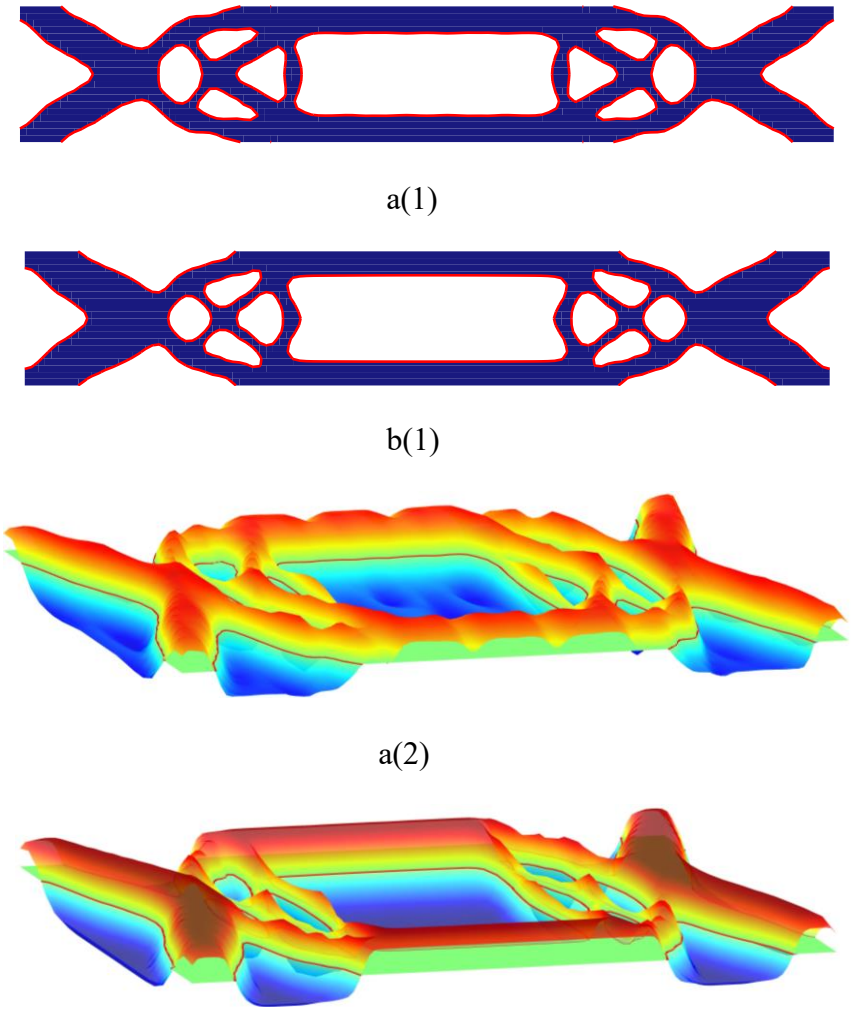

a(1)

b(1)

a(2)

b(2)

Figure 5-8 Optimized results for deterministic and robust designs for example 1

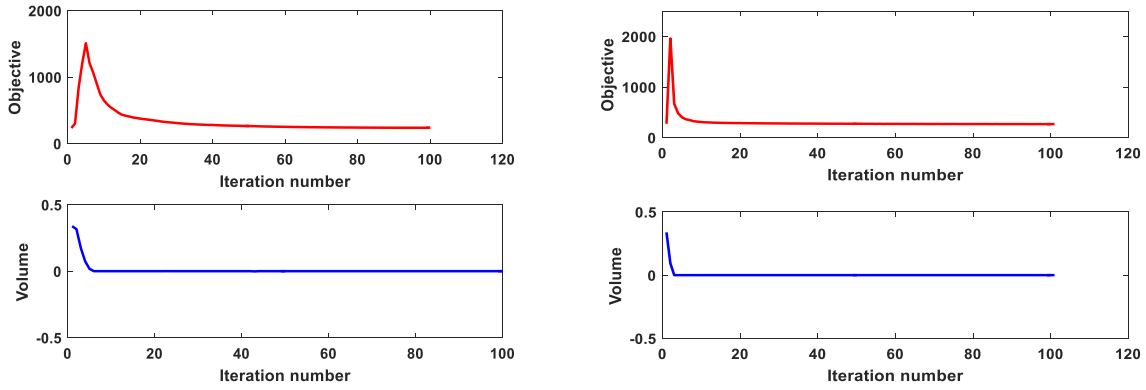

a(1) b(1)

Figure 5-9 Convergent histories of example 1

Figure 5-8 presents the topological design results for both deterministic and robust topology optimization. Figure 5-8 a(1)~a(2) are results of the deterministic design, b(1)~b(2) are results of the robust design under uncertainties. In Figure 5-8, a(1) and b(1) are the optimized topologies, a(2) and b(2) are the LSFs. It can be seen that the final topologies for the structure with uncertainties are different from the deterministic design. The convergent histories of the objective function and volume constraint are shown in Figure 5-9. In order to prove the effectiveness of the proposed method, some detailed results about the robust objective function values (e.g. mean and standard variance) of the robust and the deterministic designs under the uncertainties are given in Table 5-4. When applying the uncertainties on both deterministic and robust designs, the robust objective function values are 285.69 and 270.34, respectively, which means the robust topology optimization will result in a more robust design compared with the deterministic design. The FEA calls of the proposed method are also shown in Table 5-4. We can see that the proposed method will achieve close results to MCS results, and at the same time save computational costs.

Table 5-4 Robust objective function of optimized designs for example 1

Situations	Method	Mean	Standard variance	Robust objective function value	FEA calls
Deterministic design under uncertainties	iPCCI	280.30	5.39	285.69	2025
	MCS	282.64	5.10	287.74	1×10^7

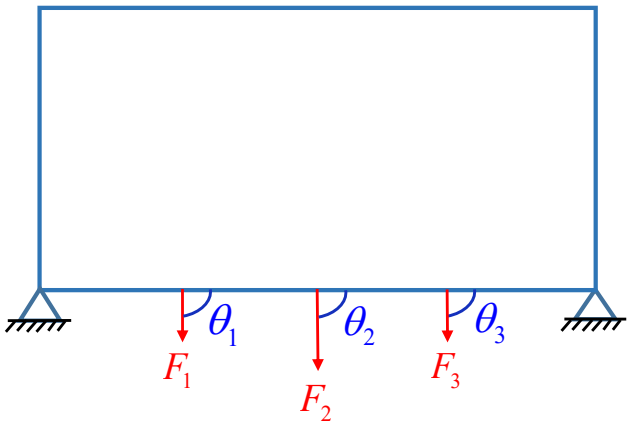

Figure 5-10 Design domain and boundary condition for example 2

A 2:1 beam is investigated in this example. The length of the structure is 1.6m and the width is 0.8m. The lower left and right corners of the beam are clamped. The elastic tensor is given as $E=7\times10^{10}$ Pa and the Poisson's ratio is given as $\upsilon=0.3$. As shown in Figure 5-10, three dynamic loads F_1, F_2 and F_3 with frequency $w=100Hz$ are applied on the lower side of the structure. The three load magnitudes are assumed as interval variables, and the three load

directions are considered as random variables. The load directions are assumed as normal variables with mean values $[\pi/2,\pi/2,\pi/2]$ and standard variances $[\pi/18,\pi/18,\pi/18]$. The loads values are assumed as interval variables. The midpoints of the three load magnitudes are 4×10^5N, 8×10^5N and 4×10^5N, and the radius are 4×10^4N, 8×10^4N and 4×10^4N. The structure is discretized by 80×40 Q4 elements, and the volume fraction is 0.5.

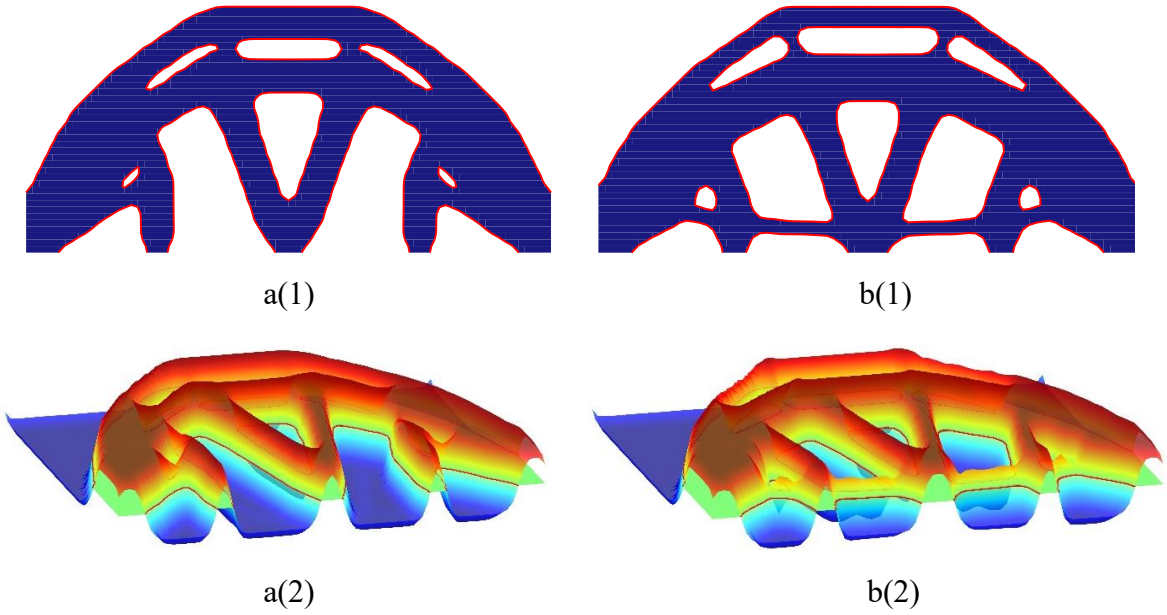

a(1) b(1)

a(2) b(2)

Figure 5-11 Optimized results for deterministic and robust designs for example 2

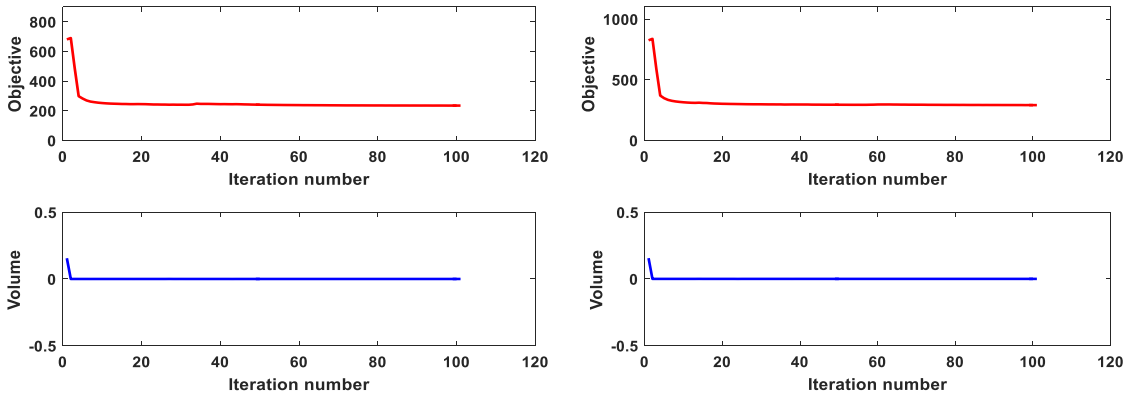

a(1) b(1)

Figure 5-12 Convergent histories of example 2

Table 5-5 Robust objective function of optimized designs for example 2

Situations	Method	Mean	Standard variance	Robust objective function value	FEA calls
Deterministic design under uncertainties	iPCCI	311.23	34.73	345.96	784
	MCS	310.43	34.32	344.75	1×10^7
Robust design under uncertainties	iPCCI	285.07	6.28	291.35	784
	MCS	285.39	5.88	291.27	1×10^7

The optimized results and the convergent histories are provided in Figure 5-11 and Figure 5-12. Figure 5-11 a(1) and b(1) are the deterministic and robust design results, a(2) and b(2) are the deterministic and robust LSFs. The robust design is obviously different from the deterministic design, which shows that the uncertainties have impacts on the topology optimization. With given uncertainties, the means and the standard deviations of the deterministic and robust designs are given in Table 5-5. The mean and the standard deviation of the robust design (285.07 and 6.28 respectively) are smaller than those of the deterministic design (311.23 and 34.73 respectively). It shows that the robust topology optimization can provide a design with better robustness compared with the deterministic one under uncertainties.

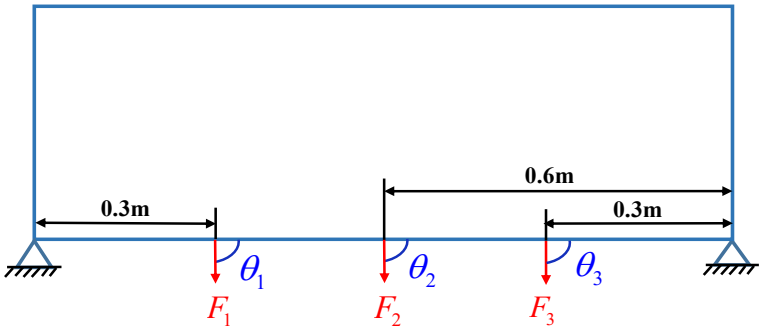

Figure 5-13 Design domain and boundary condition for example 3

A 1:3 beam is considered in this example. The length of the structure is $1.2m$ and the width is $0.4m$. The lower left and right corners of the beam are clamped. As shown in Figure 5-13, three dynamic loads F_1, F_2 and F_3 with frequency $w=100Hz$ are applied on the lower side of the structure. The three load magnitudes F_1, F_2 and F_3 and the load directions θ_1, θ_2, and θ_3 are considered as normal random variables, while the Young's modulus and the Poisson's ratio are assumed to be interval variables. The mean values of the three load magnitudes are all $5\times10^5 N$, the standard variance values of the three load magnitudes are $5\times10^4 N$. The load directions are with mean values $\pi/2$ and standard variances $\pi/12$. The interval variables are set to be $E=\left[6.3\times10^{10}\text{ Pa}, 7.7\times10^{10}\text{ Pa}\right]$ and $\upsilon=[0.27, 0.33]$. The structure is discretized by 120×40 Q4 elements, and the volume fraction is 0.5.

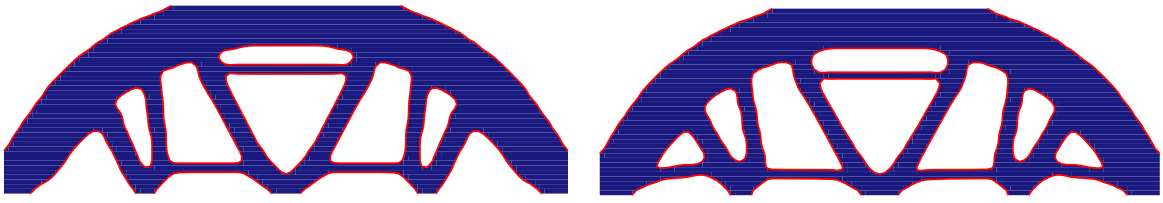

a(1) b(1)

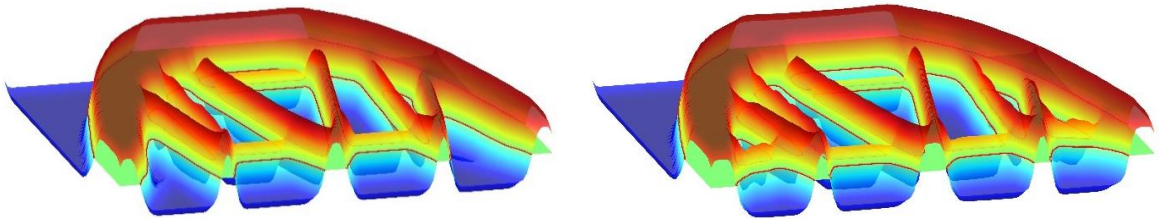

a(2) b(2)

Figure 5-14 Optimized results for deterministic and robust designs for example 3

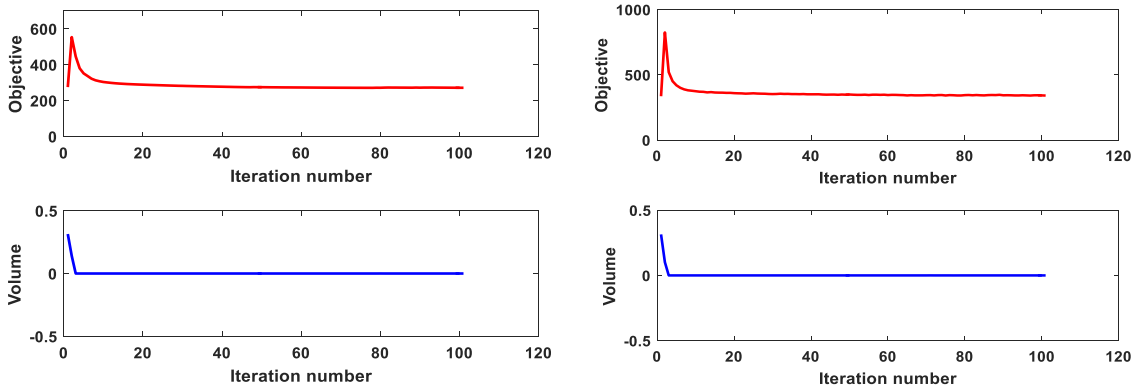

a(1) b(1)

Figure 5-15 Convergent histories of example 3

In this example, there are six random uncertain variables and two uncertain interval variables. The optimized results and the convergent histories are shown in Figure 5-14 and Figure 5-15. In Figure 5-14, a(1) and b(1) are the design results, while a(2) and b(2) are the LSFs. The topological differences which exist between the deterministic and the robust design results reveal the importance of considering uncertainties in the topology optimization. The robust objective function values for both deterministic and robust designs are given in Table 5-6. The mean value of the robust design is 301.81, which is 4.49% smaller than that of the deterministic design; the standard variance of the robust design is 38.08, which is 18.81% smaller than that of the deterministic design. These results show that the robust design will

result in robust performances than the deterministic design under uncertainties. The results from MCS are also provided as references. We can see that the function values obtained from the proposed method are quite close to those obtained from the MCS. That is to say, the proposed method has good accuracy as well as good efficiency.

Table 5-6 Robust objective function of optimized designs for example 3

Situations	Method	Mean	Standard variance	Robust objective function value	FEA calls
Deterministic design under uncertainties	iPCCI	315.99	46.90	362.89	1365
	MCS	316.77	47.71	364.48	1×10^7
Robust design under uncertainties	iPCCI	301.81	38.08	339.89	1365
	MCS	302.68	37.59	340.27	1×10^7

5.3 Summary

This Chapter is focused on the development of the RTOs for static and dynamic structures with random and interval hybrid uncertainties. The uncertainty analysis methods based on orthogonal polynomials are employed and applied to evaluate the robust objective function of the structures. The RTO formulations and the sensitivities are given based on the uncertainty analysis. The numerical examples have demonstrated that the uncertainties have impacts on the topological designs for structures, and the robust optimizations by using the proposed methods can achieve more robust results than the deterministic optimizations. The

results also show that the proposed robust topology optimization methods have good computational efficiency and numerical accuracy.

Chapter 6 Robust topology optimization for cellular composites based on dimension reduction methods

Most conventional topology optimization methods are focused on the use of full solid materials. Material design for the microstructure may provide more flexibility in the design optimization. Inspired by the porous materials, concurrent topology optimizations have been explored a lot, in which the structure and material are optimized simultaneously. More favorably, the periodic assumption is often made to meet the computational design and manufacturing requirements in practice. Based on the periodic assumption, the macroscopic composite structure is often assumed to have an array of identical microstructures that are periodically configured with the same shape and topology. However, random and interval hybrid uncertainties haven't yet been considered in the formulation of integrated topology optimization problems. In this Chapter, we will introduce the hybrid uncertainties into the concurrent design for structures under static and dynamic loadings. The dimension reduction based methods proposed in section 4.2 will be employed in the hybrid uncertainty analysis for the robust optimizations.

6.1 Homogenization method

The homogenization theory was built on the small asymptotic expansion theory and based on the assumption that the composite material structure is constituted by a large number of periodic microstructures (unit cells). The macro homogenized material elasticity properties can be calculated from its representative volume element by the homogenization method. As

shown in Figure 6-1, there are two coordinate systems, the global macro-coordinates $\mathbf{x}$ and the local micro-coordinates $\mathbf{y}$. The size of the microstructure is assumed to be small enough compared with the dimension of the macrostructure, and the microstructure is supposed to have the periodicity.

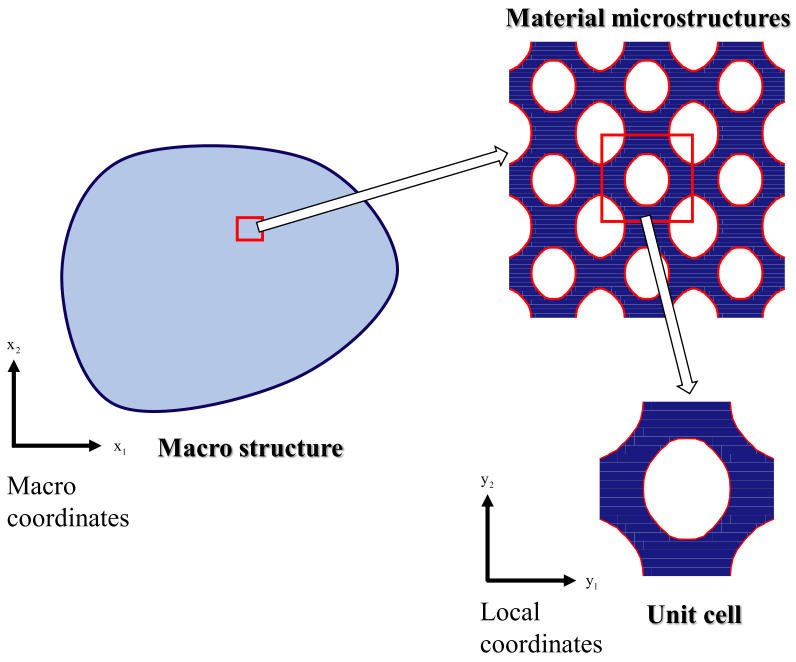

Figure 6-1 The schematic diagram of the homogenization method

The relationship between the two co-ordinate systems is:

$$\mathbf{y}=\mathbf{x}/\varepsilon \tag{6-1}$$

where ε indicates the existence of the microstructure and ε is assumed to be small enough compared with the dimension of the macrostructure. The displacement field can be approximated by an asymptotic expansion:

$$\mathbf{u}^{\varepsilon}=\mathbf{u}(\mathbf{x},\mathbf{y})\approx\mathbf{u}_0(\mathbf{x})+\varepsilon\mathbf{u}_1(\mathbf{x},\mathbf{y}) \tag{6-2}$$

in which $\mathbf{u}_0$ is the average displacement of the microstructure, $\mathbf{u}_1$ is the first-order variation from the average displacement. It is remarked that only the first-order variation is considered in the asymptotic expansion. Similarly, the strain is approximately as:

$$\boldsymbol{\varepsilon}\left(\mathbf{u}^{\varepsilon}\right)=\partial_{\mathbf{x}}\left(\mathbf{u}^{\varepsilon}\right)\approx\partial_{\mathbf{x}}\left(\mathbf{u}_0\right)+\partial_{\mathbf{y}}\left(\mathbf{u}_1\right)=\boldsymbol{\varepsilon}_0+\boldsymbol{\varepsilon}_1 \tag{6-3}$$

where $\boldsymbol{\varepsilon}_0$ is the strain due to the average displacement, $\boldsymbol{\varepsilon}_1$ is the strain due to the first deviation of the average displacement of the unit cell. $\partial_{\mathbf{x}}$ and $\partial_{\mathbf{y}}$ are the differential operators, which are defined by:

$$\partial_{\mathbf{x}}=\begin{bmatrix}\partial/\partial \mathrm{x}_1 & 0\\ 0 & \partial/\partial \mathrm{x}_2\\ \partial/\partial \mathrm{x}_2 & \partial/\partial \mathrm{x}_1\end{bmatrix}\quad\text{and}\quad\partial_{\mathbf{y}}=\begin{bmatrix}\partial/\partial \mathrm{y}_1 & 0\\ 0 & \partial/\partial \mathrm{y}_2\\ \partial/\partial \mathrm{y}_2 & \partial/\partial \mathrm{y}_1\end{bmatrix} \tag{6-4}$$

The stress tensor is approximately as:

$$\boldsymbol{\sigma}\left(\mathbf{u}^{\varepsilon}\right)=\mathbf{E}\left(\mathbf{x},\mathbf{y}\right)\cdot\boldsymbol{\varepsilon}\left(\mathbf{u}^{\varepsilon}\right)=\mathbf{E}\left(\mathbf{x},\mathbf{y}\right)\cdot\left(\partial_{\mathbf{x}}\left(\mathbf{u}_0\right)+\partial_{\mathbf{y}}\left(\mathbf{u}_1\right)\right) \tag{6-5}$$

where $\mathbf{E}$ is the elastic matrix of the material. The first-order variation $\mathbf{u}_1$ of the average displacement can be considered to be proportional for the strain $\boldsymbol{\varepsilon}_0$:

$$\mathbf{u}_1=-\boldsymbol{\chi}\left(\mathbf{y}\right)\varepsilon_0\left(\mathbf{x}\right)=-\boldsymbol{\chi}\left(\mathbf{y}\right)\partial_{\mathbf{x}}\left(\mathbf{u}_0\right) \tag{6-6}$$

where $\boldsymbol{\chi}$ is the characteristic displacement function of the microstructure. From Eqs. (6-3), (6-5) and (6-6), the total potential energy can be expressed as:

$$f\left(\mathbf{u}^{\varepsilon}\right)=\frac{1}{2}\int_{\Omega^{\varepsilon}}\left(\partial_{\mathbf{x}}\left(\mathbf{u}_0\right)\right)^{\mathrm{T}}\left(\mathbf{I}-\partial_{\mathbf{y}}\boldsymbol{\chi}\right)^{\mathrm{T}}\mathbf{E}\left(\mathbf{x},\mathbf{y}\right)\left(\mathbf{I}-\partial_{\mathbf{y}}\boldsymbol{\chi}\right)\left(\partial_{\mathbf{x}}\left(\mathbf{u}_0\right)\right)d\Omega^{\varepsilon} \tag{6-7}$$

For a *Y*-periodic function $\mathrm{H}(\mathbf{y})$, considering the limit $\varepsilon \to 0$, the following equation can be obtained:

$$\lim_{\varepsilon\to 0}\int_{\Omega^\varepsilon}\mathrm{H}\left(\frac{\mathbf{y}}{\varepsilon}\right)d\Omega^\varepsilon=\int_D\left(\frac{1}{|\mathrm{Y}|}\int_{\mathrm{Y}}\mathrm{H}(\mathbf{y})d\mathrm{Y}\right)d\Omega \tag{6-8}$$

Then Eq. (6-7) can be rewritten as:

$$f\left(\mathbf{u}^\varepsilon\right)=\frac{1}{2}\int_\Omega\left(\partial_{\mathbf{x}}\left(\mathbf{u}_0\right)\right)^{\mathrm{T}}\frac{1}{|\mathrm{Y}|}\int_{\mathrm{Y}}\left(\mathbf{I}-\partial_{\mathrm{y}}\boldsymbol{\chi}\right)^{\mathrm{T}}\mathbf{E}(\mathbf{x},\mathbf{y})\left(\mathbf{I}-\partial_{\mathrm{y}}\boldsymbol{\chi}\right)d\mathrm{Y}\left(\partial_{\mathbf{x}}\left(\mathbf{u}_0\right)\right)d\Omega \tag{6-9}$$

The homogenized elasticity matrix defined as follows:

$$\mathbf{E}^{\mathrm{H}}=\frac{1}{|\mathrm{Y}|}\int_{\mathrm{Y}}\left(\mathbf{I}-\partial_{\mathrm{y}}\boldsymbol{\chi}\right)^{\mathrm{T}}\mathbf{E}(\mathbf{x},\mathbf{y})\left(\mathbf{I}-\partial_{\mathrm{y}}\boldsymbol{\chi}\right)d\mathrm{Y} \tag{6-10}$$

where $\boldsymbol{\chi}(\mathbf{x},\mathbf{y})$ is the characteristic displacements of the unit cell due to the initial strain, and the term $\partial_{\mathrm{y}}\boldsymbol{\chi}(\mathbf{x},\mathbf{y})$ can be regarded as the strain field caused by the inhomogeneous material distribution. $\boldsymbol{\chi}(\mathbf{x},\mathbf{y})$ and $\partial_y\boldsymbol{\chi}(\mathbf{x},\mathbf{y})$ could be approximated using the nodal displacement $\mathbf{u}^*$, as follows:

$$\begin{cases}\boldsymbol{\chi}=\mathbf{N}\mathbf{u}^*\\ \partial_{\mathrm{y}}\boldsymbol{\chi}=\mathbf{B}\mathbf{u}^*\end{cases} \tag{6-11}$$

where **N** and **B** are the shape interpolation function and the stain-displacement matrix for the microstructure respectively. Then the homogenized elasticity property $\mathbf{E}^{\mathrm{H}}$ can be written in the form:

$$\mathbf{E}^{\mathrm{H}}=\frac{1}{\left|\mathrm{Y}\right|}\int_{\mathrm{Y}}\left(\mathbf{I}-\mathbf{B}\mathbf{u}^{*}\right)^{\mathrm{T}}\mathbf{E}\left(\mathbf{x},\mathbf{y}\right)\left(\mathbf{I}-\mathbf{B}\mathbf{u}^{*}\right)d\mathrm{Y} \tag{6-12}$$

On the other hand, the strain index notation is introduced in the calculation of the elasticity property, the homogenized elasticity matrix is expressed as:

$$E_{ijkl}^{\mathrm{H}}=\frac{1}{\left|\mathrm{Y}\right|}\int_{\Omega}\left(\varepsilon_{pq}^{0(ij)}-\varepsilon_{pq}^{*(ij)}\right)E_{pqrs}\left(\varepsilon_{rs}^{0(kl)}-\varepsilon_{rs}^{*(kl)}\right)d\mathrm{Y} \tag{6-13}$$

where the $\varepsilon_{pq}^{0(ij)}$ is the initial unit three test strains (six unit strains in 3D) that include the horizontal unit strain $\varepsilon_{pq}^{0(11)}=\left(1,0,0\right)^{\mathrm{T}}$, the vertical unit strain $\varepsilon_{pq}^{0(22)}=\left(0,1,0\right)^{\mathrm{T}}$, and the shear unit strain $\varepsilon_{pq}^{0(12)}=\left(0,0,1\right)^{\mathrm{T}}$ in 2D. The locally varying strain field $\varepsilon_{pq}^{(ij)}$ is defined as:

$$\varepsilon_{pq}^{(ij)}=\varepsilon_{pq}\left(\mathbf{u}^{*(kl)}\right)=\frac{1}{2}\left(\mathbf{u}_{p,q}^{*(ij)}+\mathbf{u}_{q,p}^{*(ij)}\right) \tag{6-14}$$

in which $\mathbf{u}^{*(ij)}$ is the displacement field which can be solved by the elasticity equation with a prescribed macroscopic strain:

$$\int_{\mathrm{Y}}E_{pqrs}\varepsilon_{rs}\left(\mathbf{v}\right)\varepsilon_{pq}\left(\mathbf{u}^{*(ij)}\right)d\mathrm{Y}=\int_{\mathrm{Y}}E_{pqrs}\varepsilon_{rs}\left(\mathbf{v}\right)\varepsilon_{pq}^{0(ij)}d\mathrm{Y} \tag{6-15}$$

where **v** is a virtual displacement field. In practice, the above equation can be solved using the finite element method. The homogenization elasticity property of the microstructure is then computed by the Eq. (6-13) after obtaining the displacement field.

For a microstructure with arbitrary topology, the numerical homogenization can be used to calculate the homogenized elastic matrix. With *NE* finite elements, the homogenization elasticity property of a unit cell could be written in the discretized form as:

$$E_{ijkl}^{\mathrm{H}}=\frac{1}{\left|\mathrm{Y}\right|}\sum_{e=1}^{NE}\left(\int_{\mathrm{Y}_e}\left(\varepsilon_{pq}^{0\mathrm{e}(ij)}-\varepsilon_{pq}^{*\mathrm{e}(ij)}\right)^{\mathrm{T}}E_{pqrs}\left(\varepsilon_{rs}^{0\mathrm{e}(kl)}-\varepsilon_{rs}^{*\mathrm{e}(kl)}\right)d\mathrm{Y}_e\right) \tag{6-16}$$

where Y_e is the area of the *e*th element. Performing the integration over each element, the homogenization elasticity tensor matrix can be found as:

$$E_{ijkl}^{\mathrm{H}}=\frac{1}{\left|\mathrm{Y}\right|}\sum_{e=1}^{NE}\left(\left(\mathbf{u}_e^{0(ij)}-\mathbf{u}_e^{*(ij)}\right)^{T}\mathbf{k}_{\mathrm{e}}\left(\mathbf{u}_e^{0(kl)}-\mathbf{u}_e^{*(kl)}\right)\right) \tag{6-17}$$

where the $\mathbf{u}_e^0$ and $\mathbf{u}_e^*$ are the displacement fields according to the unit test strain $\varepsilon_{pq}^{0\mathrm{e}(ij)}$ and the strain field $\varepsilon_{pq}^{*\mathrm{e}(ij)}$ of the element *e*, respectively. $\mathbf{k}_{\mathrm{e}}$ represents the element stiffness matrix, which is defined by:

$$\mathbf{k}_{\mathrm{e}}=\int_{\mathrm{Y}_e}\left(\mathbf{b}^e\right)^{\mathrm{T}}\mathbf{E}^e\mathbf{b}^e d\mathrm{Y}_e \tag{6-18}$$

in which $\mathbf{b}^e$ is the element strain-displacement matrix, Y_e is the volume of an element, $\mathbf{E}^e$ is the elastic property for an element, which for an isotropic material is:

$$\mathbf{E}^e=\lambda_e\begin{bmatrix}1&1&0\\1&1&0\\0&0&0\end{bmatrix}+\nu_e\begin{bmatrix}2&0&0\\0&2&0\\0&0&1\end{bmatrix} \tag{6-19}$$

where the terms λ_e and ν_e are the Lames first and second parameter for the element *e* respectively. Lames parameters can be computed from Young's modulus *E* and the Poisson's ratio υ:

$$\lambda=\frac{\upsilon E}{(1+\upsilon)(1-2\upsilon)},\nu=\frac{E}{2(1+\upsilon)} \tag{6-20}$$

In this case, the stiffness matrix and the load matrix for an element can be split into two corresponding parts:

$$\mathbf{k}=\sum_{e=1}^{NE}\mathbf{k}_{\mathrm{e}}=\sum_{e=1}^{NE}\left(\lambda_e\left(\mathbf{k}_{\mathrm{e}}\right)_{\lambda}+\nu_e\left(\mathbf{k}_{\mathrm{e}}\right)_{\mu}\right)=\sum_{e=1}^{NE}\left(\int_{\mathrm{Y}_e}\left(\mathbf{b}^e\right)^{\mathrm{T}}\mathbf{E}^e\mathbf{b}^e d\mathrm{Y}_e\right) \tag{6-21}$$

$$\mathbf{f}=\sum_{e=1}^{NE}\mathbf{f}_e=\sum_{e=1}^{NE}\left(\lambda_e\left(\mathbf{f}_e\right)_{\lambda}+\nu_e\left(\mathbf{f}_e\right)_{\mu}\right)=\sum_{e=1}^{NE}\left(\int_{\mathrm{Y}_e}\left(\mathbf{b}^e\right)^{\mathrm{T}}\mathbf{E}^e\boldsymbol{\varepsilon}^{0e}d\mathrm{Y}_e\right) \tag{6-22}$$

where $\mathbf{f}_{\mathrm{e}}$ represents the element load vector. Finally, the displacement field is computed by solving the finite element equation:

$$\mathbf{k}\mathbf{u}^{*}=\mathbf{f} \tag{6-23}$$

After obtaining the displacement field, the homogenized elastic matrix can be calculated by Eq. (6-17).

6.2 Parametric level sets for the multi-scale system

Multi-scale topology optimization is to find the material layout for structures in both macro and micro scales to minimize the compliance under constraints. The macrostructure is assumed to be constructed by periodical microstructures to improve the possibility of practical applications. The optimization formulation is constructed follow the same assumption in [71 . There are two materials involved here, the base material and the composite material. The material microstructure is assumed to be made of the base material and the macrostructure is assumed to be made of periodic microstructures.

The schematic diagram of the multiscale system is illustrated in Figure 6-2. The material point of the macrostructure A is periodically composed of microstructure C. As shown in Figure 6-2, there are two coordinate systems, the global macro-coordinate $\mathbf{x}$ and the local micro-coordinate $\mathbf{y}$. The size of the microstructure is assumed to be small enough compared with the dimension of the macrostructure, and the microstructure is supposed to have the periodicity. In this case, the material properties at macro level can be calculated by the numerical homogenization method [2 .

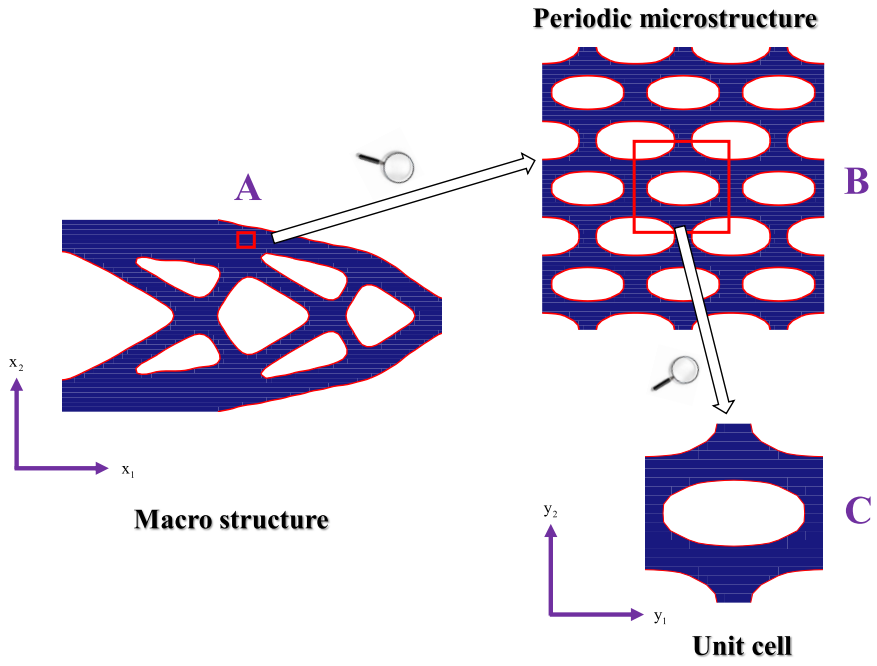

Figure 6-2 The schematic diagram of the multiscale system

In the multiscale system, two LSFs are defined in reference domains to present the macrostructure and microstructure respectively. In the macro scale, $D^{\mathrm{MA}} \subset \mathbf{R}^d \left(d = 2,3\right)$ is the reference space, Ω^{MA} is a set of all the possible shapes, and Γ^{MA} represents the structural boundary and corresponds to the zero level set. In the micro scale, $D^{\mathrm{MI}} \subset \mathbf{R}^d \left(d = 2,3\right)$ is the

reference space, Ω^{MI} is a set of all the possible shapes, and Γ^{MI} represents the structural boundary and corresponds to the zero level set. The design domain in macro and micro scales can be divided into three parts, the solid region, design boundary, and void region respectively, as follows:

$$\begin{cases} \Phi^{\mathrm{MA}}(\mathbf{x}) > 0, & \forall \mathbf{x} \in \Omega^{\mathrm{MA}} \setminus \Gamma^{\mathrm{MA}} \quad \text{(macro solid)} \\ \Phi^{\mathrm{MA}}(\mathbf{x}) = 0, & \forall \mathbf{x} \in \Gamma^{\mathrm{MA}} \bigcap D^{\mathrm{MA}} \quad \text{(macro boundary)} \\ \Phi^{\mathrm{MA}}(\mathbf{x}) < 0, & \forall \mathbf{x} \in D^{\mathrm{MA}} \setminus \Omega^{\mathrm{MA}} \quad \text{(macro void)} \end{cases} \tag{6-24}$$

$$\begin{cases} \Phi^{\mathrm{MI}}(\mathbf{y}) > 0, & \forall \mathbf{y} \in \Omega^{\mathrm{MI}} \setminus \Gamma^{\mathrm{MI}} \quad \text{(micro solid)} \\ \Phi^{\mathrm{MI}}(\mathbf{y}) = 0, & \forall \mathbf{y} \in \Gamma^{\mathrm{MI}} \bigcap D^{\mathrm{MI}} \quad \text{(micro boundary)} \\ \Phi^{\mathrm{MI}}(\mathbf{y}) < 0, & \forall \mathbf{y} \in D^{\mathrm{MI}} \setminus \Omega^{\mathrm{MI}} \quad \text{(micro void)} \end{cases} \tag{6-25}$$

The Hamilton-Jacobian partial derivative equation (H-J PDE) in both scales can be obtained:

$$\begin{cases} \dfrac{\partial \Phi^{\mathrm{MA}}}{\partial t} - \mathbf{v}_n^{\mathrm{MA}} \left| \nabla \Phi^{\mathrm{MA}} \right| = 0 \\ \dfrac{\partial \Phi^{\mathrm{MI}}}{\partial t} - \mathbf{v}_n^{\mathrm{MI}} \left| \nabla \Phi^{\mathrm{MI}} \right| = 0 \end{cases} \tag{6-26}$$

where $\mathbf{v}_n^{\mathrm{MA}}$ and $\mathbf{v}_n^{\mathrm{MI}}$ are the corresponding normal velocity fields in two scales. The LSFs are approximated by a set of centrally positioning CSRBFs:

$$\begin{cases} \Phi^{\mathrm{MA}}(\mathbf{x},t) = \boldsymbol{\phi}(\mathbf{x})^{\mathrm{T}} \boldsymbol{\alpha}^{\mathrm{MA}}(t) = \sum_{e=1}^{N} \phi_e(\mathbf{x}) \alpha_e^{\mathrm{MA}}(t) \\ \Phi^{\mathrm{MI}}(\mathbf{x},t) = \boldsymbol{\phi}(\mathbf{x})^{\mathrm{T}} \boldsymbol{\alpha}^{\mathrm{MI}}(t) = \sum_{t=1}^{M} \phi_t(\mathbf{x}) \alpha_t^{\mathrm{MI}}(t) \end{cases} \tag{6-27}$$

where N and M are the number of the knots in the macrostructure and microstructure respectively. It can be found that the LSFs are decoupled by the CSRBFs terms $\boldsymbol{\phi}$ which are

only spatial-dependent and the expansion coefficients $\boldsymbol{\alpha}$ which are only time-dependent. With the parameterized scheme, the H-J PDEs will be transformed into new time-space independent forms:

$$\begin{cases} \boldsymbol{\phi}\left(\mathbf{x}\right)^{\mathrm{T}} \dot{\boldsymbol{\alpha}}^{\mathrm{MA}}\left(t\right) - \mathbf{v}_n^{\mathrm{MA}} \cdot \left|\nabla \boldsymbol{\phi}\left(\mathbf{x}\right)^{\mathrm{T}} \boldsymbol{\alpha}^{\mathrm{MA}}\left(t\right)\right| = 0 \\ \boldsymbol{\phi}\left(\mathbf{x}\right)^{\mathrm{T}} \dot{\boldsymbol{\alpha}}^{\mathrm{MI}}\left(t\right) - \mathbf{v}_n^{\mathrm{MI}} \cdot \left|\nabla \boldsymbol{\phi}\left(\mathbf{x}\right)^{\mathrm{T}} \boldsymbol{\alpha}^{\mathrm{MI}}\left(t\right)\right| = 0 \end{cases} \tag{6-28}$$

in which the normal velocities are given by:

$$\begin{cases} \mathbf{v}_n^{\mathrm{MA}} = \dfrac{\boldsymbol{\phi}\left(\mathbf{x}\right)^{\mathrm{T}}}{\left|\nabla \boldsymbol{\phi}\left(\mathbf{x}\right)^{\mathrm{T}} \boldsymbol{\alpha}^{\mathrm{MA}}\left(t\right)\right|} \cdot \dfrac{d\boldsymbol{\alpha}^{\mathrm{MA}}\left(t\right)}{dt} \\ \mathbf{v}_n^{\mathrm{MI}} = \dfrac{\boldsymbol{\phi}\left(\mathbf{x}\right)^{\mathrm{T}}}{\left|\nabla \boldsymbol{\phi}\left(\mathbf{x}\right)^{\mathrm{T}} \boldsymbol{\alpha}^{\mathrm{MI}}\left(t\right)\right|} \cdot \dfrac{d\boldsymbol{\alpha}^{\mathrm{MI}}\left(t\right)}{dt} \end{cases} \tag{6-29}$$

Then the initial H-J PDEs have been transformed into a series of ordinary differential equations with a series of expansion coefficients which are regarded as the design variables in the topology optimization. In the multi-scale design, the design variables in the macro scale are the expansion coefficients to discretize the macro LSF, and design variables in the micro scale are the expansion coefficients to discretize the micro LSF.

6.3 Robust topology optimization for multi-scale design of static structures with hybrid uncertainties

6.3.1 Deterministic multi-scale topology optimization

6.3.1.1 Mathematical formulation

Macro structural design and micro material design are combined into one system by using the homogenization theory. The concurrent design for both levels generally includes a two-stage coupled process: the outer stage is topology optimization for macrostructure to obtain the best layout for the macro structure, and the inner stage is topology optimization for the microstructure to optimize the unit cell and obtain the effective elastic matrix. The mathematical formulation is given as follows:

$$
\begin{aligned}
&\min_{\boldsymbol{\alpha}^{\mathrm{MA}},\boldsymbol{\alpha}^{\mathrm{MI}}} \; C\left(\boldsymbol{\alpha}^{\mathrm{MA}},\boldsymbol{\alpha}^{\mathrm{MI}}\right)=\int_{\Omega^{\mathrm{MA}}}\varepsilon_{ij}^{\mathrm{T}}\left(\mathbf{u}^{\mathrm{MA}}\right)E_{ijkl}^{\mathrm{H}}\left(\mathbf{u}^{\mathrm{MI}},\Phi^{\mathrm{MI}}\right)\varepsilon_{kl}\left(\mathbf{u}^{\mathrm{MA}}\right)H\left(\Phi^{\mathrm{MA}}\right)d\Omega^{\mathrm{MA}}\\
&\text{s.t.}\quad a^{\mathrm{MA}}\left(\mathbf{u}^{\mathrm{MA}},\mathbf{v}^{\mathrm{MA}},\Phi^{\mathrm{MA}}\right)=l^{\mathrm{MA}}\left(\mathbf{v}^{\mathrm{MA}},\Phi^{\mathrm{MA}}\right),\;\forall\mathbf{v}^{\mathrm{MA}}\in\tilde{\mathbf{U}}^{\mathrm{MA}}\\
&\qquad a^{\mathrm{MI}}\left(\mathbf{u}^{\mathrm{MI}},\mathbf{v}^{\mathrm{MI}},\Phi^{\mathrm{MI}}\right)=l^{\mathrm{MI}}\left(\mathbf{v}^{\mathrm{MI}},\Phi^{\mathrm{MI}}\right),\;\forall\mathbf{v}^{\mathrm{MI}}\in\tilde{\mathbf{U}}^{\mathrm{MI}}\\
&\qquad G\left(\Phi^{\mathrm{MA}}\right)=\int_{\Omega}H\left(\Phi^{\mathrm{MA}}\right)d\Omega^{\mathrm{MA}}-f^{\mathrm{MA}}V_0^{\mathrm{MA}}\le 0\\
&\qquad G\left(\Phi^{\mathrm{MI}}\right)=\int_{\Omega}H\left(\Phi^{\mathrm{MI}}\right)d\Omega^{\mathrm{MI}}-f^{\mathrm{MI}}V_0^{\mathrm{MI}}\le 0\\
&\qquad \alpha_{\min}^{\mathrm{MA}}\le\alpha_e^{\mathrm{MA}}\le\alpha_{\max}^{\mathrm{MA}},e=1,2,\cdots,N\\
&\qquad \alpha_{\min}^{\mathrm{MI}}\le\alpha_t^{\mathrm{MI}}\le\alpha_{\max}^{\mathrm{MI}},t=1,2,\cdots,M
\end{aligned}
\tag{6-30}
$$

where $\boldsymbol{\alpha}^{\mathrm{MA}}$ represents the macro design variables within the bounds $\alpha_{\min}^{\mathrm{MA}}$ and $\alpha_{\max}^{\mathrm{MA}}$, $\boldsymbol{\alpha}^{\mathrm{MI}}$ represents the macro design variables within the bounds $\alpha_{\min}^{\mathrm{MI}}$ and $\alpha_{\max}^{\mathrm{MI}}$. N and M are the numbers of macro and micro design variables respectively. C is the structural compliance,

$G\left(\Phi^{\mathrm{MA}}\right)$ and $G\left(\Phi^{\mathrm{MI}}\right)$ indicate the volume constraints in the macro and micro scale respectively. V_0^{MA} and V_0^{MI} are the volumes, and f^{MA} and f^{MI} are the volume fractions of the macrostructure and the microstructure, respectively. H is the Heaviside function. $\mathbf{u}^{\mathrm{MA}}$ denotes the macro displacement field in the macrostructure, and $\mathbf{u}^{\mathrm{MI}}$ denotes the micro displacement field. $\mathbf{v}^{\mathrm{MA}}$ is the macro virtual displacement field belonging to the macro kinematically admissible displacement $\tilde{\mathbf{U}}^{\mathrm{MA}}$, and $\mathbf{v}^{\mathrm{MI}}$ is the macro virtual displacement field belonging to the macro kinematically admissible displacement $\tilde{\mathbf{U}}^{\mathrm{MI}}$. E_{ijkl}^{MA} is the homogenized elasticity tensor. The macro elastic equilibrium equation can be expressed in the weak form, the bilinear energy form and the linear load form are:

$$\begin{cases} a^{\mathrm{MA}}\left(\mathbf{u}^{\mathrm{MA}},\mathbf{v}^{\mathrm{MA}},\Phi^{\mathrm{MA}}\right)=\int_{\Omega^{\mathrm{MA}}}\varepsilon_{ij}^{\mathrm{T}}\left(\mathbf{u}^{\mathrm{MA}}\right)E_{ijkl}^{\mathrm{H}}\left(\mathbf{u}^{\mathrm{MI}},\Phi^{\mathrm{MI}}\right)\varepsilon_{kl}\left(\mathbf{v}^{\mathrm{MA}}\right)H\left(\Phi^{\mathrm{MA}}\right)d\Omega^{\mathrm{MA}} \\ l^{\mathrm{MA}}\left(\mathbf{v}^{\mathrm{MA}},\Phi^{\mathrm{MA}}\right)=\int_{\Omega^{\mathrm{MA}}}\mathbf{p}^{\mathrm{MA}}\mathbf{v}^{\mathrm{MA}}H\left(\Phi^{\mathrm{MA}}\right)d\Omega^{\mathrm{MA}}+\int_{\Omega^{\mathrm{MA}}}\boldsymbol{\tau}^{\mathrm{MA}}\mathbf{v}^{\mathrm{MA}}\delta\left(\Phi^{\mathrm{MA}}\right)\left|\nabla\Phi^{\mathrm{MA}}\right|d\Omega^{\mathrm{MA}} \end{cases} \tag{6-31}$$

where $\mathbf{p}^{MA}$ is the macro body force, $\boldsymbol{\tau}^{MA}$ indicates the macro boundary force, and δ is the Dirac function. $E_{ijkl}^{\mathrm{H}}\left(\mathbf{u}^{\mathrm{MI}},\Phi^{\mathrm{MI}}\right)$ represents the homogenized elasticity tensor which is evaluated by numerical homogenization method:

$$E_{ijkl}^{\mathrm{H}}=\frac{1}{\left|\Omega^{\mathrm{MI}}\right|}\int_{\Omega^{\mathrm{MI}}}\left(\varepsilon_{pq}^{0(ij)}-\varepsilon_{pq}^{*}\left(\mathbf{u}^{MI(ij)}\right)\right)E_{pqrs}\left(\varepsilon_{rs}^{0(kl)}-\varepsilon_{rs}^{*}\left(\mathbf{u}^{MI(kl)}\right)\right)H\left(\Phi^{\mathrm{MI}}\right)d\Omega^{\mathrm{MI}} \tag{6-32}$$

where E_{pqrs} is the elasticity tensor of the solid material. The $\varepsilon_{pq}^{0(ij)}$ is the initial unit test strains. The unknown strain field $\varepsilon_{pq}^{*(ij)}$ is computed by the micro linear elasticity equilibrium equation

which can be stated in the weak variational form by the bilinear energy term and the load linear term given by:

$$\begin{cases} a^{\mathrm{MI}}\left(\mathbf{u}^{\mathrm{MI}},\mathbf{v}^{\mathrm{MI}},\Phi^{\mathrm{MI}}\right)=\int_{\Omega^{\mathrm{MI}}}\varepsilon_{pq}^{*}\left(\mathbf{u}^{\mathrm{MI}(ij)}\right)E_{pqrs}\varepsilon_{rs}^{*}\left(\mathbf{v}^{\mathrm{MI}(ij)}\right)H\left(\Phi^{\mathrm{MI}}\right)d\Omega^{\mathrm{MI}} \\ l^{\mathrm{MI}}\left(\mathbf{v}^{\mathrm{MI}},\Phi^{\mathrm{MI}}\right)=\int_{\Omega^{\mathrm{MI}}}\varepsilon_{pq}^{0(ij)}E_{pqrs}\varepsilon_{rs}^{*}\left(\mathbf{v}^{\mathrm{MI}(ij)}\right)H\left(\Phi^{\mathrm{MI}}\right)d\Omega^{\mathrm{MI}} \end{cases} \tag{6-33}$$

6.3.1.2 Sensitivity analysis

The OC method is employed to update the design variables at both scales, so the first-order derivatives of the objective functions and the volume constraints need to be calculated. In the follows, the sensitivities are presented in both scales, respectively. With the homogenized material property, we can derive the derivative of the structural compliance with respect to the macro design variables by using the adjoint variable method:

$$\frac{\partial C}{\partial \alpha_e^{\mathrm{MA}}}=\int_{\Omega^{\mathrm{MA}}}\left[-\varepsilon_{ij}^{T}\left(\mathbf{u}\right)E_{ijkl}^{\mathrm{H}}\varepsilon_{kl}\left(\mathbf{u}\right)\right]\phi_e\left(\mathbf{x}\right)\delta\left(\Phi^{\mathrm{MA}}\right)d\Omega^{\mathrm{MA}} \tag{6-34}$$

The derivative of the volume constraint with respect to the macro design variable is obtained by:

$$\frac{\partial G\left(\Phi^{\mathrm{MA}}\right)}{\partial \alpha_e^{\mathrm{MA}}}=\int_{\Omega^{\mathrm{MA}}}\varphi_e\left(\mathbf{x}\right)\delta\left(\Phi^{\mathrm{MA}}\right)d\Omega^{\mathrm{MA}} \tag{6-35}$$

Also, the shape derivative theory is introduced to compute the design sensitivity of the microstructure. The shape derivative of E_{ijkl}^{H}, $a^{\mathrm{MI}}\left(\mathbf{u}^{\mathrm{MI}},\mathbf{v}^{\mathrm{MI}},\Phi^{\mathrm{MI}}\right)$, and $l^{\mathrm{MI}}\left(\mathbf{v}^{\mathrm{MI}},\Phi^{\mathrm{MI}}\right)$ are expressed as follows:

$$\begin{aligned}\frac{\partial E_{ijkl}^{\mathrm{H}}}{\partial t}=&\frac{1}{\left|\Omega^{\mathrm{MI}}\right|}\int_{\Omega^{\mathrm{MI}}}\left(\varepsilon_{pq}^{0(ij)}-\varepsilon_{pq}^{*}\left(\mathbf{u}^{MI(ij)}\right)\right)E_{pqrs}\left(\varepsilon_{rs}^{0(kl)}-\varepsilon_{rs}^{*}\left(\mathbf{u}^{MI(kl)}\right)\right)\mathbf{v}_{n}^{\mathrm{MI}}\left|\nabla\Phi^{\mathrm{MI}}\right|\delta\left(\Phi^{\mathrm{MI}}\right)d\Omega^{\mathrm{MI}}\\&-\frac{2}{\left|\Omega^{\mathrm{MI}}\right|}\int_{\Omega^{\mathrm{MI}}}\left(\varepsilon_{pq}^{*}\left(\dot{\mathbf{u}}^{MI(ij)}\right)\right)E_{pqrs}\left(\varepsilon_{rs}^{0(kl)}-\varepsilon_{rs}^{*}\left(\mathbf{u}^{MI(kl)}\right)\right)H\left(\Phi^{\mathrm{MI}}\right)d\Omega^{\mathrm{MI}}\end{aligned}\tag{6-36}$$

$$\begin{aligned}\frac{\partial a^{\mathrm{MI}}}{\partial t}=&\int_{\Omega^{\mathrm{MI}}}\varepsilon_{pq}^{*}\left(\mathbf{u}^{\mathrm{MI}(ij)}\right)E_{pqrs}\varepsilon_{rs}^{*}\left(\mathbf{v}^{\mathrm{MI}(ij)}\right)\mathbf{v}_{n}^{\mathrm{MI}}\left|\nabla\Phi^{\mathrm{MI}}\right|\delta\left(\Phi^{\mathrm{MI}}\right)d\Omega^{\mathrm{MI}}\\&+\int_{\Omega^{\mathrm{MI}}}\left[\varepsilon_{pq}^{*}\left(\dot{\mathbf{u}}^{\mathrm{MI}(ij)}\right)E_{pqrs}\varepsilon_{rs}^{*}\left(\mathbf{v}^{\mathrm{MI}(ij)}\right)+\varepsilon_{pq}^{*}\left(\mathbf{u}^{\mathrm{MI}(ij)}\right)E_{pqrs}\varepsilon_{rs}^{*}\left(\dot{\mathbf{v}}^{\mathrm{MI}(ij)}\right)\right]H\left(\Phi^{\mathrm{MI}}\right)d\Omega^{\mathrm{MI}}\end{aligned}\tag{6-37}$$

$$\begin{aligned}\frac{\partial l^{\mathrm{MI}}}{\partial t}=&\int_{\Omega^{\mathrm{MI}}}\varepsilon_{pq}^{0(ij)}E_{pqrs}\varepsilon_{rs}^{*}\left(\mathbf{v}^{\mathrm{MI}(ij)}\right)\mathbf{v}_{n}^{\mathrm{MI}}\left|\nabla\Phi^{\mathrm{MI}}\right|\delta\left(\Phi^{\mathrm{MI}}\right)d\Omega^{\mathrm{MI}}\\&+\int_{\Omega^{\mathrm{MI}}}\varepsilon_{pq}^{0(ij)}E_{pqrs}\varepsilon_{rs}^{*}\left(\dot{\mathbf{v}}^{\mathrm{MI}(ij)}\right)H\left(\Phi^{\mathrm{MI}}\right)d\Omega^{\mathrm{MI}}\end{aligned}\tag{6-38}$$

In addition, the following conjugate equation can be established:

$$\int_{\Omega^{\mathrm{MI}}}\varepsilon_{pq}^{*}\left(\mathbf{u}^{\mathrm{MI}(ij)}\right)E_{pqrs}\varepsilon_{rs}^{*}\left(\dot{\mathbf{v}}^{\mathrm{MI}(ij)}\right)H\left(\Phi^{\mathrm{MI}}\right)d\Omega^{\mathrm{MI}}=\int_{\Omega^{\mathrm{MI}}}\varepsilon_{pq}^{0(ij)}E_{ijpq}\varepsilon_{rs}^{*}\left(\dot{\mathbf{v}}^{\mathrm{MI}(ij)}\right)H\left(\Phi^{\mathrm{MI}}\right)d\Omega^{\mathrm{MI}}\tag{6-39}$$

Differentiating the micro scale equilibrium equation in (6-30) with respect to *t*, we can acquire:

$$\frac{\partial a^{\mathrm{MI}}\left(\mathbf{u}^{\mathrm{MI}},\mathbf{v}^{\mathrm{MI}},\Phi^{\mathrm{MI}}\right)}{\partial t}=\frac{\partial l^{\mathrm{MI}}\left(\mathbf{v}^{\mathrm{MI}},\Phi^{\mathrm{MI}}\right)}{\partial t}\tag{6-40}$$

Substituting Eqs. (6-37),(6-38) and (6-39) into (6-40):

$$\begin{aligned}&\int_{\Omega^{\mathrm{MI}}}\left(\varepsilon_{pq}^{0(ij)}-\varepsilon_{pq}^{*}\left(\mathbf{u}^{\mathrm{MI}(ij)}\right)\right)E_{pqrs}\varepsilon_{rs}^{*}\left(\mathbf{v}^{\mathrm{MI}(ij)}\right)v_{n}^{\mathrm{MI}}\left|\nabla\Phi^{\mathrm{MI}}\right|\delta\left(\Phi^{\mathrm{MI}}\right)d\Omega^{\mathrm{MI}}\\&=\int_{\Omega^{\mathrm{MI}}}\left(\varepsilon_{pq}^{*}\left(\dot{\mathbf{u}}^{\mathrm{MI}(ij)}\right)\right)E_{pqrs}\varepsilon_{rs}^{*}\left(\mathbf{v}^{\mathrm{MI}(ij)}\right)H\left(\Phi^{\mathrm{MI}}\right)d\Omega^{\mathrm{MI}}\end{aligned}\tag{6-41}$$

Since the elastic system is a self-adjoint problem, from Eqs. (6-36) and (6-41), we can get:

$$\frac{\partial E_{ijkl}^{\mathrm{H}}}{\partial t}=-\frac{1}{\left|\Omega^{\mathrm{MI}}\right|}\int_{\Omega^{\mathrm{MI}}}\beta\left(\mathbf{u}^{\mathrm{MI}}\right)\mathbf{v}_{n}^{\mathrm{MI}}\left|\nabla\Phi^{\mathrm{MI}}\right|\delta\left(\Phi^{\mathrm{MI}}\right)d\Omega^{\mathrm{MI}}\tag{6-42}$$

in which

$$\beta\left(u^{\mathrm{MI}}\right)=\left(\varepsilon_{pq}^{0(ij)}-\varepsilon_{pq}^{*}\left(\mathbf{u}^{\mathrm{MI}(ij)}\right)\right)E_{pqrs}\left(\varepsilon_{rs}^{0(kl)}-\varepsilon_{rs}^{*}\left(\mathbf{u}^{\mathrm{MI}(kl)}\right)\right) \tag{6-43}$$

With the normal velocity in Eq. (6-29), Eq. (6-42) will be expressed as:

$$\frac{\partial E_{ijkl}^{\mathrm{H}}}{\partial t}=-\sum_{t=1}^{M}\left(\frac{1}{\left|\Omega^{\mathrm{MI}}\right|}\int_{\Omega^{\mathrm{MI}}}\beta\left(\mathbf{u}^{\mathrm{MI}}\right)\phi_t\left(\mathbf{x}\right)^{\mathrm{T}}\delta\left(\Phi^{\mathrm{MI}}\right)d\Omega^{\mathrm{MI}}\right)\cdot\frac{d\alpha_t^{\mathrm{MI}}\left(t\right)}{dt} \tag{6-44}$$

According to the chain rule:

$$\frac{\partial E_{ijkl}^{\mathrm{H}}}{\partial t}=\sum_{t=1}^{M}\frac{\partial E_{ijkl}^{\mathrm{H}}}{\partial\alpha_t^{\mathrm{MI}}}\cdot\frac{\partial\alpha_t^{\mathrm{MI}}}{\partial t} \tag{6-45}$$

Comparing the Eqs. (6-44) and (6-45), we can get the sensitivities of the elastic tensor with respect to the design variables:

$$\frac{\partial E_{ijkl}^{\mathrm{H}}}{\partial\alpha_t^{\mathrm{MI}}}=-\frac{1}{\left|\Omega^{\mathrm{MI}}\right|}\int_{\Omega^{\mathrm{MI}}}\beta\left(\mathbf{u}^{\mathrm{MI}}\right)\phi_t\left(\mathbf{x}\right)^{\mathrm{T}}\delta\left(\Phi^{\mathrm{MI}}\right)d\Omega^{\mathrm{MI}} \tag{6-46}$$

The sensitivities of the objective function C with respect to the micro design variables can be computed as:

$$\frac{\partial C}{\partial\alpha_t^{\mathrm{MI}}}=-\int_{\Omega^{\mathrm{MA}}}\varepsilon_{ij}^{\mathrm{T}}\left(\mathbf{u}^{\mathrm{MA}}\right)\frac{\partial E_{ijkl}^{\mathrm{H}}}{\partial\alpha_t^{\mathrm{MI}}}\varepsilon_{kl}\left(\mathbf{u}^{\mathrm{MA}}\right)d\Omega^{\mathrm{MA}} \tag{6-47}$$

Finally, with the first-order derivative of the homogenized elastic tensor in (6-46), the design sensitivities of the objective function are given as:

$$\frac{\partial C}{\partial\alpha_t^{\mathrm{MI}}}=\frac{1}{\left|\Omega^{\mathrm{MI}}\right|}\int_{\Omega^{\mathrm{MA}}}\varepsilon_{ij}^{\mathrm{T}}\left(\mathbf{u}^{\mathrm{MA}}\right)\left(\int_{\Omega^{\mathrm{MI}}}\beta\left(\mathbf{u}^{\mathrm{MI}}\right)\phi_t\left(\mathbf{x}\right)^{\mathrm{T}}\delta\left(\Phi^{\mathrm{MI}}\right)d\Omega^{\mathrm{MI}}\right)\varepsilon_{kl}\left(\mathbf{u}^{\mathrm{MA}}\right)d\Omega^{\mathrm{MA}} \tag{6-48}$$

Similarly, the sensitivities of the constraint with respect to the micro design variables are:

$$\frac{\partial G\left(\Phi^{\mathrm{MI}}\right)}{\partial \alpha_t^{\mathrm{MI}}}=\int_{\Omega^{\mathrm{MI}}} \varphi_t\left(\mathbf{x}\right)\delta\left(\Phi^{\mathrm{MI}}\right)d\Omega^{\mathrm{MI}} \tag{6-49}$$

6.3.2 Robust topology optimization

6.3.2.1 Mathematical formulation

Assume $\mathbf{X}=\left(X_1,X_2,...,X_n\right)$ is the probability vector and $\mathbf{Y}=\left(Y_1,Y_2,...,Y_m\right)$ is the interval vector in the structure. $X_i(i=1,2,\cdots,n)$ is the *i*th probability uncertain variable and the probability distribution function is given as $f_{X_i}\left(X_i\right)$. $Y_i(i=1,2,\cdots,m)$ is the *i*th interval variable, and the interval variation of the interval variable is given as $[Y_i^L,Y_i^R]$. $Y_i^C=\dfrac{Y_i^L+Y_i^R}{2}$ and $Y_i^W=\dfrac{Y_i^R-Y_i^L}{2}$ represent the interval midpoint and the interval radius of Y_i, respectively.

With random and interval variables, the optimization problem can be rewritten as:

$$\begin{aligned}
&\min_{\boldsymbol{\alpha}^{\mathrm{MA}},\boldsymbol{\alpha}^{\mathrm{MI}}} C(\mathbf{X},\mathbf{Y})=\int_{\Omega^{\mathrm{MA}}}\mathbf{U}^{\mathrm{T}}(\mathbf{X},\mathbf{Y})\mathbf{K}(\mathbf{X},\mathbf{Y})\mathbf{U}(\mathbf{X},\mathbf{Y})d\Omega^{\mathrm{MA}}\\
&\text{s.t.}\quad \mathbf{K}(\mathbf{X},\mathbf{Y})\mathbf{U}(\mathbf{X},\mathbf{Y})=\mathbf{F}(\mathbf{X},\mathbf{Y})\\
&\quad \sum_{e=1}^{N}\alpha_e^{\mathrm{MA}}V_e\le f^{\mathrm{MA}}V,\sum_{t=1}^{M}\alpha_t^{\mathrm{MI}}V_t^e\le f^{\mathrm{MI}}V_e\\
&\quad \alpha_{\min}^{\mathrm{MA}}\le\alpha_e^{\mathrm{MA}}\le\alpha_{\max}^{\mathrm{MA}},e=1,2,\cdots,N\\
&\quad \alpha_{\min}^{\mathrm{MI}}\le\alpha_t^{\mathrm{MI}}\le\alpha_{\max}^{\mathrm{MI}},t=1,2,\cdots,M
\end{aligned} \tag{6-50}$$

in which $\alpha_e^{\mathrm{MA}}(e=1,2,\cdots,N)$ and $\alpha_t^{\mathrm{MI}}(t=1,2,\cdots,M)$ are the design variables (relative densities) of the *e*th and *t*th elements of the macrostructure and microstructure, respectively, *N* and *M* are the numbers of macro and micro design variables respectively. $\mathbf{U}$ denotes the

global displacement matrix of the macrostructure. **K** denotes the global stiffness matrix. **F** is the external force of the structure. V and V_e represent the volume of the macrostructure and the unit cell, and V_t^e represents the element volume of the unit cell. f^{MA} and f^{MI} are volume fractions for volume constraints.

The compliance C illustrates the stiffness of the structure, and it is known that smaller compliance means stiffer structure. The robust objective function is defined as a linear combination of the mean and standard deviation of structure compliance due to the probabilistic and interval variables. The robust topology optimization can be reformulated under the worst case:

$$\begin{aligned}
&\min_{\boldsymbol{\alpha}^{\mathrm{MA}},\boldsymbol{\alpha}^{\mathrm{MI}}} g = \max_{\mathbf{Y}} \mu(C) + h \cdot \sigma(C) \\
&st.\ \mathbf{K}(\mathbf{X},\mathbf{Y})\mathbf{U}(\mathbf{X},\mathbf{Y}) = \mathbf{F}(\mathbf{X},\mathbf{Y}) \\
&\quad \sum_{e=1}^{N} \alpha_e^{\mathrm{MA}} V_e \le f^{\mathrm{MA}} V, \sum_{t=1}^{M} \alpha_t^{\mathrm{MI}} V_t^e \le f^{\mathrm{MI}} V_{ei} \\
&\quad \alpha_{\min}^{\mathrm{MA}} \le \alpha_e^{\mathrm{MA}} \le \alpha_{\max}^{\mathrm{MA}}, e = 1,2,\cdots,N \\
&\quad \alpha_{\min}^{\mathrm{MI}} \le \alpha_t^{\mathrm{MI}} \le \alpha_{\max}^{\mathrm{MI}}, t = 1,2,\cdots,M
\end{aligned} \tag{6-51}$$

where $\mu(C) = E(C)$ represents the mean value of the compliance. $\sigma(C) = \left(E(C^2) - E^2(C)\right)^{1/2}$ is the standard deviation of compliance, where $E(C^k), k = 1,2$ denote the first and second origin moments of the structure compliance respectively, and h represents a given weight value which is set as 1 here.

The HUDR method proposed in 4.2.1 is employed here to evaluate the objective function of the robust topology optimization problem in Eq. (6-51). Fixing the interval variables, the mean and the standard variance of the structural compliance can be evaluated by Eqs. (4-43)

and (4-44). Taking into consideration the interval uncertainties, by Eqs. (4-46) and (4-47), the robust objective function can be approximated as:

$$\begin{aligned} g &= \max_{\mathbf{Y}} \mu(C(Y_1, Y_2, \cdots, Y_m)) + h \cdot \sigma(C(Y_1, Y_2, \cdots, Y_m)) \\ &\cong \max_{\mathbf{Y}} \mu(C(Y_1, Y_2^C, \cdots, Y_m^C)) + \mu(C(Y_1^C, Y_2, \cdots, Y_m^C)) + \cdots \\ &+ \mu(C(Y_1^C, Y_2^C, \cdots, Y_m)) - (h-1) \cdot \mu(C(Y_1^C, Y_2^C, \cdots, Y_m^C)) \\ &+ h \cdot \sigma(C(Y_1, Y_2^C, \cdots, Y_m^C)) + h \cdot \sigma(C(Y_1^C, Y_2, \cdots, Y_m^C)) + \cdots \\ &+ h \cdot \sigma(C(Y_1^C, Y_2^C, \cdots, Y_m)) - (h-1) \cdot h \cdot \sigma(C(Y_1^C, Y_2^C, \cdots, Y_m^C)) \\ &= \max_{\mathbf{Y}} d_1(Y_1) + d_2(Y_2) + \cdots + d_h(Y_m) - d_C \end{aligned} \tag{6-52}$$

where

$$d_i(Y_i) = \mu(C(Y_1^C, \cdots, Y_i, \cdots, Y_m^C)) + h \cdot \sigma(C(Y_1^C, \cdots, Y_i, \cdots, Y_m^C)), i = 1, 2, \cdots, m \tag{6-53}$$

$$d_C = (m-1) \cdot \mu(C(Y_1^C, Y_2^C, \cdots, Y_m^C)) + (m-1) \cdot h \cdot \sigma(C(Y_1^C, Y_2^C, \cdots, Y_m^C)) \tag{6-54}$$

From the above we can see that, $d_i(Y_i)$ is a function with an interval variable Y_i, and d_C is a constant. Using the first order Taylor series:

$$d_i(Y_i) \cong d_i(Y_i^C) + \nabla d_i \cdot (Y_i - Y_i^C) \tag{6-55}$$

where ∇d_i represents the sensitivity of d_i with respect to interval variable Y_i. In order to obtain the maximum value of d_i, we can get the corresponding interval value from the sign of the sensitivity of d_i: if $\nabla d_i > 0, Y_i = Y_i^R$; if $\nabla d_i < 0, Y_i = Y_i^L$. As a result, the value of the objective function $g = \max \mu(C) + h \cdot \sigma(C)$ can be obtained.

6.3.2.2 Sensitivity analysis

In this work, the OC method is used to update both macro and micro design variables in both scales. The sensitivities of the objective function with respect to the macro design variables can be calculated by:

$$\frac{\partial(\mu(C)+w\cdot\sigma(C))}{\partial\alpha_e^{\mathrm{MA}}}=\frac{\partial\mu(C)}{\partial\alpha_e^{\mathrm{MA}}}+w\cdot\frac{\partial\sigma(C)}{\partial\alpha_e^{\mathrm{MA}}} \tag{6-56}$$

Based on the compound function derivation law, we have:

$$\frac{\partial\sigma^2(C)}{\partial\alpha_e^{\mathrm{MA}}}=2\cdot\sigma(C)\cdot\frac{\partial\sigma(C)}{\partial\alpha_e^{\mathrm{MA}}} \tag{6-57}$$

Then Eq. (6-56) will be changed to the following:

$$\begin{aligned}\frac{\partial(\mu(C)+w\cdot\sigma(C))}{\partial\alpha_e^{\mathrm{MA}}}&=\frac{\partial\sum_{l=1}^{L}C_l/L}{\partial\alpha_e^{\mathrm{MA}}}+w\cdot\frac{\partial\sum_{l=1}^{L}(C_l-\mu(C))^2/L}{2\cdot\sigma(C)\cdot\partial\alpha_e^{\mathrm{MA}}}\\&=\frac{\partial\sum_{l=1}^{L}C_l}{\partial\alpha_e^{\mathrm{MA}}}/L+2w\cdot\sum_{l=1}^{L}\left|C_l-\mu(C)\right|\cdot\frac{\partial(C_l-\mu(C))}{2\cdot\sigma(C)\cdot\partial\alpha_e^{\mathrm{MA}}}/L\\&=\sum_{l=1}^{L}\frac{\partial C_l}{\partial\alpha_e^{\mathrm{MA}}}/L+\frac{w}{\sigma(C)}\cdot\sum_{l=1}^{L}\left|C_l-\mu(C)\right|\cdot\frac{\partial C_l}{\partial\alpha_e^{\mathrm{MA}}}/L\end{aligned} \tag{6-58}$$

where C_l means the lth value of L samples of compliance values. From the above we can see that $\left(\sum_{l=1}^{L}\partial C_l/\partial\alpha_e^{\mathrm{MA}}\right)\Big/L$ is just the mean value of the function $\partial C/\partial\alpha_e^{\mathrm{MA}}$, and $\left(\sum_{l=1}^{L}\left|C_l-\mu(C)\right|\cdot\left(\partial C/\partial\alpha_e^{\mathrm{MA}}\right)\right)\Big/L$ is just the mean value of the function $\left|C-\mu(C)\right|\cdot\left(\partial C/\partial\alpha_e^{\mathrm{MA}}\right)$. From Eq. (6-34), the explicit expression of $\partial C/\partial\alpha_e^{\mathrm{MA}}$ and $\left|C-\mu(C)\right|\cdot\left(\partial C/\partial\alpha_e^{\mathrm{MA}}\right)$ can be obtained, and the mean value $E\left(\partial C/\partial\alpha_e^{\mathrm{MA}}\right)$ and $E\left(\left|C-\mu(C)\right|\cdot\left(\partial C/\partial\alpha_e^{\mathrm{MA}}\right)\right)$ can be easily obtained using the same formula as Eq.(4-43).

Similarly, the sensitivity analysis of the objective function with respect to micro design variables is:

$$\frac{\partial(\mu(C)+w\cdot\sigma(C))}{\partial\alpha_t^{\mathrm{MI}}}=\frac{\partial\mu(C)}{\partial\alpha_t^{\mathrm{MI}}}+w\cdot\frac{\partial\sigma(C)}{\partial\alpha_t^{\mathrm{MI}}} \tag{6-59}$$

In the same way, we will obtain:

$$\frac{\partial(\mu(C)+w\cdot\sigma(C))}{\partial\alpha_t^{\mathrm{MI}}}=\sum_{l=1}^{L}\frac{\partial C_l}{\partial\alpha_t^{\mathrm{MI}}}/L+\frac{w}{\sigma(C)}\cdot\sum_{l=1}^{L}\left|C_l-\mu(C)\right|\cdot\frac{\partial C_l}{\partial\alpha_t^{\mathrm{MI}}}/L \tag{6-60}$$

Based on Eq. (6-48), we can also easily obtain the sensitivities in Eq. (6-60).

6.3.2.3 Optimization procedure

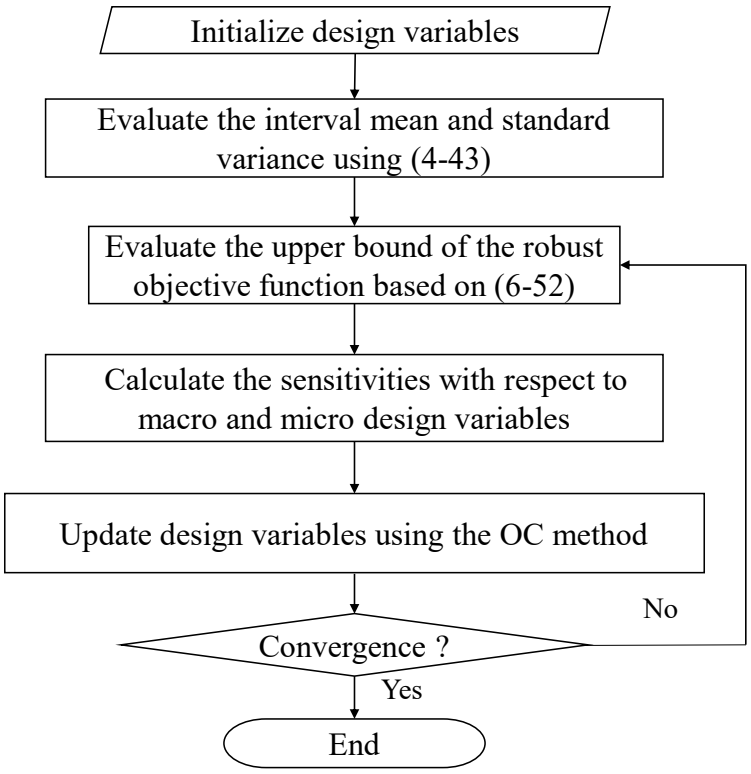

Figure 6-3 The flowchart of the proposed method

The process of the proposed multi-scale robust topology optimization method under hybrid uncertainties can be summarized as follows (Figure 6-3):

(1) Initialize the design variables α_e^{MA} and α_i^{MI} in both scales;

(2) Regarded the interval variables as constants, evaluate the interval mean and standard variance of the uncertain objective function using Eq. (4-44);

(3) Taken interval variation into consideration, evaluate the upper bound of the robust objective function based on Eq. (6-52);

(4) Compute the sensitivities of the objective function with respect to design variables based on Eqs. (6-58) and (6-60);

(5) Update the macro and micro design variables using the OC method;

(6) Check convergence. The convergence criterion is $\left|g_m - g_{m-1}\right| / \max\left(g_m, g_{m-1}\right) \le \varepsilon_{\max}$. m is the current iteration step number, and $\varepsilon_{\max}$ is set to be 10^{-5}. If it is not convergent, go back to step (2); if it is, stop the iteration process.

6.3.3 Numerical examples

In this section, three examples are presented. The loadings and/or the material properties are considered as random and interval uncertain parameters in the examples. Deterministic designs are also provided for comparison. In the deterministic situations, the uncertain parameters are set as the mean values of the random variables and the midpoint values of the interval variables.

Example 1

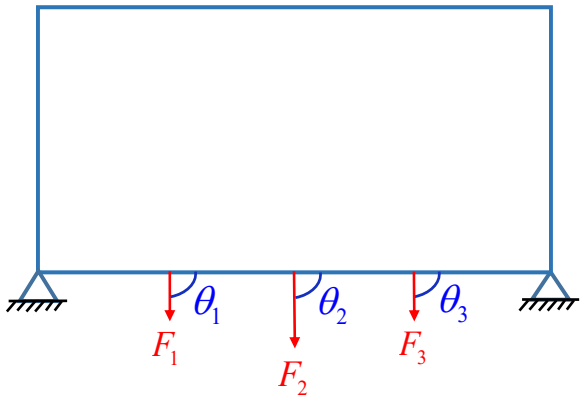

Figure 6-4 Design domain and boundary condition for example 1

A beam with 1.6m length and 0.8m is investigated in this example. The lower left and right corners of the beam are clamped. As shown in Figure 6-4, three loads F_1, F_2 and F_3 are applied on the lower side of the structure. The magnitudes of the three loads are $4\times10^5 N$, $8\times10^5 N$ and $4\times10^5 N$. The loading directions θ_1, θ_2, and θ_3 are assumed as normal variables with mean values $[\pi/2,\pi/2,\pi/2]$ and standard variances $[\pi/18,\pi/18,\pi/18]$. The Young's modulus and the Poisson's ratio are assumed to be interval variables, and set to be $E=\left[6.3\times10^{10}\text{ Pa},7.7\times10^{10}\text{ Pa}\right]$ and $\upsilon=[0.27,0.33]$ respectively. The macro structure is discretized by 80×40 Q4 elements, while the micro structures are discretized by 40×40 Q4 elements. The volume fractions for both scales are set to be 0.5.

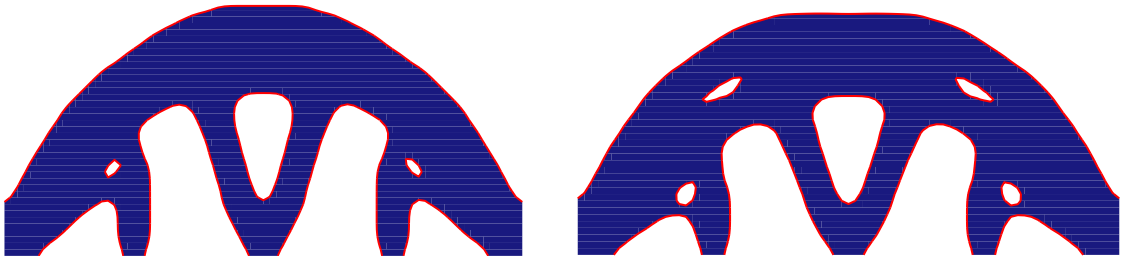

a(1) b(1)

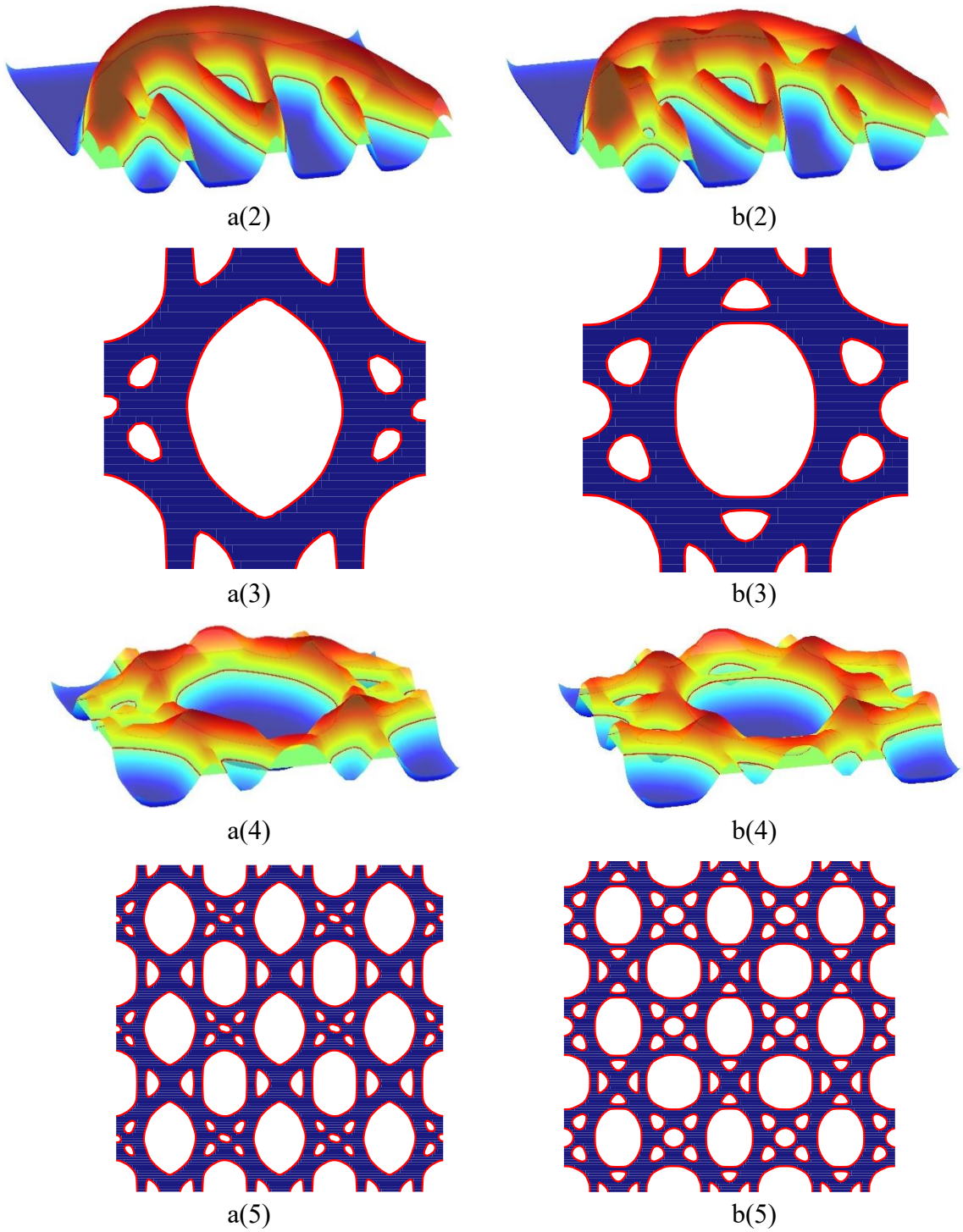

Figure 6-5 Optimized results in macro and micro scales for example 1 (left: deterministic design; right: robust design)

As shown in Figure 6-5, a(1)~a(5) are results of the deterministic design, and b(1)~b(5) are results of the robust design. In Figure 6-5, the first four pictures are results in the macro scale: a(1) and b(1) are the final topologies of the macro structures, while a(2) and b(2) give the LSFs for the macro designs. The last six pictures are results in the micro scale: a(3)-a(4) and b(3)-b(4) represent the individual unit cells, while a(5) and b(5) are three by three arrays of the identical unit cells. It can be seen that the final topologies for the structure with uncertainties are different from the deterministic ones at both scales. For comparison and verification purpose, the robust objective function values (including the mean and standard variance) and the FEA calls of the robust and the deterministic designs under the uncertainties are given in Table 6-1.

The results denote that uncertainties have an obvious influence on the optimization results, so it is important and essential to consider uncertainties during the topological design process. When applying the uncertain loads to both deterministic and uncertain designs, we can obtain the robust objective function values 1398.46 and 1242.32, respectively, which indicate that the robust design can result in a smaller or better robust objective function value. For the given uncertain loads, the mean and the standard deviation of the robust design (1162.58 and 79.74 respectively) are both much smaller than those of the deterministic design (1240.51 and 157.95 respectively). It shows that the robust topology optimization considering uncertainties can provide a design with better robustness compared with the deterministic one. To verify the accuracy, 10^7 Monte Carlo simulations are used as references. It can be seen that the results obtained by our proposed method are close to the MCS results, and at the same time, the proposed method only need a small number of FEA calls. To evaluate the value of the robust

objective function, the proposed method only needs 70 ((3×3+1)× (2×3+1)) FEA calls, but remains a very good accuracy. The convergent histories of both objective function and volume constraints as given in Figure 6-6 show that the proposed method has good computational efficiency and stability.

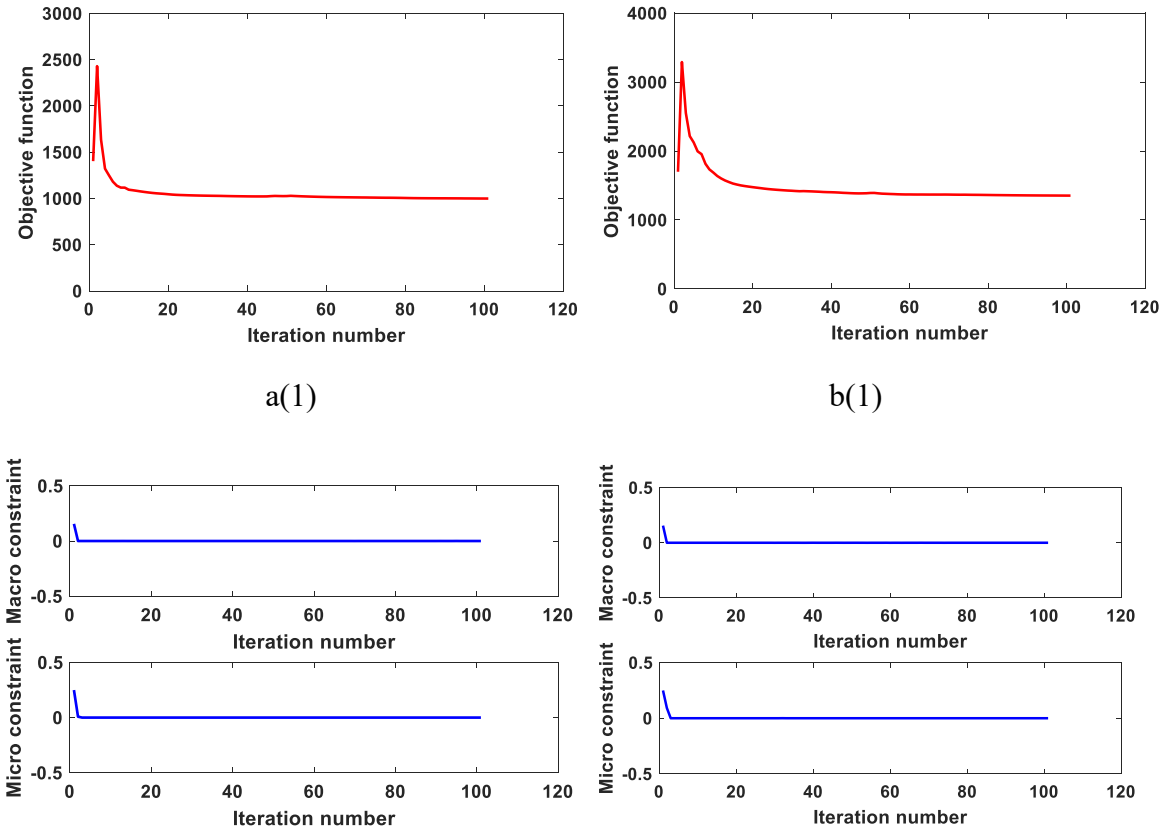

Figure 6-6 Convergent histories for example 1
(left: deterministic design; right: robust design)

Table 6-1 Robust objective function of optimized designs for example 1

Situations	Method	Mean	Standard variance	Robust objective function value	FEA calls
Deterministic design under uncertainties	HUDR	1240.51	157.95	1398.46	70
	MCS	1241.85	155.97	1397.82	1×10^7
Robust design under uncertainties	HUDR	1162.58	79.74	1242.32	70

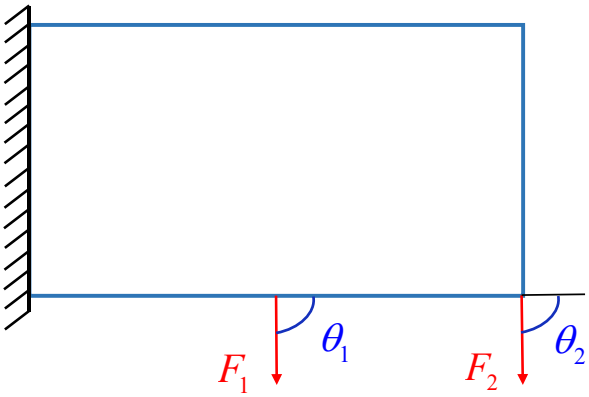

Figure 6-7 Design domain and boundary condition for example 2

Consider a 2:1 (length=1.6m and width=0.8m) cantilever beam, the boundary conditions and loads are given in Figure 6-7. The elastic tensor is given as $E=7\times10^{10}$ Pa and the Poisson's ratio is given as $\upsilon=0.3$. Two vertical loads F_1 and F_2 are applied on the middle point of the lower bound and the lower-right corner of the beam. The loading directions are considered as normal random variables with mean values $[\pi/2,\pi/2]$ and standard variances $[\pi/18,\pi/18]$,

and the loading magnitudes are considered as interval variables with nominal values $4\times10^5 N, 8\times10^5 N$ and radius $4\times10^4 N, 8\times10^4 N$ for F_1 and F_2 respectively. The macro structure is discretized by 80×40 Q4 elements, while the micro structures are discretized by 40×40 Q4 elements. The volume fractions for both scales are set to be 0.5.

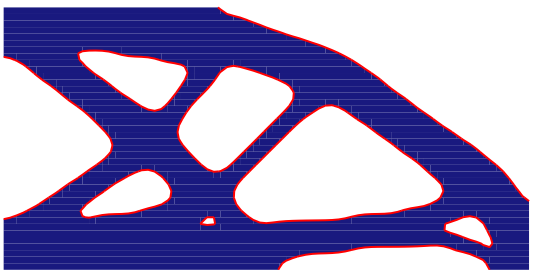

a(1)

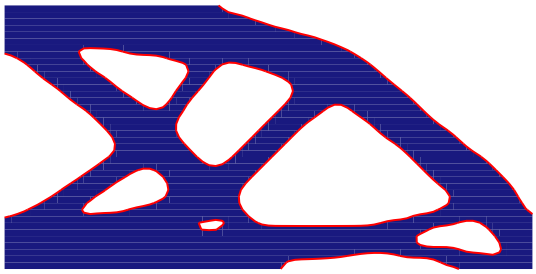

b(1)

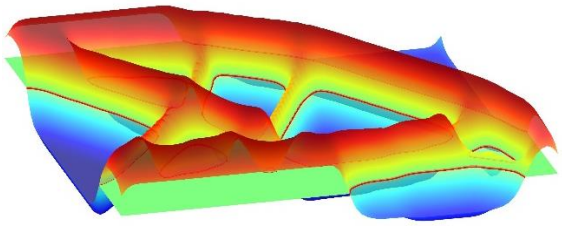

a(2)

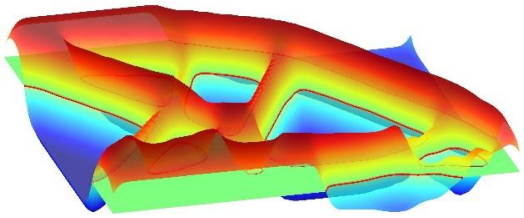

b(2)

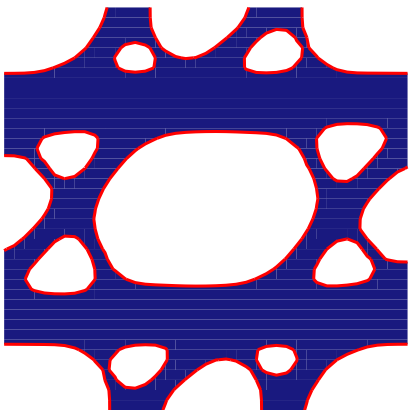

a(3)

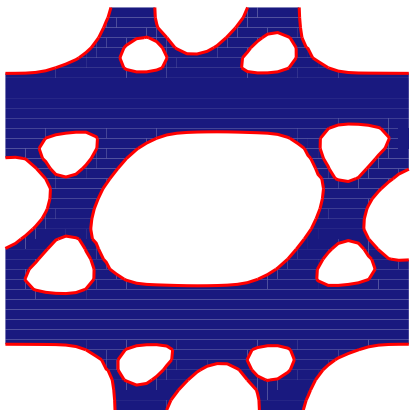

b(3)

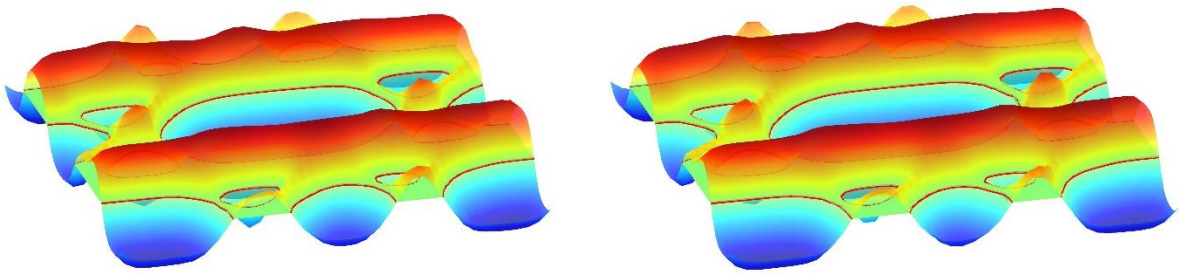

a(4) b(4)

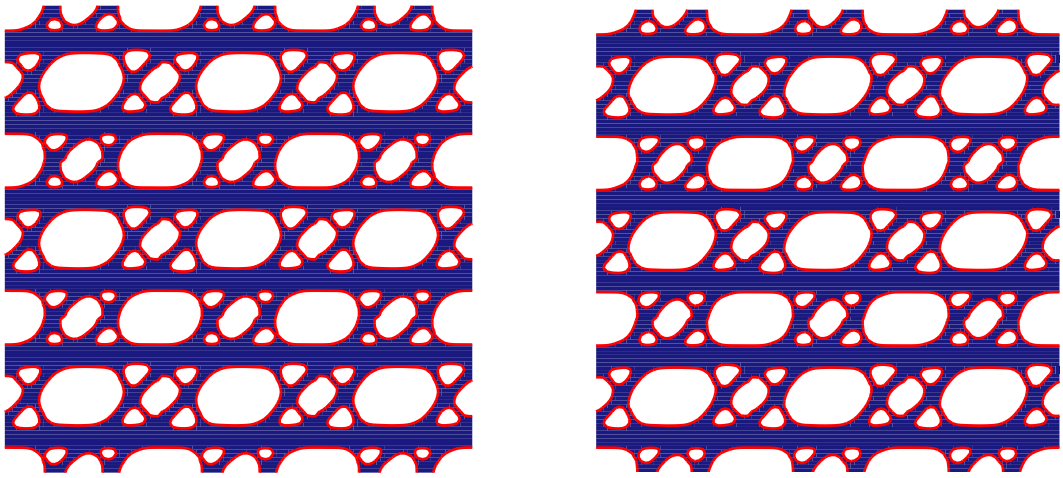

a(5) b(5)

Figure 6-8 Optimized results in macro and micro scales for example 2 (left: deterministic design; right: robust design)

Figure 6-8 gives the optimized results in the macro and micro scales for the cantilever beam. It can be seen that the topological results for the structure with uncertainties are different from the deterministic ones. The robust objective function values for both deterministic and uncertain designs are shown in Table 6-2. Under the same uncertain loads, the robust objective function value for the deterministic design is 4207.66, while the robust objective function value for the uncertain design is 4132.33. It can be found that the robust topology optimization results in more robust designs than the deterministic topology optimization. The results by 10^6 Monte Carlo simulations are provided to verify the accuracy of the proposed method. It

can be seen that the results obtained by the proposed method have very good accuracy. The convergence histories of the objective function and volume constraints in Figure 6-9 indicate that the proposed method can obtain the optimization designs efficiently.

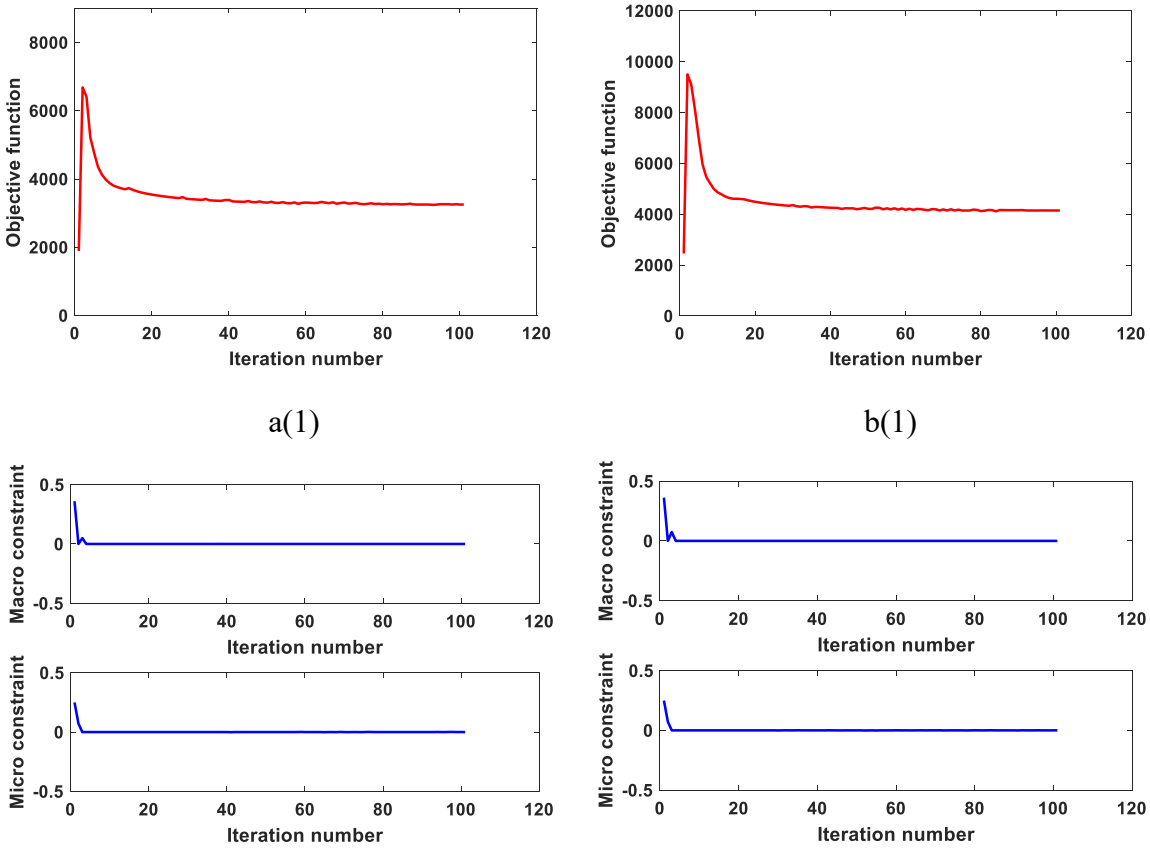

Figure 6-9 Convergent histories for example 2
(left: deterministic design; right: robust design)

Table 6-2 Robust objective function of optimized designs for example 2

Situations	Method	Mean	Standard variance	Robust objective function value	FEA calls
Deterministic design under uncertainties	HUDR	3842.42	365.24	4207.66	35
	MCS	3842.72	368.72	4211.44	1×10^6
Robust design under uncertainties	HUDR	3788.64	343.69	4132.33	35
	MCS	3788.93	343.02	4131.95	1×10^6

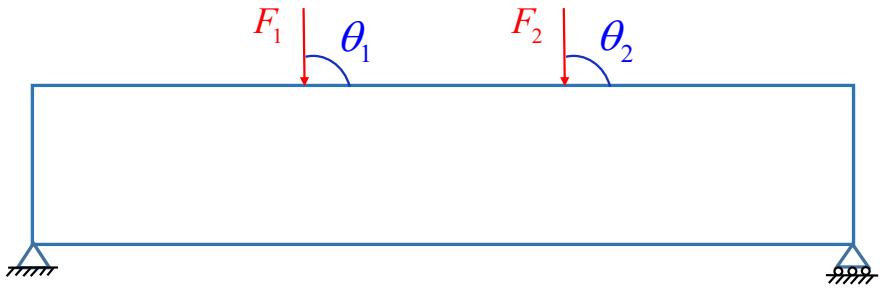

Figure 6-10 Design domain and boundary condition for example 3

Consider a 6:1 (length=1.2m and width=0.2m) MBB beam, the boundary conditions and loads are given in Figure 6-10. The elastic tensor is given as $E=7\times10^{10}$ Pa and the Poisson's ratio is given as $\upsilon=0.3$. Two vertical loads F_1 and F_2 are applied on the upper bound of the beam. The loading directions are considered as normal random variables with mean values $[\pi/2,\pi/2]$ and standard variances $[\pi/18,\pi/18]$, and the loading magnitudes are considered as interval variables with nominal values $5\times10^5N,5\times10^5N$ and radius $5\times10^4N,5\times10^4N$

for F_1 and F_2 respectively. The macro structure is discretized by 120×20 Q4 elements, while the micro structures are discretized by 40×40 Q4 elements. The volume fractions for both scales are set to be 0.5.

a(1)

b(1)

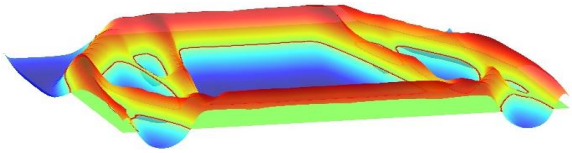

a(2)

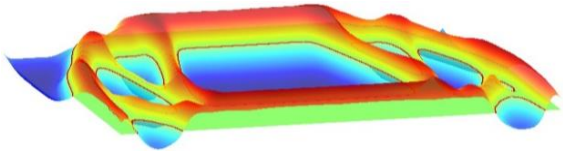

b(2)

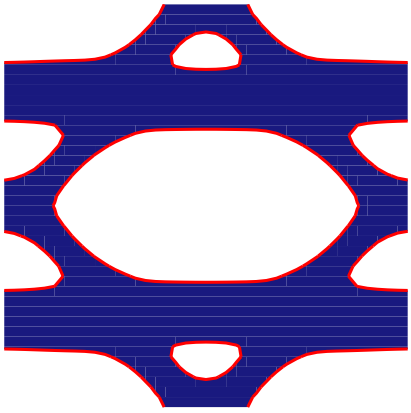

a(3)

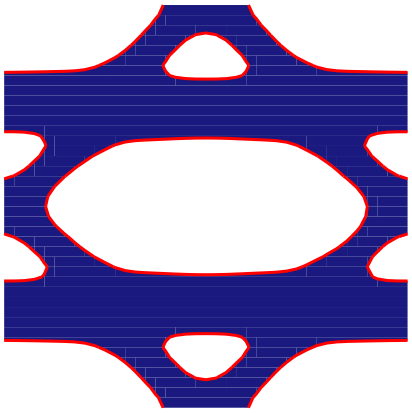

b(3)

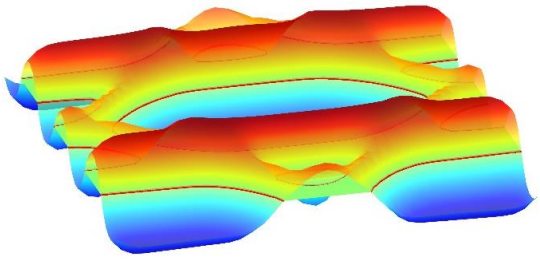

a(4)

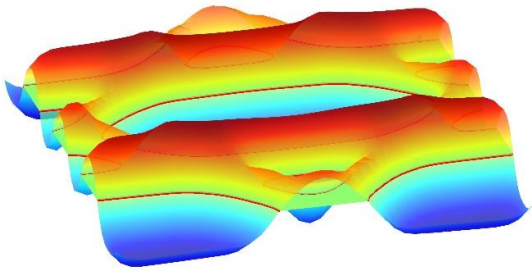

b(4)

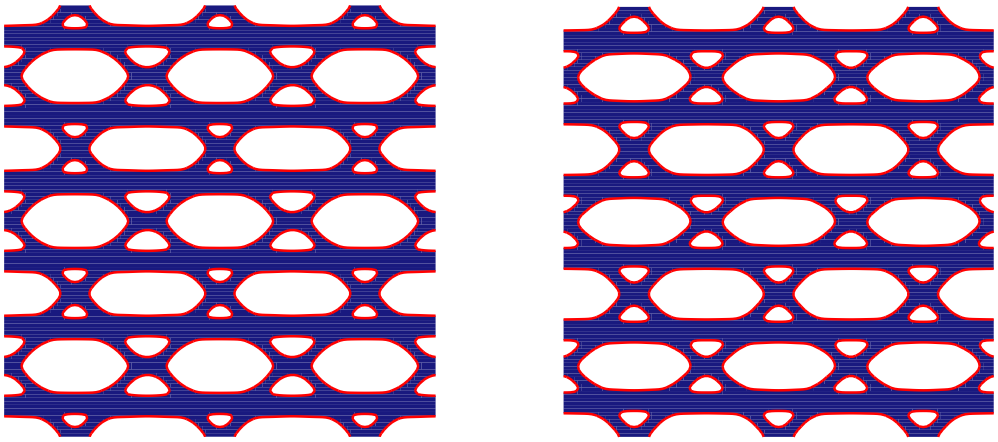

a(5) b(5)

Figure 6-11 Optimized results in macro and micro scales for example 3 (left: deterministic design; right: robust design)

The optimized results for the MBB structure with uncertainties are given in Figure 6-11. Robust macro structure design in Fig. 11 b(1) is different from the deterministic macro design in a(1), although they have similar topologies. The robust macrostructure and microstructure designs in b(1) and b(3) are obviously different from the deterministic macro and micro designs in a(1) and a(3). Table 6-3 gives the robust objective function values for both the deterministic and uncertain designs under the same uncertain loads. The mean and variance of the uncertain design are smaller than those of the deterministic design, that is to say, the robust topology optimization provides robsut design than the deterministic optimization when uncertainties involved. As a reference, the results by 10^6 Monte Carlo simulations are also provided. The convergent histories of the objective function and volume constraints are plotted in Figure 6-12.

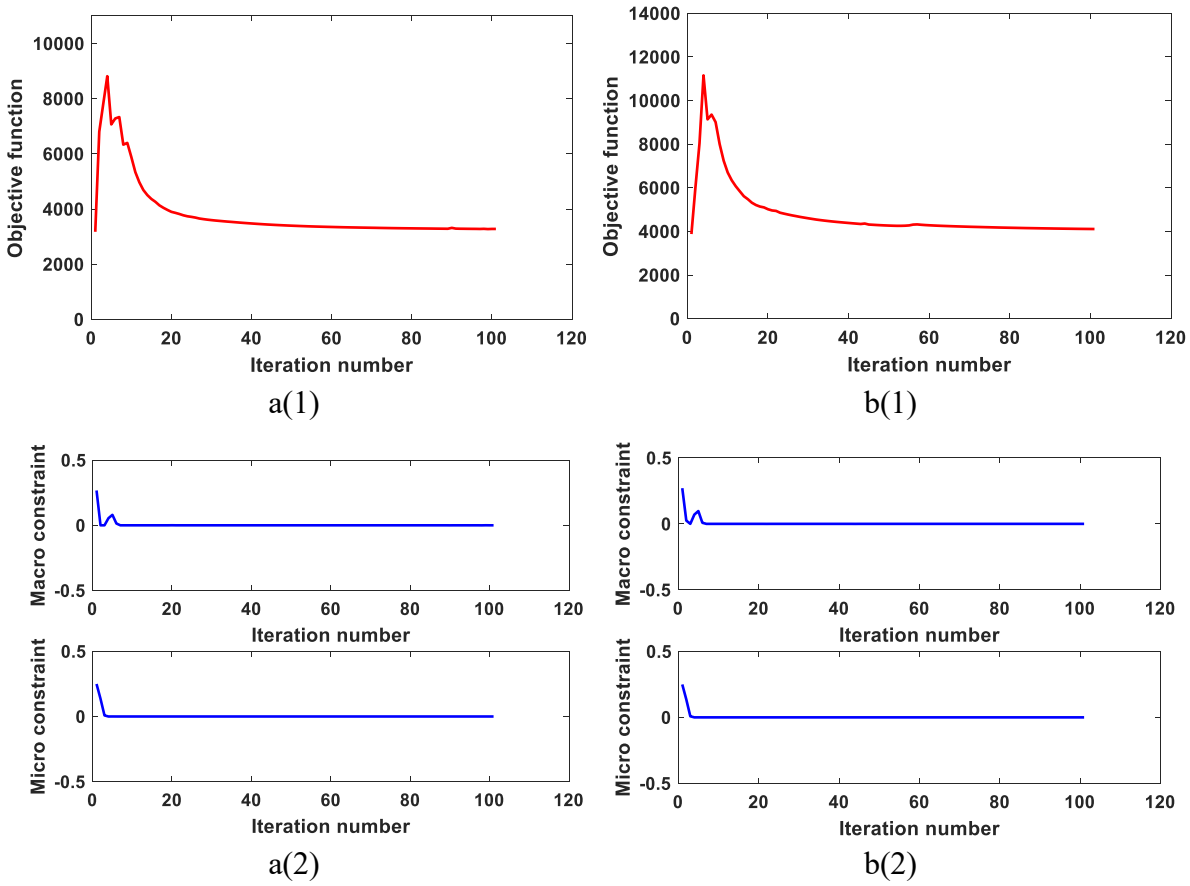

Figure 6-12 Convergent histories for example 3

(left: deterministic design; right: robust design)

Table 6-3 Robust objective function of optimized designs for example 3

Situations	Method	Mean	Standard variance	Robust objective function value	FEA calls
Deterministic design under uncertainties	HUDR	3903.42	286.05	4189.47	35
	MCS	3904.41	283.56	4187.97	1×10^6
Robust design under uncertainties	HUDR	3828.74	277.84	4106.58	35
	MCS	3829.79	273.72	4103.51	1×10^6

6.4 Robust topology optimization for multi-scale design of dynamic structures with hybrid uncertainties

6.4.1 Deterministic multi-scale dynamic topology optimization

6.4.1.1 Mathematical formulation

Similar to the multi-scale framework for static structures, two LSFs Φ^{MA} and Φ^{MI} are also defined to implicitly represent the structural boundaries in the macro and micro scale respectively. The design variables are defined in both scales as expansion coefficients for the approximated LSFs. The concurrent topology optimization model for structural dynamic compliance can be formulated as follows:

$$
\begin{aligned}
&\min_{\boldsymbol{\alpha}^{\mathrm{MA}},\boldsymbol{\alpha}^{\mathrm{MI}}} \; J\left(\boldsymbol{\alpha}^{\mathrm{MA}},\boldsymbol{\alpha}^{\mathrm{MI}}\right)=\left|J_C\left(\boldsymbol{\alpha}^{\mathrm{MA}},\boldsymbol{\alpha}^{\mathrm{MI}}\right)\right| \\
&\quad =\int_{\Omega^{\mathrm{MA}}}\left|\varepsilon_{ij}^{\mathrm{T}}\left(\mathbf{u}^{\mathrm{MA}}\right)E_{ijkl}^{\mathrm{H}}\left(\mathbf{u}^{\mathrm{MI}},\Phi^{\mathrm{MI}}\right)\varepsilon_{kl}\left(\mathbf{u}^{\mathrm{MA}}\right)\right|H\left(\Phi^{\mathrm{MA}}\right)d\Omega^{\mathrm{MA}} \\
&\text{s.t.}\quad \left\{\begin{array}{l} k\left(\mathbf{u}^{\mathrm{MA}},\mathbf{v}^{\mathrm{MA}},\Phi^{\mathrm{MA}}\right)+i\omega c\left(\mathbf{u}^{\mathrm{MA}},\mathbf{v}^{\mathrm{MA}},\Phi^{\mathrm{MA}}\right) \\ -\omega^2 m\left(\mathbf{u}^{\mathrm{MA}},\mathbf{v}^{\mathrm{MA}},\Phi^{\mathrm{MA}}\right)\end{array}\right\}=l^{\mathrm{MA}}\left(\mathbf{v}^{\mathrm{MA}},\Phi^{\mathrm{MA}}\right),\ \forall\mathbf{v}^{\mathrm{MA}}\in\tilde{\mathbf{U}}^{\mathrm{MA}} \\
&\quad a^{\mathrm{MI}}\left(\mathbf{u}^{\mathrm{MI}},\mathbf{v}^{\mathrm{MI}},\Phi^{\mathrm{MI}}\right)=l^{\mathrm{MI}}\left(\mathbf{v}^{\mathrm{MI}},\Phi^{\mathrm{MI}}\right),\ \forall\mathbf{v}^{\mathrm{MI}}\in\tilde{\mathbf{U}}^{\mathrm{MI}} \\
&\quad G^{\mathrm{MA}}\left(\Phi^{\mathrm{MA}}\right)=\int_{\Omega}H\left(\Phi^{\mathrm{MA}}\right)d\Omega^{\mathrm{MA}}-f^{\mathrm{MA}}V_0^{\mathrm{MA}}\le 0 \\
&\quad G^{\mathrm{MI}}\left(\Phi^{\mathrm{MI}}\right)=\int_{\Omega}H\left(\Phi^{\mathrm{MI}}\right)d\Omega^{\mathrm{MI}}-f^{\mathrm{MI}}V_0^{\mathrm{MI}}\le 0 \\
&\quad \alpha_{\min}^{\mathrm{MA}}\le\alpha_e^{\mathrm{MA}}\le\alpha_{\max}^{\mathrm{MA}},e=1,2,\cdots,N \\
&\quad \alpha_{\min}^{\mathrm{MI}}\le\alpha_t^{\mathrm{MI}}\le\alpha_{\max}^{\mathrm{MI}},t=1,2,\cdots,M
\end{aligned}
\tag{6-61}
$$

where $\boldsymbol{\alpha}^{\mathrm{MA}}$ represents the macro design variables within the bounds $\alpha_{\min}^{\mathrm{MA}}$ and $\alpha_{\max}^{\mathrm{MA}}$, $\boldsymbol{\alpha}^{\mathrm{MI}}$ represents the micro design variables within the bounds $\alpha_{\min}^{\mathrm{MI}}$ and $\alpha_{\max}^{\mathrm{MI}}$. N and M are the numbers of macro and micro design variables respectively. J_C is the complex structural

dynamic compliance. The objective function J is the module of the structural dynamic compliance, which is defined by $J=\sqrt{J_R{}^2+J_I{}^2}$. J_R and J_I are the real and image parts of the dynamic compliance J_C. $G^{\mathrm{MA}}\left(\Phi^{\mathrm{MA}}\right)$ and $G^{\mathrm{MI}}\left(\Phi^{\mathrm{MI}}\right)$ indicate the volume constraints in the macro and micro scale respectively. V_0^{MA} and V_0^{MI} are the volumes, and f^{MA} and f^{MI} are the volume fractions of the macrostructure and the microstructure, respectively. H is the Heaviside function. $\mathbf{u}^{\mathrm{MA}}$ denotes the macro displacement field in the macrostructure, and u^{MI} denotes the micro displacement field. $\mathbf{v}^{\mathrm{MA}}$ is the macro virtual displacement field belonging to the macro kinematically admissible displacement $\tilde{\mathbf{U}}^{\mathrm{MA}}$, and $\mathbf{v}^{\mathrm{MI}}$ is the micro virtual displacement field belonging to the micro kinematically admissible displacement $\tilde{\mathbf{U}}^{\mathrm{MI}}$. E_{ijkl}^{H} is the homogenized elasticity matrix. The semi-bilinear form of the stiffness, the damping, the mass and the loading are:

$$\begin{cases} k\left(\Phi^{\mathrm{MA}},\mathbf{u}^{\mathrm{MA}},\mathbf{v}^{\mathrm{MA}},E_{ijkl}^{\mathrm{H}}\right)=\int_{\Omega^{\mathrm{MA}}}\varepsilon_{ij}^{\mathrm{T}}\left(\mathbf{u}^{\mathrm{MA}}\right)E_{ijkl}^{\mathrm{H}}\left(\mathbf{u}^{\mathrm{MI}},\Phi^{\mathrm{MI}}\right)\varepsilon_{kl}\left(\mathbf{v}^{\mathrm{MA}}\right)H\left(\Phi^{\mathrm{MA}}\right)d\Omega^{\mathrm{MA}} \\ m\left(\Phi^{\mathrm{MA}},\mathbf{u}^{\mathrm{MA}},\mathbf{v}^{\mathrm{MA}},E_{ijkl}^{\mathrm{H}}\right)=\int_{\Omega^{\mathrm{MA}}}\rho^{\mathrm{H}}\mathbf{u}^{\mathrm{MA}}\mathbf{v}^{\mathrm{MA}}H\left(\Phi^{\mathrm{MI}}\right)d\Omega^{\mathrm{MA}} \\ c\left(\Phi^{\mathrm{MA}},\mathbf{u}^{\mathrm{MA}},\mathbf{v}^{\mathrm{MA}},E_{ijkl}^{\mathrm{H}}\right)=Ak\left(\Phi^{\mathrm{MA}},\mathbf{u}^{\mathrm{MA}},\mathbf{v}^{\mathrm{MA}},E_{ijkl}^{\mathrm{H}}\right)+Bm\left(\Phi^{\mathrm{MA}},\mathbf{u}^{\mathrm{MA}},\mathbf{v}^{\mathrm{MA}},E_{ijkl}^{\mathrm{H}}\right) \\ l\left(\Phi^{\mathrm{MA}},\mathbf{v}^{\mathrm{MA}}\right)=\int_{\Omega^{\mathrm{MA}}}\mathbf{p}^{\mathrm{MA}}\mathbf{v}^{\mathrm{MA}}H\left(\Phi^{\mathrm{MA}}\right)d\Omega^{\mathrm{MA}}+\int_{\Omega^{\mathrm{MA}}}\boldsymbol{\tau}^{\mathrm{MA}}\mathbf{v}^{\mathrm{MA}}\delta\left(\Phi^{\mathrm{MA}}\right)\left|\nabla\Phi^{\mathrm{MA}}\right|d\Omega^{\mathrm{MA}} \end{cases} \tag{6-62}$$

where $\mathbf{p}^{MA}$ is the macro body force, $\boldsymbol{\tau}^{MA}$ indicates the macro boundary force, ω is the excitation frequency and δ is the partial derivative of the Heaviside function H, namely the Dirac function. ρ^{H} denotes the mass density of the cellular composites, and which is calculated by the simple but efficient 'ersatz material' model [12,40 :

$$\rho^{\mathrm{H}}=\frac{1}{\left|\Omega^{\mathrm{MI}}\right|}\int_{\Omega^{\mathrm{MI}}}\rho_0 H\left(\Phi^{\mathrm{MI}}\right)d\Omega^{\mathrm{MI}} \tag{6-63}$$

where Ω^{MI} denotes the area of a microstructure, and ρ_0 is the mass density of the base material. $E_{ijkl}^{\mathrm{H}}\left(\mathbf{u}^{\mathrm{MI}},\Phi^{\mathrm{MI}}\right)$ represents the homogenized elasticity tensor which is evaluated by numerical homogenization method:

$$E_{ijkl}^{\mathrm{H}}=\frac{1}{\left|\Omega^{\mathrm{MI}}\right|}\int_{\Omega^{\mathrm{MI}}}\left(\varepsilon_{pq}^{0(ij)}-\varepsilon_{pq}^{*}\left(\mathbf{u}^{\mathrm{MI}(ij)}\right)\right)E_{pqrs}\left(\varepsilon_{rs}^{0(kl)}-\varepsilon_{rs}^{*}\left(\mathbf{u}^{\mathrm{MI}(kl)}\right)\right)H\left(\Phi^{\mathrm{MI}}\right)d\Omega^{\mathrm{MI}} \tag{6-64}$$

where $i, j, k, l = 1, 2$. The displacement field $\mathbf{u}^{\mathrm{MI}(ij)}$ in a microstructure can be solved by:

$$\int_{\Omega^{\mathrm{MI}}}\left(\varepsilon_{pq}^{0(ij)}-\varepsilon_{pq}^{*}\left(\mathbf{u}^{\mathrm{MI}(ij)}\right)\right)E_{pqrs}\varepsilon_{rs}^{*}\left(\mathbf{v}^{\mathrm{MI}(ij)}\right)H\left(\Phi^{\mathrm{MI}}\right)d\Omega^{\mathrm{MI}}=0 \tag{6-65}$$

6.4.1.2 Sensitivity analysis

In order to update the design variables in both macro and micro scales, the sensitivities of the objective function and the volume constraints with respect to the variables need to be calculated. The OC method is employed at both scales to efficiently deal with the optimization in this problem.

Sensitivity analysis in the macro scale

The macro expansion coefficients of the CSRBFs are the corresponding design variables in the macro scale optimization. The shape derivate is applied to calculate the derivatives of the objective and constraints with regard to the expansion coefficients. According to Eqs. (6-61) and (6-62), the structural dynamic compliance can be expressed as:

$$J_C=\int_{\Omega^{MA}}\left\{\left(1+i\omega A\right)\varepsilon_{ij}^{\mathrm{T}}\left(\mathbf{u}^{\mathrm{MA}}\right)E_{ijkl}^{\mathrm{H}}\left(\mathbf{u}^{\mathrm{MI}},\Phi^{\mathrm{MI}}\right)\varepsilon_{kl}\left(\mathbf{u}^{\mathrm{MA}}\right)+\left(i\omega B-\omega^2\right)\rho^{\mathrm{H}}\mathbf{u}^{\mathrm{MA}}\mathbf{u}^{\mathrm{MA}}\right\}H\left(\Phi^{\mathrm{MA}}\right)d\Omega^{\mathrm{MA}} \tag{6-66}$$

The material derivatives of the structural dynamic compliance can be derived as follows:

$$\begin{aligned}\dot{J}_C=&2\int_{\Omega^{MA}}\left\{\left(1+i\omega A\right)\varepsilon_{ij}^{\mathrm{T}}\left(\dot{\mathbf{u}}^{\mathrm{MA}}\right)E_{ijkl}^{\mathrm{H}}\varepsilon_{kl}\left(\mathbf{u}^{\mathrm{MA}}\right)+\left(i\omega B-\omega^2\right)\rho^{\mathrm{H}}\dot{\mathbf{u}}^{\mathrm{MA}}\mathbf{u}^{\mathrm{MA}}\right\}H\left(\Phi_{\psi}^{MA}\right)d\Omega^{MA}\\&+\int_{\Gamma^{\mathrm{MA}}}\left\{\left(1+i\omega A\right)\varepsilon_{ij}^{\mathrm{T}}\left(\mathbf{u}^{\mathrm{MA}}\right)E_{ijkl}^{\mathrm{H}}\varepsilon_{kl}\left(\mathbf{u}^{\mathrm{MA}}\right)+\left(i\omega B-\omega^2\right)\rho^{\mathrm{H}}\mathbf{u}^{\mathrm{MA}}\mathbf{u}^{\mathrm{MA}}\right\}\mathbf{v}_n^{\mathrm{MA}}d\Gamma^{\mathrm{MA}}\end{aligned} \tag{6-67}$$

Taking the material derivatives on both sides of the equilibrium equation at macro scale, the following equation is obtained:

$$\begin{aligned}&\left(1+i\omega A\right)\left[k\left(\dot{\mathbf{u}}^{\mathrm{MA}},\mathbf{v}^{\mathrm{MA}}\right)+k\left(u^{\mathrm{MA}},\dot{v}^{\mathrm{MA}}\right)+\int_{\Gamma^{MA}}\left(\varepsilon^{\mathrm{T}}\left(u^{\mathrm{MA}}\right)E_{ijkl}^{\mathrm{H}}\varepsilon\left(\mathbf{v}^{\mathrm{MA}}\right)\right)\mathbf{v}_n^{\mathrm{MA}}d\Gamma^{\mathrm{MA}}\right]\\&+\left(i\omega B-\omega^2\right)\left[m\left(\dot{\mathbf{u}}^{\mathrm{MA}},\mathbf{v}^{\mathrm{MA}}\right)+m\left(\mathbf{u}^{\mathrm{MA}},\dot{\mathbf{v}}^{\mathrm{MA}}\right)+\int_{\Gamma^{MA}}\left(\rho^{\mathrm{H}}\mathbf{u}^{\mathrm{MA}}\mathbf{v}^{\mathrm{MA}}\right)\mathbf{v}_n^{\mathrm{MA}}d\Gamma^{\mathrm{MA}}\right]\\&=\int_{\Omega^{\mathrm{MA}}}\mathbf{p}^{\mathrm{MA}}\dot{\mathbf{v}}^{\mathrm{MA}}H\left(\Phi^{\mathrm{MA}}\right)d\Omega^{\mathrm{MA}}+\int_{\Gamma^{\mathrm{MA}}}\left(\mathbf{p}^{\mathrm{MA}}\mathbf{v}^{\mathrm{MA}}\right)\mathbf{v}_n^{\mathrm{MA}}d\Gamma^{\mathrm{MA}}\\&+\int_{\Gamma^{\mathrm{MA}}}\boldsymbol{\tau}^{\mathrm{MA}}\dot{\mathbf{v}}^{\mathrm{MA}}d\Gamma^{\mathrm{MA}}+\int_{\Gamma^{\mathrm{MA}}}\left(\nabla\left(\boldsymbol{\tau}^{\mathrm{MA}}\mathbf{v}^{\mathrm{MA}}\right)\cdot\mathbf{n}+\kappa\left(\boldsymbol{\tau}^{MA}\mathbf{v}^{\mathrm{MA}}\right)\right)\mathbf{v}_n^{\mathrm{MA}}d\Gamma^{\mathrm{MA}}\end{aligned} \tag{6-68}$$

where $\dot{\mathbf{u}}^{\mathrm{MA}}$ and $\dot{\mathbf{v}}^{\mathrm{MA}}$ denote the partial derivatives of $\mathbf{u}^{\mathrm{MA}}$ and $\mathbf{v}^{\mathrm{MA}}$ with respect to time respectively, $\kappa=div\,\mathbf{n}=\nabla\cdot\mathbf{n}=\nabla\cdot\left(-\nabla\Phi^{MA}\big/\left|\nabla\Phi^{MA}\right|\right)$ is the mean curvature in two dimensions. Since $\dot{\mathbf{v}}^{\mathrm{MA}}\in\tilde{\mathbf{U}}^{\mathrm{MA}}$, the following equation can be derived from the vibrational state equation in the macro scale:

$$\begin{aligned}&\left(1+i\omega A\right)k\left(\mathbf{u}^{\mathrm{MA}},\dot{\mathbf{v}}^{\mathrm{MA}}\right)+\left(i\omega B-\omega^2\right)m\left(\mathbf{u}^{\mathrm{MA}},\dot{\mathbf{v}}^{\mathrm{MA}}\right)\\&=\int_{\Omega^{\mathrm{MA}}}\mathbf{p}^{\mathrm{MA}}\dot{\mathbf{v}}^{\mathrm{MA}}H\left(\Phi^{\mathrm{MA}}\right)d\Omega^{\mathrm{MA}}+\int_{\Gamma^{\mathrm{MA}}}\boldsymbol{\tau}^{\mathrm{MA}}\dot{\mathbf{v}}^{\mathrm{MA}}d\Gamma^{\mathrm{MA}}\end{aligned} \tag{6-69}$$

By substituting Eq. (6-69) into Eq. (6-68), we can get:

$$\begin{aligned}&\left(1+i\omega A\right)k\left(\dot{\mathbf{u}}^{\mathrm{MA}},\mathbf{v}^{\mathrm{MA}}\right)+\left(i\omega B-\omega^2\right)m\left(\dot{\mathbf{u}}^{\mathrm{MA}},\mathbf{v}^{\mathrm{MA}}\right)=\\&-\int_{\Gamma^{\mathrm{MA}}}\left(\left(1+i\omega\beta\right)\left(\varepsilon^{\mathrm{T}}\left(\mathbf{u}^{\mathrm{MA}}\right)E_{ijkl}^{\mathrm{H}}\varepsilon\left(\mathbf{v}^{\mathrm{MA}}\right)\right)+\left(i\omega\alpha-\omega^2\right)\rho^{\mathrm{H}}\mathbf{u}^{\mathrm{MA}}\mathbf{v}^{\mathrm{MA}}\right)\mathbf{v}_n^{\mathrm{MA}}d\Gamma^{\mathrm{MA}}\\&+\int_{\Gamma^{\mathrm{MA}}}\left(\mathbf{p}^{\mathrm{MA}}\mathbf{v}^{\mathrm{MA}}+\nabla\left(\boldsymbol{\tau}^{\mathrm{MA}}\mathbf{v}^{\mathrm{MA}}\right)\cdot\mathbf{n}+\kappa\left(\boldsymbol{\tau}^{\mathrm{MA}}\mathbf{v}^{\mathrm{MA}}\right)\right)\mathbf{v}_n^{\mathrm{MA}}d\Gamma^{\mathrm{MA}}\end{aligned}\tag{6-70}$$

Since the problem is self-adjoint, the virtual displacement field **v** can be defined to be *u*, the above equation can be rewritten as:

$$\begin{aligned}&\left(1+i\omega A\right)\int_{\Omega^{MA}}\varepsilon_{ij}^{\mathrm{T}}\left(\dot{\mathbf{u}}^{\mathrm{MA}}\right)E_{ijkl}^{\mathrm{H}}\left(\mathbf{u}^{\mathrm{MI}},\Phi^{\mathrm{MI}}\right)\varepsilon_{kl}\left(\mathbf{u}^{\mathrm{MA}}\right)H\left(\Phi^{\mathrm{MA}}\right)d\Omega^{\mathrm{MA}}\\&+\left(i\omega B-\omega^2\right)\int_{\Omega^{MA}}\rho^{\mathrm{H}}\dot{\mathbf{u}}^{\mathrm{MA}}\mathbf{u}^{\mathrm{MA}}H\left(\Phi^{\mathrm{MI}}\right)d\Omega^{\mathrm{MA}}=\\&-\int_{\Gamma^{\mathrm{MA}}}\left(\left(1+i\omega A\right)\left(\varepsilon^{\mathrm{T}}\left(\mathbf{u}^{\mathrm{MA}}\right)E_{ijkl}^{\mathrm{H}}\varepsilon\left(\mathbf{u}^{\mathrm{MA}}\right)\right)+\left(i\omega B-\omega^2\right)\rho^{\mathrm{H}}\mathbf{u}^{\mathrm{MA}}\mathbf{u}^{\mathrm{MA}}\right)\mathbf{v}_n^{\mathrm{MA}}d\Gamma^{\mathrm{MA}}\\&+\int_{\Gamma^{\mathrm{MA}}}\left(\mathbf{p}^{\mathrm{MA}}\mathbf{u}^{\mathrm{MA}}+\nabla\left(\boldsymbol{\tau}^{\mathrm{MA}}\mathbf{u}^{\mathrm{MA}}\right)\cdot\mathbf{n}+\kappa\left(\boldsymbol{\tau}^{\mathrm{MA}}\mathbf{u}^{\mathrm{MA}}\right)\right)\mathbf{v}_n^{\mathrm{MA}}d\Gamma^{\mathrm{MA}}\end{aligned}\tag{6-71}$$

Substituting Eq. (6-71) into Eq. (6-67), the material derivatives of the objective function can be transformed into the follows:

$$\dot{J}_C=\int_{\Gamma^{\mathrm{MA}}}\gamma\left(\mathbf{u}^{\mathrm{MA}}\right)\mathbf{v}_n^{\mathrm{MA}}d\Gamma^{MA}\tag{6-72}$$

where

$$\begin{aligned}&\gamma\left(\mathbf{u}^{\mathrm{MA}}\right)=-\left(1+i\omega A\right)\varepsilon^{\mathrm{T}}\left(\mathbf{u}^{\mathrm{MA}}\right)E_{ijkl}^{\mathrm{H}}\varepsilon\left(\mathbf{u}^{\mathrm{MA}}\right)-\left(i\omega B-\omega^2\right)\rho^{\mathrm{H}}\mathbf{u}^{\mathrm{MA}}\mathbf{u}^{\mathrm{MA}}\\&+2\left(\mathbf{p}^{MA}\mathbf{u}^{\mathrm{MA}}+\nabla\left(\boldsymbol{\tau}^{MA}\mathbf{u}^{\mathrm{MA}}\right)\cdot\mathbf{n}+\kappa\left(\boldsymbol{\tau}^{MA}\mathbf{u}^{\mathrm{MA}}\right)\right)\end{aligned}\tag{6-73}$$

The following Lagrangian function is defined with Lagrange multipliers Λ and λ:

$$L=J_C+\lambda\left(\left(1+j\omega A\right)k+\left(j\omega B-\omega^2\right)m-l\right)+\Lambda G^{\mathrm{MA}}\tag{6-74}$$

The shape derivative of the Lagrangian function is:

$$\begin{aligned}\frac{\partial L}{\partial t}&=\frac{\partial J_C}{\partial t}+\Lambda\frac{\partial G^{\mathrm{MA}}\left(\Phi^{\mathrm{MA}}\right)}{\partial t}=\int_{\Gamma^{\mathrm{MA}}}\gamma\left(\mathbf{u}^{\mathrm{MA}}\right)\mathbf{v}_n^{\mathrm{MA}}d\Gamma^{\mathrm{MA}}+\Lambda\int_{\Gamma^{\mathrm{MA}}}\mathbf{v}_n^{\mathrm{MA}}d\Gamma^{\mathrm{MA}}\\&=\int_{\Omega^{\mathrm{MA}}}\gamma\left(\mathbf{u}\right)\mathbf{v}_n^{\mathrm{MA}}\delta\left(\Phi^{\mathrm{MA}}\right)\left|\nabla\Phi^{\mathrm{MA}}\right|d\Omega^{\mathrm{MA}}+\Lambda\int_{\Omega^{\mathrm{MA}}}\mathbf{v}_n^{\mathrm{MA}}\delta\left(\Phi^{\mathrm{MA}}\right)\left|\nabla\Phi^{\mathrm{MA}}\right|d\Omega^{\mathrm{MA}}\end{aligned}\tag{6-75}$$

Based on the velocity field from the CSRBF interpolation, we can obtain:

$$\begin{aligned}\frac{\partial L}{\partial t}=&\left[\int_{\Omega^{\mathrm{MA}}}\gamma\left(\mathbf{u}^{\mathrm{MA}}\right)\frac{\boldsymbol{\phi}\left(\mathbf{x}\right)^{\mathrm{T}}}{\left|\nabla\boldsymbol{\phi}\left(\mathbf{x}\right)^{\mathrm{T}}\boldsymbol{\alpha}^{\mathrm{MA}}\left(t\right)\right|}\delta\left(\Phi^{\mathrm{MA}}\right)\left|\nabla\Phi^{\mathrm{MA}}\right|d\Omega^{\mathrm{MA}}\right]\dot{\boldsymbol{\alpha}}^{\mathrm{MA}}\left(t\right)\\&+\Lambda\left[\int_{\Omega^{\mathrm{MA}}}\frac{\boldsymbol{\phi}\left(\mathbf{x}\right)^{\mathrm{T}}}{\left|\nabla\boldsymbol{\phi}\left(\mathbf{x}\right)^{\mathrm{T}}\boldsymbol{\alpha}^{\mathrm{MA}}\left(t\right)\right|}\delta\left(\Phi^{\mathrm{MA}}\right)\left|\nabla\Phi^{\mathrm{MA}}\right|d\Omega^{\mathrm{MA}}\right]\dot{\boldsymbol{\alpha}}^{\mathrm{MA}}\left(t\right)\\&=\left[\sum_{i=1}^{N}\int_{\Omega^{\mathrm{MA}}}\gamma\left(\mathbf{u}^{\mathrm{MA}}\right)\frac{\varphi_i\left(\mathbf{x}\right)^{\mathrm{T}}}{\left|\nabla\boldsymbol{\phi}\left(\mathbf{x}\right)^{\mathrm{T}}\boldsymbol{\alpha}^{\mathrm{MA}}\left(t\right)\right|}\delta\left(\Phi^{\mathrm{MA}}\right)\left|\nabla\Phi^{\mathrm{MA}}\right|d\Omega^{\mathrm{MA}}\right]\dot{\boldsymbol{\alpha}}^{\mathrm{MA}}\left(t\right)\\&+\Lambda\left[\sum_{i=1}^{N}\int_{\Omega^{\mathrm{MA}}}\frac{\varphi_i\left(\mathbf{x}\right)^{\mathrm{T}}}{\left|\nabla\boldsymbol{\phi}\left(\mathbf{x}\right)^{\mathrm{T}}\boldsymbol{\alpha}^{\mathrm{MA}}\left(t\right)\right|}\delta\left(\Phi^{\mathrm{MA}}\right)\left|\nabla\Phi^{\mathrm{MA}}\right|d\Omega^{\mathrm{MA}}\right]\dot{\boldsymbol{\alpha}}^{\mathrm{MA}}\left(t\right)\end{aligned}\tag{6-76}$$

On the other hand, according to the chain rule:

$$\frac{\partial L}{\partial t}=\left[\sum_{i=1}^{N}\frac{\partial J_C}{\partial\alpha_e^{\mathrm{MA}}\left(t\right)}\right]\dot{\boldsymbol{\alpha}}^{\mathrm{MA}}\left(t\right)+\Lambda\left[\sum_{i=1}^{N}\frac{\partial J_C}{\partial\alpha_e^{\mathrm{MA}}}\right]\dot{\boldsymbol{\alpha}}^{\mathrm{MA}}\left(t\right)\tag{6-77}$$

Comparing Eqs. (6-76) and (6-77), the design sensitivities of the complex structural dynamic compliance with respect to the macro expansion coefficients are:

$$\begin{aligned}\frac{\partial J_C}{\partial\alpha_e^{\mathrm{MA}}}&=\frac{\partial J_R}{\partial\alpha_e^{\mathrm{MA}}}+i\frac{\partial J_I}{\partial\alpha_e^{\mathrm{MA}}}\\&=\int_{\Omega^{\mathrm{MA}}}\gamma\left(\mathbf{u}^{\mathrm{MA}}\right)\frac{\varphi_e\left(\mathbf{x}\right)}{\left|\left(\nabla\boldsymbol{\varphi}\right)^{T}\boldsymbol{\alpha}^{\mathrm{MA}}\left(t\right)\right|}\delta\left(\Phi^{\mathrm{MA}}\right)\left|\nabla\Phi^{\mathrm{MA}}\right|d\Omega^{\mathrm{MA}}\\&=\int_{\Omega^{\mathrm{MA}}}\gamma\left(\mathbf{u}^{\mathrm{MA}}\right)\varphi_e\left(\mathbf{x}\right)\delta\left(\Phi^{\mathrm{MA}}\right)d\Omega^{\mathrm{MA}}\end{aligned}\tag{6-78}$$

Finally, the sensitivities of the objective function can be calculated as follows:

$$\frac{\partial J}{\partial \alpha_e^{\mathrm{MA}}}=\frac{1}{J_d}\left(J_R\frac{\partial J_R}{\partial \alpha_e^{\mathrm{MA}}}+J_I\frac{\partial J_I}{\partial \alpha_e^{\mathrm{MA}}}\right) \tag{6-79}$$

Similarly, the sensitivities of the macro volume constraint with respect to the macro expansion coefficients are:

$$\frac{\partial G^{\mathrm{MA}}}{\partial \alpha_e^{\mathrm{MA}}}=\int_{\Omega^{\mathrm{MA}}}\varphi_e(\mathbf{x})\delta\left(\Phi^{\mathrm{MA}}\right)d\Omega^{\mathrm{MA}} \tag{6-80}$$

Sensitivity analysis in the micro scale

The derivatives of the dynamic compliance with respect to the micro design variables are:

$$\begin{aligned}\frac{\partial J_C}{\partial \alpha_t^{\mathrm{MI}}}&=\frac{\partial J_R}{\partial \alpha_t^{\mathrm{MI}}}+i\frac{\partial J_I}{\partial \alpha_t^{\mathrm{MI}}}\\&=\int_{\Omega^{\mathrm{MA}}}\left\{(1+i\omega A)\varepsilon^{\mathrm{T}}\left(\mathbf{u}^{\mathrm{MA}}\right)\frac{\partial E_{ijkl}^{\mathrm{H}}}{\partial \alpha_t^{\mathrm{MI}}}\varepsilon\left(\mathbf{u}^{\mathrm{MA}}\right)+\left(i\omega B-\omega^2\right)\frac{\partial \rho^{\mathrm{H}}}{\partial \alpha_t^{\mathrm{MI}}}\mathbf{u}^{\mathrm{MA}}\mathbf{u}^{\mathrm{MA}}\right\}H\left(\Phi^{\mathrm{MA}}\right)d\Omega^{\mathrm{MA}}\end{aligned} \tag{6-81}$$

The first-order derivatives of E_{ijkl}^{H} and ρ^{H} with respect to the micro design variables are the unknown part in the sensitivities in Eq. (6-81). From section 6.3, we know that the first-order derivative of the homogenized elastic tensor E_{ijkl}^{H} with respect to the micro design variable is given as:

$$\frac{\partial E_{ijkl}^{\mathrm{H}}}{\partial \alpha_t^{\mathrm{MI}}}=-\frac{1}{\left|\Omega^{\mathrm{MI}}\right|}\int_{\Omega^{\mathrm{MI}}}\beta\left(\mathbf{u}^{\mathrm{MI}}\right)\phi_t(\mathbf{y})^{\mathrm{T}}\,\delta\left(\Phi^{\mathrm{MI}}\right)d\Omega^{\mathrm{MI}} \tag{6-82}$$

where

$$\beta\left(\mathbf{u}^{\mathrm{MI}}\right)=\left(\varepsilon_{pq}^{0(ij)}-\varepsilon_{pq}^{*}\left(\mathbf{u}^{\mathrm{MI}(ij)}\right)\right)E_{pqrs}\left(\varepsilon_{rs}^{0(kl)}-\varepsilon_{rs}^{*}\left(\mathbf{u}^{\mathrm{MI}(kl)}\right)\right) \tag{6-83}$$

The first-order derivatives of mass density with respect to micro design variables are stated as:

$$\frac{\partial\rho^{\mathrm{H}}}{\partial\alpha_t^{\mathrm{MI}}}=\frac{1}{\left|\Omega^{\mathrm{MI}}\right|}\int_{\Omega^{\mathrm{MI}}}\rho_0\phi_t\left(\mathbf{y}\right)^{\mathrm{T}}\delta\left(\Phi^{\mathrm{MI}}\right)d\Omega^{\mathrm{MI}} \tag{6-84}$$

Substituting Eq. (6-82) and (6-84) into Eq. (6-81), the sensitivities of J_C with respect to the micro design variables are calculated. Finally, the design sensitivities of the objective can be computed by the chain rule, as follows:

$$\frac{\partial J}{\partial\alpha_t^{\mathrm{MI}}}=\frac{1}{J_d}\left(J_R\frac{\partial J_R}{\partial\alpha_t^{\mathrm{MI}}}+J_I\frac{\partial J_I}{\partial\alpha_t^{\mathrm{MI}}}\right) \tag{6-85}$$

Similarly, the sensitivities of the micro volume constraint with respect to the micro design variables is defined by:

$$\frac{\partial G^{\mathrm{MI}}}{\partial\alpha_t^{\mathrm{MI}}}=\frac{1}{\left|\Omega^{\mathrm{MI}}\right|}\int_{\Omega^{\mathrm{MI}}}\phi_t\left(\mathbf{y}\right)^{\mathrm{T}}\delta\left(\Phi_{\psi}^{MI}\right)d\Omega^{\mathrm{MI}} \tag{6-86}$$

6.4.2 Robust dynamic topology optimization

6.4.2.1 Mathematical formulation

$\mathbf{X}=\left(X_1,X_2,...,X_n\right)$ is the probability vector and $\mathbf{Y}=\left(Y_1,Y_2,...,Y_m\right)$ is the interval vector in the structure. $X_i(i=1,2,\cdots,n)$ is the ith probability uncertain variable and the probability distribution function is given as $f_{X_i}\left(X_i\right)$. $Y_i(i=1,2,\cdots,m)$ is the ith interval variable, and the

interval variation of the interval variable is given as $[Y_i^L, Y_i^R]$. $Y_i^C = \frac{Y_i^L + Y_i^R}{2}$ and $Y_i^W = \frac{Y_i^R - Y_i^L}{2}$ represent the interval midpoint and the interval radius of Y_i, respectively.

The robust objective function is defined as a linear combination of the mean and standard deviation of structure compliance due to the random and interval variables. The robust topology optimization can be reformulated under the worst case:

$$\begin{aligned} &\min_{\boldsymbol{\alpha}^{\mathrm{MA}},\boldsymbol{\alpha}^{\mathrm{MI}}} \ g = \max_{\mathbf{Y}} \mu(J) + h \cdot \sigma(J) \\ &st. \ \left(\mathbf{K} + jw\mathbf{C} - w^2\mathbf{M}\right)\mathbf{U} = \mathbf{P} \\ &\quad \sum_{e=1}^{N} \alpha_e^{\mathrm{MA}} V_e \le f^{\mathrm{MA}} V, \sum_{t=1}^{M} \alpha_t^{\mathrm{MI}} V_t^e \le f^{\mathrm{MI}} V_e \\ &\quad \alpha_{\min}^{\mathrm{MA}} \le \alpha_e^{\mathrm{MA}} \le \alpha_{\max}^{\mathrm{MA}}, e = 1,2,\cdots,N \\ &\quad \alpha_{\min}^{\mathrm{MI}} \le \alpha_t^{\mathrm{MI}} \le \alpha_{\max}^{\mathrm{MI}}, t = 1,2,\cdots,M \end{aligned} \tag{6-87}$$

where $\alpha_e^{\mathrm{MA}}(e = 1,2,\cdots,N)$ and $\alpha_t^{\mathrm{MI}}(t = 1,2,\cdots,M)$ are the design variables of the *e*th and *t*th elements of the macrostructure and microstructure respectively, *N* and *M* are the numbers of macro and micro design variables respectively. **M** is the global mass matrix, **C** is the global damping matrix, **K** is the global stiffness matrix, and **P** is the magnitude of the dynamic load with frequency w. V and V_e represent the volume of the macrostructure and the unit cell, and V_t^e represents the element volume of the unit cell. f^{MA} and f^{MI} are volume fractions for volume constraints. $\mu(J)$ represents the mean value of the objective function. $\sigma(J)$ is the standard deviation of the objective function, and h represents a given weight value which is set as 1 here.

The HDR method proposed in 4.2.2 is employed here to evaluate the objective function of the robust topology optimization problem in Eq. (6-87). Fixing the interval variables, the mean and the standard variance of the structural compliance can be evaluated by Eqs. (4-53) and (4-44). Taking into consideration the interval uncertainties, by Eqs. (4-46) and (4-47), the robust objective function can be approximated as:

$$\begin{aligned} g &= \max_{\mathbf{Y}} \mu(J(Y_1, Y_2, \cdots, Y_m)) + h \cdot \sigma(J(Y_1, Y_2, \cdots, Y_m)) \\ &\cong \max_{\mathbf{Y}} \left(\begin{array}{l} \sum_{i=1}^{m} \mu(J(Y_1^C, \cdots, Y_i, \cdots, Y_m^C)) - (m-1) \cdot \mu(J(Y_1^C, Y_2^C, \cdots, Y_m^C)) \\ + h \cdot \sum_{i=1}^{m} \sigma(J(Y_1^C, \cdots, Y_i, \cdots, Y_m^C)) - (m-1) \cdot h \cdot \sigma(J(Y_1^C, Y_2^C, \cdots, Y_m^C)) \end{array} \right) \\ &= \max_{\mathbf{Y}} P_1(Y_1) + P_2(Y_2) + \cdots + P_m(Y_m) - P_C \end{aligned} \tag{6-88}$$

where

$$\begin{cases} P_i(Y_i) = \mu(J(Y_1^C, \cdots, Y_i, \cdots, Y_m^C)) + h \cdot \sigma(J(Y_1^C, \cdots, Y_i, \cdots, Y_m^C)), i = 1, 2, \cdots, m \\ P_C = (m-1) \cdot \mu(J(Y_1^C, Y_2^C, \cdots, Y_m^C)) + (m-1) \cdot h \cdot \sigma(J(Y_1^C, Y_2^C, \cdots, Y_m^C)) \end{cases} \tag{6-89}$$

From the above we can see that, $P_i(Y_i)$ is a function with an interval variable Y_i, and P_C is a constant. Using the first order Taylor series:

$$P_i(Y_i) \cong P_i(Y_i^C) + \nabla P_i \cdot (Y_i - Y_i^C) \tag{6-90}$$

where ∇P_i represents the sensitivity of P_i with respect to interval variable Y_i. In order to obtain the maximum value of P_i, we can get the corresponding interval value from the sign of the sensitivity of P_i: if $\nabla P_i > 0, Y_i = Y_i^R$; if $\nabla P_i < 0, Y_i = Y_i^L$. As a result, the value of the robust objective function $g = \max \mu(J) + h \cdot \sigma(J)$ can be obtained.

6.4.2.2 Sensitivity analysis

The OC method is a gradient-based optimization method, so the sensitivities with respect to the design variables need to be calculated. In this work, the OC method is used to update both macro and micro design variables in both scales.

Sensitivity analysis in the macro scale

The sensitivities of the objective function with respect to the macro design variables can be expressed by:

$$\frac{\partial(\mu(J)+h\cdot\sigma(J))}{\partial\alpha_e^{\mathrm{MA}}}=\frac{\partial\mu(J)}{\partial\alpha_e^{\mathrm{MA}}}+h\cdot\frac{\partial\sigma(J)}{\partial\alpha_e^{\mathrm{MA}}} \tag{6-91}$$

Based on the compound function derivation law, we have:

$$\frac{\partial\sigma^2(J)}{\partial\alpha_e^{\mathrm{MA}}}=2\cdot\sigma(J)\cdot\frac{\partial\sigma(J)}{\partial\alpha_e^{\mathrm{MA}}} \tag{6-92}$$

Then Eq. (6-91) will be changed to the following:

$$\begin{aligned}\frac{\partial(\mu(J)+h\cdot\sigma(J))}{\partial\alpha_e^{\mathrm{MA}}}&=\frac{\partial\mu(J)}{\partial\alpha_e^{\mathrm{MA}}}+h\cdot\frac{\partial\sigma^2(J)}{2\cdot\sigma(J)\cdot\partial\alpha_e^{\mathrm{MA}}}=\frac{\partial\sum_{l=1}^{L}J_l/L}{\partial\alpha_e^{\mathrm{MA}}}+h\cdot\frac{\partial\sum_{l=1}^{L}(J_l-\mu(J))^2/L}{2\cdot\sigma(J)\cdot\partial\alpha_e^{\mathrm{MA}}}\\&=\sum_{l=1}^{L}\left(\partial J_l/\partial\alpha_e^{\mathrm{MA}}\right)/L+\frac{h}{\sigma(J)}\cdot\sum_{l=1}^{L}\left|J_l-\mu(J)\right|\cdot\left(\partial J_l/\partial\alpha_e^{\mathrm{MA}}\right)/L\\&=E\left(\partial J/\partial\alpha_e^{\mathrm{MA}}\right)+\frac{h}{\sigma(J)}\cdot E\left(\left|J-\mu(J)\right|\cdot\left(\partial J/\partial\alpha_e^{\mathrm{MA}}\right)\right)\end{aligned} \tag{6-93}$$

where J_l means the l th value of L samples of objective values. From Eq. (6-79), the explicit expression of $\partial J/\partial\alpha_e^{\mathrm{MA}}$ and $\left|J-\mu(J)\right|\cdot\left(\partial J/\partial\alpha_e^{\mathrm{MA}}\right)$ can be obtained, and the mean value

$E\left(\partial J/\partial \alpha_e^{\mathrm{MA}}\right)$ and $E\left(\left|J-\mu(J)\right|\cdot\left(\partial J/\partial \alpha_e^{\mathrm{MA}}\right)\right)$ can be easily obtained using the same formula as Eq. (4-53).

Sensitivity analysis in the micro scale

Similarly, the sensitivity analysis of the objective function with respect to micro design variables is:

$$\frac{\partial(\mu(J)+h\cdot\sigma(J))}{\partial \alpha_t^{\mathrm{MI}}}=\frac{\partial \mu(J)}{\partial \alpha_t^{\mathrm{MI}}}+h\cdot\frac{\partial \sigma(J)}{\partial \alpha_t^{\mathrm{MI}}} \tag{6-94}$$

In the same way, we will obtain:

$$\begin{aligned}\frac{\partial(\mu(J)+h\cdot\sigma(J))}{\partial \alpha_t^{\mathrm{MI}}}&=\sum_{l=1}^{L}\frac{\partial J_l}{\partial \alpha_t^{\mathrm{MI}}}/L+\frac{h}{\sigma(J)}\cdot\sum_{l=1}^{L}\left|J_l-\mu(J)\right|\cdot\frac{\partial J_l}{\partial \alpha_t^{\mathrm{MI}}}/L\\&=E\left(\partial J/\partial \alpha_t^{\mathrm{MI}}\right)+\frac{h}{\sigma(J)}\cdot E\left(\left|J-\mu(J)\right|\cdot\left(\partial J/\partial \alpha_t^{\mathrm{MI}}\right)\right)\end{aligned} \tag{6-95}$$

Based on Eq. (6-85), the explicit expression of $\partial J/\partial \alpha_t^{\mathrm{MI}}$ and $\left|J-\mu(J)\right|\cdot\left(\partial J/\partial \alpha_t^{\mathrm{MI}}\right)$ can be obtained. With the mean value $E\left(\partial J/\partial \alpha_t^{\mathrm{MI}}\right)$ and $E\left(\left|J-\mu(J)\right|\cdot\left(\partial J/\partial \alpha_t^{\mathrm{MI}}\right)\right)$, we can also easily obtain the sensitivities in (6-95).

6.4.2.3 Optimization procedure

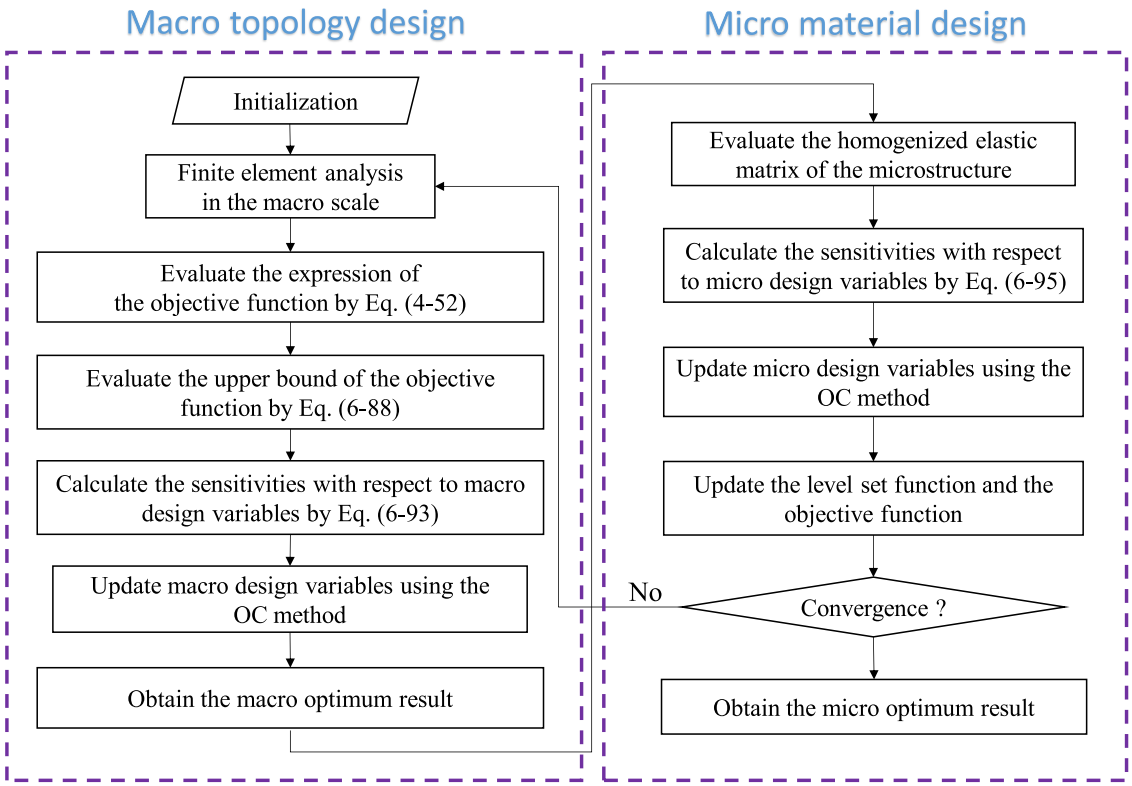

Figure 6-13 The flowchart of the proposed method

The process of the proposed multi-scale robust topology optimization method under hybrid uncertainties can be summarized as follows (Figure 6-13):

Step 1: Initialize the design variables α_i and ρ_e in both scales;

Step 2: Obtain the displacement field by the FEA in the macro scale;

Step 3: Evaluate the robust objective function value by using Eqs. (4-53) and (6-88);

Step 4: Compute the sensitivities of the objective function with respect to the macro design variables based on Eq. (6-93), and update the macro design variables using the OC method;

Step 5: Evaluate the homogenized elastic matrix in the micro scale;

Step 6: Compute the sensitivities of the objective function with respect to the micro design variables based on Eq. (6-95), and update the micro design variables using the OC method;

Step 7: Update the LSF and the robust objective function;

Step 8: Check convergence.

6.4.3 Numerical examples

In this section, the damping coefficients for all examples are set as $A = 0.03$ and $B = 0.001$, and the mass density is $\rho = 2700 g / cm^3$. In the deterministic designs, the corresponding

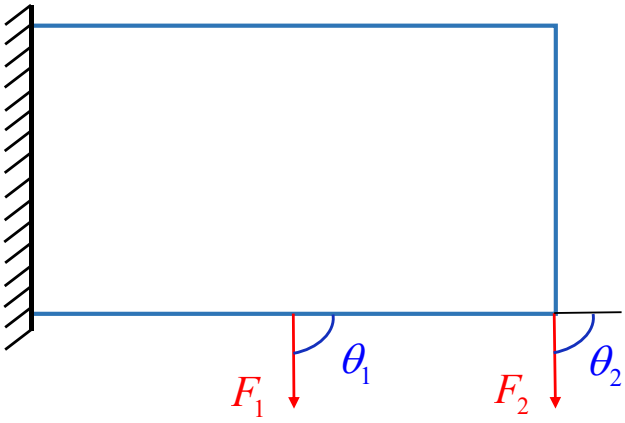

Figure 6-14 Design domain and boundary condition for example 1

Consider a 2:1 (length=1.6m and width=0.8m) cantilever beam, the boundary conditions and loads are given in Figure 6-14. Two vertical loads F_1 and F_2 are applied on the middle point

of the lower bound and the lower-right corner of the beam. The load magnitudes and the load directions are considered as normal random variables, while the Young's modulus and the Poisson's ratio are assumed to be interval variables. The mean values of the loads are all set to be $3\times10^5 N$, the standard variances of the loads are all set to be $3\times10^4 N$. The load directions are with mean values $\frac{\pi}{2}$ and standard variances $\frac{\pi}{18}$. The interval variables are set to be $E=\left[6.3\times10^{10}\,\text{Pa}, 7.7\times10^{10}\,\text{Pa}\right]$ and $\upsilon=[0.27, 0.33]$. The macro structure is discretized by 80×40 Q4 elements, while the micro structures are discretized by 40×40 Q4 elements. The volume fractions for both scales are set to be 0.5.

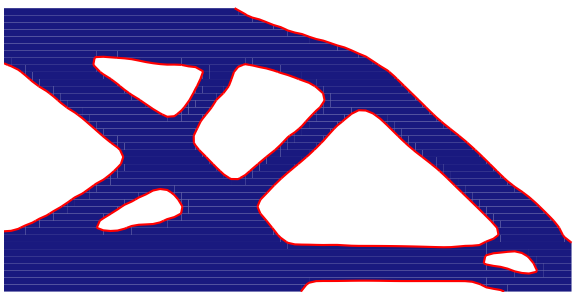

a(1)

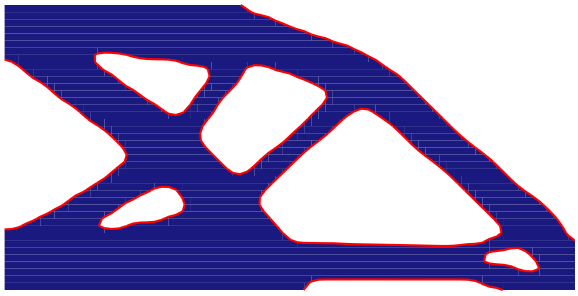

b(1)

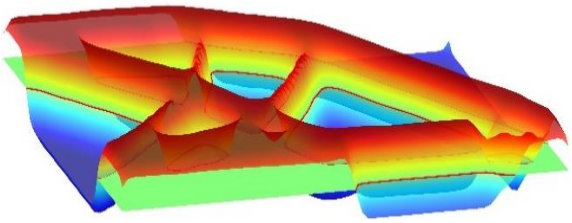

a(2)

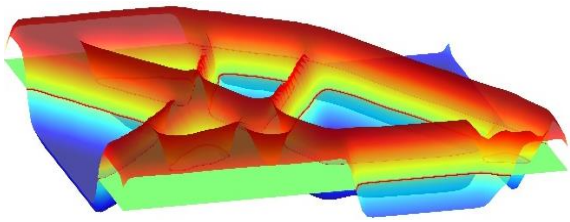

b(2)

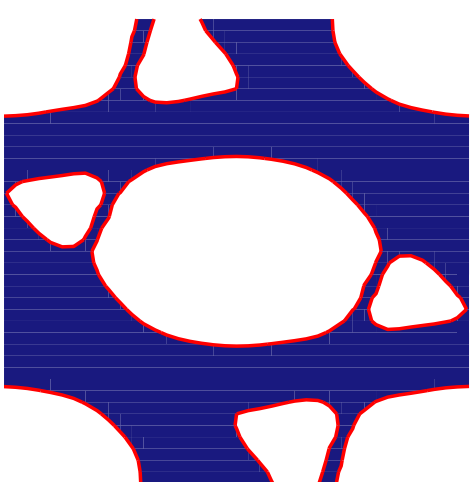

a(3)

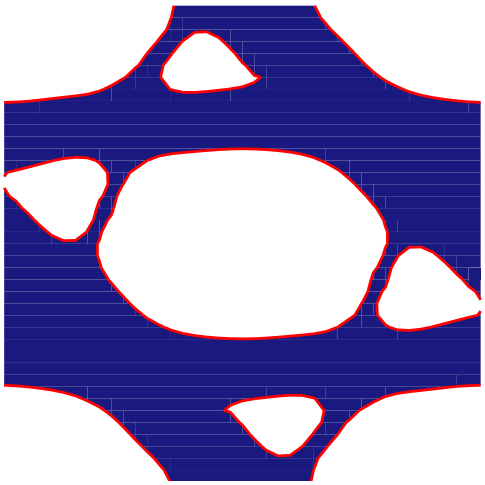

b(3)

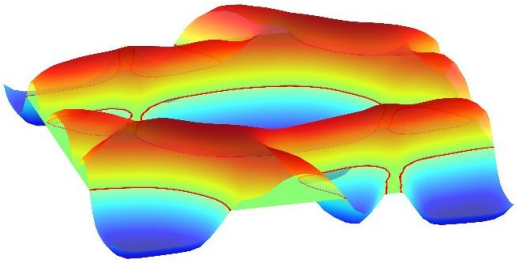

a(4)

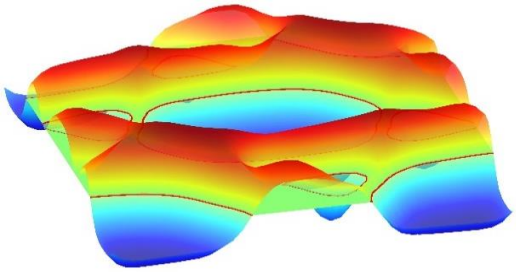

b(4)

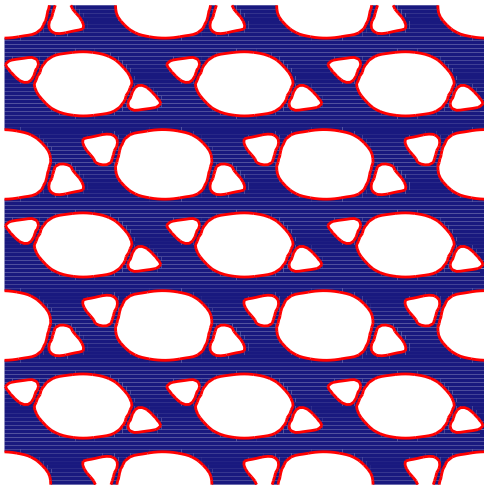

a(5)

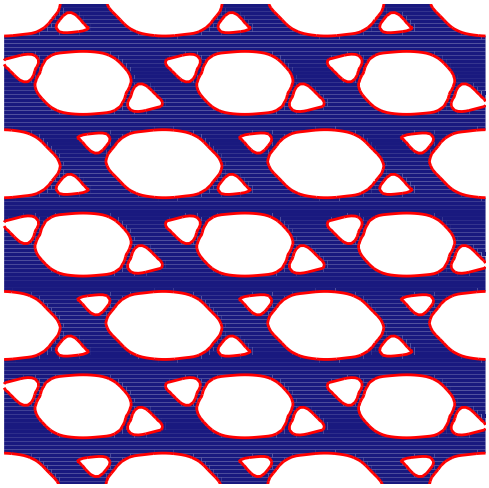

b(5)

Figure 6-15 Optimized results in macro and micro scales for example 1

(left: deterministic design; right: robust design)

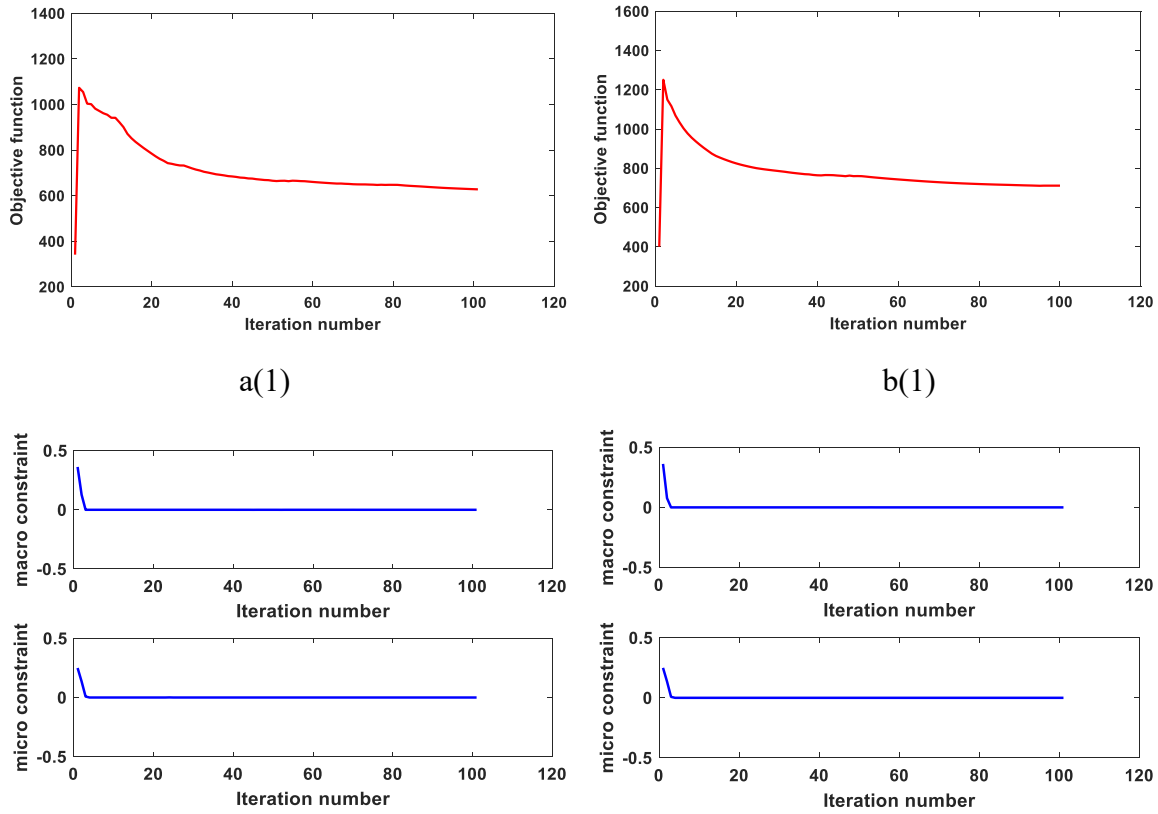

Figure 6-16 Convergent histories for example 1

(left: deterministic design; right: robust design)

The optimal design results are shown in Figure 6-15 and Figure 6-16. Figure 6-15 a(1)~a(5) are results of the deterministic design, and Figure 6-15 b(1)~b(5) are results of the robust design. In Figure 6-15, the first four pictures are results in the macro scale: a(1) and b(1) are the optimal topologies of the macro structures, while a(2) and b(2) give the LSFs for the macro designs. The last six pictures are results in the micro scale: a(3) and b(3) are the optimal microstructures, a(4) and b(4) show the LSFs for the micro designs, while a(5) and b(5) are three by three arrays of the identical microstructures. The robust macro structure design in Figure 6-15 b(1) is different from the deterministic macro design in Figure 6-15 a(1), although

they have similar topologies. The robust microstructure design in b(3) is obviously different from the deterministic micro design in a(3). In Figure 6-16, a(1)~a(2) are convergent histories of the deterministic design, and b(1)~b(2) are iteration histories of the robust design. Figure 6-16 a(1) and b(1) present the iteration histories of the robust objective functions, while Figure 6-16 a(2) and b(2) show convergent histories of the volume constraints in both macro and micro scales. The iteration histories show that the proposed method has good computational stability.

For comparison and verification purpose, the robust objective function values (including the mean and standard variance) and the FEA calls of the deterministic and the robust designs under uncertainties are given in Table 6-4. To evaluate the value of the robust objective function, the proposed method only needs 335 FEA calls. The robust objective function values of the deterministic and the robust designs are 809.81 and 788.59 respectively, which means that the robust topology optimization may provide better results than the deterministic topology optimization. It indicates that the robust topology optimization considering uncertainties can provide a design with better robustness compared with the deterministic one. 10^6 Monte Carlo simulations are used to evaluate the reference values to verify the accuracy. The error of the deterministic result from HDR is 0.28% compared with MCS result, while the error of the robust result from HDR is 0.29% compared with MCS result. It shows that the robust objevtive values obtained by our proposed method are very close to the MCS results, but with only need a small number of FEA calls.

Table 6-4 Robust objective function of optimized designs for example 1

Situations	Method	Mean	Standard variance	Robust objective function value	FEA calls
Deterministic design under uncertainties	HDR	686.81	123.00	809.81	335
	MCS	688.00	124.11	812.11	1×10^6
Robust design under uncertainties	HDR	668.05	120.54	788.59	335
	MCS	669.24	121.65	790.89	1×10^6

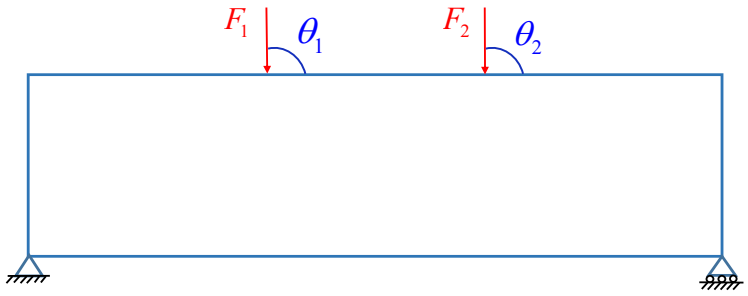

Figure 6-17 Design domain and boundary condition for example 2

Consider a 4:1 (length=1.2m and width=0.3m) MBB beam, the boundary conditions and loads are given in Figure 6-17. Two vertical loads F_1 and F_2 are applied on the upper bound of the beam. The load magnitudes and the load directions are considered as normal random variables, while the Young's modulus and the Poisson's ratio are assumed to be interval variables. The mean values of the loads are set to be $3\times10^5 N$, the standard variance values of the loads are given as $3\times10^4 N$. The directions are with mean values $\frac{\pi}{2}$ and standard variances $\frac{\pi}{18}$. The

interval variables are set to be $E=\left[6.3\times10^{10}\,\text{Pa},7.7\times10^{10}\,\text{Pa}\right]$ and $\upsilon=\left[0.27,0.33\right]$. The macro structure is discretized by 120×30 Q4 elements, while the micro structures are discretized by 40×40 Q4 elements. The volume fractions for both scales are given as 0.5.

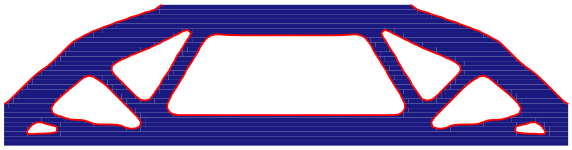

a(1)

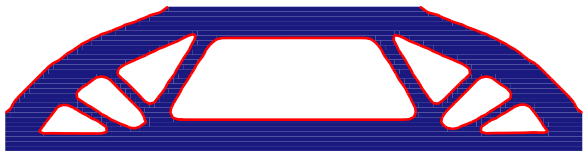

b(1)

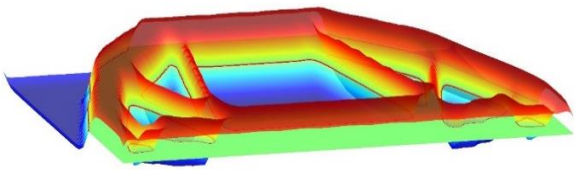

a(2)

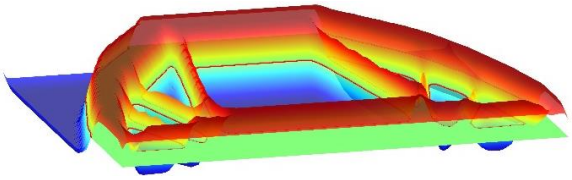

b(2)

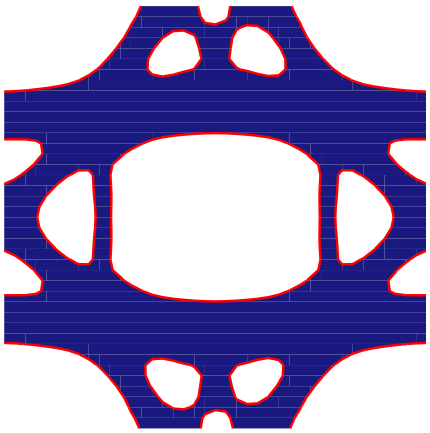

a(3)

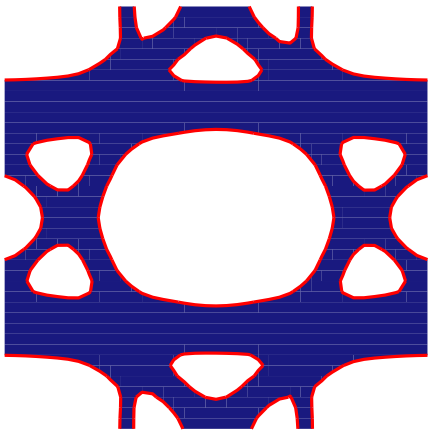

b(3)

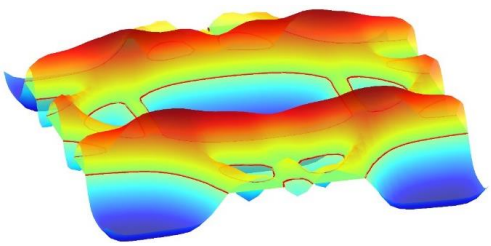

a(4)

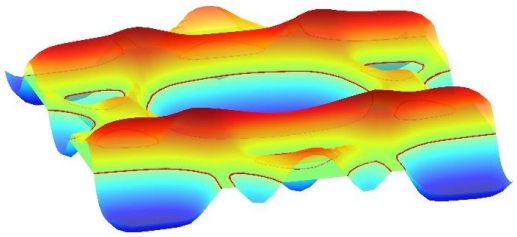

b(4)

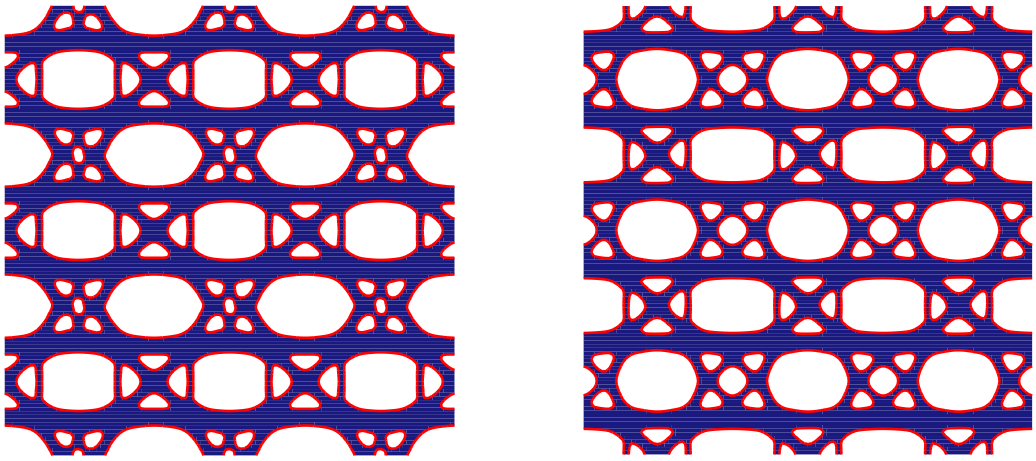

a(5) b(5)

Figure 6-18 Optimized results in macro and micro scales for example 2

(left: deterministic design; right: robust design)

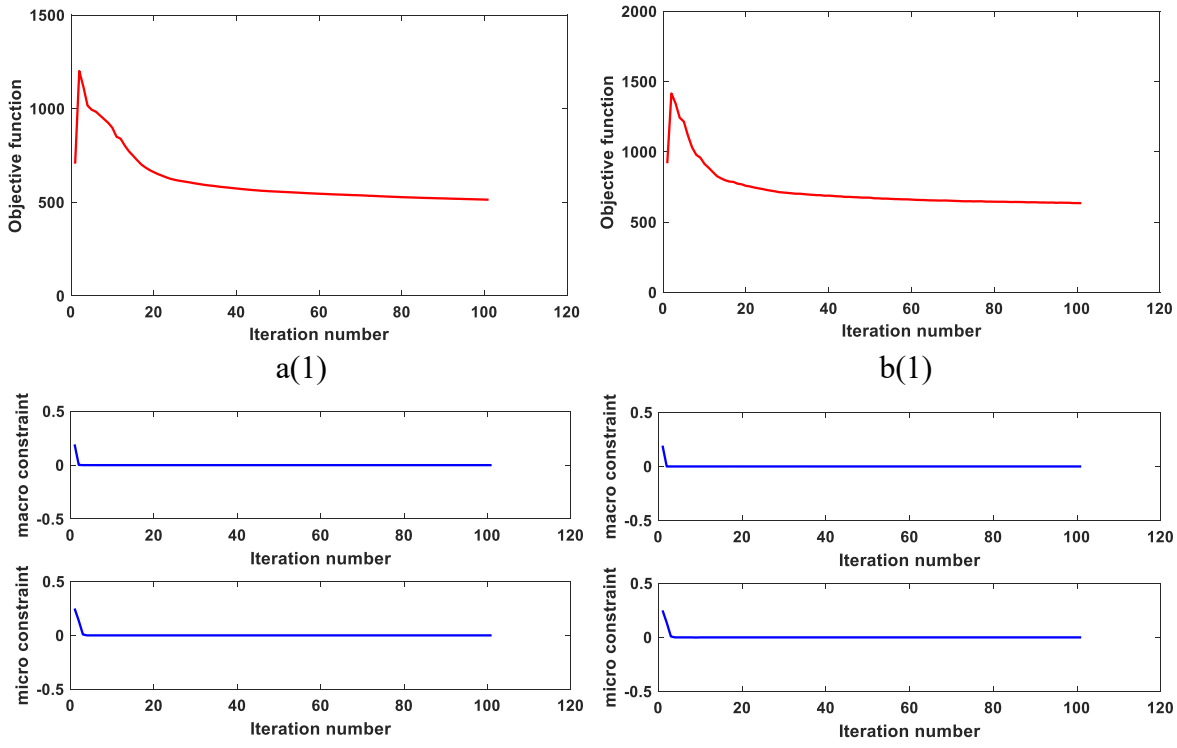

a(1) b(1)

a(2) b(2)

Figure 6-19 Convergent histories for example 2

(left: deterministic design; right: robust design)

Figure 6-18 and Figure 6-19 present the optimized results and the convergent histories for the deterministic and robust optimizations at both the macro and micro scales of the beam. It can be seen that uncertainties may have an obvious influence on the concurrent topology optimization at both scales, so it is essential to consider the uncertainties during the topological design process. Table 6-5 gives the detailed results of the optimization designs. The robust objective function value for the deterministic design is 663.83, and the robust objective function value for the robust design is 635.13. Based on the above, we can conclude that robust design has a more robust performance under uncertainties, when compared with the deterministic design. As a reference, the robust objective function values are also provided by 10^6 MCS. The mean and standard variance values from the HDR are very close to those from the MCS, so the proposed method is proved to have very good accuacy while only need a small number of FEA calls.

Table 6-5 Robust objective function of optimized designs for example 2

Situations	Method	Mean	Standard variance	Robust objective function value	FEA calls
Deterministic design under uncertainties	HDR	568.99	94.84	663.83	335
	MCS	568.92	95.76	664.68	1×10^6
Robust design under uncertainties	HDR	544.37	90.76	635.13	335
	MCS	544.87	91.94	636.81	1×10^6

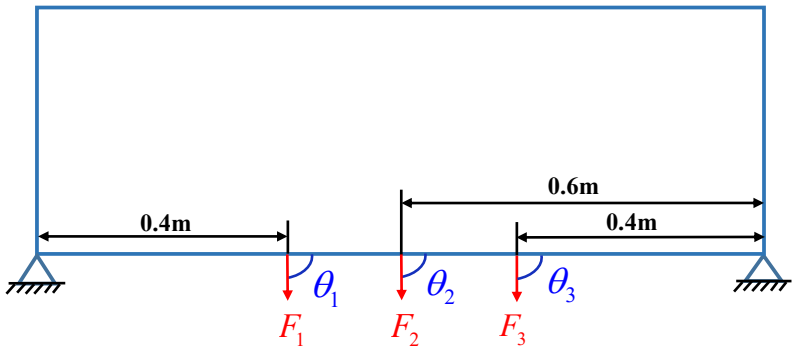

Figure 6-20 Design domain and boundary condition for example 3

A 1:3 beam is considered in this example. The length of the structure is $1.2m$ and the width is $0.4m$. The lower left and right corners of the beam are clamped. As shown in Figure 6-20 , three dynamic loads F_1, F_2 and F_3 with frequency $w = 100Hz$ are applied on the lower side of the structure. The three load magnitudes F_1, F_2 and F_3 and the load directions θ_1, θ_2, and θ_3 are considered as normal random variables, while the Young's modulus and the Poisson's ratio are assumed to be interval variables. The mean values of the three loads are $3\times10^5 N, 6\times10^5 N$ and $3\times10^5 N$, the standard variance values of the three loads are $3\times10^4 N, 6\times10^4 N$ and $3\times10^4 N$. The loads directions are with mean values $\pi/2$ and standard variances $\pi/9$. The interval variables are given as $E = \left[6.3\times10^{10}\ \text{Pa}, 7.7\times10^{10}\ \text{Pa}\right]$ and $\upsilon = [0.27, 0.33]$. The mesh size for the macro structure is 120 by 40, and the mesh size for the micro structure is 40 by 40. The volume fractions for both scales are 0.5.

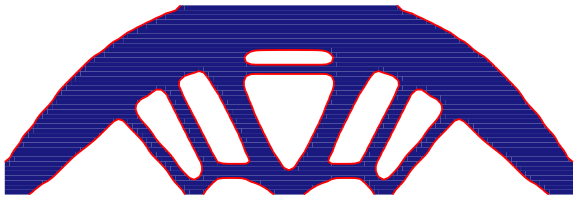

a(1)

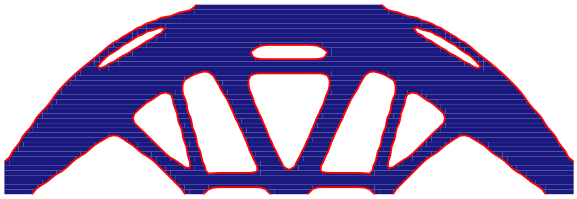

b(1)

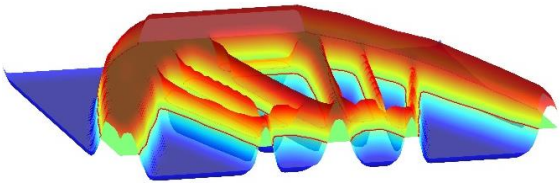

a(2)

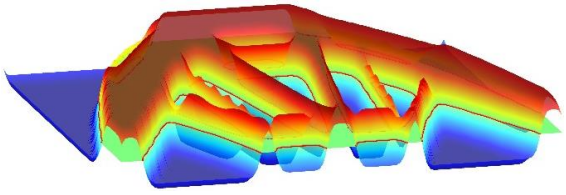

b(2)

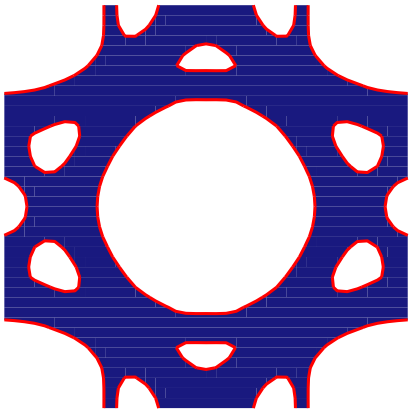

a(3)

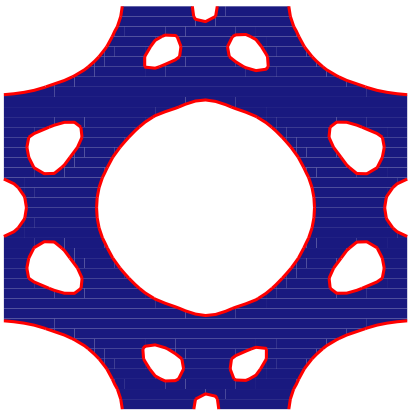

b(3)

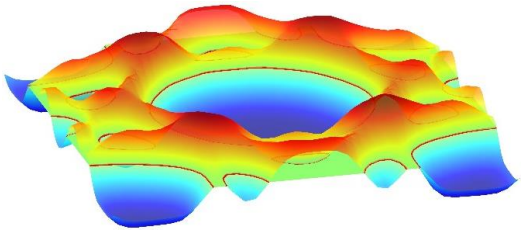

a(4)

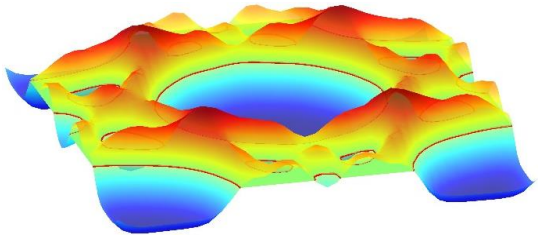

b(4)

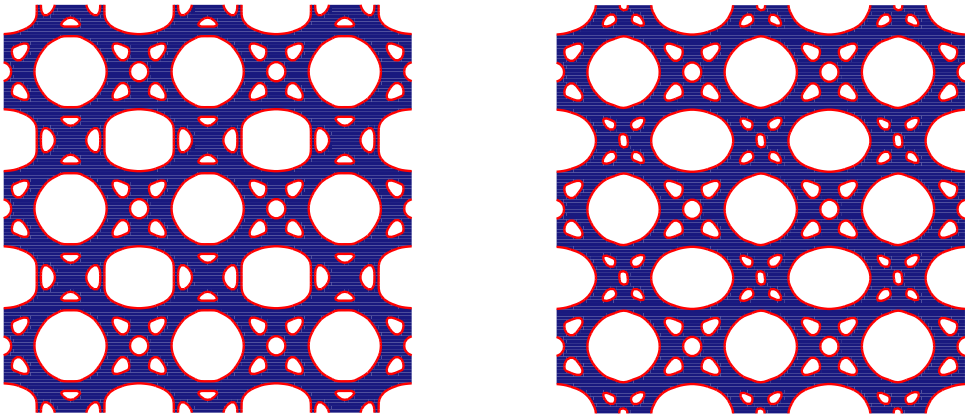

a(5) b(5)

Figure 6-21 Optimized results in macro and micro scales for example 3

(left: deterministic design; right: robust design)

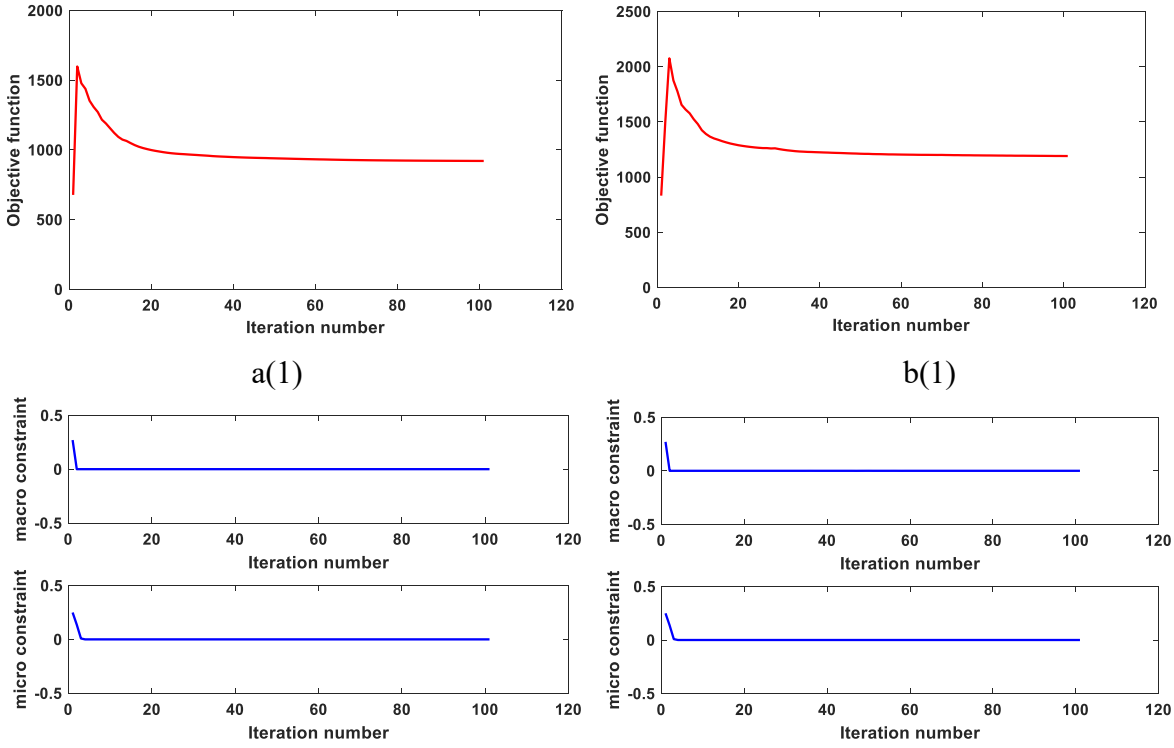

a(1) b(1)

a(2) b(2)

Figure 6-22 Convergent histories for example 3

(left: deterministic design; right: robust design)

Figure 6-21 and Figure 6-22 give the design results and the convergent histories for both deterministic and uncertain situations. The robust optimization will result in quite different optimal results in both macro and micro scales compared with the deterministic optimization for the dynamic structure. Table 6-6 presents the objective function values for deterministic and robust designs under the uncertainties. With the uncertain boundary conditions, the robust objective function value for the deterministic design is 1385.60, which is 13.39% larger than the robust objective function value for the robust design. That is to say, the topology optimization considering uncertainties can provide more robust results than the deterministic topology optimization. As a reference, the results by 10^6 MCS are also provided to verify the accuracy of the proposed method. The numerical error of the deterministic result from HDR is 0.17% compared with MCS result, and the numerical error of the robust result from HDR is 0.19% compared with MCS result. In conclusion, uncertainties play an important role in topology optimizations. The proposed method has good accuracy and efficiency to deal with robust topology optimization problems.

Table 6-6 Robust objective function of optimized designs for example 3

Situations	Method	Mean	Standard variance	Robust objective function value	FEA calls
Deterministic design under uncertainties	HDR	1128.87	256.73	1385.60	770
	MCS	1132.90	255.01	1387.91	1×10^6
Robust design under uncertainties	HDR	1051.81	170.13	1221.94	770
	MCS	1053.50	170.80	1224.30	1×10^6

6.5 Summary

In this Chapter, new RTO methods are developed for the integrated designs for static and dynamic structures subject to random-interval uncertainties, in which the dimensional reduction based uncertainties analysis methods are applied to estimate the interval means and interval variances of the objective functions. The uncertainties are proved to have influences on the optimized designs both at macro and micro scales in the numerical examples, and the robust designs obtained by using the proposed methods are more robust than the deterministic designs. The numerical results have also shown that the proposed methods have good computational efficiency and accuracy.

Chapter 7 Summary and prospect

7.1 Summary

This work is mainly focused on the hybrid uncertainties and relevant topology optimization for structures using a level set method. Four typical topology optimization problems including the static and dynamic topology optimization of continuum structures, as well as the static and dynamic topology optimization for cellular composites are discussed. Several efficient hybrid uncertainty analysis methods have been developed and the corresponding robust topology optimization methods are proposed.

Chapter 2 provides a comprehensive review of uncertainty analysis, including the probabilistic analysis, interval analysis, hybrid analysis, as well as the deterministic topology optimization and the topology optimization under uncertainty. The review shows that there are some important problems not well solved. For example, (1) the hybrid uncertainty analysis is generally focused on discrete parameters, the hybrid uncertainties with random fields have been seldom studied; (2) the efficiency and accuracy of the hybrid uncertainty analysis need to be improved; (3) the hybrid uncertainties are seldom studied in the topology optimization for cellular composites. Chapter 3 gives an introduction of the CSRBF-based PLSM which can avoid many numerical issues in traditional LSMs. In this thesis, the robust topology optimizations are all built and solved by this PLSM.

In Chapter 4, several hybrid uncertainty analysis methods have been developed. They can be divided into two types. The first type is based on the orthogonal polynomials. The traditional

PCCI method is efficient for hybrid uncertainty analysis, but the computational cost will increase exponentially as the increasing of the uncertain variables. In this case, this work has tried to improve the PCCI method from the polynomial terms and the samples to improve the efficiency. The second type is based on dimension reduction schemes. The dimensional reduction methods have been proved to be efficient in traditional random uncertainty analysis and they have not been employed for the hybrid uncertainty analysis. By combining the dimensional reduction methods with the hybrid uncertain model, we proposed the HUDR and HDR methods for efficient hybrid uncertainty analysis.

In Chapter 5, based on the polynomial-based uncertainty analysis methods, new RTO methods have been proposed for static and dynamic structures with random and interval hybrid uncertainties. In Chapter 6, concurrent topology optimizations based on PLSM in both scales have been presented for static and dynamic structures. Robust topology optimization methods are then developed for integrated material-structural designs subject to hybrid uncertainties, in which the HUDR and HDR methods are used to estimate the interval means and interval variances of the objective functions.

7.2 Perspective for future work

The future works need to be studied are outlined as follows:

Currently, the majority of hybrid uncertain analysis methods consider the discrete parameters. However, under some circumstances, it is more realistic to model both types of uncertainties as random fields, e.g. material properties and loading distribution. Although in this thesis the random field has been considered in the design, it is more reasonable to model both

uncertainties including the interval uncertainties as fields when only limited samples are available. How to develop efficient uncertain analysis methods for random-interval hybrid fields is an important problem and open topic to be resolved.

The main focus of this thesis is on material and loading uncertainties in topology optimization problems. However, geometric or boundary uncertainty is also an important kind of uncertainties. Geometric uncertainty is often involved in the structural boundary that may vary during the optimization process, so it will have influence on the performance of a final design. Hence, it is essential to incorporate geometric uncertainties into topology optimization designs.

Most of existing topology optimizations focus on single-material problems, but sometimes the single-material designs cannot meet the requirements in practice. It is of high interest to develop topology optimization methods for the multi-material designs. Multi-material topology optimization faces more challenges than single-material optimizations, and have wide applications in multiphysics designs with piezoelectric materials, electrothermoelastic materials, etc. How to incorporate uncertainties into multi-material design problems will be an important issue of the future works.

The topology optimization for concurrent design often involve a typical assumption that the microstructures are identical throughout the macrostructure since the periodic assumption can save computational calculations and meet manufacturing requirements. However, multiple kinds of microstructures may provide more flexibility in the integrated designs and result in

better structure performances. Considering uncertainties in the concurrent design with multiple kinds of microstructures may be another important research direction.

The proposed methods in this thesis are general approaches so that they can be applied to any topology optimization applications involving hybrid uncertainties. In the future, the proposed methods can also be extended to other advanced topology optimization problems, including the problems mentioned above like multi-material, piezoelectric, electrothermoelastic problems, as well as other material-structural designs such as mechanical metamaterials, phononic metamaterials, photonic metamaterials and so on.

References

[1 Miche UAM. The limits of economy of material in frame-structures. The London, Edinburgh, and Dublin Philosophical Magazine and Journal of Science, 1904, 8(47): 589-597.
[2 Bendsøe MP, Kikuchi N. Generating optimal topologies in structural design using a homogenization method. Comput Methods Appl Mech Eng 1998, 71(2): 197-224.
[3 Sigmund O, Maute K. Topology optimization approaches. Struct Multidiscip Optim 2013, 48(6), 1031-1055.
[4 Deaton JD, Grandhi RV. A survey of structural and multidisciplinary continuum topology optimization: post 2000. Struct Multidiscip Optim 2014, 49(1): 1-38.
[5 Eschenauer H A, Olhoff N. Topology optimization of continuum structures: a review. Appl Mech Rev 2001, 54(4): 331-390.
[6 Bendsøe MP, Sigmund O. Material interpolation schemes in topology optimization. Arch Appl Mech 1999, 69(9-10): 635-654.
[7 Sigmund O. A 99 line topology optimization code written in Matlab. Struct Multidiscip Optim 2001, 21(2): 120-127.
[8 Xie YM, Steven GP. A simple evolutionary procedure for structural optimization. Comput Struct 1993, 49(5): 885-896.
[9 Huang X, Xie YM. Bi-directional evolutionary topology optimization of continuum structures with one or multiple materials. Comput Mech, 2009, 43(3): 393-401.
[10 Sethian JA, Wiegmann A. Structural boundary design via level set and immersed interface methods. J comput phys 2000, 163(2): 489-528.
[11 Wang MY, Wang X, Guo D. A level set method for structural topology optimization. Comput Methods Appl Mech Eng 2003, 192(1): 227-246.
[12 Allaire G, Jouve F, Toader AM. Structural optimization using sensitivity analysis and a level-set method. J comput phys 2004, 194(1): 363-393.
[13 Cheng GD, Olhoff N. An investigation concerning optimal design of solid elastic plates. Int J Solids Struct 1981, 17: 305-323.
[14 Díaz AR, Kikuchi N. Solutions to shape and topology eigenvalue optimization problem using a homogenization method. Int J Numer Meth Eng 1992, 35(7): 1487-1502.
[15 Nishiwaki S, Frecker MI, Min S, et al. Topology optimization of compliant mechanisms using the homogenization method. Int J Numer Meth Eng 1998, 42: 535-559.
[16 Sigmund O. Materials with prescribed constitutive parameters: an inverse homogenization problem. Int J Solids Struct 1994, 31(17): 2313-2329.
[17 Sigmund O. Tailoring materials with prescribed elastic properties. Mech Mater 1995, 20: 351-368.
[18 Díaz AR, Sigmund O. A topology optimization method for design of negative permeability metamaterials. Struct Multidiscip Optim 2009, 41(2): 163-177.
[19 Sigmund O. A new class of extremal composites. J Mech Phys Solids 2000, 48(2): 397-428.
[20 Hassani B, Hinton E. A review of homogenization and topology optimization I - homogenization theory for media with periodic structure. Comput Struct 1998, 69(6): 707-717.
[21 Hassani B, Hinton E. A review of homogenization and topology opimization II-analytical and numerical solution of homogenization equations. Comput Struct 1998, 69(6): 719-738.
[22 Allaire G. Shape optimization by the homogenization method. New York: Springer Verlag. 2001.
[23 Sigmund O, Petersson J. Numerical instabilities in topology optimization: A survey on procedures

dealing with checkboards, mesh-dependencies and local minima. Struct Optim 1998, 16(1): 68-75.
[24 Guest JK, Prévost JH, Belytschko T. Achieving minimum length scale in topology optimization using nodal design variables and projection functions. Int J Numer Meth Eng 2004, 61(2): 238-254.
[25 Paulino GH, Le CH. A modified Q4/Q4 element for topology optimization. Struct Multidiscip Optim 2009, 37(3): 255-264.
[26 Kang Z, Wang Y. Structural topology optimization based on non-local Shepard interpolation of density field. Comput Methods Appl Mech Eng 2011, 200(49-52): 3515-3525.
[27 Yang DQ, Sui YK, Liu ZX, et al. Topology optimization design of continuum structures under stress and displacement constraints. Appl Math Mech 2000, 21(1): 19-26.
[28 Sui YK, Peng XR. The ICM method with objective function transformed by variable discrete condition for continuum structure. Acta Mech Sinica 2006, 22(1): 68-75.
[29 Osher S, Sethian J A. Front propagating with curvature dependent speed: algorithms based on Hamilton–Jacobi formulations. J Comput Phys 1988, 78:12–49.
[30 Wang MY, Wang X. "Color" level sets: a multi-phase method for structural topology optimization with multiple materials. Comput Methods Appl Mech Eng 2004, 193(6): 469-496.
[31 Allaire G, Jouve F. A level-set method for vibration and multiple loads structural optimization. Comput Methods Appl Mech Eng 2004, 194(30-33): 3269-3290.
[32 Burger M, Hackl B, Ring W. Incorporating topological derivatives into level set methods. J Comput Phys 2004, 194(1): 344-362.
[33 Mei YL, Wang XM. A level set method for structural topology optimization and its applications. Adv Eng Softw 2004, 35(7): 415-441.
[34 Xia Q, Wang MY, Wang SY et al. Semi-Lagrange method for level-set-based structural topology and shape optimization. Struct Multidiscip Optim 2006, 31(6): 419-429.
[35 Chen JQ, Shapiro V, Suresh K, et al. Shape optimization with topological changes and parametric control. Int J Numer Meth Eng 2007, 71(3): 313-346.
[36 Wei P, Wang MY. Piecewise constant level set method for structural topology optimization. Int J Numer Meth Eng 2009, 78(4): 379-402.
[37 Luo Z, Zhang N, Gao W, et al. Structural shape and topology optimization using a meshless Galerkin level set method. Int J Numer Meth Eng 2012, 90(3): 369-389.
[38 Wang SY, Wang MY. Radial basis functions and level set method for structural topology optimization. Int J Numer Meth Eng 2006, 65(12): 2060-2090.
[39 Ho HS, Wang MY, Zhou MD. Parametric structural optimization with dynamic knot RBFs and partition of unity method. Struct Multidiscip Optim 2012, 47(3): 353-365.
[40 Luo Z, Wang MY, Wang SY, et al. A level set-based parameterization method for structural shape and topology optimization. Int J Numer Meth Eng 2008, 76(1): 1-26.
[41 Luo Z, Tong LY, Kang Z. A level set method for structural shape and topology optimization using radial basis functions. Comput Struct 2009, 87(7-8): 425-434.
[42 Díaz AR, Kikuchi N. Solutions to shape and topology eigenvalue optimization problems using a homogenization method. Int J Numer Meth Eng 1992, 35(7): 1487-1502.
[43 Ma ZD, Kikuchi N, Cheng HC, et al. Topological optimization technique for free vibration problems. J Appl Mech 1995, 62(1), 200-207.
[44 Pedersen N. Maximization of eigenvalues using topology optimization. Struct Multidiscip Optim 2000, 20 (1): 2–11.
[45 Du JB, Olhoff N. Topological design of freely vibrating continuum structures for maximum values of simple and multiple eigenfrequencies and frequency gaps. Struct Multidiscip Optim 2007, 34(2): 91-110.
[46 Kim TS, Kim YY. Mac-based mode-tracking in structural topology optimization. Comput Struct

2000, 74(3): 375-383.
[47 Maeda Y, Nishiwaki S, Izui K, et al. Structural topology optimization of vibrating structures with specified eigenfrequencies and eigenmode shapes. Int J Numer Meth Eng 2006, 67(5), 597-628.
[48 Ma ZD, Kikuchi N, Hagiwara I. Structural topology and shape optimization for a frequency response problem. Comput Mech 1993, 13(3): 157-174.
[49 Ma ZD, Kikuchi N, Cheng HC. Topological design for vibrating structures. Comput Methods Appl Mech Eng 1995, 121(1-4): 259-280.
[50 Jog CS. Topology design of structures subjected to periodic loading. J Sound Vib 2002, 253(3): 687-709.
[51 Yoon GH. Structural topology optimization for frequency response problem using model reduction schemes. Comput Methods Appl Mech Eng 2010, 199(25-28): 1744-1763.
[52 Liu B, Huang X, Huang C, et al. Topological design of structures under dynamic periodic loads. Eng Struct 2017, 142: 128-136.
[53 Shu L, Wang MY, Fang Z, et al. Level set based structural topology optimization for minimizing frequency response. J Sound Vib 2011, 330(24), 5820-5834.
[54 Rong JH, Tang ZL, Xie YM, et al. Topological optimization design of structures under random excitations using SQP method. Eng Struct 2013, 56: 2098-2106.
[55 Liu H, Zhang WH, Gao T. A comparative study of dynamic analysis methods for structural topology optimization under harmonic force excitations. Struct Multidisc Optimiz 2015, 51(6): 1321-1333.
[56 Fleck NA, Deshpande VS, Ashby MF. Micro-architectured materials: past, present and future. Proceedings of the royal society of London a: mathematical, physical and engineering sciences. The Royal Society. 2010, 466(2121): 2495-2516.
[57 Gibson LJ, Ashby MF. Cellular solids: structure and properties. Cambridge university press; 1999.
[58 Guedes J, Kikuchi N. Preprocessing and postprocessing for materials based on the homogenization method with adaptive finite element methods. Comput Methods Appl Mech Eng 1990, 83(2):143-198.
[59 Gibiansky LV, Sigmund O. Multiphase composites with extremal bulk modulus. J Mech Phys Solids 2000;48(3):461-498.
[60 Radman A, Huang X, Xie YM. Topological optimization for the design of microstructures of isotropic cellular materials. Eng Optimiz 2013, 45(11):1331-1348.
[61 Guest JK, Prévost JH. Optimizing multifunctional materials: design of microstructures for maximized stiffness and fluid permeability. Int J Solids Struct 2006, 43(22-23):7028-7047.
[62 Challis VJ, Guest JK, Grotowski JF, et al. Computationally generated cross-property bounds for stiffness and fluid permeability using topology optimization. Int J Solids Struct 2012, 49(23): 3397-3408.
[63 Berger JB, Wadley HNG, McMeeking RM. Mechanical metamaterials at the theoretical limit of isotropic elastic stiffness. Nature. 2017, 543(7646): 533.
[64 Wang Y, Gao J, Luo Z, et al. Level-set topology optimization for multimaterial and multifunctional mechanical metamaterials. Eng Optimiz 2017, 49(1):22-42.
[65 Sigmund O, Torquato S. Design of materials with extreme thermal expansion using a three-phase topology optimization method. J Mech Phys Solids 1997, 45(6):1037-1067.
[66 Xia L, Breitkopf P. Design of materials using topology optimization and energy-based homogenization approach in Matlab. Struct Multidiscip Optim 2015, 52(6): 1229-1241.
[67 Wang Y, Luo Z, Zhang N, et al. Topological shape optimization of microstructural metamaterials using a level set method. Comput Mater Sci 2014, 87: 178-186.
[68 Podshivalov L, Fischer A, Bar-Yoseph PZ. On the road to personalized medicine: multiscale computational modeling of bone tissue. Arch Comput Method E 2014, 21(4): 399-479.
[69 Yan J, Yang SX, Duan ZY, et al. Minimum compliance optimization of a thermoelastic lattice

structure with size-coupled effects. J Therm Stress 2015; 38(3): 338-357.
[70 Yan J, Guo X, Cheng GD. Multi-scale concurrent material and structural design under mechanical and thermal loads. Comput Mech 2016; 57(3): 437-446.
[71 Rodrigues H, Guedes JM, Bendsoe MP. Hierarchical optimization of material and structure. Struct Multidiscip Optim 2002, 24(1): 1-10.
[72 Xia L, Breitkopf P. Concurrent topology optimization design of material and structure within FE2 nonlinear multiscale analysis framework. Comput Methods Appl Mech Eng 2014, 278: 524-542.
[73 Zhang WH, Sun SP. Scale-related topology optimization of cellular materials and structures. Int J Numer Meth Eng 2006, 68(9): 993-1011.
[74 Coelho PG, Rodrigues HC. Hierarchical topology optimization addressing material design constraints and application to sandwich-type structures. Struct Multidiscip Optim 2015, 52(1): 91-104.
[75 Li H, Luo Z, Zhang N, et al. Integrated design of cellular composites using a level-set topology optimization method. Comput Methods Appl Mech Eng 2016; 309: 453–475.
[76 Li H, Luo Z, Gao L, et al. Topology optimization for concurrent design of structures with multi-patch microstructures by level sets. Comput Methods Appl Mech Eng 2018; 331: 536-561.
[77 Liu L, Yan, J, Cheng GD. Optimum structure with homogeneous optimum truss-like material. Comput Struct 2008; 86(13): 1417-1425.
[78 Fujii D, Chen BC, Kikuchi N. Composite material design of two-dimensional structures using the homogenization design method. Int J Numer Meth Eng 2001, 50(9): 2031-2051.
[79 Niu B, Yan J, Cheng GD. Optimum structure with homogeneous optimum cellular material for maximum fundamental frequency. Struct Multidisc Optimiz 2009, 39(2): 115-132.
[80 Liu Q, Chan R, Huang X. Concurrent topology optimization of macrostructures and material microstructures for natural frequency. Mater Design 2016, 106: 380-390.
[81 Zuo ZH, Huang XD, Rong JH, et al. Multi-scale design of composite materials and structures for maximum natural frequencies. Mater Design 2013, 51: 1023-1034.
[82 Vicente WM, Zuo ZH, Pavanello R, et al. Concurrent topology optimization for minimizing frequency responses of two-level hierarchical structures. Comput Methods Appl Mech Eng 2016, 301: 116-136.
[83 Xu B, Jiang JS, Xie YM. Concurrent design of composite macrostructure and multi-phase material microstructure for minimum dynamic compliance. Compos Struct 2015,128: 221-233.
[84 Wiener N. The homogeneous chaos. Am J Math 1938, 60(4): 897-936.
[85 Xiu D, Karniadakis GE. The Wiener-Askey polynomial chaos for stochastic differential equations. SIAM J Sci Comput 2002, 24(2): 619-644.
[86 Rahman S, Xu H. A univariate dimension-reduction method for multi-dimensional integration in stochastic mechanics. Probab Eng Mech 2004, 19(4): 393-408.
[87 Xu H, Rahman S. A generalized dimension-reduction method for multidimensional integration in stochastic mechanics. Int J Numer Meth Eng 2004, 61(12): 1992-2019.
[88 Xiu D. Fast numerical methods for stochastic computations: a review. Commun comput phys 2009, 5(2-4): 242-272.
[89 Ghanem R, Spanos P. Stochastic Finite Elements: A Spectral Approach. Courier Dover Publications, 2003.
[90 Hadigol M, Doostan A. Least squares polynomial chaos expansion: A review of sampling strategies. Comput Methods Appl Mech Eng 2018, 332: 382-407.
[91 Sudret B, Der Kiureghian A. Stochastic finite element methods and reliability: a state-of-the-art report. Berkeley: Department of Civil and Environmental Engineering, University of California, 2000.
[92 Blatman G, Sudret B. Adaptive sparse polynomial chaos expansion based on least angle regression. J Comput Phys 2011, 230(6): 2345-2367.

[93 Ghiocel DM, Ghanem RG. Stochastic finite element analysis of seismic soil-structure interaction. J Eng Mech 2002, 128: 66-77.
[94 Le Maître OP, Reagan M, Najm HN, et al. A stochastic projection method for fluid flow – II. Random process. J Comput Phys 2002, 181: 9-44.
[95 Choi SK, Grandhi RV, Canfield RA, et al. Polynomial chaos expansion with Latin Hypercube sampling for estimating response variability. AIAA J. 2004, 45: 1191–1198.
[96 Berveiller M, Sudret B, Lemaire M. Stochastic finite elements: a non intrusive approach by regression. Eur J Comput Mech 2006, 15 (1-3): 81-92.
[97 Sudret B. Global sensitivity analysis using polynomial chaos expansions. Reliab Eng Syst Safe 2008, 93: 964-979.
[98 Hampton J, Doostan A. Coherence motivated sampling and convergence analysis of least squares polynomial chaos regression. Comput Methods Appl Mech Eng 2015, 290: 73-97.
[99 Xu H, Rahman S. Decomposition methods for structural reliability analysis. Probab Eng Mech 2005, 20(3): 239-250.
[100 Huang B, Du XP. Uncertainty analysis by dimension reduction integration and saddlepoint approximations. J Mech Des 2006, 128(1): 26-33.
[101 Lee I, Choi KK, Du L, et al. Dimension reduction method for reliability-based robust design optimization. Comput Struct 2008, 86(13-14):1550-1562.
[102 Lee SH, Chen W. A comparative study of uncertainty propagation methods for black-box-type problems. Struct Multidiscip Optim 2009, 37(3):239-253.
[103 Chen SK, Chen W, Lee S. Level set based robust shape and topology optimization under random field uncertainties. Struct Multidiscip Optim 2010, 41(4): 507-524.
[104 Hasofer AM, Lind NC. Exact and invariant second-moment code format. J Eng Mech Div 1974, 100(1): 111-121.
[105 Rackwitz R, Flessler B. Structural reliability under combined random load sequences. Comput Struct, 1978, 9(5): 489-494.
[106 Rosenblatt M. Remarks on a multivariate transformation. The annals of mathematical statistics, 1952, 23(3): 470-472.
[107 Nataf A. Statistique mathematique-determination des distributions de probabilities dont les marges sont donnees. Comptes Rendus Hebdomadaires des Seances de l Academie des Sciences, 1962, 255(1): 42-43.
[108 Schuëller GI, Jensen HA. Computational methods in optimization considering uncertainties–an overview. Comput Methods Appl Mech Eng 2008, 198(1): 2-13
[109 Valdebenito MA, Schuëller GI. A survey on approaches for reliability-based optimization. Struct Multidiscip Optim 2010, 42(5), 645-663.
[110 Kuschel N, Rackwitz R. Two basic problems in reliability-based structural optimization. Math Method Oper Res 1997, 46(3), 309-333.
[111 Aoues Y, Chateauneuf A. Benchmark study of numerical methods for reliability-based design optimization. Struct Multidiscip Optim 2010, 41(2), 277-294.
[112 Lopez R H, Beck A T. Reliability-based design optimization strategies based on FORM: a review. J Braz Soc Mech Sci, 2012, 34(4), 506-514.
[113 Chen X, Hasselman T, Neill D, et al. Reliability based structural design optimization for practical applications. In 38th Structures, structural dynamics, and materials conference. 1997: 1403.
[114 Phoon KK. (Ed.) Reliability-based design in geotechnical engineering: computations and applications. CRC Press, 2008.
[115 Gu L, Yang RJ. Recent applications on reliability-based optimization of automotive structures. (No. 2003-01-0152). SAE Technical Paper, 2003.
[116 Qu X, Haftka RT. Reliability-based design optimization using probabilistic sufficiency factor.

Struct Multidiscip Optim 2004, 27(5), 314-325.
[117 Youn BD, Choi KK. A new response surface methodology for reliability-based design optimization. Comput Struct 2004, 82(2), 241-256.
[118 Zhuang XT, Pan RP. A sequential sampling strategy to improve reliability-based design optimization with implicit constraint functions. J Mech Des 2012, 134(2), 021002.
[119 Du XP, Chen W. Sequential optimization and reliability assessment method for efficient probabilistic design. J Mech Des 2004, 126(2), 225-233.
[120 Liang J, Mourelatos ZP, Tu J. A single-loop method for reliability-based design optimization. ASME 2004 International Design Engineering Technical Conferences and Computers and Information in Engineering Conference. American Society of Mechanical Engineers, 2004: 419-430.
[121 Huang ZL, Jiang C, Zhou YS, et al. An incremental shifting vector approach for reliability-based design optimization. Struct Multidiscip Optim 2016, 53(3): 523-543.
[122 Marler RT, Arora JS. Survey of multi-objective optimization methods for engineering. Struct Multidiscip Optim 2004, 26(6), 369-395.
[123 Alexandrov NM, Hussaini MY (Eds.) Multidisciplinary design optimization: State of the art (Vol. 80). SIAM, 1997.
[124 Rackwitz R. Computational techniques in stationary and non-stationary load combination—a review and some extensions. J struct Eng, 1998, 25(1), 1-20.
[125 Ben-Haim Y, Elishakoff I. Convex models of uncertainty in applied mechanics. Amsterdam: Elsevier, 2013.
[126 Jiang C, Han X, Liu GR, et al. The optimization of the variable binder force in U-shaped forming with uncertain friction coefficient. J Mater Process Tech 2007, 182: 262-267.
[127 Moore RE. Methods and applications of interval analysis. Philadelphia: Siam, 1979.
[128 Ben-Haim Y. Convex models of uncertainty in radial pulse buckling of shells. J Appl Mech 1993, 60(3): 683-688.
[129 Elishakoff I, Elisseeff P, Glegg SA. Nonprobabilistic, convex-theoretic modeling of scatter in material properties. AIAA J 1994, 32(4): 843-849.
[130 Qiu ZP. Interval analysis for static response and eigenvalue problem of structures with uncertain parameters. Dissertation of Doctoral Degree. Jilin: Jilin University, 1994.
[131 Qiu ZP, Wang XJ. Comparison of dynamic response of structures with uncertain-but-bounded parameters using non-probabilistic interval analysis method and probabilistic approach. Int J Solid Struct 2003, 40(20): 5423-5439.
[132 Qiu ZP, Wang XJ. Parameter perturbation method for dynamic responses of structures with uncertain-but-bounded parameters based on interval analysis. Int J Solid Struct 2005, 42(18): 4958-4970.
[133 Wu J, Zhao YQ, Chen SH. An improved interval analysis method for uncertain structures. Struct Eng Mech 2005, 20(6): 713-726.
[134 Zhang XM, Ding H, Chen SH. Interval finite element method for dynamic response of closed-loop system with uncertain parameters. Int J Numer Meth Eng 2007, 70(5): 543-562.
[135 Jiang C, Han X, Liu GP. A sequential nonlinear interval number programming method for uncertain structures. Comput Methods Appl Mech Eng 2008, 197(49): 4250-4265.
[136 Wu JL, Zhang YQ, Chen LP, et al. A Chebyshev interval method for nonlinear dynamic systems under uncertainty. Appl Math Model 2013, 37(6): 4578-4591.
[137 Wu JL, Luo Z, Zhang N, et al. Interval uncertain method for multibody mechanical systems using Chebyshev inclusion functions. Int J Numer Meth Eng 2013, 95(7): 608-630.
[138 Lindberg HE. Convex models for uncertain imperfection control in multimode dynamic buckling. J Appl Mech 1992, 59(4): 937-945.
[139 Elishakoff I, Bekel Y. Application of Lamé's Super Ellipsoids to Model Initial Imperfections. J

Appl Mech 2013, 80(6):061006.
[140 Luo YJ, Kang Z, Li A. Structural reliability assessment based on probability and convex set mixed model. Comput Struct 2009, 87(21):1408-1415.
[141 Kang Z, Luo YJ. Reliability-based structural optimization with probability and convex set hybrid models. Struct Multidiscip Optim 2010, 42(1):89-102.
[142 Jiang C, Zhang QF, Han X, et al. Multidimensional parallelepiped model—a new type of non-probabilistic convex model for structural uncertainty analysis. Int J Num Meth Eng 2015, 103(1): 31-59.
[143 Ni BY, Jiang C, Han X. An improved multidimensional parallelepiped non-probabilistic model for structural uncertainty analysis. Appl Math Model 2016, 40(7): 4727-4745.
[144 Penmetsa RC, Grandhi RV. Efficient estimation of structural reliability for problems with uncertain intervals. Comput struct 2002, 80(12):1103-1112.
[145 Oberkampf WL, Helton JC, Joslyn CA, et al. Challenge problems: uncertainty in system response given uncertain parameters. Reliab Eng Syst Safe 2004, 85(1):11-19.
[146 Berleant DJ, Ferson S, Kreinovich V, et al. Combining interval and probabilistic uncertainty: foundations, algorithms, challenges-an overview. In 4th International Symposium on Imprecise Probabilities and Their Applications. 2005.
[147 Jiang C, Zheng J, Han X. Probability-interval hybrid uncertainty analysis for structures with both aleatory and epistemic uncertainties: a review. Struct Multidiscip Optim 2018, 57(6), 2485–2502.
[148 Elishakoff I, Colombi P. Combination of probabilistic and convex models of uncertainty when scarce knowledge is present on acoustic excitation parameters. Comput Methods Appl Mech Eng 1993, 104(2):187-209.
[149 Zhu LP, Elishakoff I. Hybrid probabilistic and convex modeling of excitation and response of periodic structures. Math Probl Eng 1996, 2(2):143-163.
[150 Xia BZ, Yu DJ, Liu J. Hybrid uncertain analysis of acoustic field with interval random parameters. Comput Methods Appl Mech Eng 2013, 256: 56-69.
[151 Gao W, Song CM, Tin-Loi F. Probabilistic interval analysis for structures with uncertainty. Struct Saf 2010, 32(3):191-199.
[152 Li LY, Lu ZZ. Importance analysis for model with mixed uncertainties. Fuzzy Set Syst 2017, 310:90-107
[153 Du XP, Venigella PK, Liu D. Robust mechanism synthesis with random and interval variables. Mech Mach Theory 2009, 44(7):1321-1337.
[154 Gao W, Wu D, Song CM, et al. Hybrid probabilistic interval analysis of bar structures with uncertainty using a mixed perturbation Monte-Carlo method. Finite Elem Anal Des 2011, 47(7):643-652.
[155 Xia BZ, Yu DJ, Liu J. Probabilistic Interval Perturbation Methods for Hybrid Uncertain Acoustic Field Prediction. J Vib Acoust 2013, 135(2):021009.
[156 Xia BZ, Yu DJ. Change-of-variable interval stochastic perturbation method for hybrid uncertain structural-acoustic systems with random and interval variables. J Fluid Struct 2014, 50: 461-478.
[157 Wu JL, Luo Z, Zhang N, et al. A new uncertain analysis method and its application in vehicle dynamics. Mech Syst Signal Pr 2015, 50: 659-675.
[158 Zi B, Zhou B. A modified hybrid uncertain analysis method for dynamic response field of the LSOAAC with random and interval parameters. J Sound Vib 2016, 374:111-137.
[159 Yin SW, Yu DJ, Yin H, et al. Interval and random analysis for structure–acoustic systems with large uncertain-but-bounded parameters. Comput Methods Appl Mech Eng, 2016, 305:910-935.
[160 Feng J, Wu D, Gao W, et al. Hybrid uncertain natural frequency analysis for structures with random and interval fields. Comput Methods Appl Mech Eng 2018, 328: 365-389.
[161 Wu D, Gao W. Hybrid uncertain static analysis with random and interval fields. Comput

Methods Appl Mech Eng 2017, 315: 222-246.
[162 Gao W, Wu D, Gao K, et al. Structural reliability analysis with imprecise random and interval fields. Appl Math Model 2018, 55: 49-67.
[163 Qiu ZP, Yang D, Elishakoff I. Combination of structural reliability and interval analysis. Acta Mech Sinica 2008, 24(1): 61-67.
[164 Qiu ZP, Yang D, Elishakoff I. Probabilistic interval reliability of structural systems. Int J Solids Struct 2008, 45(10):2850-2860.
[165 Jiang C, Han X, Li WX, et al. A hybrid reliability approach based on probability and interval for uncertain structures. J Mech Des 2012, 134(3): 031001.
[166 Jiang C, Li WX, Han X, et al. Structural reliability analysis based on random distributions with interval parameters. Comput Struct 2011, 89(23):2292-2302.
[167 Xiao NC, Huang HZ, Wang ZL, et al. Reliability sensitivity analysis for structural systems in interval probability form. Struct Multidisc Optim 2011, 44(5): 691-705.
[168 Zhang DQ, Han X, Jiang C, et al. The interval PHI2 analysis method for time-dependent reliability. Sci Sin-Phys Mech Astron 2015, 45(5): 54601.
[169 Du XP. Interval reliability analysis. ASME 2007 international design engineering technical conferences and computers and information in engineering conference. American Society of Mechanical Engineers, 2007: 1103-1109.
[170 Jiang C, Long XY, Han X, et al. Probability-interval hybrid reliability analysis for cracked structures existing epistemic uncertainty. Eng Frac Mech 2013, 112:148-164.
[171 Yang XF, Liu YS, Gao Y, et al. An active learning kriging model for hybrid reliability analysis with both random and interval variables. Struct Multidisc Optim 2015, 51(5):1003-1016.
[172 Yang XF, Liu YS, Zhang YS, et al. Probability and convex set hybrid reliability analysis based on active learning kriging model. Appl Math Model 2015, 39(14):3954-3971.
[173 Jiang C, Lu GY, Han X, et al. A new reliability analysis method for uncertain structures with random and interval variables. Int J Mech Mater Des 2012, 8(2):169-182.
[174 Liu X, Zhang ZY. A Hybrid Reliability Approach for Structure Optimization Based on Probability and Ellipsoidal Convex Models. J Eng Des 2014, 25(4-6):238-258.
[175 Hu Z. Probabilistic engineering analysis and design under time-dependent uncertainty. Ph. D. dissertation, Missouri University of Science and Technology, 2014.
[176 Wang L, Wang XJ, Xia Y. Hybrid reliability analysis of structures with multi-source uncertainties. Acta Mech 2014, 225(2): 413-430.
[177 Jiang C, Zheng J, Ni BY, et al. A Probabilistic and Interval Hybrid Reliability Analysis Method for Structures with Correlated Uncertain Parameters. Int J Comput Methods 2015, 12(4):1540006
[178 Du XP, Sudjianto A, Huang BQ. Reliability-based design with the mixture of random and interval variables. J Mech Des 2005, 127(6):1068-1076.
[179 Du XP. Reliability-based design optimization with dependent interval variables. Int J Numer Methods Eng 2012, 91(2): 218-228.
[180 Luo YJ, Li A, Kang Z. Reliability-based design optimization of adhesive bonded steel–concrete composite beams with probabilistic and non-probabilistic uncertainties. Eng Struct 2011, 33(7): 2110-2119.
[181 Xia BZ, Lu H, Yu DJ, et al. Reliability-based design optimization of structural systems under hybrid probabilistic and interval model. Comput Struct 2015, 160: 126-134.
[182 Zhou JH, Xu M, Li M. Reliability-based design optimization concerning objective variation under mixed probabilistic and interval uncertainties. J Mech Des 2016, 138(11):114501
[183 Wang L, Wang XJ, Wang RX, et al. Reliability-based design optimization under mixture of random, interval and convex uncertainties. Arch Appl Mech 2016, 86(7):1341-1367.
[184 Wu JL, Luo Z, Li H, et al. A new hybrid uncertainty optimization method for structures using orthogonal series expansion. Appl Math Model 2017, 45:474-490.

[185 Huang ZL, Jiang C, Zhou YS, et al. Reliability-based design optimization for problems with interval distribution parameters. Struct Multidisc Optim 2017, 55(2):513-528.
[186 Liu Y, Collette MD. Efficient optimization framework for robust and reliable structural design considering interval uncertainty. Analysis and design of marine structures. CRC Press, London, 2015: 555-563.
[187 Li FY, Sun GY, Huang XD, et al. Multiobjective robust optimization for crashworthiness design of foam filled thin-walled structures with random and interval uncertainties. Eng Struct 2015, 88:111-124.
[188 Guo X, Cheng GD. Recent development in structural design and optimization. Acta Mechanica Sinica 2010, 26(6): 807-823.
[189 Maute K, Frangopol DM. Reliability-based design of MEMS mechanisms by topology optimization. Comput Struct 2003, 81(8): 813-824.
[190 Jung HS, Cho S. Reliability-based topology optimization of geometrically nonlinear structures with loading and material uncertainties. Finite Elem Anal Des 2004, 41(3): 311-331.
[191 Jalalpour M, Guest JK, Igusa T. Reliability-based topology optimization of trusses with stochastic stiffness. Struct Saf 2013, 43: 41-49.
[192 Kharmanda G, Olhoff N, Mohamed A, et al. Reliability-based topology optimization. Struct Multidiscip Optim 2004, 26(5): 295-307.
[193 Silva M, Tortorelli DA, Norato JA, et al. Component and system reliability-based topology optimization using a single-loop method. Struct Multidiscip Optim 2010, 41(1): 87–106.
[194 Nguyen TH, Song J, Paulino GH. Single-loop system reliability-based topology optimization considering statistical dependence between limit-states. Struct Multidiscip Optim 2011, 44(5): 593-611.
[195 Bobby S, Suksuwan A, Spence SMJ, et al. Reliability-based topology optimization of uncertain building systems subject to stochastic excitation. Struct Saf 2017, 66: 1-16.
[196 Chiralaksanakul A, Mahadevan S. First-order approximation methods in reliability-based design optimization. J Mech Des 2005, 127(5): 851-857.
[197 Liu J, Wen G, Zuo HZ, et al. A simple reliability-based topology optimization approach for continuum structures using a topology description function. Eng Optimiz 2016, 48(7): 1182-1201.
[198 Du JB, Sun CC. Reliability-based vibro-acoustic microstructural topology optimization. Struct Multidiscip Optim 2017, 55(4): 1195-1215.
[199 Patel J, Choi SK. Classification approach for reliability-based topology optimization using probabilistic neural networks. Struct Multidiscip Optim 2012, 45(4): 529-543.
[200 Jalalpour M, Tootkaboni M. An efficient approach to reliability-based topology optimization for continua under material uncertainty. Struct Multidiscip Optim 2016, 53(4): 759-772.
[201 Keshavarzzadeh V, Fernandez F, Tortorelli DA. Topology optimization under uncertainty via non-intrusive polynomial chaos expansion. Comput Methods Appl Mech Eng 2017, 318: 120-147.
[202 Luo YJ, Kang Z, Luo Z, et al. Continuum topology optimization with non-probabilistic reliability constraints based on multi-ellipsoid convex model. Struct Multidiscip Optim 2009, 39(3): 297-310.
[203 Xu B. Dynamic non-probabilistic reliability-based topology optimization of truss with uncertain-but-bounded parameters. J Vib Control 2015, 21(12): 2484-2496.
[204 Zheng J, Luo Z, Jiang C, et al. Non-probabilistic reliability-based topology optimization with multidimensional parallelepiped convex model. Struct Multidiscip Optim 2018, 57(6): 2205-2221.
[205 Guest JK, Igusa T. Structural optimization under uncertain loads and nodal locations. Comput Methods Appl Mech Eng 2008, 198(1): 116-124.
[206 Guo X, Zhang W, Zhang L. Robust structural topology optimization considering boundary

uncertainties. Comput Methods Appl Mech Eng 2013, 253: 356-368.
[207 Zhao JP, Wang CJ. Robust topology optimization under loading uncertainty based on linear elastic theory and orthogonal diagonalization of symmetric matrices. Comput Methods Appl Mech Eng 2014, 273: 204-218.
[208 Zhang WH, Liu H, Gao T. Topology optimization of large-scale structures subjected to stationary random excitation: An efficient optimization procedure integrating pseudo excitation method and mode acceleration method. Comput Struct 2015, 158: 61-70.
[209 Csébfalvi A. Robust Topology Optimization: A New Algorithm for Volume-constrained Expected Compliance Minimization with Probabilistic Loading Directions using Exact Analytical Objective and Gradient. Periodica Polytechnica. Civil Eng 2017, 61(1): 154-163.
[210 Zhu M, Yang Y, Guest JK, et al. Topology optimization for linear stationary stochastic dynamics: Applications to frame structures. Struct Saf 2017, 67: 116-131.
[211 Csébfalvi A, Lógó J. A critical analysis of expected-compliance model in volume-constrained robust topology optimization with normally distributed loading directions, using a minimax-compliance approach alternatively. Adv Eng Softw 2018, 120: 107-115.
[212 Long K, Wang X, Du YX. Robust topology optimization formulation including local failure and load uncertainty using sequential quadratic programming. Int J Mech Mater Des 2018; 1-16. https://doi.org/ 10.1007/ s10999-018-9411-z.
[213 Wang XJ, Geng XY, Wang L, et al. Motion error based robust topology optimization for compliant mechanisms under material dispersion and uncertain forces. Struct Multidisc Optim 2018, 57(6): 2161-2175.
[214 Tootkaboni M, Asadpoure A, Guest JK. Topology optimization of continuum structures under uncertainty–a polynomial chaos approach. Comput Methods Appl Mech Eng 2012, 201: 263-275.
[215 Zhao JP, Wang CJ. Robust structural topology optimization under random field loading uncertainty. Struct Multidiscip Optim 2014, 50(3): 517-522.
[216 Deng JD, Chen W. Concurrent topology optimization of multiscale structures with multiple porous materials under random field loading uncertainty. Struct Multidiscip Optim 2017, 56(1): 1-19.
[217 Lazarov BS, Schevenels M, Sigmund O. Topology optimization with geometric uncertainties by perturbation techniques. Int J Numer Meth Eng 2012, 90(11): 1321-1336.
[218 Jansen M, Lombaert G, Diehl M, et al. Robust topology optimization accounting for misplacement of material. Struct Multidiscip Optim 2013, 47(3): 317-333.
[219 Jansen M, Lombaert G, Schevenels M. Robust topology optimization of structures with imperfect geometry based on geometric nonlinear analysis. Computer Methods in Applied Mechanics and Engineering, 2015, 285: 452-467.
[220 da Silva GA, Cardoso EL. Stress-based topology optimization of continuum structures under uncertainties. Comput Methods Appl Mech Eng 2017, 313: 647-672.
[221 Guo X, Zhao XF, Zhang WS, et al. Multi-scale robust design and optimization considering load uncertainties. Comput Methods Appl Mech Eng, 2015, 283: 994-1009.
[222 Zhang XP, Kang Z, Zhang WB. Robust topology optimization for dynamic compliance minimization under uncertain harmonic excitations with inhomogeneous eigenvalue analysis. Struct Multidiscip Optim 2016, 54(6): 1469-1484.
[223 Wu JL, Gao J, Luo Z, et al. Robust topology optimization for structures under interval uncertainty. Adv Eng Softw 2016, 99: 36-48.
[224 Xu B, Jin YJ. Multiobjective dynamic topology optimization of truss with interval parameters based on interval possibility degree. J Vib Control 2014, 20(1): 66-81.
[225 Wu JL, Luo Z, Li H, et al. Level-set topology optimization for mechanical metamaterials under hybrid uncertainties. Comput Methods Appl Mech Eng 2017, 319, 414-441.
[226 Chen N, Yu DJ, Xia BZ, et al. Topology optimization of structures with interval random

parameters. Comput Methods Appl Mech Eng 2016, 307: 300-315.
[227 He ZC, Wu Y, Li E. Topology optimization of structure for dynamic properties considering hybrid uncertain parameters. Struct Multidiscip Optim 2018, 57(2): 625-638.
[228 Zheng J, Luo Z, Li H, et al. Robust topology optimization for cellular composites with hybrid uncertainties. Int J Numer Meth Eng 2018, 115(6): 695-713.
[229 Wang Y, Luo Z, Kang Z, et al. A multi-material level set-based topology and shape optimization method. Comput Methods Appl Mech Eng 2015, 283: 1570-1586.
[230 De Ruiter MJ, Van Keulen F. Topology optimization using a topology description function. Struct Multidiscip Optim 2004, 26(6): 406-416.
[231 Gomes AA, Suleman A. Application of spectral level set methodology in topology optimization. Struct Multidiscip Optim 2006, 31(6): 430-443.
[232 Wendland H. Computational aspects of radial basis function approximation. Elsevier BV. 2005.
[233 Wendland H. Piecewise polynomial, positive definite and compactly supported radial functions of minimal degree. Adv Comput Math 1995, 4: 389–396.
[234 Rozvany GIN, Bendsøe MP, Kirsch U. Layout Optimization of Structures. Appl Mech Rev 1995, 48(2): 41-119.
[235 Zhou M., Rozvany GIN. The COC algorithm, part II: Topological, geometry and generalized shape optimization. Comput Methods Appl Mech Eng 1991, 89(1-3): 309-336.
[236 Svanberg K. The method of moving asymptotes—a new method for structural optimization. Int J Numer Meth Eng 1987, 24(2): 359-373.
[237 Haug EJ, Choi KK, Komkov V. Design sensitivity analysis of structural systems. Orlando: Academic Press, 1986.
[238 Madsen HO, Krenk S, Lind NC. Methods of structural safety. Courier Corporation, 2006.
[239 Montgomery DC. Design and analysis of experiments. John Wiley & Sons, 2017.
[240 Blatman G, Sudret B. An adaptive algorithm to build up sparse polynomial chaos expansions for stochastic finite element analysis. Probabilist Eng Mech 2010, 25(2): 183-197.
[241 Isukapalli SS. Uncertainty analysis of transport-transformation models. New Brunswick, New Jersey, 1999.
[242 Smolyak S. Quadrature and interpolation formulas for tensor products of certain classes of functions. Soviet Math Dokl 1963, 4: 240-243.
[243 Gerstner T, Griebel M. Numerical integration using sparse grids. Numer Algorithms 1998, 18(3-4): 209.
[244 Xiong F, Xiong Y, Greene S, et al. A new sparse grid based method for uncertainty propagation. ASME 2009 International Design Engineering Technical Conferences and Computers and Information in Engineering Conference. American Society of Mechanical Engineers, 2009: 1205-1215.
[245 Barthelmann V, Novak E, Ritter K. High dimensional polynomial interpolation on sparse grids. Adv Comput Math 2000, 12(4): 273-288.
[246 Judd KL, Maliar L, Maliar S, et al. Smolyak method for solving dynamic economic models: Lagrange interpolation, anisotropic grid and adaptive domain. J Econ Dyn Control 2014, 44: 92-123.
[247 Chen SH, Ma L, Meng GW, et al. An efficient method for evaluating the natural frequencies of structures with uncertain-but-bounded parameters. Comput Struct 2009; 87(9): 582-590.
[248 Van Trees HL. Detection, estimation, and modulation theory. John Wiley & Sons, 2004.
[249 Papadrakakis M, Stefanou G, Papadopoulos V. Computational Methods in Stochastic Dynamics. Berlin: Springer, 2011.
[250 Li CC, Der Kiureghian A. Optimal discretization of random fields. J Eng Mech 1993, 119(6): 1136-1154.
[251 Choi WS, Park GJ. Structural optimization using equivalent static loads at all time intervals.

Comput Methods Appl Mech Eng 2002, 191(19): 2105-2122.
[252 Kim YI, Park GJ. Nonlinear dynamic response structural optimization using equivalent static loads. Comput Methods Appl Mech Eng 2010, 199(9): 660-676.
[253 Zhao JP, Wang CJ. Dynamic response topology optimization in the time domain using model reduction method. Struct Multidiscip Optim 2016, 53(1): 101-114.
[254 Guyan RJ. Reduction of stiffness and mass matrices. AIAA Journal 1965, 3(2): 380.
[255 Gu J, Ma ZD, Hulbert GM. A new load-dependent Ritz vector method for structural dynamics analyses: quasi-static Ritz vectors. Finite Elem Anal Des 2000, 36(3): 261-278.
[256 Dickens JM, Nakagawa JM, Wittbrodt MJ. A critique of mode acceleration and modal truncation augmentation methods for modal response analysis. Comput Struct 1997, 62(6): 985-998.
[257 Yoon GH. Toward a multifrequency quasi-static Ritz vector method for frequency-dependent acoustic system application. Int J Num Meth Eng 2012, 89(11): 1451-1470.
[258 Bathe KJ. Finite element procedures. Klaus-Jurgen Bathe, 2006.
[259 Cook RD, Malkus DS, Plesha ME, et al. Concepts and applications of finite element analysis. New York: Wiley, 1974.